COMPRESSED - AIR ENERGY STORAGE IN ROCK SALT OF THE MAHA SARAKHAM FORMATION

Mr. Decho Phueakphum

A Thesis Submitted in Partial Fulfillment of the Requirements for the Degree of

Master of Engineering in Geotechnology

Suranaree University of Technology

Academic Year 2003

ISBN 974-533-253-4

การเก็บพลังงานไฟฟ้าในรูปอากาศภายใต้แรงดันในชั้นเกลือหินชุดมหาสารคาม

นายเดโช เผือกภูมิ

วิทยานิพนธ์นี้เป็นส่วนหนึ่งของการศึกษาตามหลักสูตรปริญญาวิศวกรรมศาสตรมหาบัณฑิต

สาขาวิชาเทคโนโลยีธรณี

มหาวิทยาลัยเทคโนโลยีสุรนารี

ปีการศึกษา 2546

ISBN 974-533-253-4

COMPRESSED-AIR ENERGY STORAGE IN ROCK SALT

OF THE MAHA SARAKHAM FORMATION

Suranaree University of Technology has approved this thesis submitted in partial fulfillment of the requirements for a Master's Degree.

Thesis examining committee

.....

(Dr. Chongpan Chonglakmani)

Chairman

.....

(Assoc. Prof. Dr. Kittitep Fuenkajorn)

Member (Thesis advisor)

.....

(Dr. Helmut Duerrast)

Member

.....	.....
(Assoc. Prof. Dr. Tawit Chitsomboon)	(Assoc. Prof. Dr. Vorapot Khompis)
Vice Rector for Academic Affairs	Dean of Institute of Engineering

เดโช เผือกภูมิ: การเก็บพลังงานไฟฟ้าในรูปอากาศภายใต้แรงดันในชั้นเกลือหินชุดมหาสารคาม (COMPRESSED-AIR ENERGY STORAGE IN ROCK SALT OF THE MAHA SARAKHAM FORMATION)
อาจารย์ที่ปรึกษา: รองศาสตราจารย์ ดร. กิตติเทพ เฟื่องขจร, 293 หน้า
ISBN 974-533-253-4

วัตถุประสงค์ของงานวิจัยคือ เพื่อประเมินศักยภาพเชิงกลศาสตร์ของชั้นเกลือหินในภาคตะวันออกเฉียงเหนือของประเทศไทย เพื่อใช้ในการก่อสร้างโพรงกักเก็บพลังงานไฟฟ้าในรูปอากาศภายใต้ความดัน กิจกรรมหลักในงานวิจัยประกอบด้วย การศึกษางานวิจัยที่เกี่ยวข้อง การทดสอบคุณสมบัติเชิงกลศาสตร์พื้นฐาน การทดสอบการประสานตัวของรอยแตก และการทดสอบแรงกดแบบวัฏจักรในห้องปฏิบัติการโดยใช้ตัวอย่างเกลือหินจากแอ่งสกลนคร ทั้งนี้ยังได้สร้างแบบจำลองโพรงเพื่อใช้ในเทคโนโลยีนี้ด้วย ผลจากงานวิจัยสรุปได้ว่า ตัวอย่างเกลือหินจากแอ่งสกลนครที่นำมาใช้ในการทดสอบมีค่ากำลังรับแรงดึงและกำลังต้านแรงกด อยู่ในเกณฑ์ค่อนข้างสูงเมื่อเทียบกับเกลือหินจากแหล่งอื่น ๆ ในต่างประเทศ ผลจากการทดสอบการประสานตัวของรอยแตกในตัวอย่างเกลือหินบ่งชี้ว่ารอยแตกในเกลือหินสามารถประสานตัวกลับเป็นหินแข็งได้ และพบว่ากำลังรับแรงดึงของรอยแตกหลังจากการประสานตัวได้เพิ่มขึ้นถึง 90 % ของกำลังรับแรงดึงที่ได้จากการทดสอบเกลือหินในสภาวะความดันล้อมรอบสูงสุดเท่ากับ 1,000 psi ในระยะเวลาประมาณ 100 ชั่วโมง ผลจากการทดสอบด้วยแรงกดแบบวัฏจักรพบว่าการลดลงของกำลังรับแรงกด (S) จะแปรผกผันกับจำนวนรอบ (N) ที่ตัวอย่างหินวิบัติ โดยมีความสัมพันธ์ดังนี้คือ $S = 33.6\ N^{-0.08}$ และค่าสัมประสิทธิ์ความยืดหยุ่นของตัวอย่างเกลือหินจะลดลงเมื่อจำนวนรอบเพิ่มขึ้น โดยมีค่าอยู่ระหว่าง 20 ถึง 30 GPa ผลจากการศึกษาข้อมูลหลุมเจาะจากกรมทรัพยากรธรณีระบุว่า ในเชิงความลึกและความหนาของชั้นเกลือหินมีเพียง 2-3 พื้นที่ที่เหมาะสมสำหรับการก่อสร้างโพรงกักเก็บอากาศอัด ชั้นเกลือหินในพื้นที่บริเวณอำเภอบรบือมีคุณลักษณะเหมาะสมสำหรับเทคโนโลยี

อากาศอัด ผลจากการจำลองด้านคอมพิวเตอร์ระบุว่า โพรงรูปทรงกลมจะเหมาะสมที่สุด เพราะมีการยุบตัวน้อยที่สุด และมีขอบเขตของพลาสติกโซนแคบที่สุด ความดันของอากาศสูงสุดและต่ำสุดที่เหมาะสมเชิงกลศาสตร์มีค่าเท่ากับ 90% และ 30% ของค่าความเค้นในชั้นเกลือที่หลังคาโพรง และอัตราการอัดอากาศและการปล่อยอากาศออกจากโพรงเกลือในรอบรายวัน ควรจะอยู่ประมาณ 96 psi/hour ซึ่งจะทำให้โพรงมีเสถียรภาพเชิงกลศาสตร์ ด้วยความดันลักษณะนี้การทรุดตัวของผิวดินหรือโพรงจะมีค่าประมาณ 20 เซ็นติเมตร ในช่วง 20 ปีของการใช้งาน

สาขาวิชาเทคโนโลยีธรณี ลายมือชื่อนักศึกษา.....

ปีการศึกษา 2546 ลายมือชื่ออาจารย์ที่ปรึกษา.....

DECHO PHUEAKPHUM: COMPRESSED-AIR ENERGY STORAGE IN ROCK SALT OF THE MAHA SARAKHAM FORMATION
THESIS ADVISOR: ASSOC. PROF. KITTITEP FUENKAJORN, Ph.D., P.E.
293 pp. ISBN 974-533-253-4

ROCK SALT/ HEALING/ FRACTURE / COMPUTER MODELING/ STROAGE CAVERN

The objective of this research is to evaluate the mechanical performance of the rock salt formations in the Northeast of Thailand for use in the compressed-air energy storage. The task involves literature review of the relevant research topics, the characterization tests, the fracture healing and the cyclic loading experiments on rock salt from Sakon Nakhon basin, and computer modeling of the cavern for this technology. The test results indicate that the compressive and tensile strengths of the rock salt specimens obtained from Sakon Nakhon basin used in this research are relatively high as compared to those from various sources. The healing test results indicate that under the confining pressure of 1,000 psi for about 100 hours, salt fractures can be healed and can gain the tensile strength up to 90% of the intact strength. The cyclic loading results indicate that the fatigue strength (S) decreases with the increase of loading cycle (N): $S = 33.6\ N^{-0.08}$. The elastic modulus decreases as the number of cycle increases, and ranging between 20 and 30 GPa. Review of the drill-hole data obtained by the Department of Mineral Resources indicates that only few areas in Northeastern Thailand pose appropriate depth and thickness of the salt

formations that are suitable for the compressed-air storage caverns. In this study the depth and thickness of salt formation at Borabu District have been selected for use as an example area for computer modeling. The simulation results show that spherical cavern has the smallest closure of the cavern and the narrowest plastic zone around the cavern boundary than those of the elliptical and cylindrical caverns. For the cavern at 600 m depth, the maximum and minimum safe storage pressures should be about 90% and 30% of the in-situ stress at the cavern top. The withdrawal and injection rates for the daily cycle should be about 96 psi/hour. This will result in a long-term mechanical stability of the surrounding salt. The maximum surface subsidence at 20 years after operation would be about 20 cm.

สาขาวิชาเทคโนโลยีธรณี ลายมือชื่อนักศึกษา.....

ปีการศึกษา 2546 ลายมือชื่ออาจารย์ที่ปรึกษา.....

ACKNOWLEDGEMENTS

The author wishes to acknowledge the funding support of Suranaree University of Technology (SUT).

The author would also like to thank Mr. Keith S. Crosby, vice president and director of the Asia Pacific Resources Ltd., who provided the rock salt samples for testing.

Grateful thanks and appreciation are given to Assoc. Prof. Dr. Kittitep Fuenkajorn, thesis advisor, who lets the author work independently, but gave a critical review of this research. Many thanks are also extended to Dr. Chongpan Chonglakmani and Dr. Helmut Duerrast, who served on the thesis committee and commented on the manuscript.

Decho Phueakphum

TABLE OF CONTENTS

PAGE

TABLE OF CONTENTS (Continued)

PAGE

TABLE OF CONTENTS (Continued)

PAGE

TABLE OF CONTENTS (Continued)

PAGE

TABLE OF CONTENTS (Continued)

PAGE

LIST OF TABLES

TABLE **PAGE**

LIST OF TABLES (Continued)

TABLE **PAGE**

LIST OF FIGURES

FIGURE **PAGE**

LIST OF FIGURES (Continued)

FIGURE **PAGE**

LIST OF FIGURES (Continued)

FIGURE **PAGE**

LIST OF FIGURES (Continued)

FIGURE **PAGE**

LIST OF FIGURES (Continued)

FIGURE **PAGE**

LIST OF FIGURES (Continued)

FIGURE **PAGE**

LIST OF FIGURES (Continued)

FIGURE **PAGE**

LIST OF FIGURES (Continued)

FIGURE **PAGE**

LIST OF FIGURES (Continued)

FIGURE **PAGE**

LIST OF FIGURES (Continued)

FIGURE **PAGE**

LIST OF FIGURES (Continued)

FIGURE **PAGE**

LIST OF FIGURES (Continued)

FIGURE **PAGE**

LIST OF FIGURES (Continued)

FIGURE **PAGE**

LIST OF FIGURES (Continued)

FIGURE **PAGE**

LIST OF FIGURES (Continued)

FIGURE **PAGE**

LIST OF FIGURES (Continued)

FIGURE **PAGE**

LIST OF FIGURES (Continued)

FIGURE **PAGE**

LIST OF FIGURES (Continued)

FIGURE **PAGE**

LIST OF FIGURES (Continued)

FIGURE **PAGE**

LIST OF FIGURES (Continued)

FIGURE **PAGE**

LIST OF FIGURES (Continued)

FIGURE **PAGE**

LIST OF FIGURES (Continued)

FIGURE **PAGE**

LIST OF FIGURES (Continued)

FIGURE **PAGE**

LIST OF FIGURES (Continued)

FIGURE **PAGE**

LIST OF FIGURES (Continued)

FIGURE **PAGE**

LIST OF FIGURES (Continued)

FIGURE **PAGE**

LIST OF FIGURES (Continued)

FIGURE **PAGE**

LIST OF FIGURES (Continued)

FIGURE **PAGE**

LIST OF FIGURES (Continued)

FIGURE **PAGE**

LIST OF FIGURES (Continued)

FIGURE **PAGE**

LIST OF FIGURES (Continued)

FIGURE **PAGE**

LIST OF FIGURES (Continued)

FIGURE **PAGE**

LIST OF FIGURES (Continued)

FIGURE **PAGE**

LIST OF FIGURES (Continued)

FIGURE **PAGE**

LIST OF FIGURES (Continued)

FIGURE **PAGE**

LIST OF SYMBOLS AND ABBREVIATIONS

A	=	Initial cross-section area transverse to the direction of load
b	=	Coefficient for number of cycles
C	=	Constant value depending on fracture characteristic and property of fluid flow through fracture
D	=	Diameter
E	=	Elastic modulus
e	=	Width of opening or fracture aperture
G_1	=	Shear modulus
G_2	=	Retarded shear modulus
Δh	=	Differential of hydraulic head between two point
H_e	=	Healing effectiveness of the fracture
I	=	Percentage of inclusions
I_H	=	Point load strength index of healed fracture
I_s	=	Point load strength index of intact salt
K_1	=	Ultimate bulk modulus
K_2	=	Retarded bulk modulus
K_f	=	Hydraulic conductivity of the fracture
K_o	=	Hydraulic conductivity at time equal to 1
L	=	Length
L/D	=	Length-to-diameter ratio

LIST OF SYMBOLS AND ABBREVIATIONS (Continued)

N	=	Number of cycles
P	=	Axial load
P_c	=	Confining pressure
P_f	=	The maximum of loading at failure
P_i	=	Internal pressure
P_o	=	External pressure /or in-situ stress
P_{grad}	=	Pressure gradient
Q	=	Flow rate
S	=	Fatigue strength
S_o	=	Stress coefficient
t	=	Thickness
V	=	Flow volume
V_2	=	Elastoviscosity
V_4	=	Plastoviscosity
W	=	Weight
W_f	=	Width of aperture or fracture
ρ	=	Density
β	=	Time coefficient
γ	=	Unit weight
μ	=	Viscosity of fluid of gas flow through fracture.
σ_1	=	Maximum principal stresses

LIST OF SYMBOLS AND ABBREVIATIONS (Continued)

σ_3 = Minimum principal stresses

σ_{axial} = Axial stress

σ_{max} = Different maximum stresses

σ_B = Brazilian tensile strength

σ_c = Uniaxial compressive strength

σ_H = Fracture tensile strength

ε_{axial} = Axial strain

ε_f = Strain at failure

$\Delta\varepsilon$ = Differential strain

γ_o = Octahedral shear strain

γ_c = Critical shear strain

ν = Poisson's ratio

CHAPTER I

INTRODUCTION

1.1 Objectives

The objective of this study is to assess the mechanical performance of rock salt in the Maha Sarakham Formation in the Northeast of Thailand for compressed-air energy storage (CAES) technology by employing laboratory testing and computer modeling. The laboratory tests are conducted to experimentally assess the healing behavior of rock salt fractures under duration, stress conditions, saturation and inclusion (impurity), and to study the behavior of rock salt under cyclic loading. The computer modeling is performed to simulate the behavior of storage cavern in rock salt formations.

1.2 Problem and Rationale

In order to take advantage of rock salt deposits that distribute abundantly in the Maha Sarakham Formation, it's potential to be developed and applied in compressed-air energy storage (CAES) technology should be considered. Rock salt is generally suitable for storage of compressed air due to its low permeability. A dissolved salt cavern with a high mechanical stability can be achieved when it is properly designed. The concept of CAES is to storage and excessive energy in form of compressed air. It is then reconverted to produce electricity during demand periods. The CAES technology provides the highest efficiency compared with other

energy storage technologies. This technology is a world-wide technology, found in Europe and America, because it can enhance power plant efficiency.

The CAES technology has been developed and operated in many countries by taking advantage of suitable rock strata to store compressed air. Among those rock strata, rock salt deposits or salt domes are the most popular one because their hydraulic and mechanical properties are suitable as indicated by Katz and Lady (1976) and DeLong et al. (1989). Design and analysis of solution salt cavern for storage of compressed air have been comprehensively studied in the United States and Germany (Thoms and Martinez, 1978; Wittke et al., 1980; Serata et al., 1989; Fuenkajorn and Daemen, 1992a; and Fuenkajorn and Serata, 1992).

Most of rock types other than rock salt that have been developed for CAES are sedimentary rocks, for example conglomerate in Japan (Shidahara et al., 2000), limestone caverns (Liang and Lindblom, 1994) and other hard rocks in the United States and Great Britain (Pincus, 1980; Salter et al., 1984; and McKey et al., 1989). These references indicate that efficiency of compressing and converting air energy in those rock types is lower than in rock salt caverns.

Behavior and property of rock salt around the CAES cavern are different from those belong to other types of underground structures. For the CAES cavern, it should be designed to withstand cyclic loading. The cavern pressure will be increased and decreased continually with air compressing during excessive electricity periods and air releasing to produce electricity during demand periods. Repeated changes of cavern pressures directly affect the rock salt behavior around the cavern. The cavern is susceptible to collapse if the design of the cavern's shape and pressure level is not suitable. The important key for a success for the CAES technology in Thailand are

the mechanical properties and structural geology of the rock salt found in the Northeastern Thailand.

It is, therefore, necessary to study the mechanical behavior of rock salt subjected to cyclic loading and the self-healing of rock salt fractures during the process of air injection and withdrawal. The study can be performed by laboratory testing.

1.3 Scope of Work

The research emphasizes the mechanical properties of rock salt in the Maha Sarakham Formation. These properties are compressive strength against cyclic loading and healing of rock salt fractures. This research does not attempt to study long-term behavior of rock salt such as visco plasticity property. The temperature used in the laboratory tests and analysis is assumed to be constant at room temperature. This research will not cover the processes of reconverting of compressed air to produce electricity and will exclude either design or study of surface facility.

The rock salt specimens are obtained from the Sakon Nakhon Basin. The sample preparation and testing process are conducted in the laboratory. In-situ experiments are not performed in this research. The characterization tests include uniaxial compression tests, Brazilian tension tests, and point load strength index test to determine the uniaxial compressive strength, tensile strength, and strength index of the rock salt specimens, respectively.

In the healing tests, series of fracture initiations and fractures healing are performed in the laboratory. The healing fractures are simulated by using the saw cut smooth surfaces, tension-induced fracture and polished fractures created in the

cylindrical specimens of rock salt. The healing tests are performed as a function of stress state, time, inclusion, and saturation. The healing behavior is assessed by determining the tensile strength of the fractures using point load strength test, Brazilian tensile strength test and changing of permeability through the fractures. The cyclic loading test will involve laboratory testing under constant ambient temperature and mathematical formulation to predict the fatigue behavior of rock salt.

The computer modeling will be used to simulate or predict the state of stress around the storage cavern during operation. The parameters that used in the computer modeling will be calibrated from the experimental results. The horizontal variations of the chemical compositions and mechanical properties have not been taken into consideration since such variations remain unknown. The in-situ stresses are equivalent to the hydrostatic pressure of the rock. The sequences of rock formation in Northeastern Thailand will be continuous, isotropic and homogeneous. The design recommendations obtained for the salt formations in Northeastern Thailand may not be applicable to salt formations from other locations.

1.4 Methodology

The research effort is divided into five tasks including the literature review, sample collection and preparation, the laboratory testing, the data analysis, and the computer modeling.

1.4.1 Literature Review

All relevant references will be studied and reviewed to understand the CAES technology in rock salt, especially those related to behavior of rock salt subjected to cyclic loading and healing of rock salt fractures.

1.4.2 Sample Collection and Preparation

Rock salt samples have been donated by the Asian Pacific Potash Corporation, located in the Udon Thani Province. They are obtained from the Sakon Nakhon Basin. The core specimens are collected from the upper and the middle salt beds of the Maha Sarakham Formation at depths ranging between 250 meters and 400 meters. They are in cylindrical shape with 2.4 inches (60 mm) in diameter. Preparation of these samples will follow, as much as practical, the ASTM standards (ASTM D4543-85, 1998). There are three groups of specimens for different laboratory test methods: for basic characterization tests, cyclic loading tests, and healing tests.

The basic characterization tests will include the uniaxial compressive strength tests, Brazilian tensile strength tests, and point load strength index tests. Five specimens will be prepared to have L/D ratio of 2.5 for the uniaxial compressive strength test. Seventeen specimens with L/D ratio of 0.5 are prepared for the Brazilian tensile strength tests. Ten specimens with L/D ratio ranging between 0.8 - 1.2 will be prepared for point load strength tests. Eight specimens with L/D ratio of 2.5 will be prepared for uniaxial cyclic loading tests.

For the healing tests, nine specimens will be prepared to obtain a nominal length of 100 millimeters by a cutting machine. The saw-cut surfaces are ground flat by the grinding machine. These samples are prepared for the healing tests under uniaxial loading. Ten specimens with 100 millimeters long will be used for the point load test to induce tensile fracture. Nine specimens with tension-induced fractures and polished fractures having 38-millimeters diameter and 60-millimeters length will be prepared for healing test under confining pressure.

All specimens will be measured to determine the precise dimensions. The geologic depth will be recorded for each specimen. The physical characteristics (i.e., mineral composition, density, grain size, and color) are described. A saturated brine will be prepared for use as grinding fluid during the preparation to prevent the specimens from dissolving. After finishing preparation, the specimens will be labeled and wrapped with plastic film. The identification of specimens is given, which includes rock type, borehole number, core number, core diameter, type of experiment and sample number.

1.4.3 Experimental Work

Characterization tests includes the uniaxial compression tests (ASTM D2938-95, 1998), the Brazilian tension tests (indirect tensile strength tests) (ASTM D3967-95, 1998), and the point load tests (ASTM D5731-95, 1998). For the uniaxial tests, the specimens are loaded at constant rate of 0.1 MPa/sec. The results are shown in form of stress – strain curves. The Brazilian test determines the tensile strength of the salt. The point load strength test determines the indirect tensile strength of intact salt for comparing with the tensile strength of the healed fractures.

The cyclic loading test specimens will be loaded and unloaded with the maximum stresses varied from 60% to 90% of ultimate static strength. These tests determine the relation between strength and number of cycles (S-N curves), and between strain and time. These tests will also determine the elastic modulus (E) with the increasing number of cycles (N).

The healing tests on the specimens with tension-induced fracture and polished fracture will be carried out by performing the confining pressure. After a certain period, the healing effectiveness will be assessed by repeating the Brazilian

tensile strength test on the same specimen. The measured tensile strength of the healed fractures will be used as an indicator of the healing effectiveness. The magnitude of the confining pressure (healing stress) and duration under such stress will be the studied variables.

1.4.4 Laboratory Data Analysis

The results from the laboratory will be analyzed to understand the behavior of rock salt under cyclic loading and to explain the healing behavior as a function of stresses, duration, and inclusions (impurity). In conjunction with the basic mechanical properties, these results can be used to design and analyze the stability of rock salt cavern in the CAES technology. The analysis in this stage will, therefore, emphasize on the potential of this technology and will indicate the engineering geology problems that may occur as well as the way in which those problems should be coped in order to develop the CAES technology in Thailand.

1.4.5 Computer Modeling

Computer simulations will be conducted to assist in the design of the CAES cavern. A 2-dimensional finite element mesh will be constructed to graphically represent the salt formations and associated rocks around the cavern. The computations use the non-linear finite element code "GEO". The algorithm of this computer code is designed to calculate the stress and displacement in time domain. It is contains of eight main modules: elastic, visco-elastic, visco-plastic, strain-softening and strain-hardening, deterioration, dilation and permeability increases. This program can disclose a realistic rheological behavior of the rock salt shown by Serata and Fuenkajorn (1991, 1992a, 1992b), Stormont and Fuenkajorn (1994), and Fuenkajorn and Serata (1994).

Results from the experimental work will be used to construct computer models to simulate or predict the stress and strain of the rock salt around the storage caverns during operation.

1.5 Expected Results

It is expected that the results can improve the understanding of the knowledge on cyclic loading and healing mechanisms of the rock salt fractures in relation with the CAES technology. This knowledge can assist in the design and stability evaluation of the storage cavern in rock salt formations. The final analysis may be used to predict the fracture initiation and fracture healing in rock salt around storage caverns.

1.6 Thesis Contents

Chapter I describes the objectives, the problems and rationale, and the methodology of the research. Chapter II presents results of the literature review on the healing of rock salt fracture, the compressed air energy storage, the cyclic loading, the salt properties, the experimental research on salt, the mechanical constitutive laws of rock salt, the computer modeling, the solution mining technology, and the salt sequences in Khorat Plateau. Chapter III describes the salt sample collection and preparation. Chapter IV describes the results obtained from the laboratory testing. The experiments are divided into five tests, including 1) uniaxial compressive strength tests, 2) Brazilian tensile strength tests, 3) point load strength index tests, 4) uniaxial cyclic loading tests, and 5) healing tests. Chapter V describes the computer modeling for horizontal model to selects the suitable cavern shape. Chapter VI presents

computer modeling and the conceptual design for the CAES caverns. Chapter VII summarizes the research results, and provides recommendations for future research studies.

CHAPTER II

LITERATURE REVIEW

Literatures related to the compressed-air energy storage technology in caverns created in rock salt formations and salt domes have been reviewed in this research. This research emphasizes the mechanical potential of rock salt formations to be applied in this technology. The related knowledge to be reviewed in this research is categorized into eight groups: 1) compressed-air energy storage technology, 2) geology of rock salt formations in the Northeastern Thailand, 3) rock salt characteristics, 4) mechanical testing on rock salt, 5) rheological equations of rock salt, 6) computer modeling, 7) healing mechanisms of rock salt fracture, and 8) cyclic loading tests.

2.1 Compressed-Air Energy Storage Technology

Compressed-air energy storage (CAES) is a technology in which a surplus of electrical energy is storaged in the form of compressed air during off-peak periods and then the energy is used on demand during peak periods to produce electricity (Crotogino et al., 2001; Crotogino and Quast, 1980). CAES technology involves the production of compressed air using excess electricity available from the power system during off-peak hours. The compressed air is stored in an underground cavern. When a supply of electricity energy is required, the storage energy is converted back to electrical energy. CAES technology is a superior efficiency

technology compared with other technologies such as pumped storage technology. Since CAES can directly reduce cost and can result in enhancing the efficiency of the power plant, this technology has been widely used in Europe, Asia, and America.

The first compressed-air energy storage in the world is the Huntorf Plant in Germany which was constructed in 1978 (Crotogino et al., 2001). The plant with 290 MW of power consists of two underground caverns that have a total volume of 310,000 cubic meters. The caverns are situated 220 meters apart. The cavern ceilings are at 650 meters deep from the ground surface. The constant volume system is employed to reconvert the compressed air to produce electricity. Air is compressed into the cavern at the rate of approximately 108 kg/sec. The maximum allowable pressure in the cavern is 70 bar. The compressed air is released with the rate of 417 kg/sec to produce electricity. The minimum cavern pressure is as low as 20 bar. The caverns are designed to be stable throughout the operation period. The same technology has been also used in McIntosh, Alabama (in the United States) since 1991 with the power capacity of 110 MW.

The CAES technology in bedrock, nowadays, can be divided into two systems which including constant pressure systems and constant volume systems.

1) Constant Pressure System - The concept of this system is that water accumulated in the reservoir above the cavern is allowed to replace the air that has been compressed in the cavern. The air then flows through a turbine generator to produce electricity. Air is pumped and compressed into the underground by using excess electricity during nighttime and consequently water in the cavern flows back to the reservoir. This process recurs in cycles. This system is compatible in hard rock formations. The conceptual diagram of the constant pressure system is illustrated in Figure 2.1.

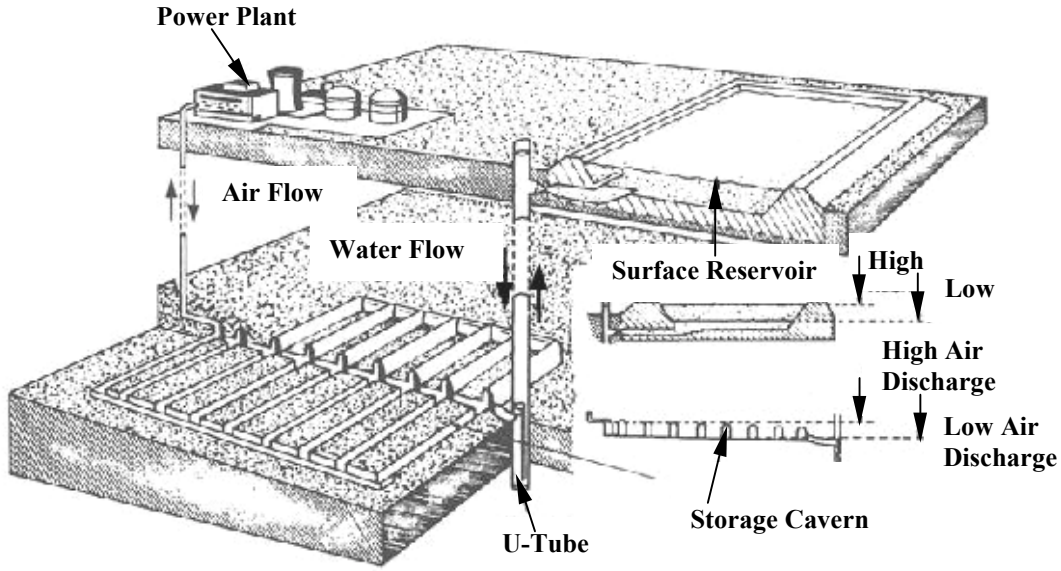

Figure 2.1 Constant pressure system to produce the electricity for Compressed-Air Energy Storage (CAES) technology (Salter et al., 1984).

2) Constant Volume System - The concept of this system is to vary the pressure in the cavern that contains only the compressed air. The compressed air is released to produce electricity and results in a gradual decrease of pressure in the cavern. Air is compressed into the cavern again by using excess electricity during the off-peak period. The process is continually repeated in cycles during operation. In order to maintain the cavern stability, the pressure in the cavern is controlled to be in allowable range from the design. This system is suitable for the caverns in rock salt formations. The conceptual diagram of the constant pressure system is illustrated in Figure 2.2

The technology of compressed air energy storage in bedrock has been developed and operated in many countries by taking advantage of suitable rock formations. Most of the rocks for CAES are sedimentary and hard rock formations with low permeability.

2.1.1 Storage in Sedimentary Rock and Hard Rock Formations

In Japan, CAES had been applied in a conglomerate (Shidhara et al., 2000) and limestone (Liang and Lindblou, 1994). In Britain and the United States, CAES had been applied in hard rock formations (Mckey et al., 1989; Salter et al., 1984; Pincus, 1980; and Morfeldt, 1975). Design of the caverns in those rock types had been comprehensively studied and analyzed by these researchers.

For the Soyland CAES project in Illinois, United States, Salter et al. (1984) have studied the design of an underground cavern in dolomite formations by employing the constant pressure system. The cavern was designed to have a total volume of 245,000 m^3 and located at 580 m depth. McKey et al. (1984) have studied and designed an underground cavern in metamorphic granite gneiss for a CAES

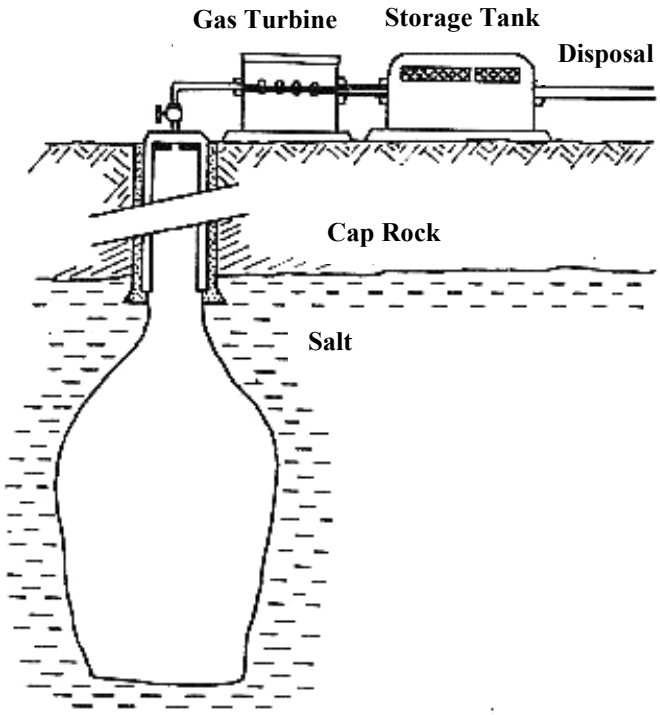

Figure 2.2 Constant volume system to produce the electricity for Compressed-Air Energy Storage (CAES) technology (Wolfgang, 1982).

project named “The Bad Creck Project”. The cavern was designed to have a dimension of 23 m width, 132 m length and 50 m height, with an approximate volume of 1,518,000 m^3. The project can produce 1,000 MW power. Besides that, the project was also viewed as a suitable project in terms of economics and safety for construction. Wittke et al. (1980) studied and analyzed CAES with a computer model to design the cavern in Vianden Clay. The designed cavern consists of elliptical cylinder shaped rooms with a diameter of 5.5 m and a length of 5 km. The rooms lie horizontally at 500 m depth. A reservoir constructed above the cavern provides the water from the reservoir that can be released to push compressed air in the cavern to produce electricity. In the meantime, water can also support the cavern stability. The total volume of the cavern is as high as 100,000 m^3. By employing the constant pressure system with the constant pressure at 50 bar, the project provides the generating capacity of 300 MW within 4 hours. DeLong et al. (1989) conducted a feasibility study on a CAES project in the northwest of the United States by taking into account of suitability of geology in parallel with the power demands. In Norton, Ohio, the United States, a 10 million cubic meters underground cavern was excavated in limestone and compressed air in the cavern was pushed by water from the reservoir located above the cavern to produce electricity (Crotogino et al., 2001).

2.1.2 Storage in Rock Salt Formations

As to the suitability in terms of hydraulic and mechanical properties, rock salt deposits or salt domes are the preferred choice among other types of underground media which can accommodate compressed air. Results from many researches indicate that rock salt deposits and salt domes have higher efficiency for the storage of compressed air than other rock types. Katz and Lady (1976), Change et al. (1980),

and DeLong et al. (1989) summarize the application of CAES technology in generally. Design and analysis of the solution mined storage cavern have been comprehensively studied in the United States and Germany (Serata et al., 1989; Thoms and Martinez, 1978; Gehle and Thoms, 1986; Wittke et al., 1980; Fuenkajorn and Daemen, 1992a; Fuenkajorn and Serata, 1992). Many researchers from various organizations have studied the mechanics and geology of the underground caverns for CAES in rock salt deposits and salt domes.

Serata et al. (1989) analyzed the geomechanical stability of salt dome in McIntosh, in the South of Alabama for the compressed air storage. The analysis was done by a computer model with an aid of REM software. Results from the analysis were used to assess the long-term effects on rock salt around the cavern. The analysis was also emphasized on the deformation of the cavern wall, stress distribution, the subsidence rates of ground surface, and the convergence of the cavern.

The Electric Power Research Institute (EPRI), a government organization in the United States, has conducted comprehensive research and developed the CAES technology. Various aspects have been studied and continually developed, for example, the design of an underground cavern in rock salt deposits (EPRI, 1990a; 1990b; 1990c; 1992a; 1992b; 1992c; 1992d; 1994a; 1994b), design of power generator for CAES (EPRI, 1994d; 1994e; 1997; 1999), economic assessment (EPRI, 1986; 1999), and CAES for other types of underground media. Due to copyrights restrictions as well as commercial competition, the results of these studies have not been published.

2.2 Geology of Rock Salt Deposits in Thailand

2.2.1 Structural Geology

Rock salt deposits are found in the Khorat Plateau as shown in Figure 2.3. In order to understand the stratigraphic succession of the area as well as the thickness of rock salt deposits, fundamental knowledge in structural geology and physical characteristics of the Khorat Plateau are needed. This knowledge is explained in this section. The Khorat Plateau is situated between latitude 14° - 19° North and longitude 101° - 106° East. The north and the east are bordered with Laos. The south of the area connects to Combodia. The plateau has a total area of approximately 150,000 m^2 and locates at 140 m above mean sea level. The plateau slopes gently to the southeast direction. The mountain ranges namely Petchaboon and Dongpayayen form the high edge in the west of the plateau. Whereas, the mountain ranges namely Sankamphaeng and Phanomdongrak form the high edge in the south of the area. Another mountain ranges called Phupan stretches in the southeast direction at the middle part of the plateau.

Rocks of the Khorat Plateau are divided into two groups according to the terrain characteristics. First, high mountains forming the edge topography forming range consist of Huai Hin Lat, Nam Phong, Phu Kradung, Phra Wihan, Sao Khua and Phu Phan Formations and second, a basin terrain forming flat and basin area consists of Khok Kruat and Maha Sarakham Formations.

Yumuang et al. (1986), Supajanya et al. (1992), Utha-aroon (1993) and Warren (1999) described the characteristics of the Khorat Group and Maha Sarakham and Phu Tok Formations in ascending order as follows:

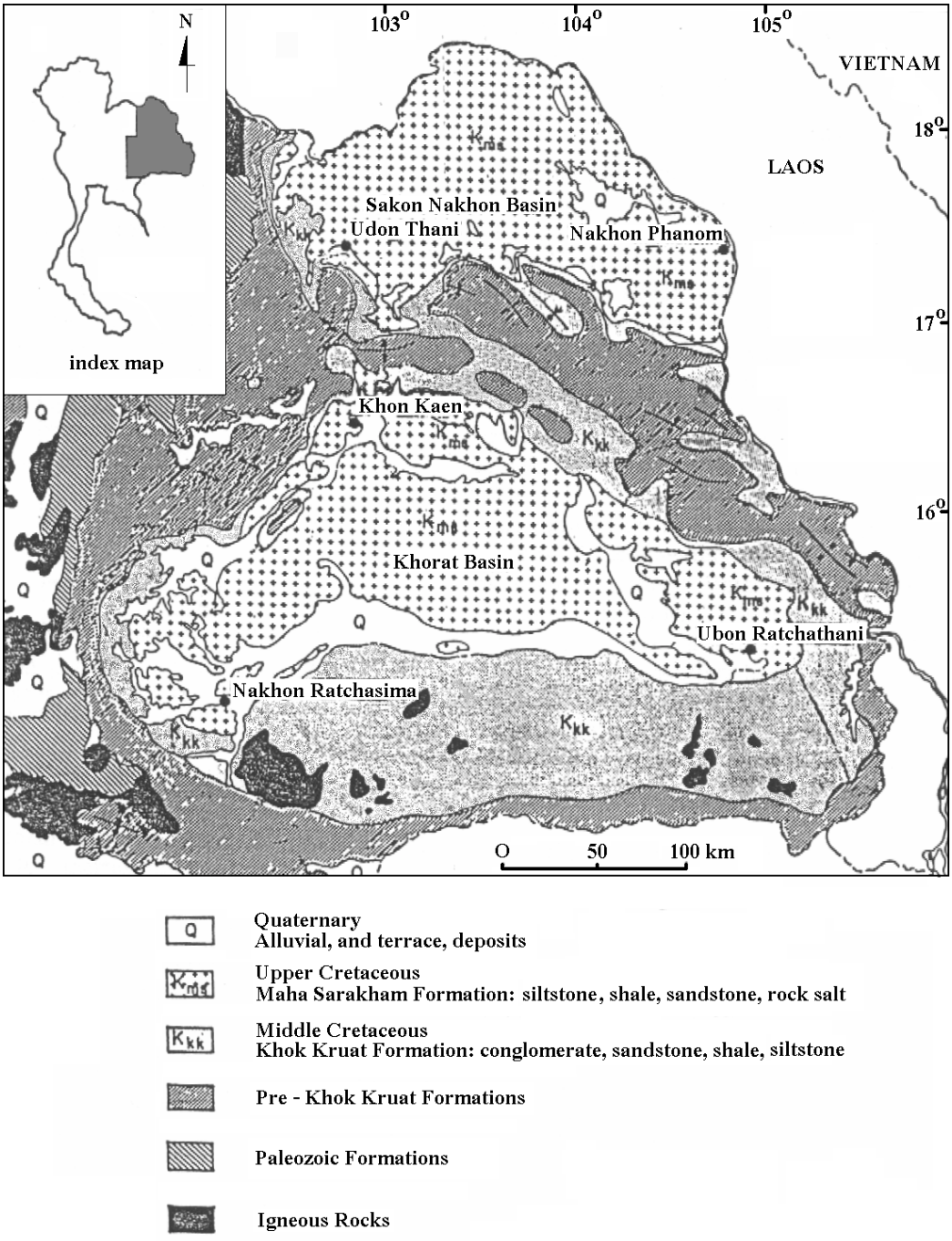

Figure 2.3 Sakon Nakhon and Khorat Basins containing rock salt in the northeast of Thailand (modified from Utha-aroon, 1993 adapted from DMR's Geological Map of Thailand scale 1:2,500,000).

1) Nam Phong Formation consists of reddish-brown sandstone and conglomerate, intercalated with claystone and siltstone in the upper and lower bed. Age of this formation is early Jurassic.
2) Phu Kradung Formation consists of reddish-brown claystone and siltstone of early Jurassic.
3) Phra Wihan Formation consists of white orthoquartzitic sandstone, reddish-brown shale and conglomerate. Age of this formation is middle Jurassic.
4) Sao Khua Formation consists of sandstone, siltstone, shale and red conglomerate. This formation formed in late Jurassic.
5) Phu Phan Formation consists of conglomerate and white and pale-gray sandstone and claystone. This formation formed in early Cretaceous.
6) Khok Kruat Formation consists of sandstone and reddish-brown shale and conglomerate. The age is early Cretaceous.
7) Maha Sarakham Formation consists of three groups of salt interbedded with sedimentary rocks and they are sandwiched by anhydrite beds. This formation formed in late Cretaceous.
8) Phu Tok Formation consists of brick-red sandstone and reddish-brown sandstone, siltstone, brick-red shale and reddish-brown shale. The rocks are of early Tertiary age.

From the structural geology point of view the Khorat Plateau is a basin caused by uplifting in the South and North of the area. Also an uplift of Phu Phan Formation stretching in the southeast direction separated the main basin into two

basins. Bedrocks of the two basins dip approximately less than 20° down to the middle of each basin. Sakon Nakhon Basin locating in the northern part covers an area of approximately 17,000 km^2 and 5 provinces e.g. Nongkai, Udon Thani, Sakon Nakhon, Nakhon Phanom and Mokdaharn Provinces and some parts of Laos. The Khorat Basin, in the South has an area of approximately 33,000 km^2, covers 11 provinces eg. Nakhon Ratchasima, Chaiyaphum, Khon Kaen, Maha Sarakham, Roy-et, Karasin, Yasothorn, Ubon Ratchathani and the northern parts of Burirum, Surin and Srisakat.

Evaporate groups, such as rock salt, gypsum and etc. exists in the two basins. The occurrence of these evaporate rocks is due to subsidence of some parts at the coastland around Cretaceous and sediment had deposited until middle Cretaceous. After that, evaporation of seawater throughout the area in late Cretaceous resulted in the deposition of the rock salt formations. Later, in Tertiary, the uplift of Phu Phan, Petchaboon and Phanomdongrak fold belt at around the edge of Khorat Plateau caused the basin to be separated.

Accumulation of sediments and the evaporation of seawater can be recognized in three cycles. Each cycle, defined by intrusion and extrusion of seawater, in-cooperated an evaporation rate that was suitable to form mineral e.g. halite and potash. Each cycle, consists of evaporitic strata and sedimentary strata (Suwanich and Rattanajaruraks, 1982, 1986; Wongswasdi and Panjasutharos, 1990) as given in the following:

- Lower Cycle consists of the lower sedimentary beds deposited during an intrusion of seawater into the basin and resulted in deposit of ferruginous clastic sediments, calcareous sandstone and

the lower evaporite layer formed during an extrusion of seawater from the basin and caused the deposition of anhydrite, potash and sylvite.

- Middle Cycle consists of the middle sedimentary beds deposited during seawater intrusion and resulted in the deposit of shale and claystone and the middle evaporate layer was formed during an extrusion of seawater that caused higher concentration of seawater and halite and thin layers of anhydrite deposited in consequence.
- Upper Cycle consists of the upper sedimentary beds deposited during seawater intrusion and resulted in the deposit of reddish-brown claystones and the upper evaporite layer deposited during seawater extrusion.

The Department of Mineral Resources (DMR) had drilled 118 drilled holes between 1976 and 1977 for the exploration of potash (Japakasetr, 1985; Japakasetr and Workman, 1981; Sattayarak, 1983, 1985). Some holes were drilled through rock salt layers to the Khok Kruat Formation. The sequences of rock layers from the bottom of this formation up to the top of the Maha Sarakham Formation are as follows:

1) Red bed sandstone or dense greenish gray siltstone sometime intercalated with reddish- brown shale;
2) Basal anhydrite with white to gray color, dense, lies beneath the lower rock salt and lies on the underlying Khok Kruat formation;
3) Lower rock salt- the thickest and cleanest rock salt layer, except in the lower part which contains organic substance. The thickness

exceeds 400 m in some area and formed salt domes with the thickness as high as 1,000 m, the average thickness is 134 m;

4) Potash - 3 types were found; carnallite ($KCl.MgCl_2.6H_2O$) with orange, red and pink color, sylvinite (KCl) – rarely found, white and pale orange color, an alteration of carnallite around salt domes, and techydrite ($CaCl_2.2MgCl_2.12H_2O$) – often found and mixed with carnallite, orange to yellow color caused by magnesium, the dissolved mineral occurred in places;
5) Rock salt - thin layers with average thickness of 3 m, red, orange, brown, gray and clear white colors;
6) Lower clastic - clay and shale, relatively pale reddish-brown colour and mixed with salt ore and carnallite ore;
7) Middle salt- argillaceous salt, pale brown to smoky color, thicker than the upper salt layer with average thickness of 70 m and carnallite and sylvite may be found at the bottom part;
8) Middle clastic - clay and shale, relatively pale reddish brown color and intercalated with white gypsum;
9) Upper salt - dirty, mixed with carbon sediment, pale brown to smoky color or orange color when mixed with clay and 3 to 65 m thick;
10) Upper anhydrite - thin layer and white to gray color;
11) Clay and claystone - reddish brown color, occurrence of siltstone and sandstone in some places, and

12) Upper sediment - brownish gray clay and soil in the upper part, and sandy soil and clay mixed with brown, pink and orange sandy soil in the lower part.

Cross-sections from seismic data across the Khorat-Ubon and Udon-Sakon Nakhon Basins (Sattayarak, 1987; Sattayarak and Poljun, 1990) reveals that rock salt can be categorized into 3 types according to the their appearances: rock salt beds, rock salt fold and salt domes. The Maha Sarakham and Phu Tok Formations fold in harmony with the Khorat megasequence. A part of the cross section through the Khorat Basin is illustrated in Figure 2.4.

Lateral compression due to collision between the Asian and Indian Plate in Tertiary caused the occurrence of cracks in the Phu Tok Formations. The plastic characteristics of the rock salt made it easy to creep. This caused the rock salt to intrude into those cracks. Differences in overburden loads could also cause a deformation of the rock salt and resulted in rock salt folds and domes respectively. Ratanajarurak (1990), Junmaha (1987) and Supanjanya et al. (1992) found that from seismic investigation data around exploration well No. K-66 in Borabue District, Maha Sarakham Province (Figure 2.5), salt domes are different in shape and size. Some had started to form domes. The lower rock salt in the middle of the Khorat and Sakon Nakhon Basins found to be well developed for dome.

2.2.2 Hydrogeology

According to the regional flow system explained by Wongsawas and Panjasutharos (1990) the groundwater flows from the recharge area, the highest area, to the discharge area, which is the lowest area. Considering Khorat Basin, the recharge area should be the mountain ranges around the edge of the basin (Phupan,

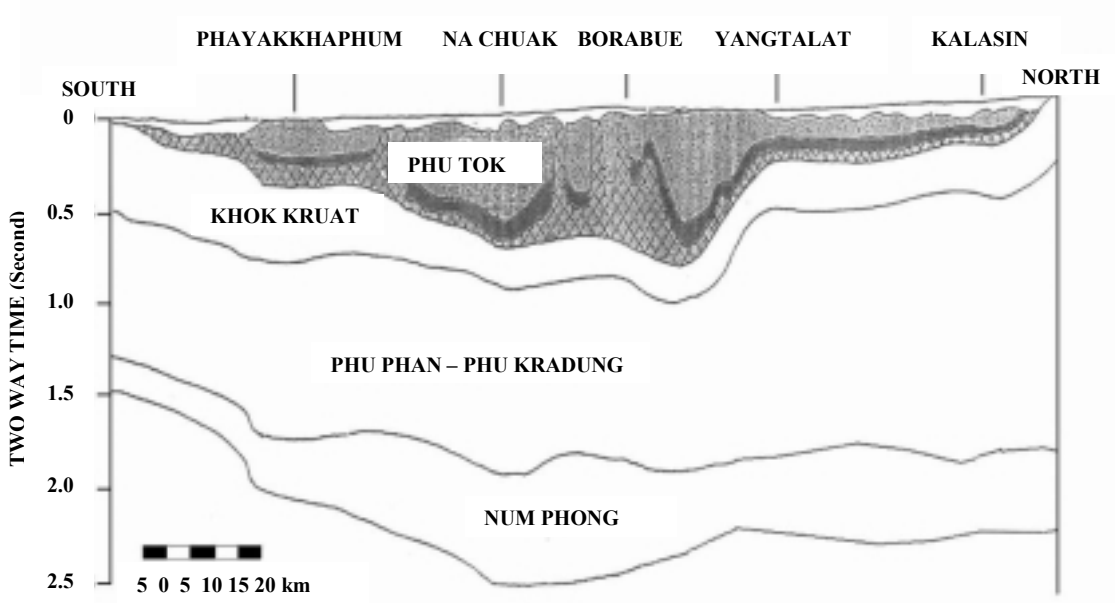

Figure 2.4 Cross-section show rock salt in the Khorat Basin (Sattayarak, 1987).

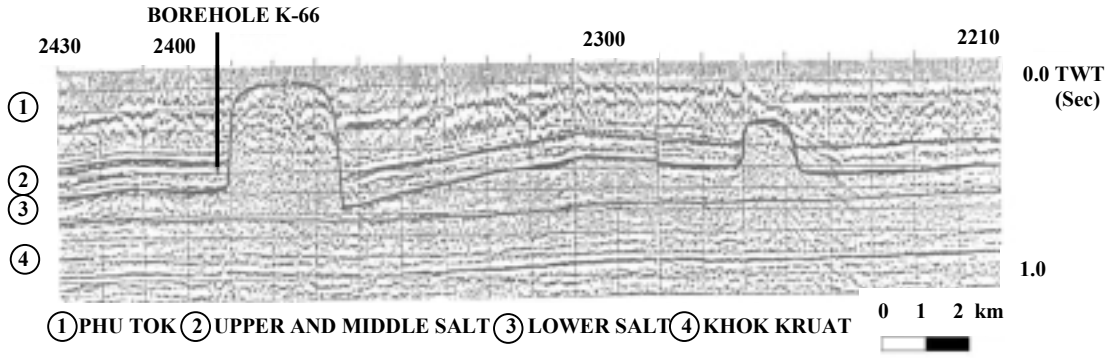

Figure 2.5 Seismic investigation data at around the exploration well No. K-66 in Borabue District, Maha Sarakham Province (Supanjanya et al., 1992).

Petchaboon, Sankamphaeng and Phanomdongrak) and discharge area is the lower plain at Thoongkularonghai. In conclusion, groundwater flows from the edge area to the bottom area of the basin. Groundwater flow systems of the Sakon Nakhon Basin should be the same as of the Khorat Basin.

The aquifers that will be emphasized in this study are the upper and lower aquifers influencing rock salt deposits such as Phu Tok aquifer, Maha Sarakham aquifer and Khok Kruat aquifer.

The Phu Tok aquifer has an average thickness of 150 m and covers mainly in Maha Sarakham, Roi-et, Yasothorn and Ubon Ratchathani Province. Groundwater is mainly stored in rock fractures which caused by settlement or intrusion of the lower rock salt strata. Groundwater source can be divided into three categories according to the structural characteristics. 1) Groundwater in syncline structure - water is stored at the contact of bedrock and it can be pumped out at the rate of 2 – 10 m^3/h. 2) Groundwater in anticline structure - this aquifer is not so thick and water is salty and can be pumped out at the rate of 5 – 20 m^3/h. 3) Groundwater stored between anticline and syncline structure – this is relatively large source with the pumping rate of 20 – 100 m^3/h.

Much of water from Maha Sarakham aquifer is salty. Water is stored in sandstone beds or porous beds especially in the beds located above the upper rock salt layer which is a large source of salty water.

In Khok Kruat aquifer, the chance that water can be found is 60% and the pumping capacity can be as low as 3 – 5 m^3/h. This is due to dense and relatively hard sandstone of this aquifer.

2.3 Rock Salt Properties

2.3.1 Mechanical Properties of Rock Salt

The objectives of the research on mechanical properties of rock salt are to study it's mechanism and it's long-term behavior by applying mechanical testing and fundamentals of engineering to determine rock salt properties and equations or mathematics rules that can be used to assess and predict behavior of bedded rock salt under compression with heat, moisture, etc. The mechanical properties of rock salt relate to stress-strain, temperature and time. These properties will be part of mathematical equations to explain various behaviors of rock salt.

Many researchers propose that rock salt is similar in it's properties to metals and ceramics (Munson and Wawersik, 1991; Chokski and Langdon, 1991). In fact, rock salt is classified to be a rock type in the alkali halide group and its properties are different from those of metals, ceramics and other rock types. Barber (1990) and Aubertin et al. (1992a, 1992b, 1993 and 1999) study rock salt properties and conclude that the properties of rock salt are semi-brittle and semi-ductile or elasto-plastic. In other word, rock salt is elastic, elasto-plastic and plastic (Jeremic, 1994; Aubertin et al., 1992a, 1992b, 1993, 1999; Fokker, 1998; Fokker and Kenter, 1994).

1) Elastic Behavior – The elastic behavior of rock salt will be considered as linearly elastic and fails in brittle failure mode. The rock salt is observed as linear elastic only when it is subjected to a low magnitude of loading which does not exceed the yielding point. The modulus of elasticity of rock salt can be derived from the calculation in range of linearly elastic. The modulus of elasticity of rock salt is generally lower than the elastic modulus of other rock types.

2) Elasto-Plastic Behavior – The elasto-plastic behavior of rock salt occur when the applied compressive stress does not exceed the yielding point. After unloading, rock salt will return to the previous state, which mean that the deformation occurs temporarily in rock salt. If the rock salt is continually loaded, it will enter to plastic state when the stress exceeds the yielding point. In this state, it will not be able to return to the previous state if the rock salt is unloaded. And if it is continually loaded, rock salt will not stand for the accumulated stress and eventually failure will take place.

3) Plastic Behavior – The permanent deformation will not occur if the applied stress does not exceed yielding point (Thorel and Ghoreychi, 1996; Frayne, 1996). The plastic behavior causes permanent deformation to rock salt. Under such constant high compressive stress that exceeds the yielding point, the rock salt is continually deformed. It will fail when the permanent strain reaches the limited strain (failure strain).

2.3.2 Permeability Properties of Rock Salt

The efficiency of underground storage in bedded rock salt has been studied for more than 30 years in overseas. Researchers from many institutes believed that rock salt is an aquitard or impermeable rock. Therefore, there were no intensive researches or studies related to permeability of rock salt at that time. Until 1990, Stormont (1990) measured permeability of bedded rock salt from salt mine in New Mexico and found that permeability of rock salt located far from the vicinity of the tunnel is about 10^{-22} m^2 (or approximately 10^{-9} darcy). Whereas permeability of rock salt in adjacent to the wall of tunnel may be higher than 10^{-18} m^2 (or approximately 10^{-5} darcy). Later, Stormont and Daemen (1991) and Peach (1991)

performed laboratory testing and the results confirmed that salt permeability could be higher than expected especially when rock salt was under anisotropic stress. Differential stress at a point can be high enough to cause micro-cracks to develop in rock salt. The direction of these micro-cracks is almost parallel to the major principal stress direction. Besides that, permeability for air or liquid of bedded rock salt depends on stress magnitude and on the difference in magnitude of principal stresses in three directions at that point. Therefore, the difference in stress magnitude will be maximum at the walls of cavern or tunnel. Rock salt deforms in elastic that depends on time. At a state where the difference in the stress magnitude is high enough, cracks develops and cause higher permeability. Whereas for the rock salt at the point located far from the tunnel or cavern walls, the difference in principal stress magnitude is low and deformation is also low. Cracks may not develop in rock salt located far from the tunnel vicinity, and the permeability value is still as low as it has not been affected by the creation of the tunnel.

The above conclusion had been confirmed by Fuenkajorn and Serata (1992) who carried out analysis with an aid of computer model in cooperated with finite element (FEM) analysis by using results derived from laboratory testing. The conclusion is that factors influencing the characteristics and distribution of permeability values of rock salt in the cavern or tunnel vicinity are 1) the depth of cavern or in-situ stress, 2) time or age of the cavern, 3) shape of the cavern, 4) mechanical behavior of salt, 5) internal pressure, and 6) distance from the cavern wall. At 3,000–4,000 feet depth, the tendency of the seepage around the cavern will be high, because the stress level and stress distribution will be high enough for developing cracks around the cavern. However, stress level is not too high to cause

rock salt to deform in plastic state. In most case permeability of rock salt will increase as the age of the cavern increases. The permeability values will be high when the age of rock salt is about 2-3 years. After that permeability values will remain constant unless the stress changes. Permeability values around spherical shaped cavern or tunnel are not so high. On the other hand, permeability values will be high around elliptical shaped caverns. For instance, permeability values of rock salt next to the cavern can be as high as 10^{-8} m^2 or about 10^{-5} darcy when the ratio of length to width of the cavern equals or exceeds 3:1. However, permeability of rock salt around the cavern can be lower when internal pressure is about half of the outside stress level. The internal pressure can reduce differences in magnitude of the major and minor principal stress acted in rock salt and consequent, developing of cracks decrease. In general, permeability values of rock salt will be maximum at the area that is adjacent to the cavern wall or tunnel wall, and permeability decreases as the distance from the cavern wall decreases. Permeability values will equal to normal value (the permeability values of intact salt that it is not influenced by the creation of cavern), which is about 10^{-9} darcy, at distance 2-3 times of cavern diameter. Since permeability is a significant factor that leads to succeeds and effectiveness in development of CAES technology in rock salt formations. Conclusion drawn by Fuenkajorn and Serata (1992) has been applied in designing size and shape of cavern as well as distances between caverns in an overseas chemical and gas storage. Furthermore, it has been also applied in designing and analyzing of the mechanical stability and hydraulic behavior of solution mined technology.

2.3.3 Factors Affecting Rock Salt Behavior

There are many factors that influence rock salt behavior, which reflect in the occurrence of deformation or creep. These factors also cause a reduction of compressive and tensile strength. Franssen (1998) and Fokker (1998) explained the influential factors on creep of crystal size, crystal adhesive and strength of rock salt in both in-situ and laboratory scale which included force, time depending deformation, temperature, moisture content, and inclusions.

Deformation or creep in rock salt is affected by crystal or grain size of salt. The comparison made between 60 mm in diameter specimens with different sizes of crystals, reveals that the possibility of an occurrence of fracture along cleavage and slip planes is higher in the specimen with larger crystal size (Aubertin et al, 1993; Billiotle et al., 1996; Aubertin, 1996). Franssen and Spiers (1990), Raj and Pharr (1992), Senseny et al. (1992), and Wanten, et al. (1996) studied the change of crystal position and plastic deformation in rock salt and found that shear strength and deformation occurred parallel to the crystal direction. Therefore in small size specimens, the compressive strength values are not constant. The derived results can not be used to compare with other sizes of specimen. For this reason, ASTM has established an international standard to put a minimum limit on diameter of specimens (ASTM D2938 and D3967; Barber, 1990). In order to have a standard size and to be able to make a comparison, the size of a specimen should not exceed 10 times of the crystal size, as stated by the ASTM.

Adhesive forces between crystals influence the strength properties of rock salt. Rock salt with heterogeneous texture has lower adhesive than rock salt with homogeneous texture. Wanten et al. (1996) and Allemandon and Dusseault (1996) had observed this characteristic in tensile test and uniaxial compressive strength tests, and

found that strain values dependent on adhesive force within and between crystals. Brittle behavior is another property of rock salt that indicated the ability of bonding between crystals in the specimen. For example, rock salt is easily cracked and fractured at the rim of the specimen during the sample preparation (e.g. cutting and grinding). This phenomena refers to the lower bonding between crystals and adhesive force.

Differences in loading rate or loading velocity applying to rock salt will result in time-dependent deformation or changes in shape and differences in deformation period. In other words, creep in rock salt changes as time changes at the difference in states of loading. Under high magnitude of loading rate, rock salt will behave as brittle material. Whereas under low magnitude of loading rate, rock salt will be more likely to behave in plastic state and reduction in yielding strength as a consequence. The above mentioned behavior was studied by Aubertin (1993) and Hardy (1996). They found that in long-term, loading acted on rock salt formation gradual decreased with time. Hardy (1996) performed the test in rock salt by applying 10.3 MPa of load and maintaining the level of deformation with the period of 12 months and found that compressive strength had decreased as much as 21%.

Heat or temperature affects the deformation of rock salt but also increases the creeping period and ductility of rock salt (Ghoreychi et al., 1992; Broek and Heilbron, 1998). Temperature related with depth of bed rock has been studied by many researchers (Franssen and Spiers, 1990; Cristescu and Hunsche, 1996; Raj and Pharr, 1992; Senseny et al., 1992; Berest and Blum, 1993; Carter et al., 1993; Schneefub and Droste, 1996; Berest et al., 1998). Conclusion drawn from the studies is that temperature in bed rock increases with the increasing depth. The temperature

in bed rock salt causes properties of rock salt to be similar to those properties to plastic materials and consequently the compressive strength decreases. Normally the melting point of rock salt is 800 °C, nevertheless when subjected to the heat of 600 °C for the period of 8 hours, rock salt can lose it compressive strength. Concerning the laboratory test related to temperature, Cristescu (1994b) and Cristescu and Hunsche (1996) suggest that at the temperatures of 100 °C and 200 °C, the strain rate should be lower than 10^{-8} s^{-1} and 10^{-7} s^{-1}, respectively. The increasing temperature causes the rock salt to deform and fail (Harmami et al., 1996).

Humidity causes a reduction of the rock salt strength (Hunsche and Schulze, 1996; Cleach et al., 1996). Due to the fact that rock salt is sensitive to humidity in atmosphere, moisture can cause chemical reaction in rock salt and results in dissolving of rock salt and allowing salty water to ooze out. In the preparation of rock salt specimen in laboratory, rock salt sample can be moisture-proofed by packing in polyethylene bags or sheets. The influence of moisture on compressive strength has been studied by Billiotte et al. (1996), Bonte (1996), and Adler et. al. (1996) by carrying out the test that intended to find out compressive strength of rock salt with high moisture content. The specimen has been increased the moisture content by salty water before loading. The result indicates that the rock salt strength decreases. Normally, dry rock salt has compressive strength of 30 MPa and strength can drop by 1 MPa when moisture content equals 7%.

Inclusions and impurities in rock salt are significant factors influencing the compressive strength of rock salt. These impurities are such as anhydrite and other sediments that are distributed in rock salt. In some cases it can cause reduction of compressive strength and can result in difference in creep behavior. Even small

amounts of inclusions and impurities in rock salt can affect the creep behavior because these inclusions and impurities can obstruct the bonding between crystals and also can obstruct the creep in rock salt. Inclusions and impurities cause mechanical inconsistency as result of inconsistent load distribution and non-uniform loading (Franssen and Spiers, 1990; Raj and Pharr, 1992; Senseny at al., 1992).

2.4 Mechanical Testing on Rock Salt

Mechanical behavior of rock salt differs from other rock types. The behavior of rock salt is time-dependent. Which means that, rock salt under loading is able to deform in plastic state. Consequently, many researchers have designed and developed the test methods to determine mechanical properties of rock salt in order to achieve the required properties and the test methods which can simulate the actual in-situ conditions. Some basic test methods that have been performed by the researchers, are following uniaxial compressive strength test, uniaxial cyclic loading test, triaxial strength test, triaxial cyclic loading test, uniaxial creep test, multi-steps uniaxial creep test, triaxial creep test, multi-steps triaxial creep test, tensile strength test, permeability test, acoustic emission test and healing test.

The uniaxial compressive strength test is a simple test to determine the strength of rock salt by applying uniaxial load to a cylindrical shaped rock salt specimen until the failure of specimen under maximum load occurs. The maximum load derived will vary with loading rate and displacement rate or strain rate. Wanten et al. (1996) carried out uniaxial compressive strength test on a rock salt crystal by controlling strain rates to be in the range of 10^{-4} to 10^{-7} s^{-1} and varying temperature from 20 °C to 200 °C. This test results in continuous creep of the rock salt crystal.

Ratigan and Votge (1993) conclude that the ultimate strength values derived from uniaxial compressive strength test are ranging between 15 – 30 MPa. Boontongloan (2000) carries out the uniaxial compressive strength test on rock salt from Sakon Nakhon Basin by controlling loading rate in such a way that failure occurs within 5 – 10 minutes of loading. The results show that the average uniaxial compressive strength values are approximately 18.5, 26 and 25 MPa for the upper salt, middle salt, and lower salt of the Maha Sarakham Formation. The tangential moduli are approximately 5.6 and 6.4 GPa for the middle salt and the lower salt, respectively. The secant moduli at 50% of the ultimate load are equal to 9.9 and 11.4 GPa for the middle salt and the lower salt. Poisson's ratio of the middle salt and the lower salt are approximately 0.35 and 0.42. The triaxial strength test is the method measure the ultimate compressive strength of rock salt by applying a confining pressure around the rock salt specimen. The axial stress is then increased until the specimen fails. Therol and Ghoreychi (1996) carry out the triaxial strength test on rock salt specimens and measure changes in volumetric strain. It is found that initial crack in the rock salt specimen occurs at the point where the volumetric strain curve starts to change. At this point, swelling occurs and micro cracks developed.

The cyclic loading test is a method of systematic loading and unloading. The test can be done in both uniaxial test and triaxial test that are so-called uniaxial cyclic loading test and triaxial cyclic loading test, respectively. When the specimen is subjected to loading and unloading, the fatigue occurs and consequently, the ultimate strength decreases (Mogi, 1962; Burdine, 1963; Hardy and Chugh, 1970; Haimson and Kim, 1972; Haimson, 1972; Atterwell and Farmer, 1973; Tharp, 1973; Kim, 1973; Fuenkajorn and Daeman, 1988). Results from cyclic loading test can be explained in

terms of relationship between stress, strain and number of cycles (fatigue life). The relationship show that fatigue accumulates with the number of cycles. Besides that a relationship between strain and time can be drawn to explain the results of creep-cyclic loading.

The uniaxial creep testing on rock salt aims to study the time-dependent behavior of rock salt. This test method is done by applying axial load through the testing period. A relationship between strain and time can be drawn from the test results. Rock salt behavior can be divided into three stages that are transient or preliminary creep stage, steady or secondary creep stage, and the tertiary creep stage. Moreover, it is also found that the rock salt properties from the same source, but from different layers, are different from each other. Hunsche et al. (1996) carry out the uniaxial creep test at various temperatures from 22 °C to 630 °C. The results show that under higher temperature, rock salt behavior is in plastic state due to higher ductility of rock salt. The triaxial creep test is similar to the uniaxial creep test. The differences are only the stress conditions. The lateral stresses applied to the specimen bring the triaxial test more closer to the actual conditions. Ong et al. (1998) study a long-term creep in potash from Patience Lake Member by employing the triaxial creep test during a long period.

The two methods of creep test that mentioned above can be applied in a multi-step creep test (Hamami et al., 1996; Allemandou and Dusseault, 1996). The multi-step uniaxial creep test is done by carrying out the uniaxial creep test, but the applied constant load is maintained to allow creep to occur and then systematically increases another step of load after creep has occurred for a period of time. It is a creep test by varying loads to the same specimen. The multi-step uniaxial creep test is an attempt

to decrease the amount of specimen to be used in each step or stress level and the results are the same as the one from the normal test with one specimen for one stress level.

Multi-step triaxial creep tests has been studied by Hamami et al. (1996). This test method is similar to the multi-step uniaxial creep test but different in the applied load. Confining pressure is applied to rock salt specimen in the multi-step triaxial creep test. Hamami et al. (1996) analyzed the results from the multi-step triaxial creep test by employing the power law and concluded that the power law is not compatible with the rock salt behavior.

Many researchers have studied the tensile strength test by applying the constant loading rate (0.057 to 0.342 MPa/s) in the direction of specimen diameter until rupture occurs. The maximum stress is then used to calculate the tensile strength, which ranges from 1.3 to 1.6 MPa. The tensile strength is low if the rate of loading is very high (Hansen et al., 1984; Khan et al., 1988; Senseny et al., 1992). Hunsche (1993) studies the rate of loading in the tensile strength test and finds that the loading rate between 0.017 and 0.248 MPa/s would not affect the tensile strength of rock salt. Pfeifle et al. (1998) study the tensile strength test by using rock salt specimen in cylindrical shape with a L/D ratio of 0.5. The displacement rate is controlled to be about 2.5×10^{-3} mm/s. Hardy (1998) carries out the tensile strength test on a fine-grained rock salt specimen by means of three test methods that include 1) direct-pull test, 2) Brazilian tensile strength test, and 3) Hoop-stress loading test. The specimens are subjected to loading rates of 0.003 to 0.059 MPa/s. The tensile strength derived from the three test methods are 1.63, 3.97, and 0.68 MPa, respectively. Moreover, sonic velocities are measured during the test.

In the last decades, researchers have carried out permeability test in both laboratory and field to study permeability of rock salt. In the laboratory, the test has been done by compression of gas and saline to flow through rock salt specimen and crushed rock salt. Permeability depends on amount of damages in rock texture and void in rock salt. Results from the test reveals that the permeability of rock salt is as low as 10^{-21} to 10^{-20} m^2 (Peach, 1991; Stormont, 1991; Billiotte et al., 1996). Permeability of the specimen from crushed rock salt depends on the number of compaction passes and density of the crush rock salt. Brodsky et al. (1998) study rock salt permeability by using crushed rock salt with density of 0.85 to 0.90 g/cm^3 and find that the permeability values are more than the permeability of intact rock specimen and range between 10^{-15} to 10^{-12} m^2. Although permeability of rock salt is relatively low, it can be higher as a result of mechanical damages such as crack developed during excavation of the cavern. Dale and Hurtado (1998) measured permeability around rock salt cavern and found that cracks developed within a distance less than 3 m around the cavern and the permeability value was as low as 10^{-21} m^2.

Sonic velocity test is a technique used to determine the mechanical properties of rock salt. It has been applied in both laboratory and field. In the laboratory, the sonic velocity test can be performed in the same specimen used for uniaxial compressive strength test during displacement of the rock salt specimen (Stead and Szezepanjk, 1991, 1995; Mlakar et al., 1993). Stead et al. (1998) perform the sonic velocity test during carrying out the creep test on rock salt and potash. The result shows that the compressional wave (P-wave) and shear wave (S-wave) velocities are 4.5 and 2.5 km/s, respectively. Later, Hardy (1998) carries out tensile strength test and performs the sonic velocity test at the same time. The relationship between

tensile strength of rock salt and the sonic velocities shows that the sonic velocities drops around 40% of the tensile strength value and pre-failure point can be determined from the sonic velocity which is about 90% of the tensile strength. This technique has been used to determine the strengths of rock salt and potash (Hardy, 1996). Reeves and Stead (1991) apply the sonic velocity test in mapping of structural geology of rock salt to find any damage area in cavern or tunnels. Borns and Stormont (1989) employ sonic reflection to find cracks occurring in salt-mine pillars of the WIPP Project in the United States. Munson et al. (1995) apply the sonic velocity test in 3-dimensional analyses to locate cracks and flows of groundwater in designing of a potash mine.

2.5 Mechanical Constitutive Laws of Rock Salt

Several mechanical constitutive laws of rock salt have been developed, which vary from simple visco-elastic models to complex dislocation theory models. Most of the laws emphasize long-term mechanical behavior under a variety of pressures and temperatures. The constitutive models for salt can be divided into three groups: 1) rheological model, 2) empirical model, and 3) physical model.

The rheological models describe the mechanical behavior of salt, but ignore the actual mechanisms of deformation. The deformational characteristics are assumed to be governed by two basic physical elements: spring elasticity and dashpot viscosity. The mechanical behavior of salt is modeled by a combination of these elements. Since the structure of the rheological models is not related to any particular test, the model can be applied to general problems of time-dependent behavior without requiring additional assumptions. The theories of rheological models have

been studied by Jin and Cristescu (1998), Cristescu (1993a, 1993b, 1994a, 1994b, 1996), Serata and Fuenkajorn (1992a), Fuenkajorn and Serata (1992, 1994), Stormont and Fuenkajorn (1994), and Massier (1996).

The empirical models are generally arbitrary functions formulated to fit a set of experimental results. Similar to the rheological approach, the development of the empirical laws ignores the actual mechanism of deformation of salt. By fitting curves to a set of data, certain relationships among the data can be established. The empirical laws can be presented in several forms (power, exponential, polynomial, etc.), depending upon the characteristics of the data. Several forms of empirical model can be studied from Fokker and Kenter (1994), Pudewills and Hornberger (1996), Zhang et al. (1996), Callahan et al. (1998), and Spiers and Carter (1998).

The physical models start from the analysis of the microscopic structural variation of the material observed under loading, and incorporate a theoretical explanation of the basis of time-dependent behavior. The method originated in metallurgy is later introduced into rock mechanics. Rocks, however, are more complex materials than metals. The atomic bonds in natural rocks are always a chemical bond rather than a metallic bond. Furthermore, most rocks are multigranular-structured in contrast to the relatively single phase structure of metals. The physical models are therefore considered inappropriate for describing the time-dependent behavior of rock salt (Aubertin, 1996; Aubertin et al., 1998, 1999; Korthaus, 1996, 1998; Durup and Xu, 1996; Senseny and Fossum, 1998; Weidinger et al., 1997, 1998; Hampel et al., 1998; Eduardo et al., 1996).

2.6 Computer Modeling

There are some computer softwares in engineering geology that have been used to model mechanical and hydraulic behavior of rock salt, e.g. behavior in terms of stress, strain, permeability, and etc. Many softwares use elasticity, viscos-elasticity, viscos-plasticity, and plasticity characteristic to predict short-term and long-term behavior as tabulated in Table 2.1. Some software is developed to be used easy, quick and convenient analysis. Most of them employ finite element methods and the rock salt mechanical behavior role is applied in the main equations to calculate and determine the constants of variable factors derived from laboratory and field testing.

The main objective of this section is to review the computer models (programs) and analytical methods for describing the rock salt behavior. In general, the computer models have been developed to simulate the time-dependent brittle-ductile behavior of rock salt and designed for the analysis of complex material behavior under a variety of loading and thermal conditions (Juliend et al., 1998). It is difficult to obtain an accurate calculation of salt behavior with respect to time by human. Advantages of the computer programs are fast and easy to use. Therefore, the computer programs are widely used for simulating the rock salt behavior. The computer models are divided into two groups: 1) boundary methods and 2) domain methods. The boundary methods include boundary element method (BEM) and displacement discontinuity method (DDM). The domain methods include finite element method (FEM) and finite difference method (FDM).

The boundary element method derives it's name from the fact that only the boundaries of the problem geometry are divided into elements. In other word, only the excavation surfaces, the free surface for shallow problems, joint surfaces, where

Table 2.1 Computer programs for describing the rock salt behavior.

Code Names	Methods	References
BEFE	BEM (3D)	Beddoes (1994)
VELMINA	DDM (3D)	Frayne (1998)
VNFOLD	DDM (3D)	Beddoes (1994)
FLAC	FDM (2D)	Itasca (1992)
FLAC	FDM (3D)	Itasca (1994), and Frayne (1996, 1998)
ADINA	FEM (2D)	Pudewills and Hornberger (1996)
ANSALT	FEM (2D)	Heusermann et al. (1998)
ANSPRE	FEM (2D)	Honecker and Wulf (1988)
ANTEMP, ANSPP	FEM (2D)	Honecker and Wulf (1988)
ASTHER	FEM (2D)	Rolnik (1988)
CODE-BRIGHT	FEM (2D)	Olivella et al. (1996, 1998a, 1998b)
COYOTE	FEM (2D)	Gartling (1981a)
DAPROK	FEM (2D)	Harrington et al. (1991)
FAST-BEST	FEM (2D)	Pudewills (1998)
GEO/REM	FEM (2D)	Serata (1991), and Serta and Fuenkajorn (1993)
GEOMEC	FEM (2D)	Nguyen-Minh and Menezes (1996)
GEOROC	FEM (2D)	Rizkalla (1991)
JAC	FEM (2D)	Biffle (1984)
LUBBY-1	FEM (2D)	Rokahr and Staudtmeister (1996)
LUBBY-2	FEM (2D)	Lux and Schmidt (1996)
MARC	FEM (2D)	Van Eekelen (1988)
MERLIN	FEM (2D)	Gartling (1981b)
SANCHO	FEM (2D)	Stone et al. (1985), and Hansen (1996)
SPECTROM-32	FEM (2D)	Callahan et al. (1989), and de Vries and Callahan (1998)
VIPLEF	FEM (2D)	Vouille et al. (1996)
VISCOT	FEM (2D)	INTERA (1982), and Frayne (1996)
SUVIC-D	FEM (2D/3D)	Julien et al. (1998)
VISAGE	FEM (3D)	Ong (1994)

Notes: FEM is finite element method, FDM is finite difference method, DDM is displacement discontinuity method, BEM is boundary element method, 2D is two-dimensional, and 3D is three-dimensional.

joints are considered explicitly, and material interfaces for multi-material problems are divided into elements. Several types of boundary element methods are collectively referred to as the boundary element method. These models may be grouped as follows: direct method, so named because the displacements are solved directly for the specified boundary conditions. Displacement discontinuity (indirect) method, so named because it represents the result of an elongated slit in an elastic continuum being pulled apart. Fictitious stress (indirect) method, so named because the first step in the solution is to find a set of fictitious stresses which satisfy pre-described boundary conditions. These stresses are then used in the calculation of actual stresses and displacements in rock mass. The computer programs for the boundary element method have been used by Beddoes (1994) and Frayne (1998).

The finite element method is compatible and appropriate to solving problems involving heterogeneous or non-linear material properties, since each element explicitly models the response of it's contained material. However, the finite element method is not well suited to modeling infinite boundaries, such as in underground excavation problems. One technique for handling infinite boundaries is to discrete beyond the zone of influence of the excavation and to apply appropriate boundary conditions to the outer edges. Another approach has been used to develop elements for which one edge extends to infinity (i.e. so-called infinity finite element). Efficient pre- and post-processors allow the user to perform parametric analyses and to assess the influence of approximated far-field boundary conditions. The time required for this process is negligible compared to the total analysis time. Joints can be represented explicitly using specific joint element. Once the model has been divided into elements, material properties have been assigned and loads have been prescribed.

Some techniques must be used to redistribute any unbalanced loads and thus determine the solution to the new equilibrium state. Available solution techniques can be broadly divided into two classes, implicit and explicit. Implicit techniques assemble systems of linear equations, which are then solved using standard matrix reduction techniques. Any non-linearity material is taken into account by modifying stiffness coefficients (second approach) and/or by adjusting prescribed variables (initial stress or initial strain approach). These changes are made in an iterative manner such that all constitutive and equilibrium equations are satisfied for the given load state. Several computer programs for the finite element methods can be studied from Blanquer-Fernandez (1991), Nguyen-Minh and Quintanilha de Menezes (1996), Callahan et al. (1990), Devries and Callahan (1998), Harrington et al. (1991), Heusermann et al. (1998), Honecker and Wulf (1988), INTERA (1982), Salzer and Scheriner (1998), Julien et al. (1998), Lux and Schmidt (1996), Rokahr and Staudtmeister (1993), Rolnik (1988), Serta and Fuenkajorn (1993), and Vouille et al. (1996).

The finite difference method is compatible and appropriate to solving problems involving inhomogeneous, complicated geometry, and non-linear material properties that are similar to that of the finite element method. The FDM is for approximating derivatives in the equations of motion. Continuous derivatives in differential equations are replaced by finite difference approximations at a discrete set of points in space and time. The resulting set of equations, with appropriate restrictions, can then be solved by algebraic methods. A finite difference model is one, which employs finite difference methods. The resolution of a finite difference model is determined by the spacing of the discrete set of points (grid points) used to approximate the derivatives. The FDM is applied for modeling geomechanical

problems that consist of several stages, such as sequential excavation, backfilling and loading. Several computer programs for describing the rock salt behavior can be studied from Itasca (1992), Itasca (1994), and Frayne (1996, 1998).

The distinct element method (DEM) is a domain method, which models each individual block of rock as a unique element (i.e. where the spacing of the joints is of the same order of magnitude as the excavation dimensions). The individual pieces of rock may be free to rotate and translate, and the deformation, that takes place at block contacts, may be significantly greater that the deformation of the intact rock, so that individual wedges may be considered rigid. For the rock mass, such as rock salt, the distinct element method is not suitable for the analysis.

2.7 Healing of Rock Fracture Mechanism

Healing is the closure of fracture or faults without any precipitation of matters in side the fracture. It is a chemical and physical process in which the material properties evolve with time or in which defects including voids and cracks decrease. Healing of rock salt due to viscoplastic deformation of grain, causing the closure of cracks and pore space. There are two healing mechanisms, closure of microcracks and healing of microcrack. It implies that microcracks and microvoids reduce in size, with a corresponding increase in stiffness and strength (Miao et al., 1995). The main driving force for crack healing is a minimization of surface tension. Healing occurs by creation of contact areas and covalent bonds between the two surfaces of the fracture. It involves a local transport of mineral material. The most important factors that may affect the rate of crack healing are time, stress, temperature, saturation, contact area and geometry of contact surface, and chemical effects that may alter diffusion

coefficients (Renard, 1999). In most cases, crack healing is achieved at grain size scale (micrometer to millimeter). The only way to observe healed cracks may be through some tiny fluid inclusions which can be related to deformation phases or metamorphic conditions. Damage in rock salt can be healed under hydrostatic compression and also occurred under nonhydrostatic compression (Chan, et al., 1995; 1998a; 1998b; 2000).

Healing of rock fractures has occurred on various scales. In geology, fracture healing is an important mechanism controlling the circulation of fluid in the earth crust (Renard, 1999). In a smaller scale, circulation of solution or fluid in rock mass can result in a precipitation or deposition of minerals and ores in fracture zones. When fractures are open, fluid can percolate and react with the rock (dissolution, precipitation of minerals, ore, etc.). This process notably modifies the fluid circulation and interactions between the lower crust and the surface. Healing reduces the fluid flow between fault zones. Healing of fractures or faults induced in rock salt formations can prevent the brine flow from contaminating the upper surface or nearby rock formations. The presence of damage in the form of microcracks in salt can alter the structural stability and permeability of salt, affecting the integrity of a repository (Chan et al., 1998b). When cracks are closed, permeability can be reduced by several orders of magnitude. The healing capability of fractures is one of the advantages for rock salt to be used as a host rock for nuclear waste repository in the United States and Germany (Habib and Berest, 1993; Broek and Heilbron, 1998). The healing process of rock salt fractures around an air or gas storage cavern also affects the designed storage capacity and the mechanical stability of the cavern (Katz and Lady, 1976). Numerous studies of fracture healing given in the literature review by

Miao et al. (1995) include, for example, the crack healing in geological, the curing concrete, the recovery and recrystallization of metals, and the liquid-phase-enhanced densification of granularly crystalline materials. In rock salt the study on crushed rock salt samples with small amounts water is capable of healing during densification creep processes (Miao et al., 1995). A treatment of damage healing in crushed salt was presented by Miao et al. (1995). In this formulation, a healing surface in the sense of a yield surface in classical plasticity theory is used in conjunction with loading and unloading conditions.

Chan et al. (1994; 1995) and Munson et al. (1999) propose a constitutive formulation for treating damage healing in damaged intact salt, referred to as the multimechanism deformation coupled fracture (MDCF) model, which is based on a generalized damage evolution equation that includes both a damage generation term and a healing term. Because, both damage generation and healing are treated, the MDCF model is suitable for treating damage accumulation and healing in disturbed rock zone in the repository at Waste Isolation Pilot Plant (WIPP) site (Chan et al., 2000). Brodsky and Munson (1994) studied the healing in rock salt fractures which is a part of project named "Waste Isolation Pilot Plant" (WIPP). The cylindrical shaped rock salt specimen was stored in a Hock cell under hydrostatic pressure of 0.5 MPa and at temperature of 25 °C. The specimen is then compressed in the axial direction to cause a little displacement. After that, the temperatures are varied to be 20 °C, 46 °C and 70 °C for each specimen to study the effect from temperature changes. The specimen is loaded with a strain rate of 1×10^{-6} sec^{-1}. Ultrasonic wave velocity test has been also employed to use in conjunction with the test. The derived data have been

used as a basic information for comparison with the result from MDCF model created to evaluate healing in anisotropic fracture of rock salt.

Allemandou and Dusseault (1993) have studied the healing of fracture by applying triaxial compressive stress at confining pressure of 2 MPa and constant axial load. The cylindrical shaped rock salt specimen is subjected to the above-mentioned stress under constant temperature within several hours. After that the axial stress is changed to be 10, 15, 20, and 25 MPa, respectively. Assessment of closing and healing of fracture from the CAT-scan reveals that healing takes place and voids decrease as stress level increases. Maio et al. (1995) study the healing in crushed salt in less water state and conclude that after the healing takes place, density, inelastic strain, Young's modulus and strength of the crushed salt increase as time increases.

2.8 Cyclic Loading Test

Cyclic loading test or fatigue test is performed by loading and unloading the sample to determine how many times or cycles (fatigue life) that the specimen is able to stand before it fails. The meaning of cyclic loading in respect of mode of failure may refer to the testing related with cyclic loading in which the magnitude of such loading is less than the static strength (e.g. uniaxial compressive strength). This applied loading is not enough to cause the specimen fails after just one cycle, but the specimen is failed after several cycles of loading. The crack in specimen then propagates until the failure takes place (Cruden, 1974). The mechanism of cyclic loading can be explained as it is a fluctuated manner of loading which causes an

accumulation of strain energy that the strain energy in each cycle is lower than the failure strain energy derived form static method. When the strain energy has accumulated up to the limit (failure strain energy), eventually failure in material or engineering structure will take place. This is phenomena is so-called fatigue.

The effect of cyclic loading often results in failure of engineering structures for instance dam, road and bridge foundations, tunnels or even air storage caverns in bed rocks. The causes could be from earthquake, traffic, blasting and the process of compressed and released air in and out of the cavern to produce electricity, etc. Even civil engineering materials such as steels, concrete or soil can be also affected by the cyclic loading. However, only the cyclic loading test on rock will be discussed here.

The objectives of the cyclic loading test in rock salt are to understand the duration of structures under cyclic loading and to apply the results in designing of air controlling systems during CAES operation. A rock salt cavern is subjected to pressure changes. The pressure will be high and low in cyclic manner according to its operation. The duration of the cavern can be referred from the number of pressurized cycles before cracking will take place. This also depends on characteristic of the acting pressure (Passaris, 1982).

Most of fatigue test results from cyclic loading show relationship between stress and strain, fatigue stress and number of cycles that cause failure or fatigue life (S-N curve). In addition, a relationship between strain and time can be drawn to explain results from cyclic loading that causes creep or known as “creep-cyclic loading”. Creep characteristic in this test is similar to the creep characteristic in the static test such as uniaxial creep test (Akai and Ohnishi, 1983).

2.8.1 Cyclic Loading Test on Sedimentary Rocks

Effect of cyclic loading test on rock properties have been studied for more than fourty years. The studies aim at to apply the result in designing engineering structures in bedrock under cyclic loading conditions. There are two types of testing, uniaxial cyclic loading and triaxial cyclic loading. Acoustic emission technique is also performed during cyclic loading test (Mogi, 1962; Burdine, 1963; Scholz, 1968; Hardy and Chugh, 1970; Saint-Leu and Sirieys, 1971; Attewell and Farmer, 1973; Haimson and Kim, 1972; Haimson, 1972,1973; Tharp, 1973; Kim, 1973; Khair, 1975; Fuenkajorn and Daeman, 1988). Various kinds of rock that have been tested such as dolomite, granite, tuff, sandstone, marble, and shale which can be briefly summarized in the following paragraphs.

Atterwell and Farmer (1973) perform the tests on dolomite by considering magnitude of maximum and minimum stress levels in each cycle and loading frequency. The frequency used in the test ranges between 0.3 and 20 Hz. The conclusions drawn are that the failure in rock specimens take place when strain has been accumulated up to the level equivalent to the critical energy level derived from static loading test (e.g. uniaxial compressive strength test). It is also found that the frequency affects fatigue life (number of cycles) that causes cracking in the specimen. The number of cycles at failure tested by higher frequency is more than the number of cycles tested by a lower frequency. The number of cycles at failure for higher fatigue stress is less than the number of cycles for the lower fatigue stress.

Akai and Ohnishi (1983) perform cyclic loading tests on tuff with the frequency of 0.01 Hz. The strain rate are constant. The permanent strain in each cycle has been increased and slope of the stress-strain curve is reduced. This means

that the elastic modulus of tuff decreased when the permanent strain accumulated from each cycle reached the failure strain level derived from static loading test. The frequency of testing affects the failure of rock specimens. The number of cycles for higher frequencies is less than of the lower frequencies (comparison made when magnitude of maximum and minimum stress level in each cycle are the same). Ishizuka and Abe (1990) study the effect of frequency, moisture, and confining pressure in granite. They conclude that the number of cycles causing failure tested at higher frequency, low moisture (dry) and with confining pressure is higher than the number of cycles tested at low frequency, high moisture (wet) and without confining pressure.

Ray et al. (1999) perform the test with sandstone by increasing and decreasing the stresses between 95% and 5% of σ_c for each cycle. After 10,000 cycles, failure does not occur. Also, the cyclic loading test is performed on sandstone by applying fatigue stress level ranging from 30% to 60% of σ_c and then unloading to zero-stress level. All specimens are tested at 100 cycles. Then all specimens are loaded until failure takes place and strength of each specimen is achieved. It is found that the failure strength of specimen decreases as the fatigue stress increases. In other words, after the specimen is subjected to cyclic loading at higher fatigue stresses level, the magnitudes of the accumulated strain in each cycle increase as percentage of σ_c increases.

2.8.2 Cyclic Loading Test on Rock Salt

Passaris (1982) performed the cyclic loading test on rock salt in order to design compressed air energy storage cavern. The tests were performed at low frequency (0.1 Hz). First, in each cycle, load had been increased up to the designed load and then decreased to zero, or called “full unloading”. The maximum loads

ranged between 60-80% of uniaxial compressive strength. The tests had been done on 16 specimens. The amounts of loading cycles were limited at 10,000 cycles. For the second series, the applied load increased to the designed load and then decreased partially, called “partial unloading”. The applied load was imitated from the up-down pressure in the rock salt cavern. The relationship between the fatigue strength (S) and the fatigue life (number of cycles causing failure-N): $S = 1.91N^{-0.05}$. The rock salt can soften by cyclic loading and the elastic modulus can decrease as the number of cycles increase. The test revels that the fatigue stress limit of rock salt is at 60% of the uniaxial compressive strength. He further suggests that during releasing air from the cavern, the pressure in the cavern should be maintained higher than 55% of the rock salt strength.

Gehle and Thoms (1986) studied the change in acoustic emission (AE) characteristics causing by cyclic loading in rock salt cavern. They drilled two holes with angle of 45° from horizontal, with a diameter of 57 mm and 6.1 m deep into the base of cavern pillar. Another drilled hole with a diameter of 64 mm was drilled at the middle of two holes. The signal interpretation equipment was put into the first two holes, whereas the equipment for applying cyclic load namely hydraulic pressure was placed in the middle hole. The result from the test showed that the AE signal pattern increased as the pressure in the drilled holed increased. This means that cracks have developed. The summary indicates that the AE-method could be used to measure the change in rock salt property which is affected by the cyclic loading and can also indicate that cracks development as the number of loading cycles increases.

Thoms et al. (1980) performed triaxial cyclic loading with low frequency (24-cycles/10 hrs.) by imitating the actual loading condition of the CAES

in rock salt cavern. The study was also carried out with an aid of the computer model. The specimen with a diameter of 100 mm and length of 200 mm was subjected to cyclic loading at 34.5 MPa. The temperature was systematically increased and decreased. It was found that change of temperature in cycle would result in creep of the rock salt. It can be concluded that frequency affects the behavior of rock salt under the cyclic loading. The different frequency causes difference in number of cycles that causes failure, even subjected to same loading characteristic. Number of cycles that cause failure in the higher frequency is more than the number of cycles in the lower frequency. And at the higher stress level (fatigue stress), the number of cycles that causes failure is less than that in the lower stress level.

Cho and Haimson (1987) used cylindrical specimen with the hole in the middle in the test by performed at the frequency of 10 to 10,000 cycles/s. The test showed the number of cycle causing failure namely “fatigue life”. Thom and Gehle (1982) performed the test on rock salt in the field and laboratory, in order to study the effects of cyclic loading and cyclic changing of temperature of the rock salt. The test had been modeled as the actual conditions in the CAES cavern. The test was done with the different stress level (fatigue stress) and consequently creep from the cyclic loading was closed to the creep from the static test (uniaxial creep test). And the conclusion drawn was that creep in rock salt from the cyclic loading test depended on the difference between the maximum and minimum loading in each cycle. Changes of temperature in the cavern could affect the creep in rock salt. It was indicated that if the cavern were constructed at the depth of approximately 900 m, temperature would have a significant effect.

From the test that have been performed by many researchers in both laboratory and field, the responses of the cyclic loading test are in the same manner and can be summarized as follows:

1) The cyclic loading influencing factor is the magnitude of up-and down-stress or so-called amplitude (Haimson and Kim, 1972). If the difference between the up and down-stress is low, the permanent strains will be low. For a large difference in up and down-stress, the failure, occurs at the lesser number of loading cycles;

2) Frequency has an influence on the cyclic loading test, the number of cycles causing failure is higher as the frequency increases (Atterwell and Farmer, 1973; Ishzuka and Abe, 1990);

3) Crystal size affects the cyclic loading. Strengths of the fine-grained rock salt are higher than that of the coarse-grained rock. The number of cycle causing failure in fine-grained rock is then higher (Burdine, 1963);

4) Water condition (dry and wet condition) and confining pressure has an influence on the cyclic loading. Creep deformation under wet condition will be higher than in dry condition. This means that the number of loading cycles causing failure in dry condition will be higher than those in the wet condition, under the same loading characteristics. The test under confining pressure results in higher number of loading cycles causing failure (Ishzuka and Abe, 1990) as compared to the unconfined test;

5) Characteristics of creep deformation from cyclic loading test are the same as the creep deformation from the static creep test (uniaxial creep test) for initial state, constant increasing of strain rate and finally failure state (Ishzuka and Abe, 1990).

CHAPTER III

SAMPLE PREPARATION

Rock salt samples used in this research have been donated by the Asian Pacific Potash Corporation, Udon Thani Province. They are collected from two deep boreholes (BD99-1 and BD99-2) located in Khumpawapi District, Udon Thani Province in the Sakon Nakhon Basin. The core specimens are collected from the upper and the middle salt beds at the depths ranging between 250 meters and 400 meters. They are in cylindrical shape with 2.4 inches (60 mm) in diameter (Figure 3.1). Preparation of these samples follows, as much as practical, the ASTM standards (ASTM D4543-85, 1998).

There are three groups of specimens for different laboratory test methods, including basic mechanical properties test (uniaxial compression tests, Brazilian tension tests, and point load test), uniaxial cyclic loading test, and healing tests. There are 25 specimens with a diameter of 60 mm prepared for the basic mechanical property test. Five specimens are prepared to have L/D ratio of 2.5 for the uniaxial compressive strength test. Seventeen specimens with L/D ratio of 0.5 are prepared for the Brazilian tensile strength tests. Ten specimens with L/D ratio between 0.7 to 1.2 are prepared for the point load test to determine the strength index of the intact rock salt. There are 8 specimens with a diameter of 60 mm and L/D ratio of 3.0 prepared for the uniaxial cyclic loading test.

Figure 3.1 Some salt core samples donated by Asia Pacific Potash Corporation, Udon Thani Province. They are collected from borehole no. BD99-1 located in Khumpawapi District, Udon Thani Province.

Three types of salt fracture will be simulated in the laboratory for healing test: 1) fractures formed by saw-cut surfaces, 2) fractures formed by smooth polished surfaces and 3) tension-induced fractures. Nine specimens formed by saw-cut surface and 10 specimens formed by tension-induced fractures will be prepared with a diameter of 60 mm and L/D ratio ranging from 1.0 to 2.0 for use in the healing test under uniaxial loading. Nine specimens with a diameter of 38 mm and L/D ratio equal 1.6 formed by smooth polished surface and tension-induced fracture will be prepared for healing test under confining pressure. To obtain the tension-induced fractures, the cylindrical specimens are subjected to point loading or by diameter loading (Brazilian tension test). The point-loaded fracture is normal to the specimen axis, and is prepared for healing under uniaxial loading. The diameter-loaded fracture is the axial fracture, parallel to the specimen axis, and will be healed under confining pressure. The fracture formed by saw-cut surfaces is also normal to the specimen axis, while the fracture formed by polished (grinding) surfaces is parallel to the specimen axis. After the fractures have been prepared, the amount of inclusions on the fracture surfaces will be measured and mapped using magnifying glass. The aerial percentage of the inclusions will be calculated with respect to the total fracture area. The inclusions defined here will include all associated and foreign minerals or materials that are not sodium chloride. Prior to the healing test, a close examination will be made to determine whether the tension-induced fractures are formed by the splitting failure of the salt crystals or by the separation of the inter-crystalline boundaries. Table 3.1 summaries the salt specimens that prepared for this research.

Table 3.1 Summary of salt specimens prepared for the laboratory testing.

Test Methods		**ASTM Standards**	**Diameter (mm)**	**L/D Ratio**	**Number of Specimens**
Basic characterization tests	Uniaxial tensile strength test	D2938	60	2.5	5
	Brazilian tensile strength test	D3967	60	0.5	17
	Point load strength index test	D5731	60	1.5-2.0	10
Cyclic loading test	Uniaxial cyclic loading test	D2938	60	2.5-3.0	8
Healing test	Healing under uniaxial loading	N/A	38	1.0-2.0	19
	Healing under confining pressure	N/A	38	1.6	9

All specimens are measured to determine the precise dimensions. The geologic depth is recorded for each specimen. The physical characteristics (i.e., mineral composition, density, grain size, and color) are described. The saturated brine is prepared for use as grinding fluid during the cutting (Figure 3.2) and grinding (Figure 3.3) to prevent the specimens from dissolving. After finishing preparation, the specimens are labeled and wrapped with plastic film. The identification of specimens is given, which includes rock type, borehole number, core number, core diameter, type of experiment and sample number. Figures 3.4 – 3.8 show some specimens used for the test in this research.

The salt used in this research has more than 99 percent of halite (NaCl) from testing with X-ray Diffractometer (reported from Suranaree University of Technology Chemical Laboratory). The rock salt is coarsely crystalline. The crystal size of halite varies from 1 to 10 millimeters. The average density of rock salt is 2,170 kg/m^3. The color is clear to white, but sometimes pink and gray color can be found. The crystals are roughs, vitreous, and transparent to translucent.

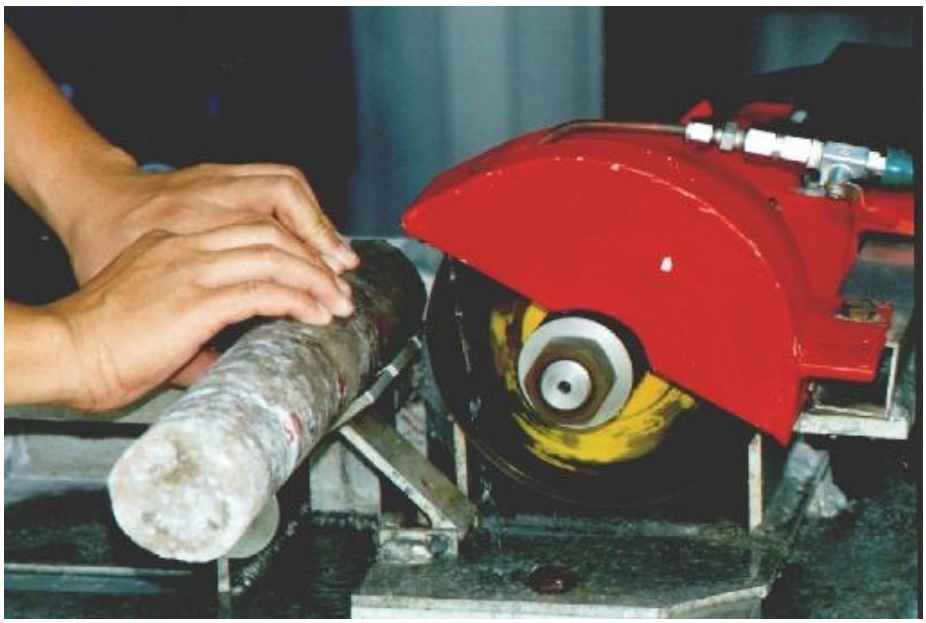

Figure 3.2 Core specimen of salt is cut to obtain the desired length.

Figure 3.3 Grinding of a salt core specimen for smooth and parallel end surfaces.

Figure 3.4 Some salt specimens prepared for uniaxial cyclic loading test.

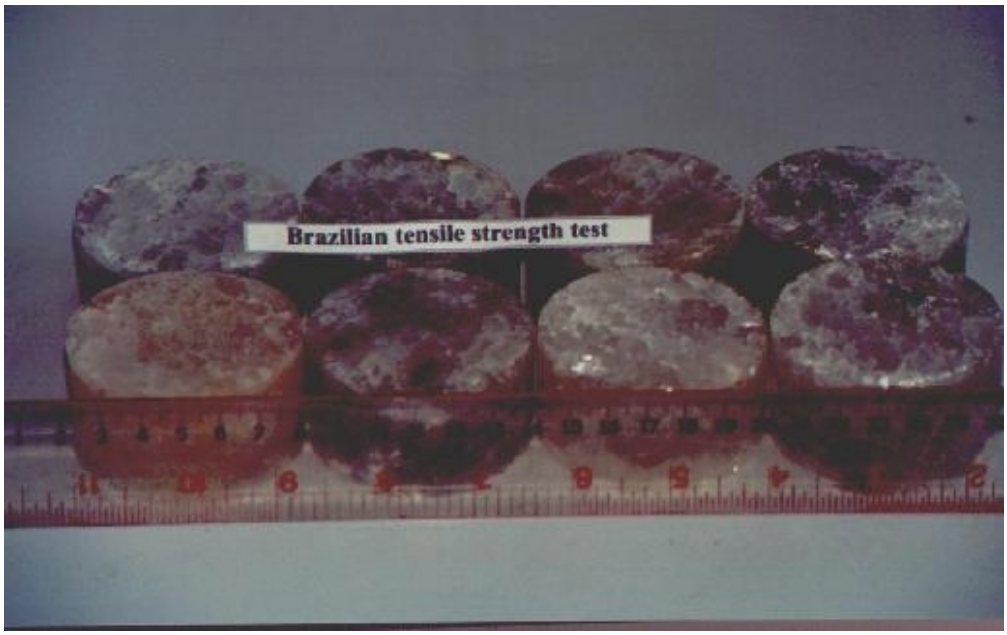

Figure 3.5 Salt specimens prepared for Brazilian tensile strength test.

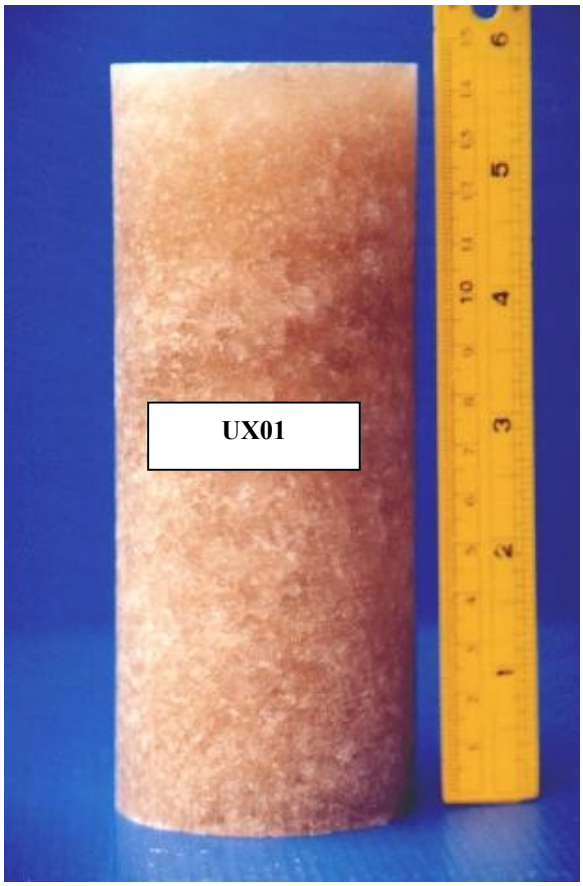

Figure 3.6 Salt specimen no. UX01 prepared for uniaxial compressive strength test.

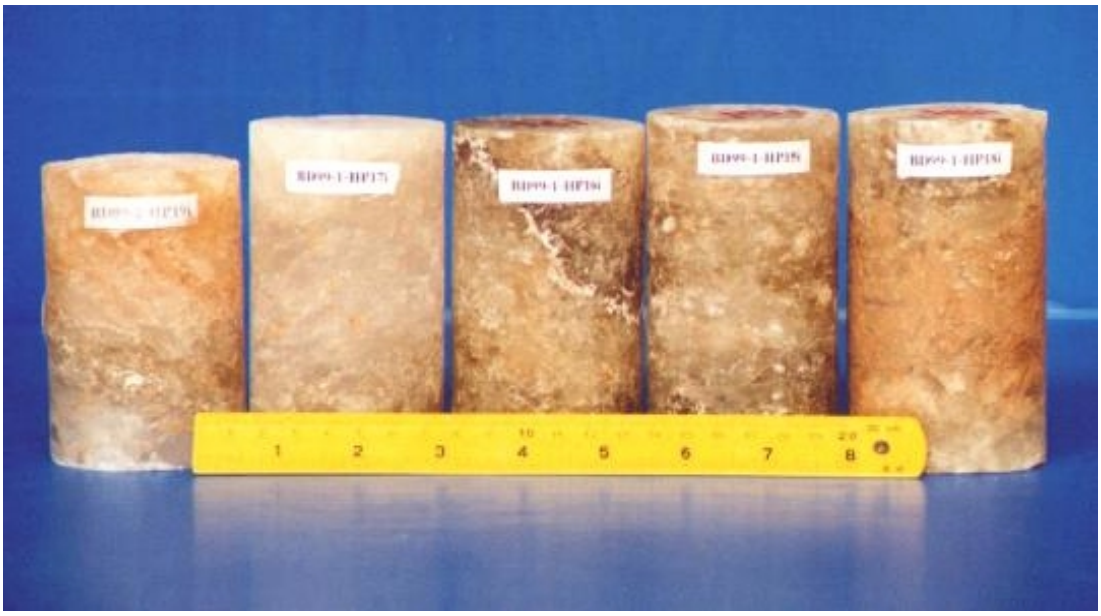

Figure 3.7 Salt specimens prepared for point load strength index test.

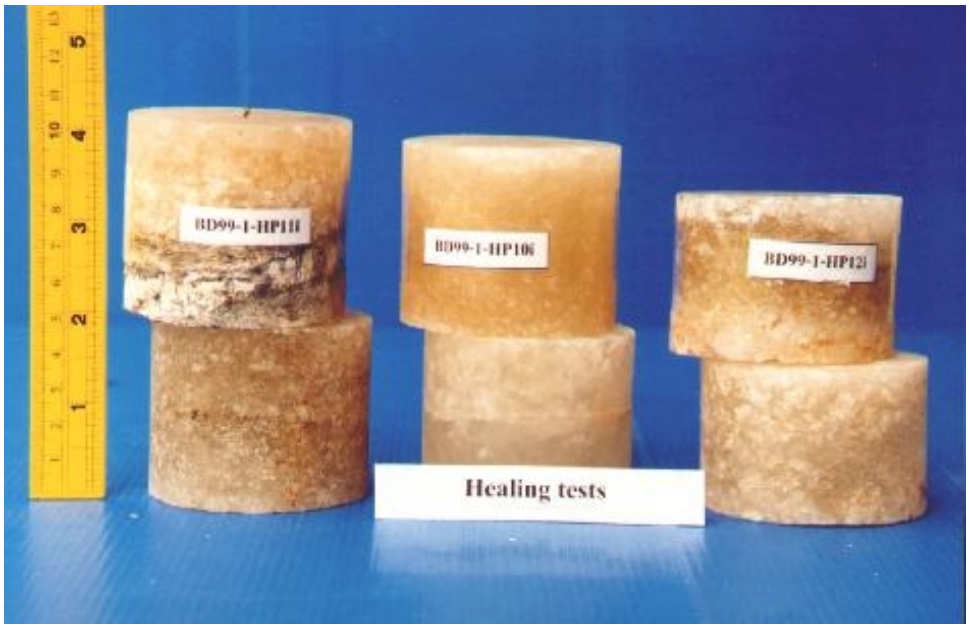

Figure 3.8 Salt specimens prepared for healing test under normal loading.

CHAPTER IV

LABORATORY TESTING

The main objective of the laboratory testing in this research is to study rock salt behavior under cyclic loading and the healing of rock salt fractures. The result derived from the test will be used to assess the mechanical stability of rock salt in vicinity of the CAES-cavern. The assessment processes will be executed in conjunction with the finite element method (FEM).

There are three test series to be presented in this chapter; 1) basic mechanical property test, 2) uniaxial cyclic loading test, and 3) fracture healing test.

4.1 Basic Mechanical Property Test

Basic mechanical properties of rock salt are usually determined by three types of test that are 1) uniaxial compression test, 2) Brazilian tension test, and 3) point load test. The properties derived from the three test methods can be used as an index property which are useful for field classification of rock mass and compared with the rock salt from other locations.

4.1.1 Uniaxial Compression Test

The rate-controlled uniaxial compression test is intended to determine the uniaxial compressive strength of rock salt. The rock salt specimens have been well selected to be clean and from the middle salt layer of the exploratory well

nos. BD99-1 and BD99-2. The specimens are prepared to have a diameter of 60 mm and a length-to-diameter ratio (L/D) of 2.5. There are 6 specimens used in this test.

The rock salt specimens are tested with constant loading rate of 0.1 MPa/min, at room temperature and in accordance with the ASTM standard D2938 and the suggestion method from ISRM (Bieniawski et al., 1978). The test is conducted by using a concrete strength testing machine no.9901X0003 series Elect/ADR2000 (ELE, 1995) which is capable of applied axial load at a constant rate until failure takes place (Figure 4.1). During the test, the given loads and displacement of rock salt with elapsed time have been recorded. The failure modes have been observed. The maximum loading values can be calculated by dividing the load by cross-sectional area. Whereas, axial strain can be calculated by dividing displacement by the initial length of the test specimen. The result is presented graphically in order to find linear relationship between stress and strain of each specimen. The equations used in the calculation are

$$\sigma_{axial} = P/A \quad (4.1)$$

$$\varepsilon_{axial} = \Delta L/L \quad (4.2)$$

where,

σ_{axial} = axial stress,

P = axial load,

A = cross section area,

ε_{axial} = axial strain,

ΔL = change in length of specimen or axial displacement, and

L = initial length of specimen.

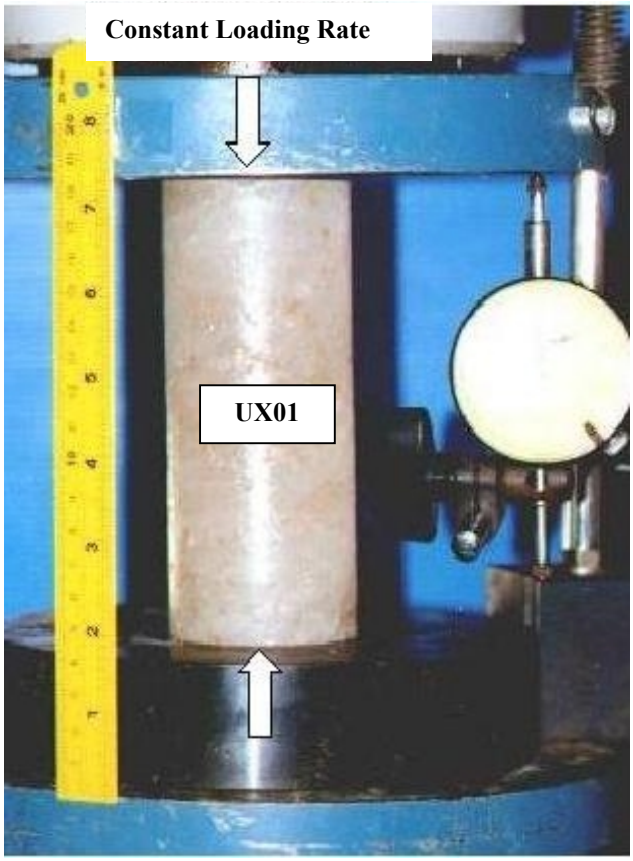

Figure 4.1 Uniaxial compressive strength test on specimen no. UX01.

The uniaxial compressive strength (σ_c) can be calculated from

$$\sigma_c = P_f / A \quad (4.3)$$

where, P_f = the maximum load at failure.

Result from uniaxial compression test on rock salt reveals that the compressive strength of rock salt is 30.2 MPa on average, failure occurs where the strain is between 0.016 and 0.045 and the critical shear strain is 0.0022, as tabulated in Table 4.1. The relationship between stress and strain is illustrated in Figure 4.2. The comparisons of the five rock salt specimens before and after failure are illustrated in Figures 4.3 through 4.7.

It is found from the test that the loading rate causing failure results in similar failure characteristics. Increase of strain with time is almost the same when the rates of loading are the same. Fracture occurs as a result of shrinkage of specimen by shearing and eventually breaking in rock salt-crystal. This characteristic confirms with similar testing on rock salt from both in Thailand and abroad (Wanten, et al, 1996; Boontongloan, 2000; Fokker, 1995; Franssen, 1998; Pfeifle, et al, 1998; Pouya, et al, 1996; Peach, 1996; Wetchasat, 2002). Table 4.1 shows the strength and strain values before failure of specimens.

Figure 4.8 compares the compressive strength from this study with other sources of rock salt. It can be seen that the compressive strength of rock salt from Udon Thani (well no. BD99-1 and BD99-2) is high compared with rock salt elsewhere.

Table 4.1 Summary of uniaxial compressive strength test results on rock salt.

Specimens No.	Average Diameter, D (mm)	Average Length, L (mm)	Weight, W (g)	Density, ρ (g/cm^3)	Depth (m)	Loading Rate (MPa/min)	Failure Stress, σ_c (MPa)	Failure Strain, ε_f	Critical Shear Strain, γ_c (%)
UX01	60.92	149.04	931.5	2.14	260.41 (MS)	0.1	35.8	0.025	0.0025
UX02	61.15	154.75	978.7	2.15	321.55 (MS)	0.1	32.2	0.021	0.0021
UX03	60.83	161.63	1029.8	2.19	295.70 (MS)	0.1	23.8	0.017	-
UX04	60.68	164.98	1036.0	2.17	258.42 (MS)	0.1	32.4	0.035	0.0019
UX05	61.12	157.93	1006.9	2.17	325.82 (MS)	0.1	26.9	0.016	-
Average Uniaxial Compressive Strength (σ_c)						30.2 ± 4.8 MPa (4,382 ± 690 psi)			
Average Critical Octahedral Shear Strain (γ_c)						0.0022 ± 0.0003			

MS –Middle Salt

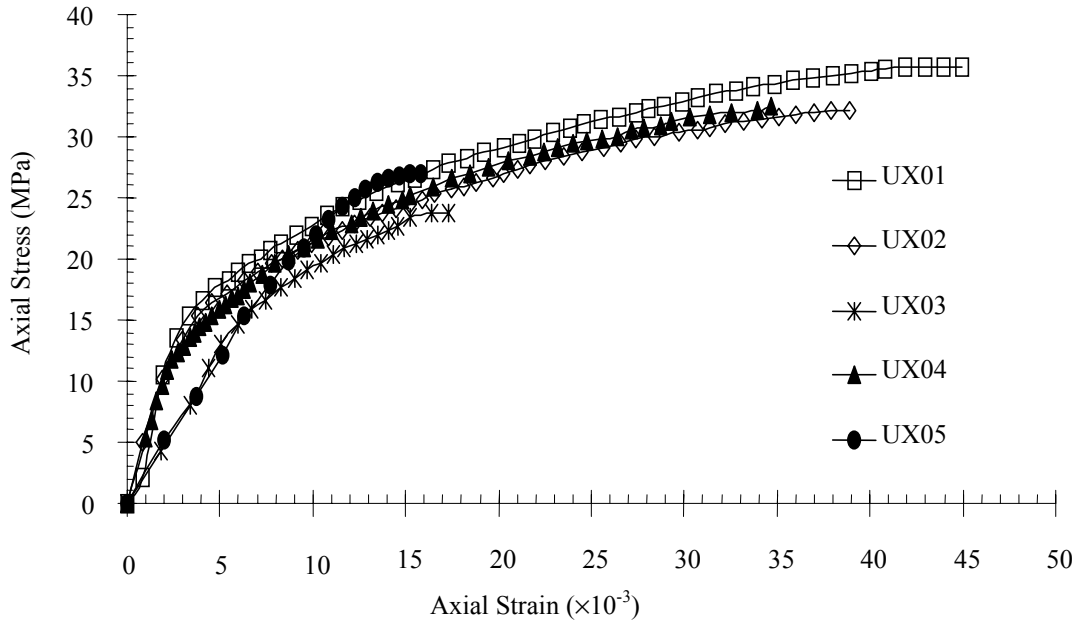

Figure 4.2 Axial stress-strain curves of specimen nos. UX01, UX02, UX03, UX04 and UX05.

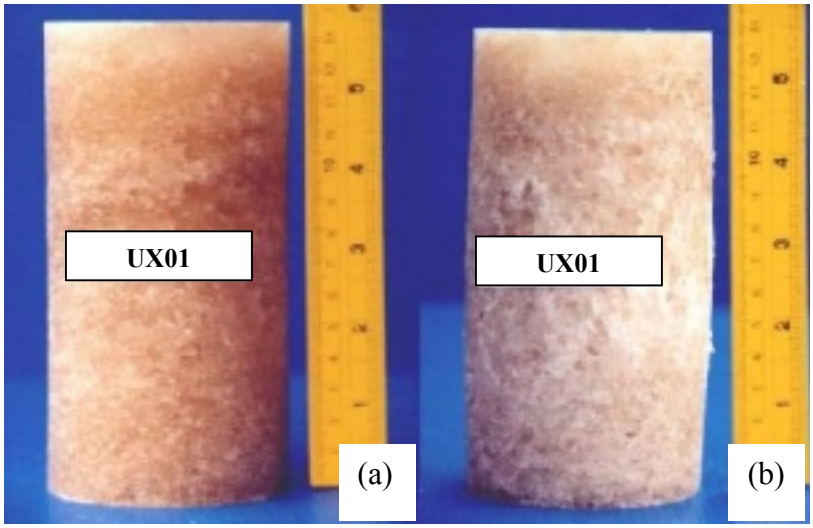

Figure 4.3 The specimen no. UX01 used for uniaxial compressive strength test. (a) before testing and (b) after testing.

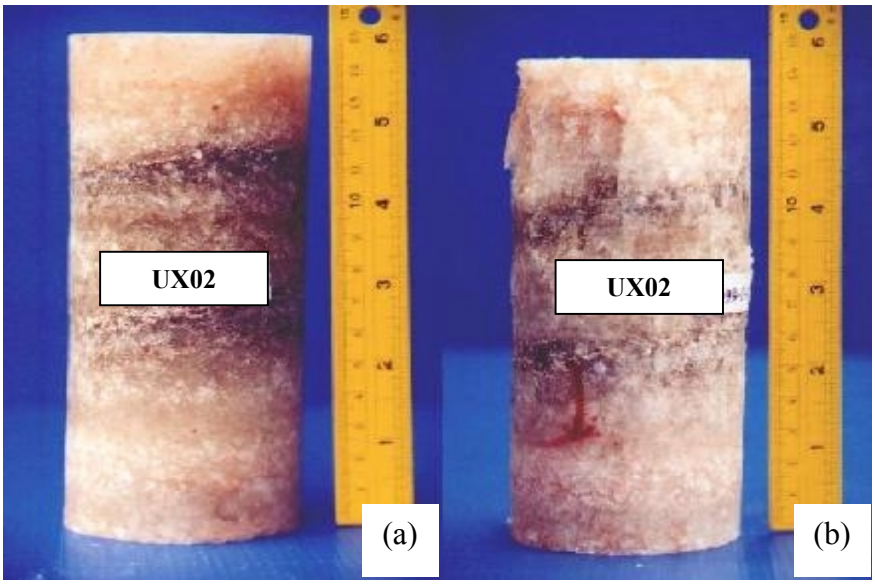

Figure 4.4 The specimen no. UX02 used for uniaxial compressive strength test. (a) before testing and (b) after testing.

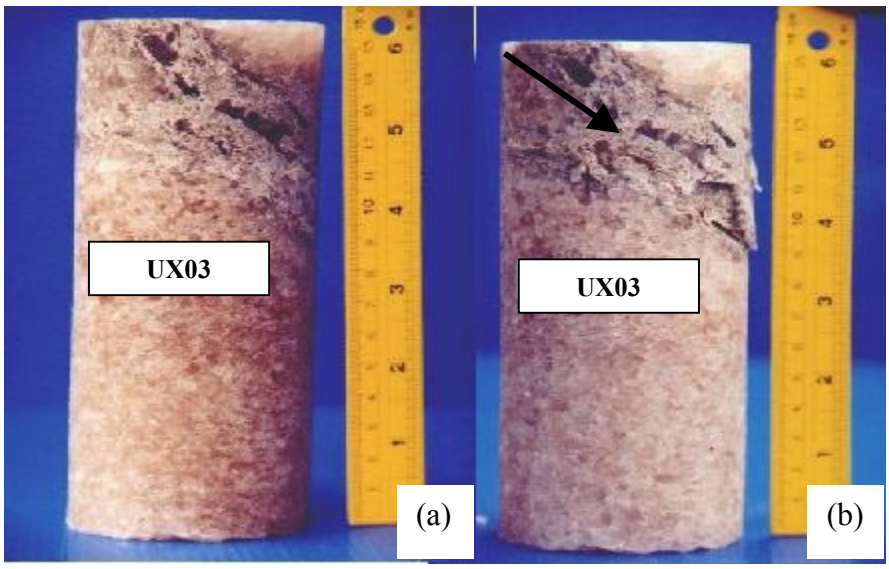

Figure 4.5 The specimen no. UX03 used for uniaxial compressive strength test. (a) before testing and (b) after testing.

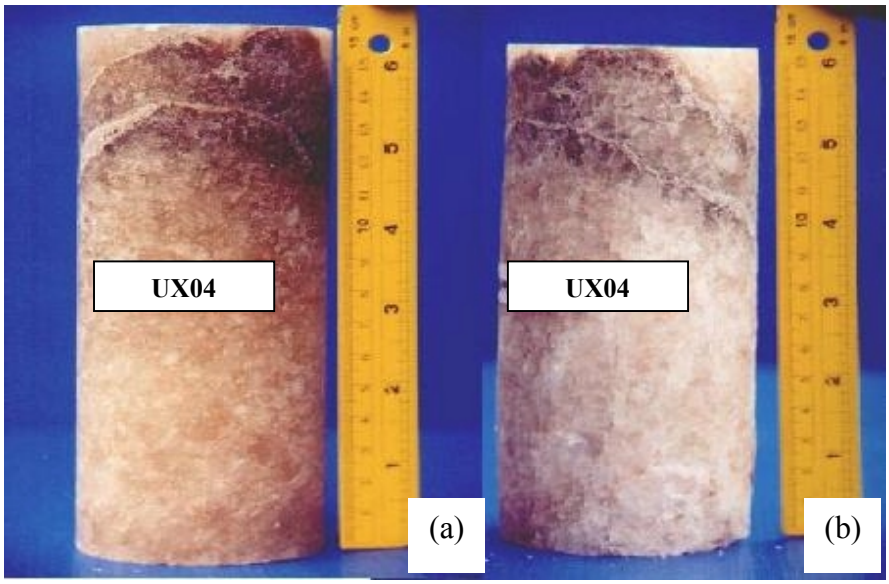

Figure 4.6 The specimen no. UX04 used for uniaxial compressive strength test. (a) before testing and (b) after testing.

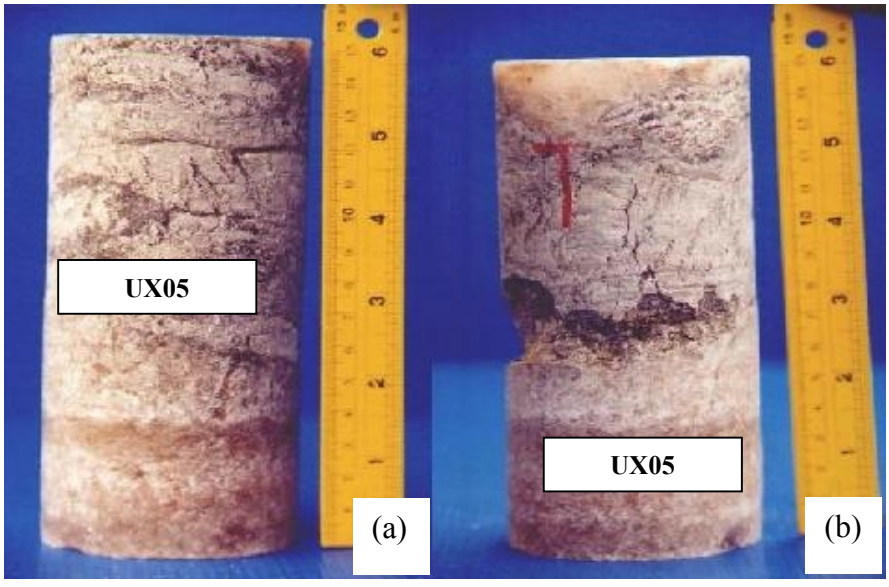

Figure 4.7 The specimen no. UX05 used for uniaxial compressive strength test. (a) before testing and (b) after testing.

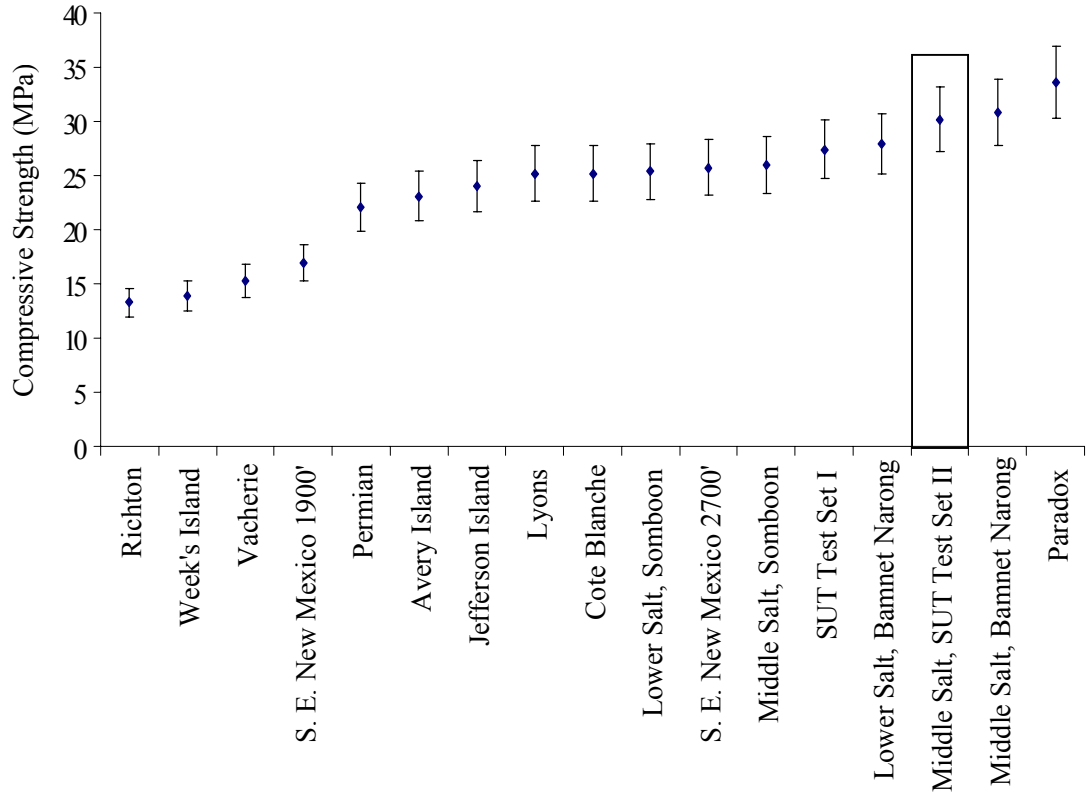

Figure 4.8 Comparison of the uniaxial compressive strength of salt from various sites (data from Wetchasat, 2002).

4.1.2 Brazilian Tensile Strength Test

The objective of this test is to determine the tensile strength of rock salt. Seventeen salt specimens have been prepared in accordance with the ASTM standard D3967 and ISRM suggestion (Bieniawski and Hawles, 1978) to have a diameter of 60 mm, with a constant length-to-diameter ratio (L/D) of 0.5. The test is conducted at room temperature.

The test uses a digital loading machine no.9901X0003, series Elect/ADR 2000 (ELE, 1995). As required by ASTM D3967, the specimen has been loaded in diametrical direction with a constant rate of 0.1 MPa/min. Two pieces of cardboard have been placed at the contact between test specimen and loading platen to ensure good distribution of load. The load on the specimen has been applied continuously until failure occurs. The test specimen is failed into two pieces along diametrical loading direction (Figure 4.9). The measured load is then used to calculate the tensile strength which is the strength in direction perpendicular to the loading direction. Results of the test are tabulated in Table 4.2. Figure 4.10 illustrates tensile cracking as result of diametrical loading.

Brazilian tensile strength can be calculated by using the measured load by the following equation:

$$\sigma_B = 2P_f / \pi DL \qquad (4.4)$$

where, σ_B = Brazilian tensile strength in Pa,

P_f = load at primary failure in N,

D = average diameter of the test specimen in m,

L = average thickness of the test specimen in m.

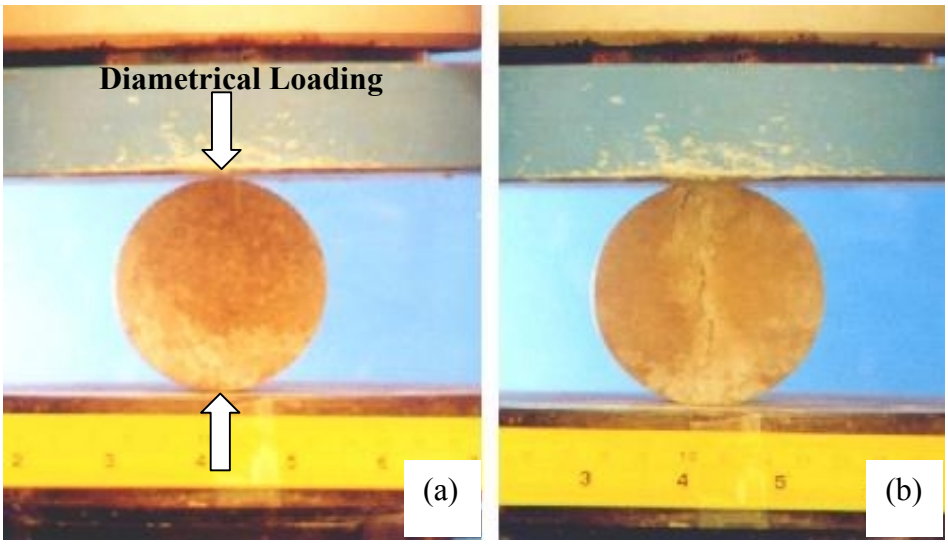

Figure 4.9 Brazilian tensile strength test (No.BD99-1-BR01i). (a) before testing and (b) after testing.

Table 4.2 Summary of Brazilian tensile strength test results on rock salt.

Specimens No.	Salt Units	Average Diameter, D (mm)	Average Length, L (mm)	Depth (m)	Brazilian Tensile Strength, σ_B (MPa)
BD99-1-BR01i	Middle Salt	61.15	29.98	264.3	1.6
BD99-1-BR02i	Middle Salt	60.92	33.68	264.1	1.9
BD99-1-BR03i	Middle Salt	60.68	34.35	264.2	2.1
BD99-2-BR04i	Middle Salt	60.92	34.43	321.4	1.4
BD99-1-BR05i	Middle Salt	60.78	35.68	264.3	1.7
BD99-2-BR06i	Middle Salt	60.3	33.15	322.9	2.0
BD99-1-BR07i	Lower Salt	61.23	34.13	391.3	1.9
BD99-2-BR08i	Middle Salt	61.17	32.03	329.1	2.1
BD99-1-BR09i	Middle Salt	58.43	36.97	254.0	1.7
BD99-1-BR10i	Middle Salt	59.63	33.73	251.9	1.8
BD99-1-BR11i	Middle Salt	58.42	34.23	254.0	1.6
BD99-1-BR12i	Middle Salt	57.63	34.65	252.9	1.7
BD99-2-BR13i	Middle Salt	61.15	32.1	328.6	1.8
BD99-2-BR14i	Middle Salt	61.08	31.5	322.7	2.4
BD99-2-BR15i	Lower Salt	61.13	32.57	403.8	1.4
BD99-1-BR16i	Middle Salt	58.55	37.72	254.0	1.8
BD99-1-BR17i	Middle Salt	60.88	35.05	391.0	2.4
Brazilian Tensile Strength Middle Salt Lower Salt			Mean Values 1.9 ± 0.3 MPa (275 ± 40 psi) 1.7 ± 0.3 MPa (246 ± 40 psi)		

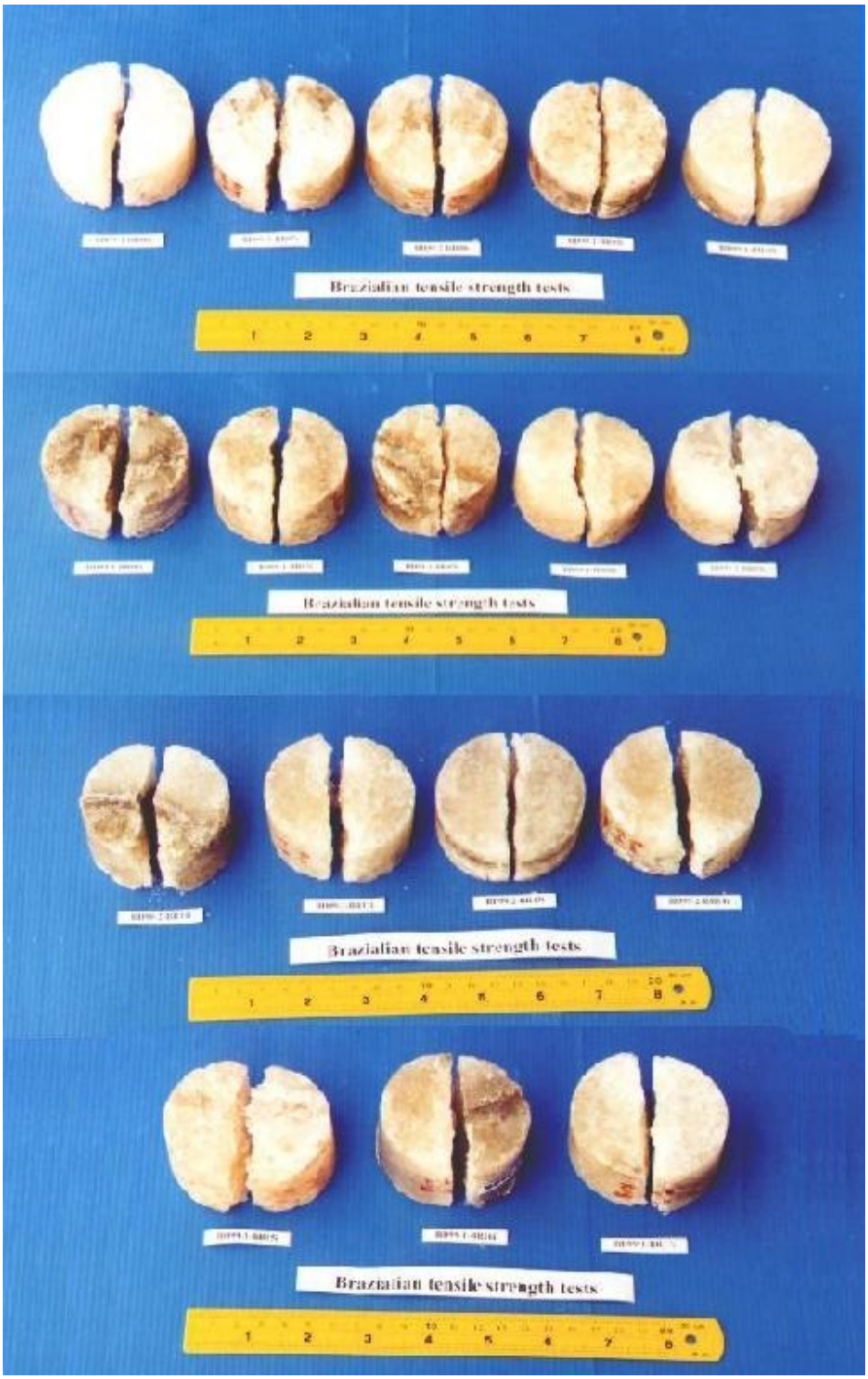

Figure 4.10 Fractures on specimens that obtained form Brazilian tensile strength test.

The result of 17 rock salt specimens shows failure in diametrical direction as illustrated in Figure 4.10. The average Brazilian tensile strength is 1.8 ± 0.3 MPa (270 ± 40 psi) which conforms with the property of rock salt from other sources, in Thailand and abroad. Figure 4.11 compares of tensile strength of rock salt with the tensile strengths of rock salt from other sources. The tensile strength values range from 1 – 2 MPa.

Some specimens have two cracks at around the loading point. Failures occur within 1 min on average for all specimens. The tensile strength deviation of 0.28 MPa or 6.75% may be caused by grain size of rock salt which is large, $10\times10\times10$ mm^3 on average, compared with specimen diameter of 60 mm. Almost all specimens with higher tensile strength have fracture across the salt crystal whereas, in specimen with lower tensile strength, crack occurs along the grain boundary. This indicates that tensile strength of bonding in crystal grain is higher than the strength between the rock salt crystals (Hardy, 1996).

4.1.3 Point Load Strength Index Test

Point load test determines point load strength index of rock salt specimens. Five rock salt specimens with a diameter of 60 mm and length of 100 mm are tested.

The test has been performed in accordance with ASTM D5731 by using SBEL PLT-75, the testing machine with maximum loading capacity of 75,000 pounds (Figure 4.12). The test specimen is loaded in diametrical direction, at the middle point of the core and perpendicular to the core axis (Figure 4.13). Maximum loading is used to calculate point load strength index using the following equation:

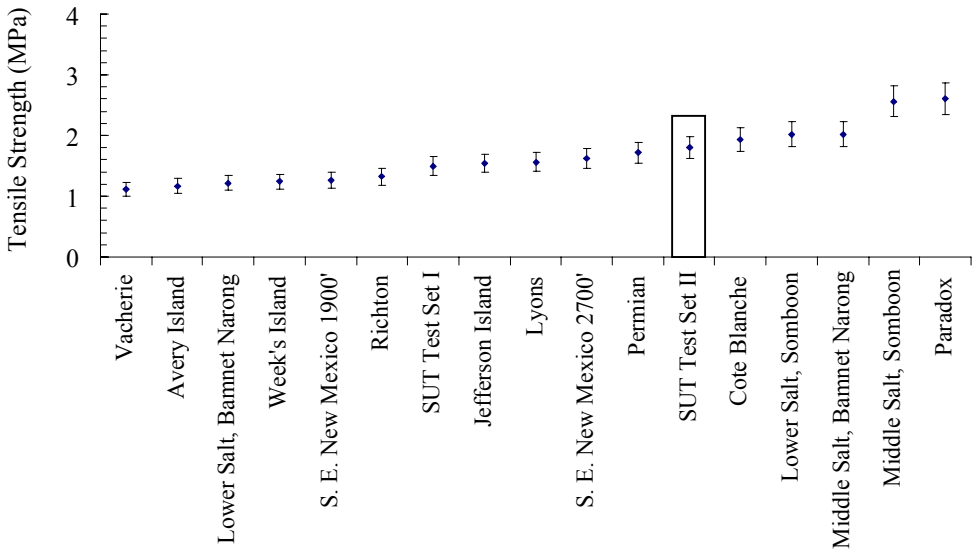

Figure 4.11 Comparison of tensile strengths of salt from various sites (data from Wetchasat, 2002).

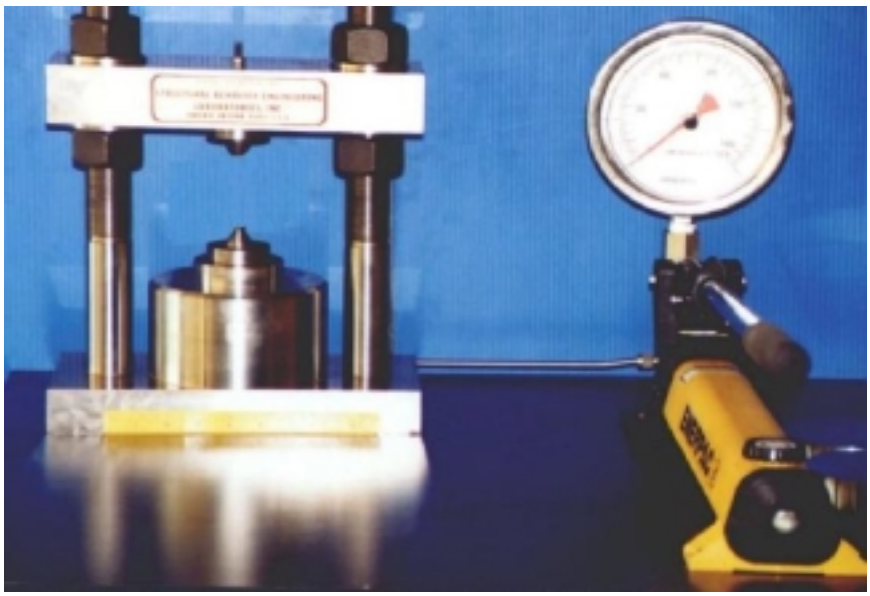

Figure 4.12 The apparatus No. SBEL PLT-75 used for point load strength index test. Capacity of maximum applied loading is 75,000 lbs.

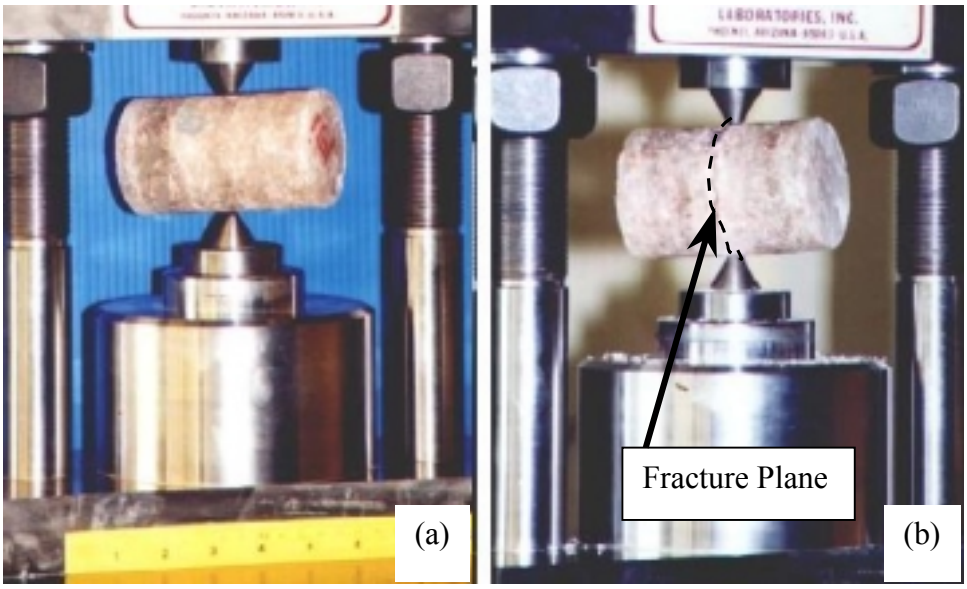

Figure 4.13 Point load strength index test on cylindrical salt specimens, (a) before applied load and (b) the fracture plane formed along the radial direction.

$$I_s = P_f / D^2 \quad (4.5)$$

where, I_s = point load strength index

P_f = stress at failure, and

D = rock salt core diameter.

Results of the test reveal that the point load strength index of the Middle salt and the Lower salt are 1.0 and 0.6 MPa, as tabulated in Table 4.3. Fracture characteristics of rock salt specimen are both failure along the crystal boundaries and failure through crystal grains. The point load strength index is higher in the specimen with the failure through crystal grains. Figure 4.14 illustrates fracture characteristic that occurs in the test specimens.

4.2 Uniaxial Cyclic Loading Test

Uniaxial cyclic loading test is that the rock salt specimen is subjected to fatigue stress (S) by repeatedly loading and unloading until failure taking place. The applied stress has to be lower than the compressive strength ($S < \sigma_c$). The test aims at finding out the number of cycles (N) that causes failure or fatigue life. The number of cycles at failure changes the elastic modulus of the salt specimens. Eight specimens are prepared from clean salt. Rock salt core from exploratory well nos. BD99-1 and BD99-2 is prepared to have a diameter of 60 mm and length-to-diameter ratio (L/D) of 2.5-3.

Uniaxial cyclic loading test is performed by systematically increasing and decreasing loads on the test specimen. In this study, the test has been done at room temperature and performed in accordance with the ASTM standard D2938 and the

Table 4.3 Summary of the results from point load strength index test on rock salt.

Specimens No.	**Rock Units**	**Depth (m)**	**Average Diameter, D (mm)**	**Average Thickness, t (mm)**	**Failure Load, P_f (kN)**	**Strength Index $I_s = P_f/D^2$ (MPa)**
HUT01	Lower Salt	410.15	61.07	107.05	2.28	0.61
HUT02	Middle Salt	260.25	60.93	104.00	3.90	1.05
HUT03	Lower Salt	390.55	61.22	104.10	3.15	0.84
HUT04	Lower Salt	410.55	60.98	107.00	4.05	1.09
HUT05	Lower Salt	391.85	61.05	74.80	3.24	0.87
HUT06	Lower Salt	392.20	60.10	100.20	2.02	0.56
HUT07	Lower Salt	392.80	60.21	120.10	4.42	1.22
HUT08	Lower Salt	393.10	60.08	115.30	4.51	1.25
HUT09	Lower Salt	394.00	61.05	119.00	2.01	0.54
HUT10	Lower Salt	396.00	61.12	118.00	2.09	0.56
Strength Index (I_s) - Middle Salt - Lower Salt				1.0 MPa 0.6 ± 0.05 MPa		

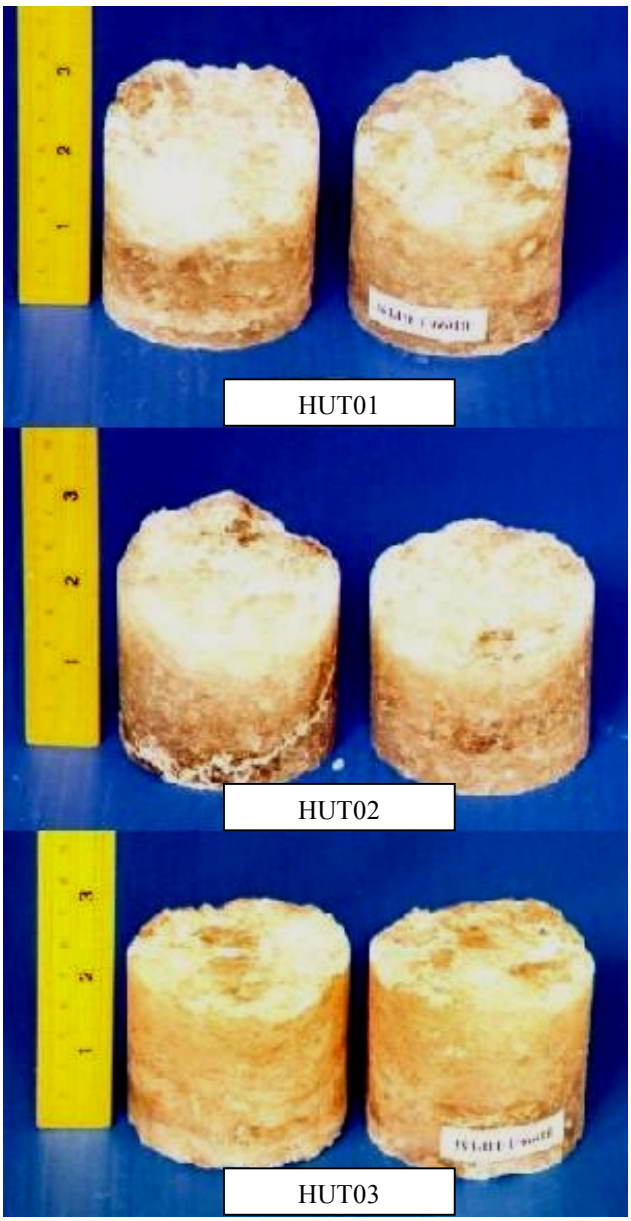

Figure 4.14 Failed specimens from point load strength index test.

suggestion of ISRM (Bieniaski et al., 1978). The tests are performed using a digital loading machine no. 9901X0003, series of Elect/ADR 2000 (ELE, 1995). The machine is capable of applying load of 2,000 kN. Each specimen is loaded to the maximum stress level (fatigue stress) and unloaded to the minimum stress level (near zero). Magnitudes of the axial load in each cycle are in range of 60-100% of the strength value determined by uniaxial compressive strength test. The unloaded stress level is about 0.1 MPa. The test is done by repeating loaded and unloaded in quick manner until failure takes place. The stress level and deformation of rock salt specimen against elapsed time as well as mode of failure are recorded during the test. The maximum load can be used to calculate for axial stress at failure.

The calculation of stress, strain and strength is performed using equations (4.1), (4.2), and (4.3), respectively. Elastic modulus (E) is determined by dividing the differential value of maximum and minimum stresses ($\Delta\sigma$) in each cycle by differential strain ($\Delta\varepsilon$):

$$E = \Delta\sigma/\Delta\varepsilon \tag{4.6}$$

Result from the above calculation can be presented in form of 1) maximum stress versus number of cycles (S-N), 2) strain versus elapsed time, to compare characteristic of creep in each test, and 3) elastic modulus versus the number of cycles. The relationship of S-N can be represented by a power equation as shown in equation (4.7). The equation shows that N increases as result of the change in fatigue stress (S).

$$S = S_o (N)^b \tag{4.7}$$

where, S_o = stress coefficient,

b = coefficient for number of cycles.

Results from the uniaxial cyclic loading test are tabulated in Table 4.4 and are shown in mathematical relation in Figure 4.15. The constants S_o and b are 33.61 and -0.08, respectively. They are found from the test that permanent strain has been accumulated from each cycle as shown in a graph of permanent strain against time (Figure 4.16), and a graph of strain against number of cycles (Figure 4.17). It can be seen from Figure 4.18 that the elastic modulus decreases as the number of cycles increases.

The result from the test shows that permanent strain has been accumulated during decreasing and increasing loads in each cycle. When permanent strain has reached the value of 0.04 – 0.05, the rock salt specimen would fail. Fracture is not clearly observed in the test with low failure stress (S). Fracture occurs along the crystal grain boundary with a little increasing in volume. This is different from the fracture occurred in the test with higher failure stress. This fracture can be clearly observed as it occurs in a plane that has an angle of 0 – 30 ° with the core axis.

The S-N curve is close to the result of the rock salt tested by Passaris (1982). The constants A and B are 59.8 and -0.05, respectively. The relation between permanent strain and time is similar to the result from creep test which corresponds to the conclusions drawn by Ishizuka and Abe (1990). Figures 4.19 through 4.22 illustrate specimens before and after testing. Considering failure strain in Figures 4.16 and 4.17, it can be seen that failure strain decreases as the failure stress increases. In other words, failure strain at higher stress is lower than the failure strain at the lower stress.

Table 4.4 Summary of uniaxial cyclic loading test results on salt specimens.

Sample No.	Average Diameter, D (mm)	Average Length, L (mm)	Average Weight, W (g)	Depth (m)	Density, ρ (g/cm^3)	Fatigue Stress, S (MPa)	Fatigue Life, N (cycle)
BD99-2-CC01i	60.50	123.33	772.9	325.0	2.18	23.0	223
BD99-1-CC02i	60.23	124.13	777.1	285.2	2.19	24.3	86
BD99-2-CC03i	61.10	118.80	749.3	408.9	2.15	21.6	235
BD99-2-CC04i	61.01	135.92	858.8	330.0	2.16	20.3	410
BD99-2-CC05i	60.50	112.00	701.5	325.5	2.18	16.0	4120
BD99-1-CC06i	61.05	128.05	790.5	253.3	2.11	26.8	103
BD99-2-CC07i	61.10	130.00	810.6	409.9	2.13	29.0	7
BD99-2-CC10i	61.20	125.20	801.6	325.2	2.18	30.4	1

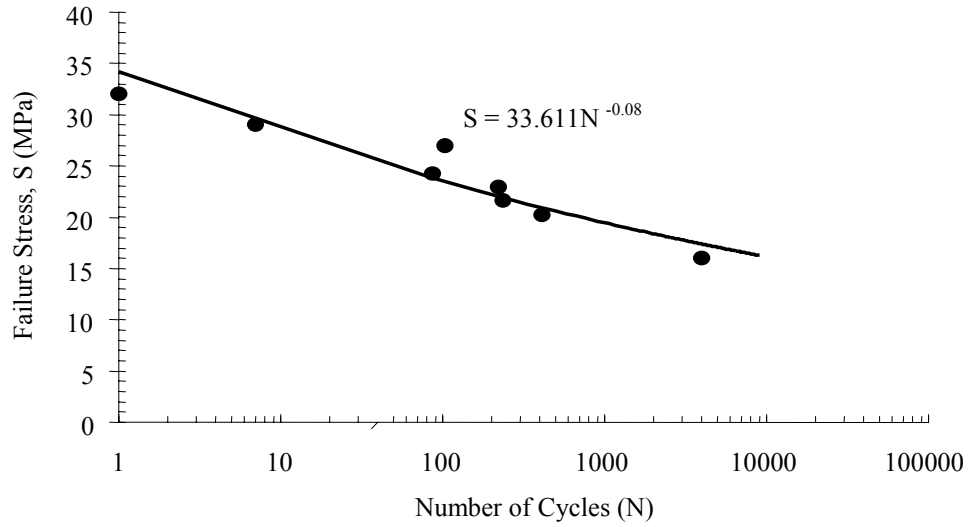

Figure 4.15 Failure stress (S) as a function of number of cycles (N) obtained for the uniaxial cyclic loading testing.

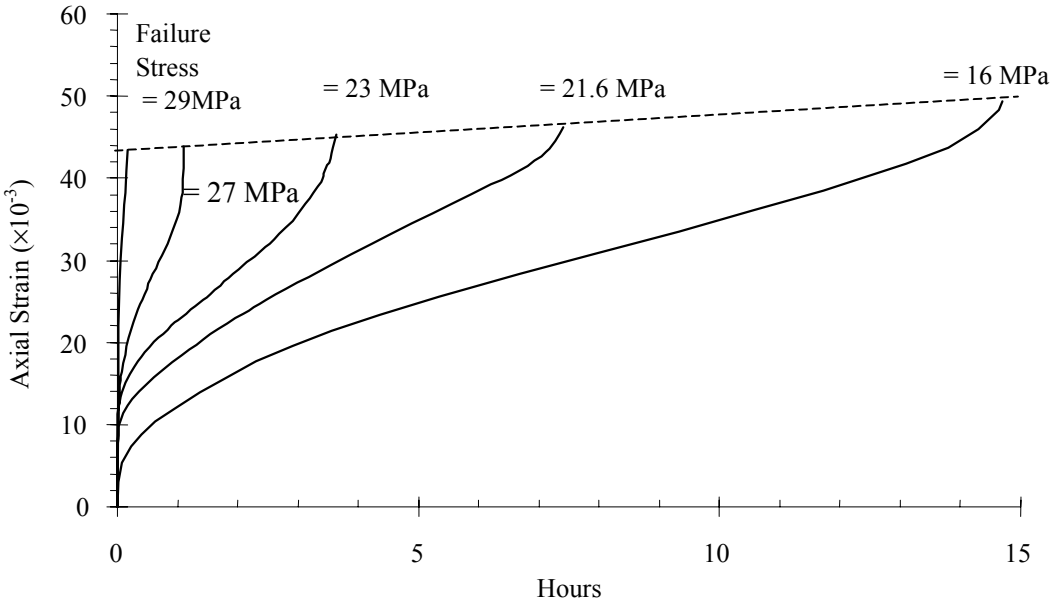

Figure 4.16 The increasing of permanent strain as a function of time from uniaxial cyclic loading test with the fatigue stress of 16, 21.6, 23, 27 and 29 MPa.

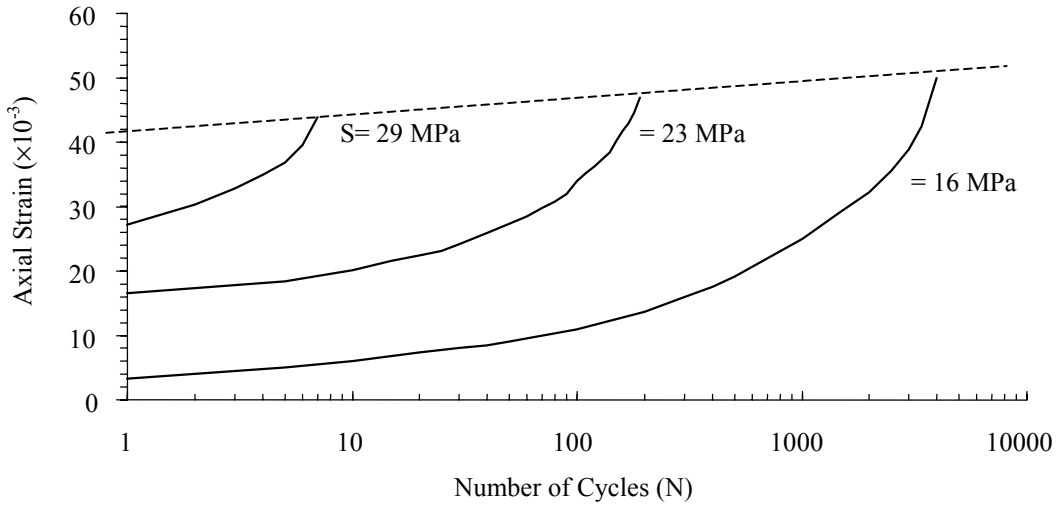

Figure 4.17 The relationship between axial strain versus number of cycles obtained from cyclic loading test.

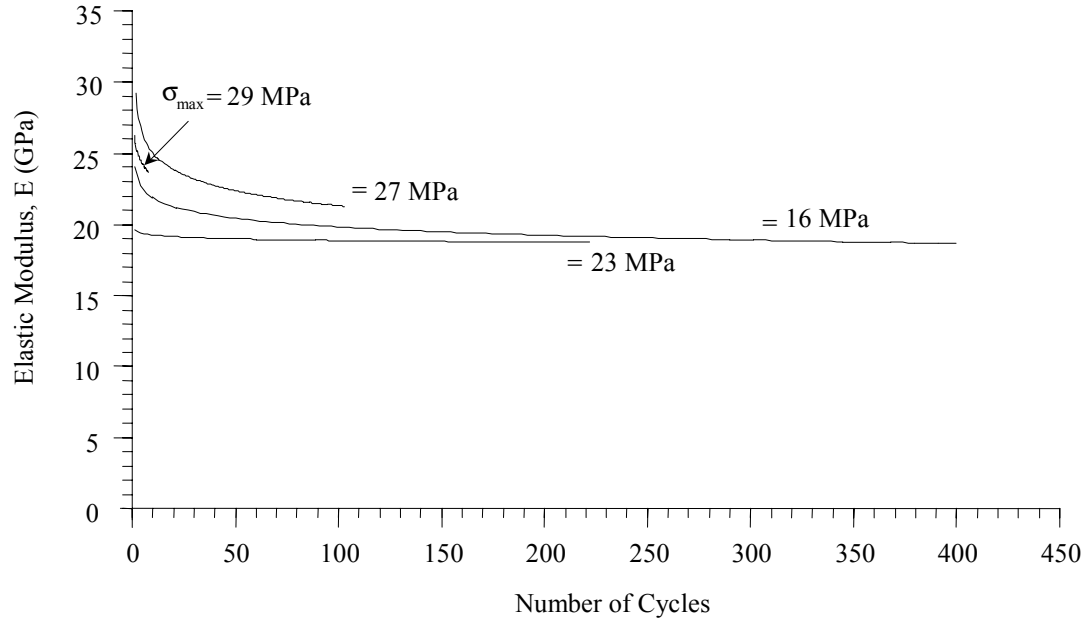

Figure 4.18 Elastic modulus (E) as a function of loading cycles for different maximum stresses (σ_{max}).

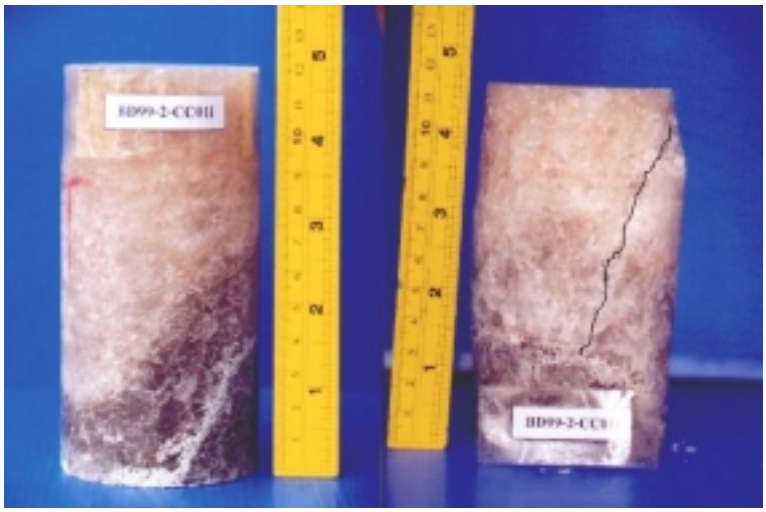

Figure 4.19 Comparison between before and post-failure specimen (no. BD99-2-CC01i). The specimen failed at a fatigue stress of 23 MPa. Angle of failure plane is 30°. Failure plane redrawn for enhancement.

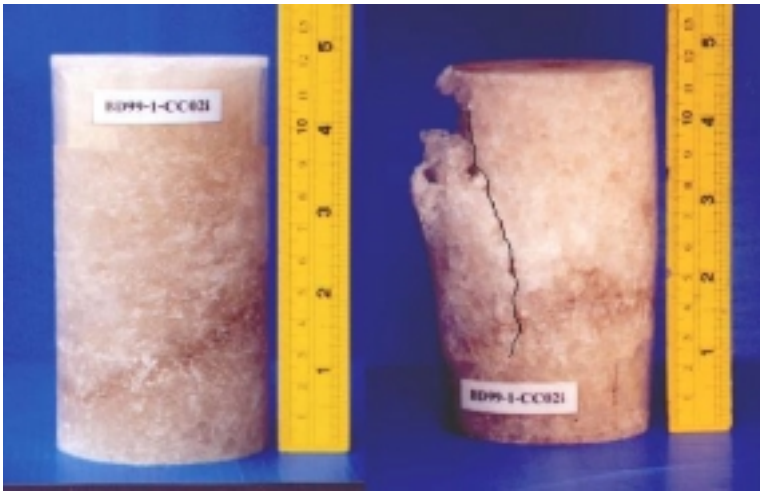

Figure 4.20 Comparison between before and post-failure specimen (no. BD99-2-CC02i). The specimen failed at a fatigue stress of 24.3 MPa. Angle of failure plane is 10°. Failure plane redrawn for enhancement.

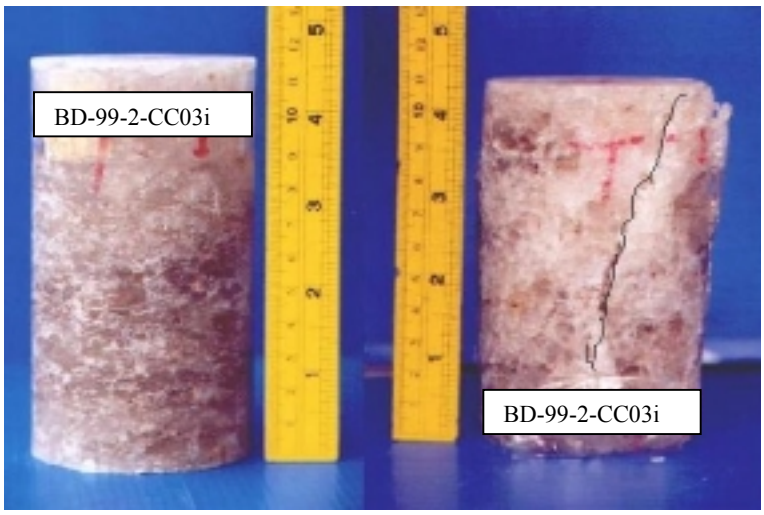

Figure 4.21 Comparison between before and post-failure specimen (no. BD99-2-CC03i). The specimen failed at a fatigue stress of 21.6 MPa. Angle of failure plane is 30°. Failure plane redrawn for enhancement.

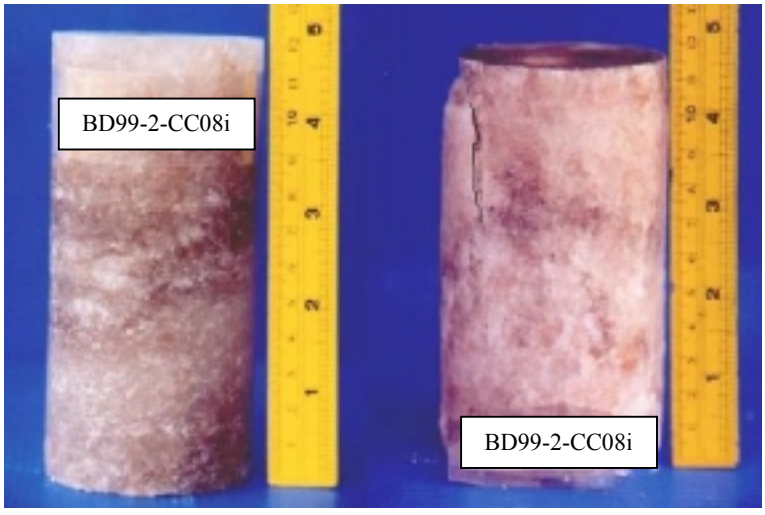

Figure 4.22 Comparison between before and post-failure specimen (no. BD99-2-CC08i). The specimen failed at a fatigue stress of 30.4 MPa. Angle of failure plane is 0°.

4.3 Healing Test

Healing test aims at studying the decrease of fracture aperture, permeability of rock salt fracture, and the mechanical properties of healed fractures. The study emphasizes on time, stress, fracture characteristic and inclusion in rock salt which are the significant factors for the healing of fracture. This study excludes other influential factors such as temperature, mineral composition and moisture in rock salt. An efficiency of healing fracture in rock salt can be evaluated from point load strength index performed on the fracture that has already healed, and the permeability of rock salt fracture. Two test schemes are proposed to assess the healing behavior of the salt fractures: healing under uniaxial (normal) loading and healing under confining pressure. All tests are conducted under isothermal conditions (20-25°C). Three types of salt fracture have been simulated in the laboratory: 1) tension-induced fractures, 2) fractures formed by saw-cut surfaces, and 3) fractures formed by smooth polished surfaces (Figure 4.23). Salt surfaces on both sides of the fracture are well mated. The salt specimens are prepared to have a diameter of 60 mm with a length-to-diameter ratio of 2.5. To obtain the tension-induced fractures, the cylindrical specimens are subjected to point loading or by diameter loading (Brazilian tension test). The point-loaded fracture is normal to the specimen axis, and is prepared for healing under uniaxial loading. The diameter-loaded fracture is the axial fracture, parallel to the specimen axis, and will be healed under confining pressure. The fracture formed by saw-cut surfaces is also normal to the specimen axis, while the fracture formed by polished (grinding) surfaces is parallel to the specimen axis. After the fractures have been prepared, the amount of inclusions on the fracture surfaces is measured and mapped using magnifying glass. The aerial percentage of the inclusions is calculated

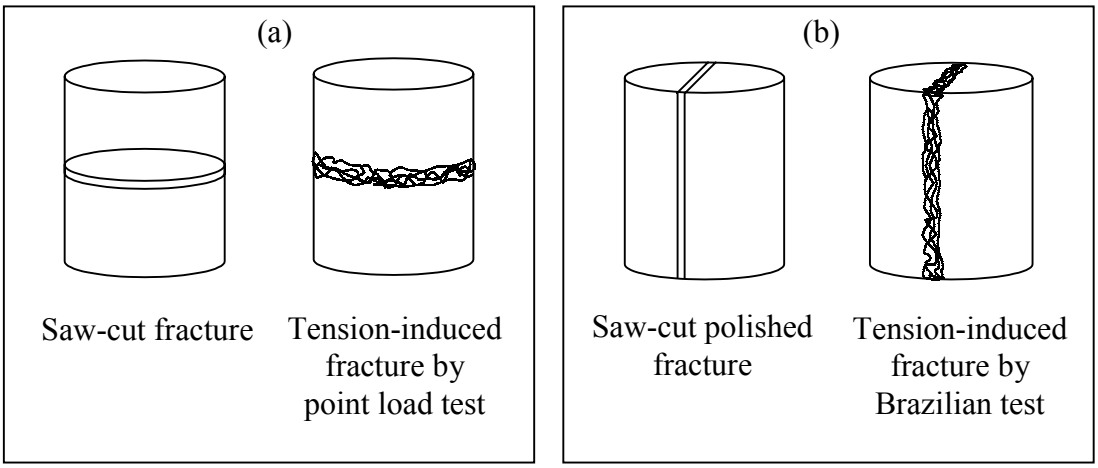

Figure 4.23 Three types of fractures: saw-cut fracture, saw-cut polished fracture and tension-induced fracture. (a) Normal fracture and (b) Axial fracture.

with respect to the total fracture area. The inclusions defined here are all associated and foreign minerals or materials that are not sodium chloride. Prior to the healing test, a close examination is made to determine whether the tension-induced fractures are formed by the splitting failure of the salt crystals or by the separation of the inter-crystalline boundaries.

4.3.1 Healing under Normal Loading

Table 4.5 shows the test matrix for the healing test under uniaxial loading. Four test series with different test conditions have been performed. For the first two series, low normal stresses of 3.2 kPa and 3.8 kPa are applied to the saw-cut surfaces under dry and saturated conditions. Three specimens are used for each normal stress. Dead weight machine applies constant loading on to the fracture. For the saturated condition, the fractures are submerged under saturated brine while loading. The load is removed after testing for 30 days. No healing has been observed for both dry and saturated fractures. All saw-cut fractures remain separable.

The third and fourth test series use a normal stress of 4.3 MPa on three saw-cut fractures, and 7.8 MPa on ten tension-induced fractures. Figures 4.24 and 4.25 show some salt specimens prepared for these test series. A consolidation machine with the maximum load capacity of 2 tons is used to apply constant stresses to the specimens (Figure 4.26). Figure 4.27 illustrated the healing test on specimens formed by saw-cut fractures under uniaxial loading of 3.8 kPa at wet and dry condition. And also, the healing tests on specimens with saw-cut fracture are conducted under dry conditions with uniaxial loading of 4.3 MPa (Figure 4.28). The specimens are unloaded after 30 days.

Table 4.5 Summary of the healing test under uniaxial loading. The fracture healing ability is assessed by point load strength index test.

Test Methods	**Fracture Characteristics**		**Number of Specimens**	**Test Conditions**
Uniaxial Loading	Normal Fracture	Saw-cut surface	9	Series 1 - 3 specimens - σ_{axial} = 3.2 kPa - dry condition - ≥ 30 days Series 2 - 3 specimens - σ_{axial} = 3.8 kPa - saturated condition - ≥ 30 days Series 3 - 3 specimens - σ_{axial} = 4.3 MPa - dry condition - ≥ 30 days
		Tension-induced fracture by point loading	10	Series 4 - σ_{axial} = 7.8 MPa - dry condition - 30 days - percentage of inclusions varies from 0 to 40%

Figure 4.24 Some salt specimens with normal tension-induced fractures prepared for healing under uniaxial loading. Top: fractures with no inclusions. Bottom: fractures with 30 % inclusions.

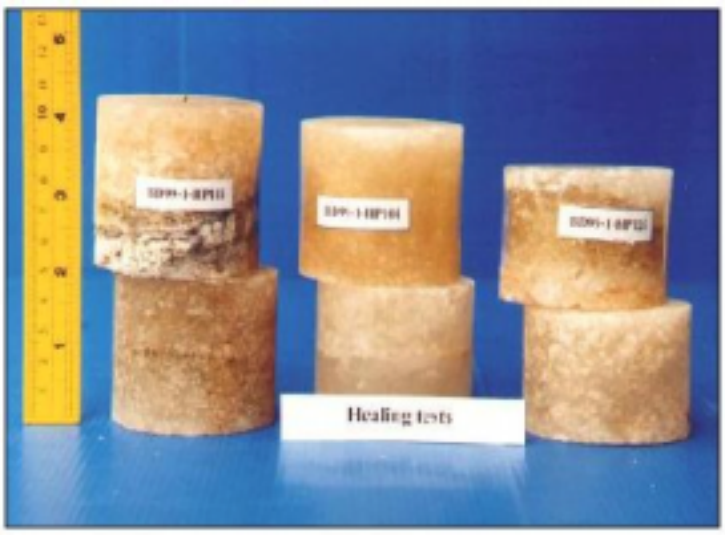

Figure 4.25 Some salt specimens with normal saw-cut fracture prepared for healing under uniaxial loading.

Figure 4.26 A consolidation machine with the maximum load capacity of 2 tons is used to apply constant stresses to the specimens.

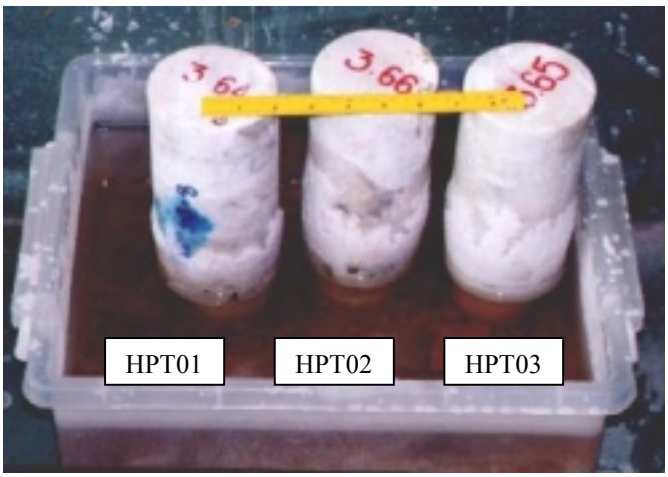

(a)

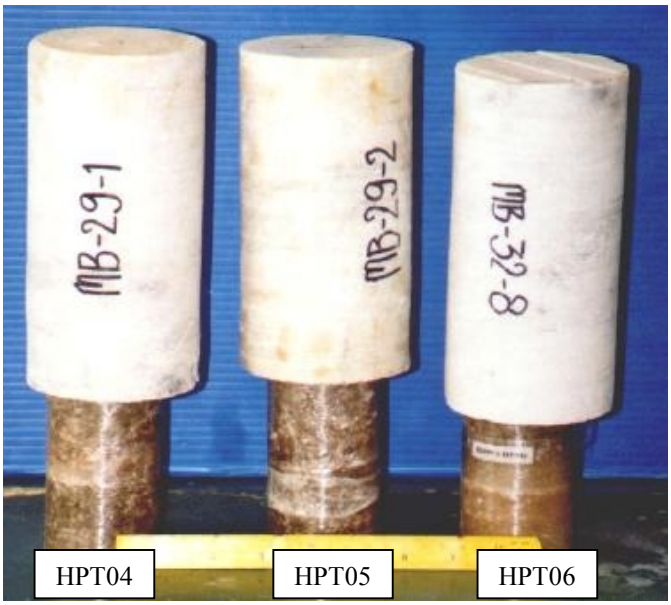

(b)

Figure 4.27 Healing test of saw-cut specimens under uniaxial loading under wet and dry condition. These specimens are loaded axially by a magnitude of 3.2 kPa. (a) Salt specimens (HPT01, HPT02 and HPT03) are test under wet condition and (b) salt specimens (HPT04, HPT05 and HPT06) are test under dry condition.

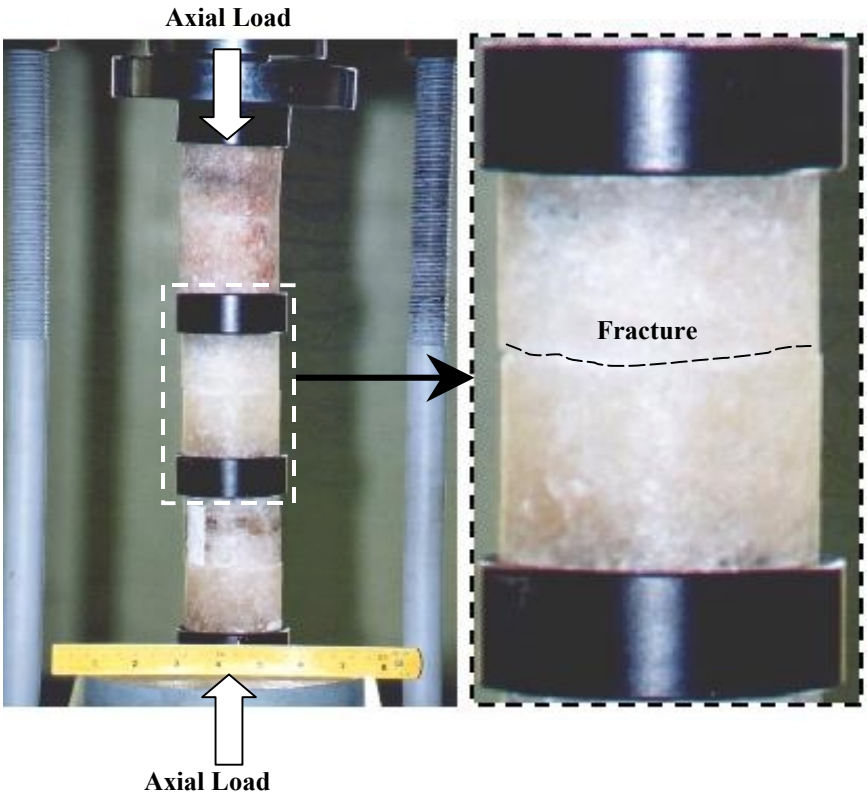

Figure 4.28 Healing test of the specimen with saw-cut fracture under uniaxial loading at dry condition. These specimens are loaded axially by a magnitude of 4.3 MPa. Fracture plane redrawn for enhancement.

In order to assess the healing effectiveness, the specimens are subjected to point load testing by having the loading points lied on and parallel to the healed fracture plane (Figure 4.29). The point load strength of the healed fracture (I_H) is calculated by dividing the failure load (P) by the diameter square (D^2). The healing effectiveness (H_e) of each fracture is defined by the percentage ratio of the I_H to I_S, where I_S represents the point load strength of the intact salt obtained previously from inducing the fracture to the same specimen. All specimens fail along the original fracture plane.

No healing has been detected on the fractures formed by saw-cut surfaces tested under 4.3 MPa normal stresses (test series 3). Table 4.6 summarizes the healing test result from test series 1, series 2 and series 3. Healing however has been observed on the tension-induced fractures tested under 7.8 MPa normal stresses (test series 4). Table 4.7 summarizes the results. Some H_e values exceed 100%. This is probably because some existing voids or fissures in salt along the fracture plane are compressed during healing period, and subsequently strengthening the fracture beyond the previous intact condition. It should be noted that before the fractures are initially induced, the intact core specimens have not been subjected to any compression. The high variation of H_e values may be also due to the accuracy of the testing technique. Even though assessment of healing effectiveness by point load testing is relatively quick and easy, the high stress gradient induced in the specimen usually results in a high intrinsic variability of the measurement results. The complex distribution, pattern and locations of the inclusions in relation to the loading points can also enhance the variability of the strength results. The healing effectiveness tends to decrease as the amount of inclusion increases (Figure 4.30). However, their mathematical relationship can not be constructed due to the high variation of the results.

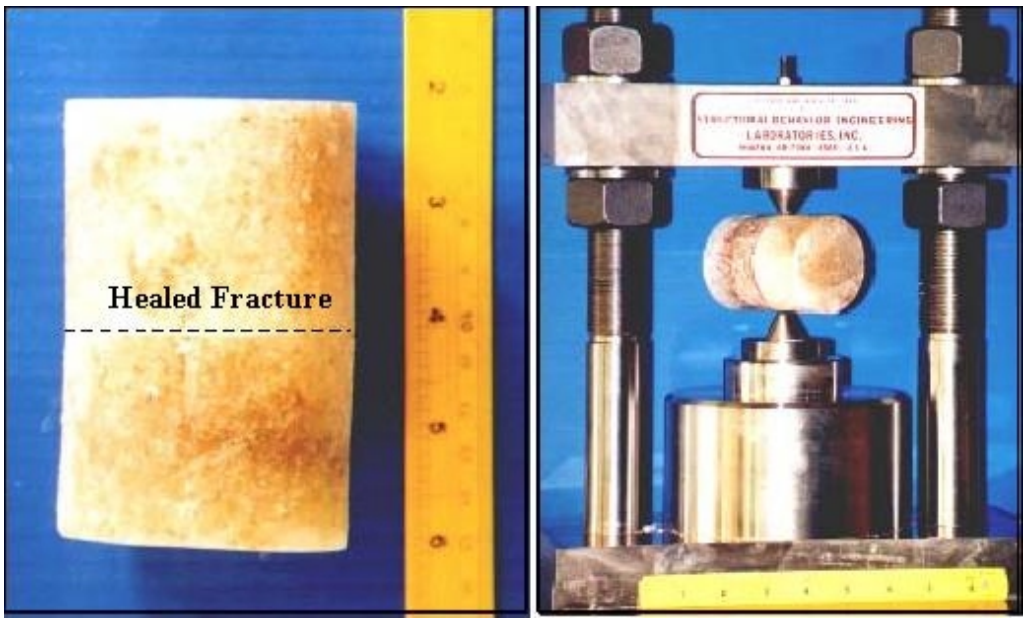

(a) (b)

Figure 4.29 Salt specimen with fracture after healing under uniaxial load (left). The healing effectiveness is assessed by point load testing (right). Fracture plane redrawn for enhancement.

Table 4.6 Summary of the healing test on specimens formed by saw-cut fracture tests are under uniaxial loading (test series 1, series 2 and series 3). Point load conducted to assess the healing effectiveness of salt fracture.

Sample No.	Test Series	Average Diameter, D (mm)	Average Length, L(mm)	Depth (m)	Axial Load (MPa)	Condition	Duration (Day)	$I_S = P_f/D^2$ (MPa)	Results
HPT01	1	60.75	91.30	264.63	3.20	Saturated with brine	7	0	Not Healed
HPT02		61.15	92.15	410.45	3.20		15	0	
HPT03		60.90	100.80	263.45	3.20		30	0	
HPT04	2	61.15	91.30	326.35	3.20	Dry	7	0	
HPT05		61.15	100.10	403.66	3.20		15	0	
HPT06		61.20	111.20	410.25	3.20		30	0	
HPT07	3	60.70	87.35	405.14	4.26		20	0	
HPT08		61.00	79.85	328.37	4.26		20	0	
HPT09		61.69	94.15	324.75	4.26		20	0.02	Partially Healed

Table 4.7 The point load test results for salt specimens with tension-induced fractures after dry healing under constant axial stress of 7.8 MPa for 30 days (test series 4).

Specimen No.	Percentage of Inclusions (%)	Point Load Strength Index		Healing Effectiveness $H_e = [I_H/I_S] \times 100$ (%)
		Intact Salt, I_S (MPa)	Salt with Healed Fracture, I_H (MPa)	
HUT01	0	0.61	1.13	185
HUT02	30	1.05	0.75	71
HUT03	5	0.84	1.00	119
HUT04	40	1.09	0.40	37
HUT05	25	0.87	0.74	85
HUT06	10	0.56	0.59	105
HUT07	5	1.22	0.49	40
HUT08	5	1.25	0.48	38
HUT09	25	0.54	0.51	94
HUT10	15	0.56	0.40	71

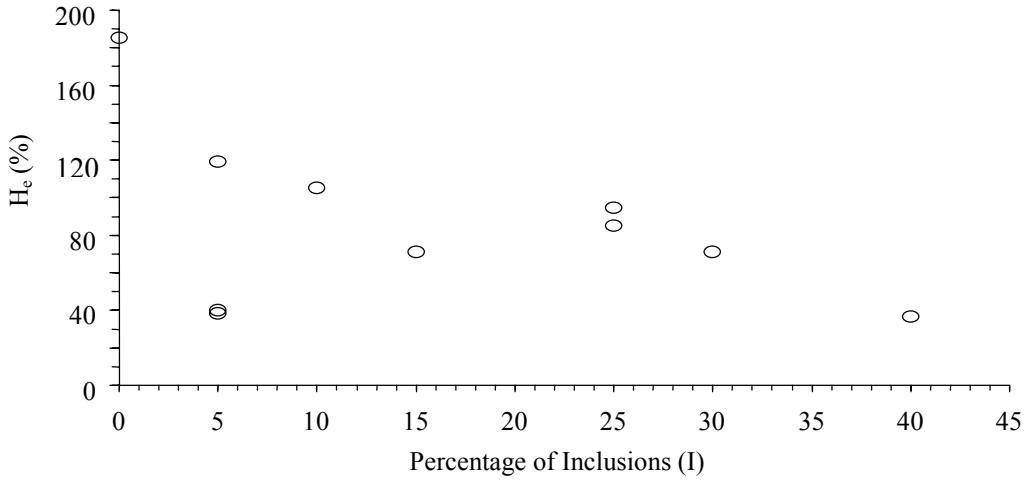

Figure 4.30 Healing effectiveness (H_e) as a function of percentage of inclusion (I) obtained from uniaxial loading. All specimens have tension-induced fractures.

4.3.2 Healing under Confining Pressure

Tension-induced fractures and the fractures formed by polished surfaces are subjected to healing test under confining pressure. Figure 4.31 shows the axial fracture in the salt specimen. The "Overburden Poro-Perm Cell" applies constant confining pressure to the salt specimen (Figure 4.32). It is capable of applying confining pressure up to 70 MPa. Each fracture type is subjected to two loading configurations: single-step loading and multi-step loading. Table 4.8 summarizes the test matrix. All specimens are tested under dry condition. During pressurization, gas flow permeability test is performed.

The gas flow test are measured to calculate the hydraulic conductivity of the fracture (K_f), based on an assumption of the flow through parallel plates (Zeigler, 1976).

$$K_f = (\gamma/12\mu)\, e^2 \qquad (4.8)$$

where, e = width of opening or fracture aperture,

γ = unit weight and

μ = viscosity of fluid of gas flow through fracture.

Fracture aperture value (e) relates to the flow rate (Q) and differential of hydraulic head (Δh) between two point as follow,

$$Q/\Delta h = C\, e^3 \qquad (4.9)$$

where, C is a constant value depending on fracture characteristics and property of fluid flow through fracture and can be determined from equation (4.10).

$$C = (W/L)(\gamma/12\mu) \qquad (4.10)$$

(a) (b)

Figure 4.31 A specimen with tension-induced fractures is prepared by diameter loading (a). A specimen with polished fracture (b). They are prepared for gas flow permeability testing.

Figure 4.32 Gas flow permeability test using "Overburden Poro-Perm Cell". The salt specimen is subject to confining pressure between 0.69 and 20.67 MPa in the pressure cell.

Table 4.8 Summary of the healing test under confining pressure. The fracture healing effectiveness is assessed by Brazilian tensile strength test.

Test Methods	**Fracture Characteristics**		**Number of Specimens**	**Test Conditions**	
				Single-step loading	**Multi-step loading**
Applied Confining Pressure	Axial Fracture	Polished surface	3	- 2 specimens - P_c = 3.4, 6.7 MPa - 100 hours/step - dry	- 1 specimen - P_c = 3.4→6.7 MPa - 100 hours - dry - two loading cycles
		Tension-induced fracture by diameter loading	8	- 5 specimens - P_c = 3.4, 6.7,10.3 and 13.8 MPa - 120 hours - dry	- 3 specimens - P_c = 3.4 → 6.7 → 10.3 → 3.8 MPa - 96 hours/step and 24 hours/step - dry - two loading cycles.

where, W = width of aperture and

L = length of fracture that fluid flow through.

For this case, W is a specimen diameter and L is a length of rock salt specimen.

From the equations (4.9) and (4.10), the width of fracture can be shown in relation of variables and constants, W, L, γ, μ, Q and Δh as follow:

$$e = [(Q/\Delta h)(L/W)(12\mu/\gamma)]^{1/3} \quad (4.11)$$

e value in equation (3.11) will be used in the calculation of hydraulic conductivity of fracture in equation (4.8). The final form of K_f can be shown as:

$$K_f = (\gamma/12\mu)^{1/3} \bullet [(Q/\Delta h)(L/W)]^{2/3} \quad (4.12)$$

It is assumed that the fracture width equals the specimen diameter, and the length equals the specimen length. The nitrogen gas pressure is injected at a constant magnitude of 0.35 MPa. The lowers measurement limit of the system is about 10^{-8} m/s.

One polished fracture is subjected to the confining pressure (P_c) of 3.45 MPa and later increased to 6.89 MPa (multi-step loading). Each loading step takes 100 hours. This pressure scheme is repeated for the second cycle. The calculation of hydraulic conductivity from gas flow test result is tabulated in Table 4.9. Figure 4.33 shows the flow test results during the pressurization. The fracture permeability decreases with increasing confining pressure. Under each pressure, the fracture permeability also decreases as the testing time increases. The second cycle of pressurization yields a lower hydraulic conductivity than do the first one. When the pressure increases to 6.89 MPa, the hydraulic conductivity becomes lower than the

Table 4.9 Summary of the gas flow test results of the specimen formed by saw-cut polished fracture (specimen no. HGT06).

(1)	(2)	(3)	(4)	(5)	(6)	(7)	(8)	(9)		(10)	
Test Duration (Hours)	**Confining Pressure, P_C (psi)**	**In Flow Pressure, P_i(psi)**	**Flow Time, t (sec)**	**Flow Volumes, V (cm^3)**	**Temperature (°C)**	**Flow Rate, Q ($x10^{-6} ft^3/sec$)**	**Change in hydraulic head ΔH (ft)**	**Aperture, e**		**Hydraulic Conductivity, K_f**	
								($x10^{-6}$ft)	**($x10^{-6}$m)**	**($x10^{-6}$ft/s)**	**($x10^{-6}$m/s)**
0	500	5	17.30	10	28	20.40	9742.90	59.10	18.01	55.87	17.03
23.5	500	5	20.51	10	27	17.21	9742.90	55.84	17.02	49.88	15.20
32	500	5	22.31	10	28	15.82	9742.90	54.30	16.55	47.16	14.37
48.5	500	5	24.27	10	28	14.54	9742.90	52.79	16.09	44.58	13.59
75.5	500	5	24.96	10	29	14.14	9742.90	52.30	15.94	43.76	13.34
100.5	500	5	29.00	10	32	12.17	9742.90	49.75	15.16	39.59	12.07
100.5	1000	10	54.44	10	32	6.48	19485.79	32.01	9.76	16.39	5.00
144	1000	50	3600	1	28	0.01	97428.96	2.15	0.65	0.07	0.02
0	500	16	32.48	1	30	1.09	31177.27	15.09	4.60	3.64	1.11
20	500	58.02	816.46	0.2	28	0.01	113056.56	1.96	0.60	0.06	0.02

Remark:

Diameter (W) = 38.04 mm, Length (L) = 60 mm, $\gamma = 0.0739$ lb/ft^3,

$\mu = 3.85 \times 10^{-7}$ lb-sec/ft^2

$(7) = \{(5) \times 0.3048^3\} \div (4)$

$(8) = \{(3) \times 144\} \div \gamma$

$(9) = [(7) \div \{(8)*C\}]^{1/3}$, $C = (W/L) \cdot (\gamma/12\mu)$

$(10) = (\gamma/12\mu) \times (9)^2$

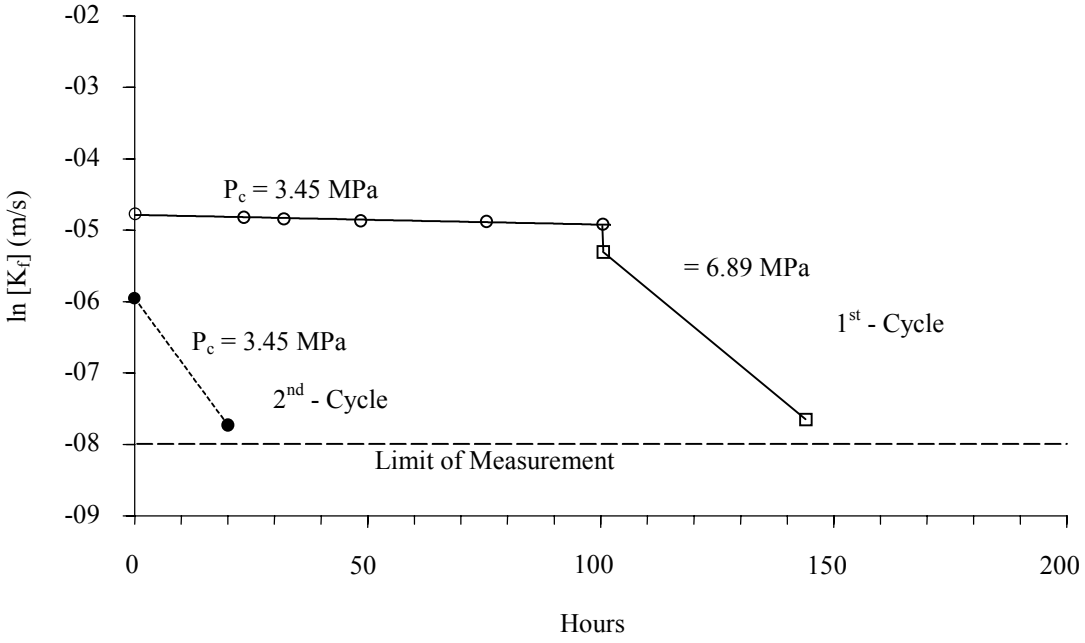

Figure 4.33 Hydraulic conductivity (K_f) of the specimen with polished surface as a function of time under multi-step confining pressure. Two loading cycles are presented for specimen no. HGT06.

limit of measurement (10^{-8} m/s). This suggests that a plastic closure of the fracture has occurred. The fracture has undergone a permanent deformation.

Three specimens with tension-induced fracture are tested under multi-step loading. The pressures are progressively increased from 3.45, 6.89, 10.34 to 13.78 MPa. The calculation of hydraulic conductivity from gas flow test result on specimen no HGT07 is tabulated in Table 4.10. The reduction of fracture permeability with increasing time and pressurization tends to be greater than that of the polished fracture. The fracture permeability obtained from the second pressure cycle is notably lower than that of the first cycle, suggesting a significant closure of the fracture (Figures 4.34 through 4.36). The closure is also plastic (permanent) and time-dependent.

For the single-step loading, five specimens subject to confining pressure of 0.69, 3.45, 6.98, 13.78 and 20.67 MPa. This test series is aimed at determining the rate change of the fracture permeability with time. A power equation is used to fit the experimental results for each pressure level: $K_f = K_o (t)^{-\beta}$, where K_o represents the fracture hydraulic conductivity at time equal to 1, and β is the time coefficient (Figure 4.37). The time coefficient β increases exponentially with the applied pressure (P_c): $\beta = 0.104 \bullet \exp(0.14\ P_c)$ as shown in Figure 4.38. This suggests that the reduction rate of fracture hydraulic conductivity is higher when the fracture subjects to a greater pressure.

It is visually observed that healing has occurred on all fractures after 120 hours of confining pressurization. Figure 4.39 shows a salt specimen with tension-induced fracture before and after healing. The Brazilian tensile strengths of each specimen conducted before and after healing are compared to assess the healing effectiveness (H_e) of the fracture. Here H_e represents the percentage ratio of the

Table 4.10 Summary of the gas flow test on specimen formed by tension-induced fracture no. HPT07.

(1)	(2)	(3)	(4)	(5)	(6)	(7)	(8)	(9)		(10)	
Test Duration (Hours)	**Confining Pressure, P_C (psi)**	**In Flow Pressure, P_i (psi)**	**Flow Time (sec)**	**Flow Volumes, V (cm^3)**	**Temperature (°C)**	**Flow Rate, Q (ft^3/sec)**	**Change in hydraulic head ΔH (ft)**	**Aperture, e**		**Hydraulic Conductivity, K_f**	
								($x10^{-6}$ft)	**($x10^{-6}$m)**	**($x10^{-6}$ft/s)**	**($x10^{-6}$m/s)**
0	500	0.18	49.97	10	27.5	7.06	350.74	128.12	39.05	262.58	80.04
7	500	0.68	19.11	10	28	18.47	1325.03	113.34	34.55	205.47	62.63
25	500	0.86	15.24	10	30.5	23.15	1675.78	113.01	34.45	204.30	62.27
54.5	500	0.87	16.24	10	31.5	21.73	1695.26	110.22	33.59	194.32	59.23
71	500	0.88	15.98	10	28.5	22.08	1714.75	110.39	33.65	194.93	59.42
94	500	0.72	19.65	10	28.5	17.96	1402.98	110.17	33.58	194.15	59.18
94	1000	1.42	12.87	10	28.5	27.42	2766.98	101.16	30.83	163.69	49.89
97	1000	1.05	18.55	10	29	19.02	2046.01	99.03	30.19	156.88	47.82
102	1000	1.06	20.05	10	29	17.60	2065.49	96.20	29.32	148.02	45.12
118	1000	1.06	22.29	10	28.5	15.83	2065.49	92.86	28.30	137.93	42.04
142.5	1000	1.07	24.79	10	28.5	14.24	2084.98	89.35	27.23	127.70	38.92
167	1000	1.08	28.02	10	27.5	12.60	2104.47	85.51	26.06	116.96	35.65
191	1000	1.07	28.72	10	29	12.29	2084.98	85.07	25.93	115.76	35.28
216.5	1000	1.06	30.83	10	28.5	11.45	2065.49	83.34	25.40	111.11	33.87
216.5	1500	2.05	19.26	10	28	18.32	3994.59	78.25	23.85	97.95	29.85
224	1500	2.05	32.74	10	30	10.78	3994.59	65.57	19.99	68.77	20.96
237	1500	2.05	34.36	10	28	10.27	3994.59	64.52	19.67	66.59	20.30
263.5	1500	2.06	41.57	10	27	8.49	4014.07	60.45	18.43	58.46	17.82
286	1500	3.66	23.14	10	26.5	15.25	7131.80	60.67	18.49	58.88	17.95
310	1500	3.56	26.63	10	26.5	13.25	6936.94	58.44	17.81	54.63	16.65

Table 4.10 (Cont.)

(1)	(2)	(3)	(4)	(5)	(6)	(7)	(8)	(9)		(10)	
Test Duration (Hours)	**Confining Pressure, P_C (psi)**	**In Flow Pressure, P_i (psi)**	**Flow Time (sec)**	**Flow Volumes, V (cm^3)**	**Temperature (°C)**	**Flow Rate, Q (ft^3/sec)**	**Change in hydraulic head ΔH (ft)**	**Aperture, e**		**Hydraulic Conductivity, K_f**	
								($x10^{-6}$ft)	**($x10^{-6}$m)**	**($x10^{-6}$ft/s)**	**($x10^{-6}$m/s)**
335.5	1500	3.56	37.79	10	26.5	9.34	6936.94	52.00	15.85	43.26	13.18
360.5	1500	8.54	15.15	10	29	23.29	16640.87	52.68	16.06	44.40	13.53
360.5	2000	9.14	15.28	10	29	23.09	17810.01	51.35	15.65	42.18	12.86
366.5	2000	10.44	21.65	10	31	16.30	20343.17	43.74	13.33	30.61	9.33
382	2000	11.33	20.45	10	29	17.25	22077.40	43.38	13.22	30.10	9.18
408.5	2000	13.65	19.34	10	27.5	18.25	26598.11	41.54	12.66	27.60	8.41
432	2000	13.65	23.57	10	27	14.97	26598.11	38.89	11.85	24.19	7.37
454	2000	13.64	25.63	10	27	13.77	26578.62	37.83	11.53	22.89	6.98
480	2000	16.96	21.06	10	27	16.76	33047.90	37.55	11.45	22.56	6.88
504	2000	23	19.86	10	27.5	17.77	44817.32	34.60	10.55	19.15	5.84
504	500	20	14.30	10	27.5	24.68	38971.58	40.44	12.33	26.16	7.97
528	500	20	18.40	10	27.5	19.18	38971.58	37.18	11.33	22.12	6.74
551	500	20	18.70	10	26.5	18.87	38971.58	36.98	11.27	21.88	6.67
575	500	20	19.27	10	27	18.31	38971.58	36.61	11.16	21.44	6.54
600	500	20	20.10	10	27	17.56	38971.58	36.10	11.00	20.85	6.36
605	500	20	21.18	10	29	16.66	38971.58	35.48	10.81	20.14	6.14
605	1000	20	17.40	10	29	20.28	38971.58	37.88	11.55	22.95	7.00
623	1000	19.99	26.14	10	27	13.50	38952.10	33.08	10.08	17.51	5.34
647.5	1000	20	27.67	10	26.5	12.75	38971.58	32.45	9.89	16.85	5.14
670	1000	20	29.74	10	26.5	11.87	38971.58	31.68	9.66	16.06	4.89

Table 4.10 (Cont.)

(1)	(2)	(3)	(4)	(5)	(6)	(7)	(8)	(9)		(10)	
Test Duration (Hours)	**Confining Pressure, P_C (psi)**	**In Flow Pressure, P_i (psi)**	**Flow Time (sec)**	**Flow Volumes, V (cm^3)**	**Temperature (°C)**	**Flow Rate, Q (ft^3/sec)**	**Change in hydraulic head ΔH (ft)**	**Aperture, e**		**Hydraulic Conductivity, K_f**	
								($\times 10^{-6}$ft)	**($\times 10^{-6}$m)**	**($\times 10^{-6}$ft/s)**	**($\times 10^{-6}$m/s)**
696.5	1000	20	33.84	10	29.5	10.43	38971.58	30.35	9.25	14.73	4.49
696.5	1500	10	35.33	10	29.5	9.99	19485.79	37.69	11.49	22.72	6.93
719	1500	20	45.31	10	29	7.79	38971.58	27.54	8.39	12.13	3.70
744.5	1500	20	55.01	10	27	6.41	38971.58	25.81	7.87	10.66	3.25
768.5	1500	20	85.00	10	27	4.15	38971.58	22.33	6.80	7.97	2.43
790.5	1500	19	161.90	10	27.0	2.18	37023.00	18.32	5.58	5.37	1.64
790.5	2000	40	485.10	10	27.8	0.73	77943.17	9.92	3.02	1.57	0.48
820	2000	58.47	157.00	2	28	0.45	113933.42	7.44	2.27	0.89	0.27
839	2000	50.02	48.70	0.2	26.0	0.14	97467.93	5.38	1.64	0.46	0.14
864	2000	50.01	18.50	0.05	28	0.10	97448.44	4.68	1.43	0.35	0.11
888	2000	50	18.50	0.05	28	0.10	97428.96	4.68	1.43	0.35	0.11
912	2000	58.61	560.00	0.1	28.5	0.01	114206.22	1.79	0.55	0.05	0.02

Remarks:

Diameter (W) = 38.3 mm, Length (L) = 64 mm, $\gamma = 0.0739$ lb/ft^3,

$\mu = 3.85 \times 10^{-7}$ lb-sec/ft^2

$(7) = \{(5) \times 0.3048^3\} \div (4)$

$(8) = \{(3) \times 144\} \div \gamma$

$(9) = [(7) \div \{(8)*C\}]^{1/3}$, $C = (W/L) \,.\, (\gamma/12\mu)$

$(10) = (\gamma/12\mu) \times (9)^2$

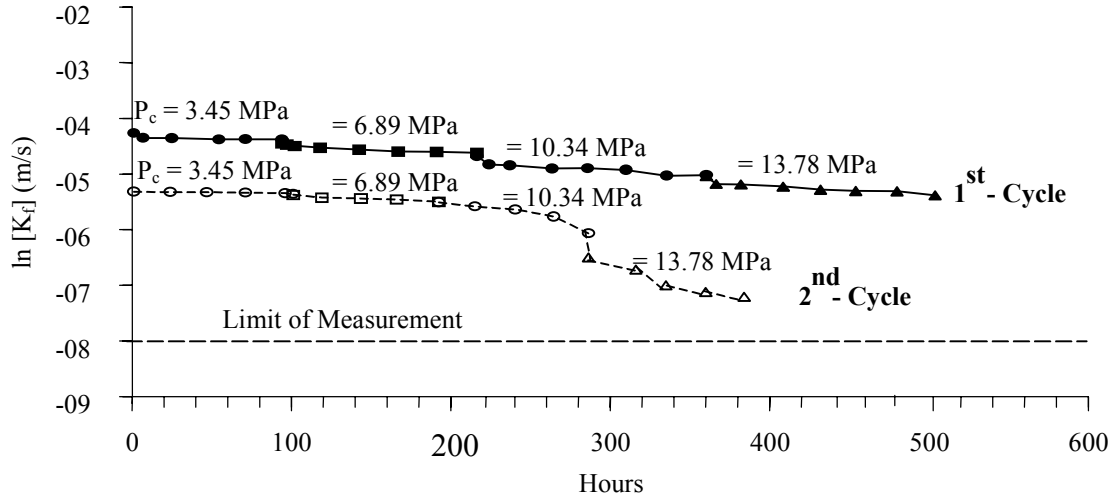

Figure 4.34 Hydraulic conductivity (K_f) of the specimen with tension-induced fracture as a function of time under multi-step confining pressure. Two loading cycles are presented for specimens no. HGT07.

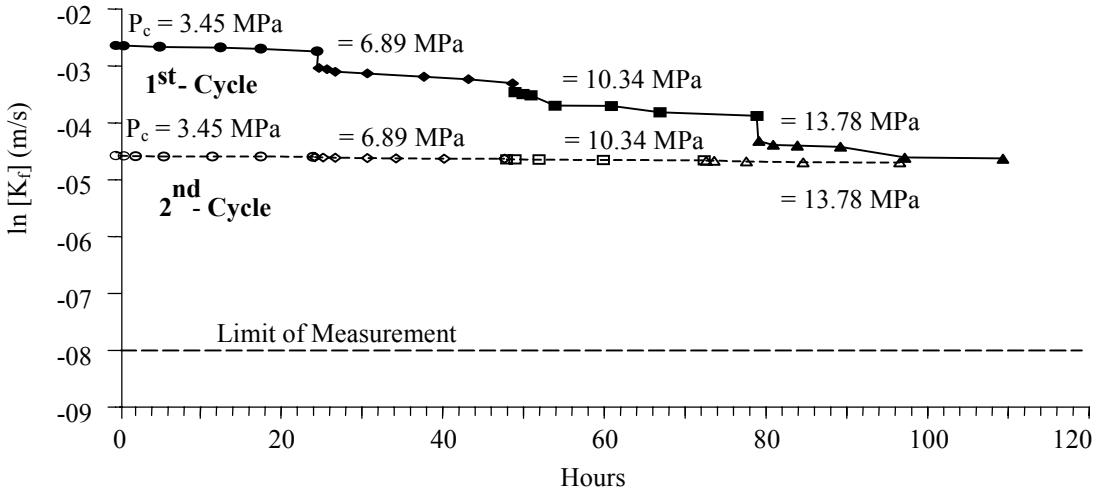

Figure 4.35 Hydraulic conductivity (K_f) of the specimen with tension-induced fracture as a function of time under multi-step confining pressure. Two loading cycles are presented for specimens no. HGT08.

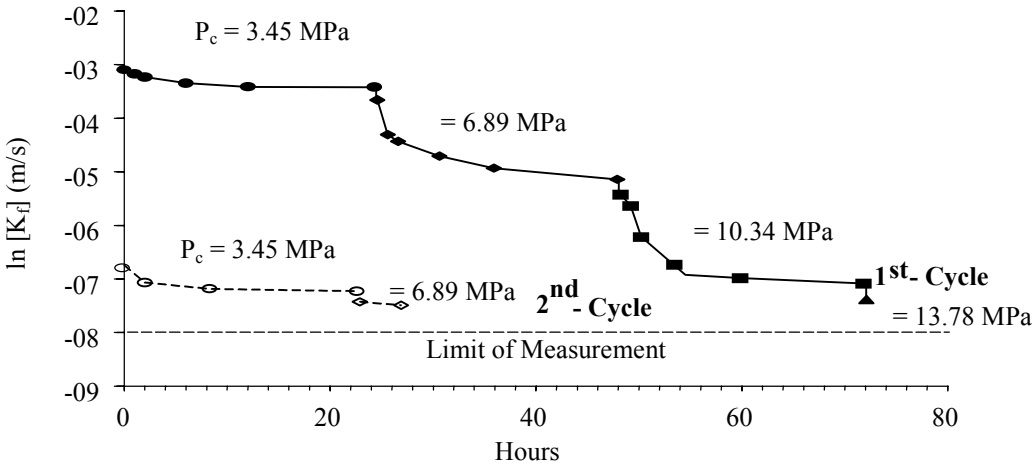

Figure 4.36 Hydraulic conductivity (K_f) of the specimen with tension-induced fracture as a function of time under multi-step confining pressure. Two loading cycles are presented for specimens no. HGT09.

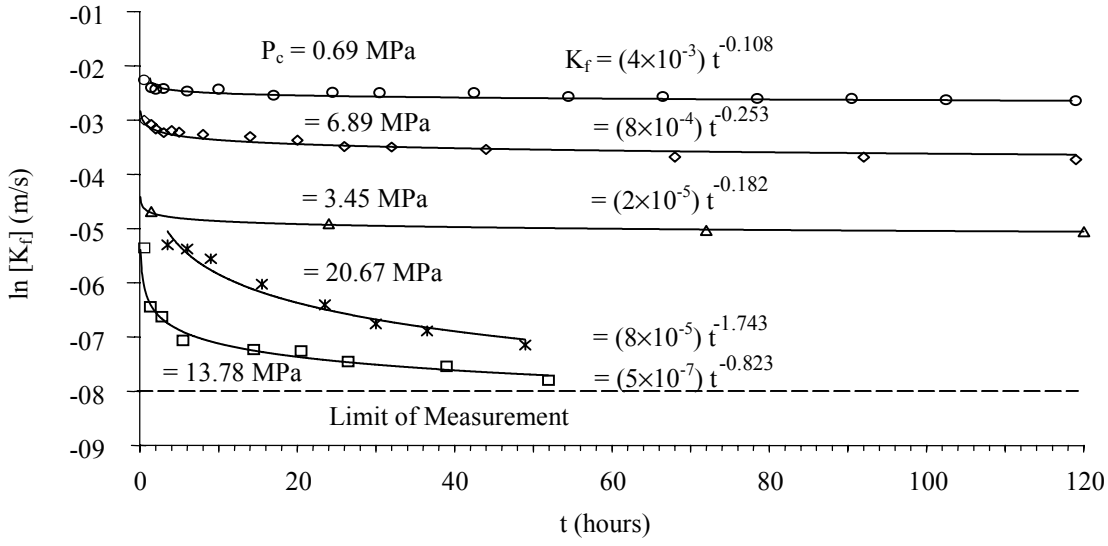

Figure 4.37 Hydraulic conductivity (K_f) of the specimens with tension-induced fractures as a function of time under single-step confining pressure. Five specimens are tested with different confining pressures (P_c).

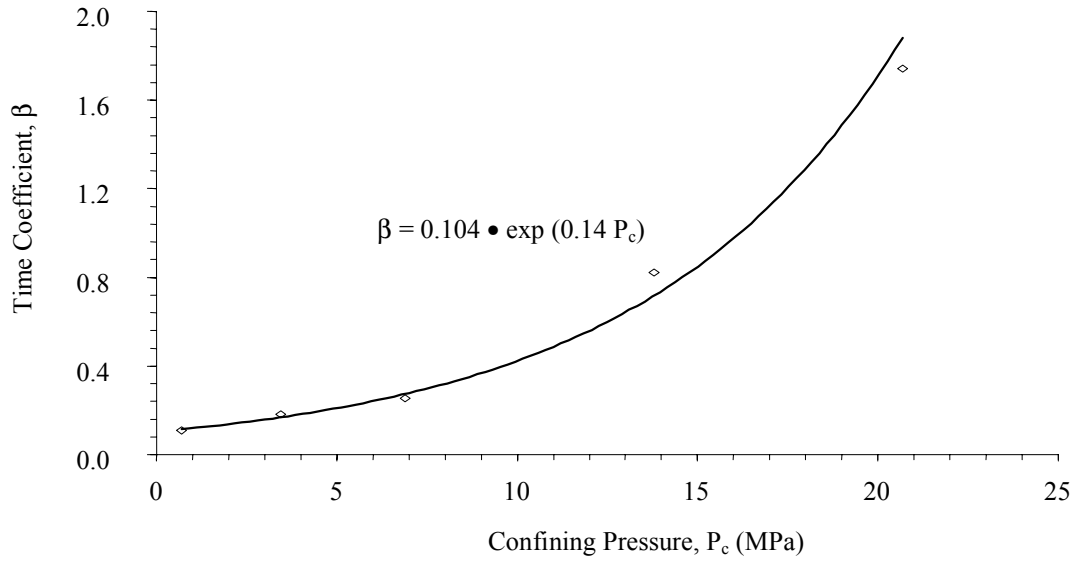

Figure 4.38 Variation of time coefficient (β) with the confining pressure (P_c).

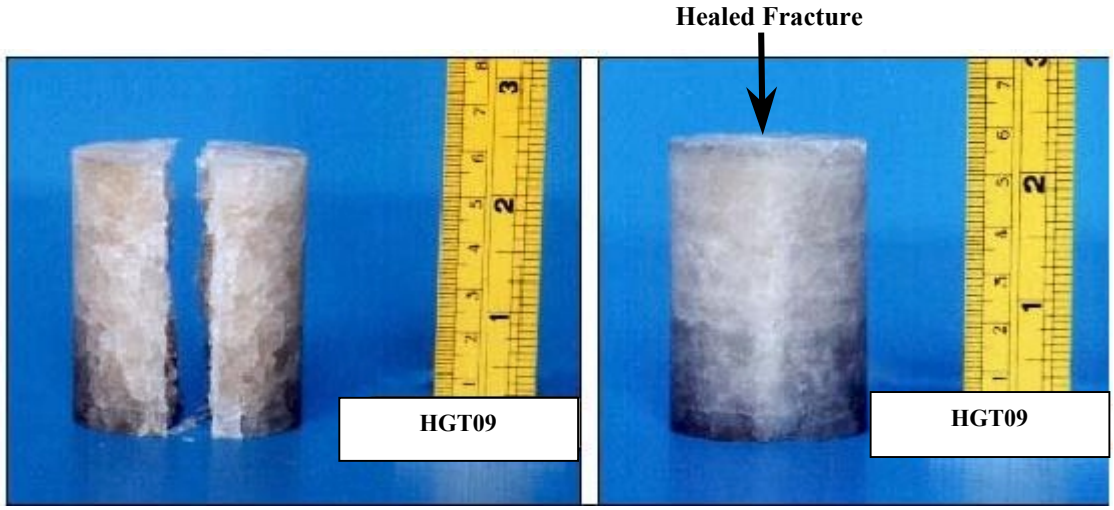

Figure 4.39 The specimen with tension-induced fractures is prepared by diameter loading, before healing (a), and after healing (b).

fracture tensile strength (σ_H) to the intact tensile strength (σ_B) of the same salt specimen. The tensile failure occurs along the same plane that was induced before and after healing. Tables 4.11 and 4.12 summarize the results of the healing assessment test. They suggest that the polished fractures can not be effectively healed even under the confining pressure of 6.89 MPa for 120 hours. Healing however can be clearly observed for the tension-induced fractures. Figure 4.40 shows the increase of H_e as the confining pressure (P_c) increases for the single-step loading on the tension-induced fractures.

4.3.3 Discussions and Conclusions

Fracture healing under confining pressure has an advantage over that under uniaxial loading, in term of the maximum applied pressures. The applied load is limited by the compressive strength of the salt. The maximum axial stress used here is therefore limited to 7.8 MPa or about 30% of the strength. This is primarily to prevent the initiation of micro-cracks or fractures in the intact salt. For the confining pressure, the specimen can subject to the pressure as high as 20 MPa. The results suggest that both applied pressure and time are important factors for fracture healing.

The healing effectiveness of salt fractures depends heavily on the origin of the fractures. If a fracture is formed by the separation or splitting of salt crystals, it can be easily healed even under relatively low stress for a short period. The splitting failure of salt crystals occurs by a separation of cleavage planes. This means that healing is effective if the salt crystals on both sides of the cleavage plane return to their original position. For the fractures formed by separation of inter-crystalline boundaries or by crystals with different orientations on the opposite sides, healing will not be easily achieved. In particular, if the fracture surface is coated with any

Table 4.11 The Brazilian tension test results for dry salt specimens with tension-induced fractures and polished surfaces after healing under single-step confining pressure for 120 hours.

Specimen No.	Type of Fracture	Confining Pressure (MPa)	Brazilian Tensile Strength		Healing Effectiveness $H_e = (\sigma_H/\sigma_B)\times100$ (%)
			Intact Salt, σ_B (MPa)	Salt with Healed Fracture, σ_H (MPa)	
HGT01	Tension-induced fracture	0.69	2.24	0.04	2
HGT02		3.45	2.23	0.37	17
HGT03		6.89	2.24	0.36	16
HGT04		13.78	2.47	1.04	42
HGT05		20.67	1.96	0.82	42

Table 4.12 The Brazilian tension test results of dry salt specimens with tension-induced fractures and polished surfaces after healing under multi-step confining pressure for 120 hours.

Specimen No.	Type of Fracture	Confining Pressure (MPa)	Test Duration	Brazilian Tensile Strength		Healing Effectiveness H_e^* (%)
				Intact Salt, σ_B (MPa)	Salt with Healed Fracture, σ_H (MPa)	
HGT06	Polished surface	3.45 → 6.89	100 hrs/step	1.68	0.06	4
HGT07	Tension-induced fracture	3.45 → 6.89 →10.34 → 13.78	96 hrs/step	1.30	1.24	94
HGT08			24 hrs/step	2.50	1.97	79
HGT09				2.23	1.17	53

$H_e = (\sigma_H/\sigma_B)\times100$

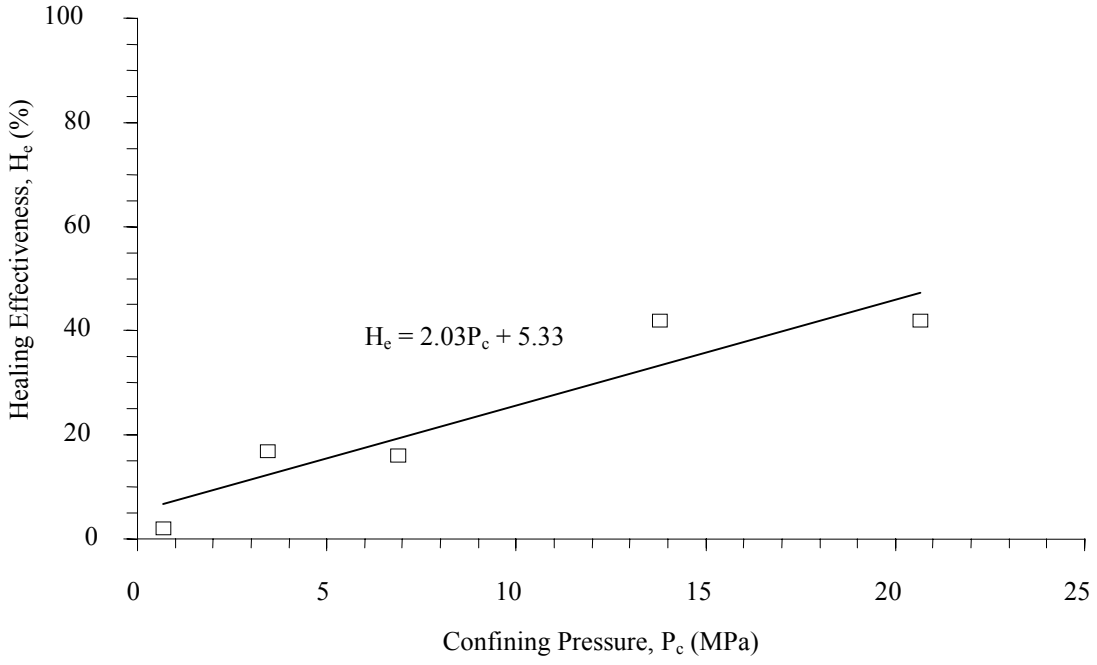

Figure 4.40 Healing effectiveness (H_e) as a function of confining pressure (P_c) for specimens with tension-induced fracture after healed for 120 hours.

inclusions, healing ability are poor. This explains why the saw-cut fractures and polished fractures can not be effectively healed under the test conditions used here. It can be postulated here that healing of fracture can be enhanced by the purity of the halite crystals on the opposite sides of the fracture. This is supported by the fact that the cleavage planes inside the salt crystal are more pure than the inter-crystalline boundaries, and more than the saw-cut and polished surfaces. These artificial surfaces could be contaminated during the preparation process. An oil film and other inclusion may be cover the artificial surfaces. This inclusions protect the chemical bonding between contact surface to heal the fracture. To heal a saw-cut or polished salt fracture, a much higher confinement and temperature than those used here may be required.

It is not clear from the experimental results that fractures under saturated brine can be healed more effective than those under dry condition. This is because the two test conditions are used on the saw-cut fractures and with a relatively low axial stress. For the saturated testing, it is found that re-crystallization of brine between the fractures has occurred in form of small salt crystals. Such process however can not hold the fractures together. The specimens can be easily pulled apart by hands.

The hydraulic conductivity for all salt fractures decreases with increasing applied confining pressure and time. This implies that the fracture healing is accompanied by the fracture closure. Both processes are time-dependent. The closure involves the visco-plastic deformation for the salt on both sides of the fracture. The healing involves a chemical process. It is permanent - remains even after the load is removed. Owing to the surface smoothness, the polished fractures show a lower

permeability than do the tension-induced fractures. This however does not necessarily mean that the polished fractures heal more effective than do the tension-induced fractures. A reduction of fracture permeability does not necessarily mean that the healing has occurred. This is evidenced by that even the polished fracture has been compressed until its hydraulic conductivity becomes lower than 10^{-8} m/s, no healing has taken place in the fracture.

Since all fractures tested here are well mated, the impact of fracture roughness can not be truly assessed. More testing is needed to confirm any mathematical relationship between the healing effectiveness and the inclusions. For the healing assessment method, a direct tension test could be used to minimize the impact of the stress gradient induced along the fracture plane. From the results obtained here, it can be postulated that under preferable conditions (stress state, time, temperature, purity, crystal orientation, etc.), a complete healing of salt fractures is possible.

CHAPTER V

COMPUTER MODEL ANALYSIS

5.1 Objective

The analysis by employing computer model in this research aims at studying of the behavior and mechanical stability of rock salt cavern with various geometries for CAES technology. The analysis emphasizes on the cavern convergence and plastic zone boundary around the rock salt cavern. Plastic zone is a boundary that rock salt property changes from elasticity to plasticity as a result of the difference between internal pressure and in-situ stress in the salt layer. The internal pressure is lower than the stress in the rock salt layer around the cavern. Results from this analysis will be further used in the evaluation of fracture in connection with the direction of stress acted on the fracture. This will indicate any possibility of leakage around the CAES cavern. In this chapter, studying of plastic zone distribution at different levels with internal pressure between 20 to 90% of the stress in salt layer at the cavern roof will be described.

To determine zone of plasticity around the cavern, the calculation assumes that the cavern has been used for storage air for 20 years and comparison is made among 5 geometries of cavern shape; a spherical shaped cavern and 4 elliptical shaped caverns with ratio of minor-to-major axis of 1:1.5, 1:2, 1:2.5, and 1:3. The calculation uses GEO program that is a finite element software (Serata and Fuenkajorn, 1991, 1992a, 1992b; Stormont and Fuenkajorn, 1994; Fuenkajorn and Serata, 1994). Suitable

geometry of cavern shape in rock salt will be determine from this analysis. Besides that the maximum and minimum internal pressures for the stability during operation will be determined as well.

5.2 Mesh Model

In the modeling of the solution cavern in salt, two-dimensional finite element mesh is created in x-y axis. The third dimensional with z-axis is omitted because this analysis is a plane strain analysis by assuming strain in z-axis to be zero. For the best efficiency, finite element mesh is created in one of the four parts in a symmetrical axis. The cavern cross section is modeled and the external pressure (P_o) is given to be a hydrostatic pressure with 4 levels of depth; that are 1500, 2000, 2500, and 3000 psi or at depth of approximately 1500, 2000, 2500 and 3000 feet, respectively. At each depth or stress level, the finite element mesh is the same, only external and internal stresses are changed. The mesh size is created to be small around the cavern wall because this zone, the stress and strain gradients are high. The mesh far from the cavern wall is bigger in size because of the low stress and strain gradients at this zone. Five geometries of cavern have been studied; spherical shape (Model SP10) and 4 elliptical shapes (Models EL15, EL20, EL25 and EL30).

Figure 5.1 illustrates the model SP10 that is created from a quarter of spherical shaped cavern cross section with a diameter of 50 m. Distance from the right and upper boundary to center are 500 m or equals 20 times of the cavern radius. The stress acted on the top and the right sides are equal. Internal pressure (P_i) varies from 20 to 90% of external pressure (P_o). The upper and the right boundaries are allowed to freely displace in both on x-axis and y-axis. The left boundary which is a symmetric

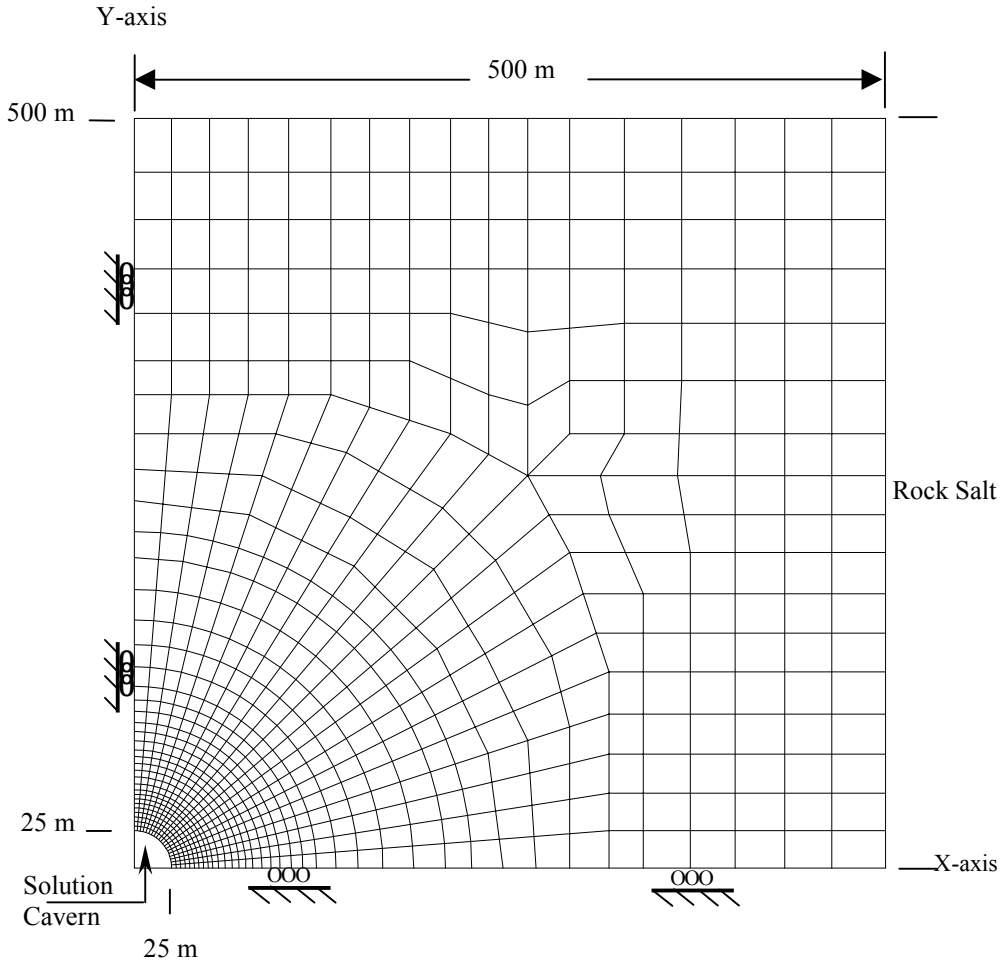

Figure 5.1 Finite element mesh for Model SP10, spherical shape with a diameter of 50 m.

axis separates the cavern into two parts, and y-axis is fixed to move only in y-direction but not in x-direction. The lower boundary is another symmetrical axis that separates the cavern in to two parts, and the x-axis is fixed in y-direction. In order to clearly illustrate the boundary of the cavern in finite element mesh, elements in the cavern are not shown in the figure. The finite element mesh consists of 818 elements and 875 nodes with the smallest size around the wall of 3×2 m^2.

Figures 5.2 to 5.5 illustrate Model EL15, EL20, EL25 and EL30, respectively. Four models are created from a quarter of cross section divided by the major x-axis and minor y-axis in a plane of elliptical shaped cavern. The minor axes in the 4 models are equal with 25 m long but the major axes are different as summarized in Table 5.1. Each mesh consists of elements and nodes. Around the cavern walls, the mesh will be smallest in size. The smallest size for the Model EL15, EL20, EL25 and EL30 are 1.5×2.5 m^2, 2.7×1.4 m^2, 1.4×2.9 m^2, 1.3×3.0 m^2, respectively. The characteristics of the models in terms of mesh, method of analysis, and boundary conditions are similar to Model SP10.

One assumption used in this study is that the CAES cavern is a single cavern which locates far away from any other underground structures, at least 20 times of its radius. This is to prevent the mechanical effect that may cause from the adjacent structure. The computer analysis will reveal if the specified distance is sufficient or not.

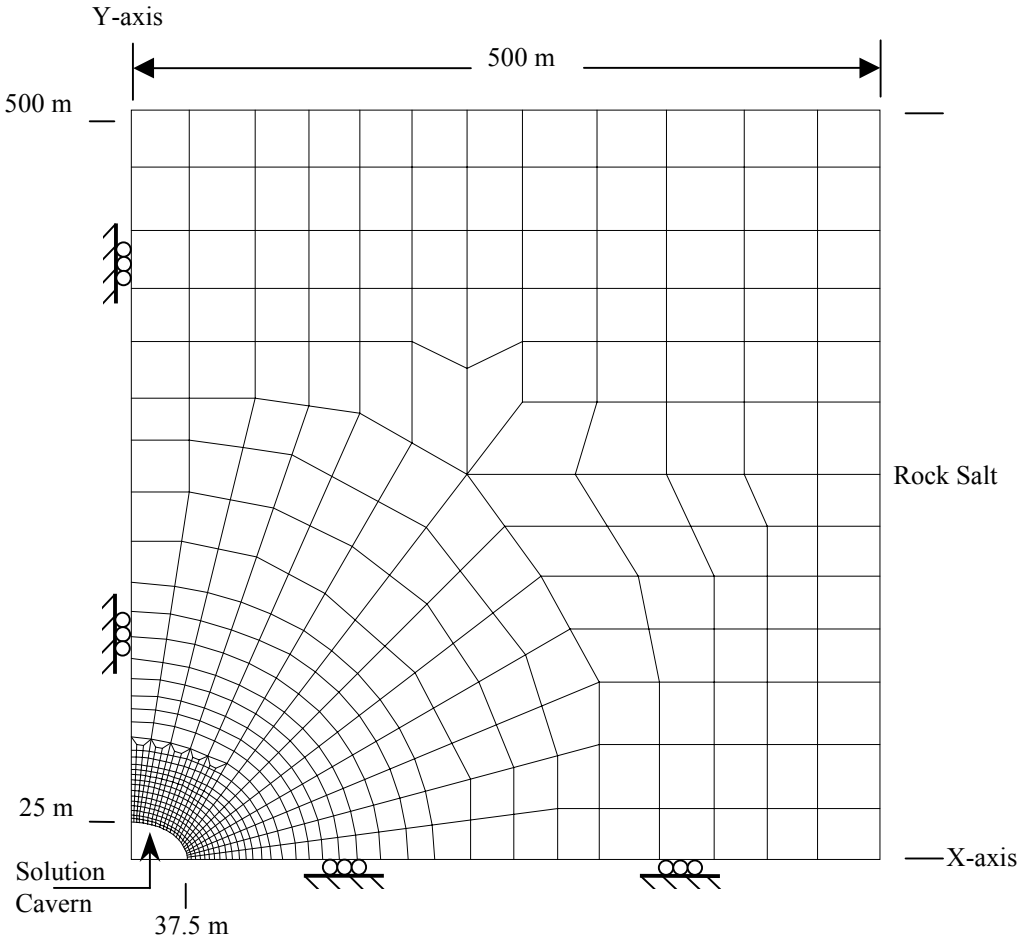

Figure 5.2 Finite element mesh for Model EL15, elliptical shape with major axis = 37.5 m and minor axis = 25 m.

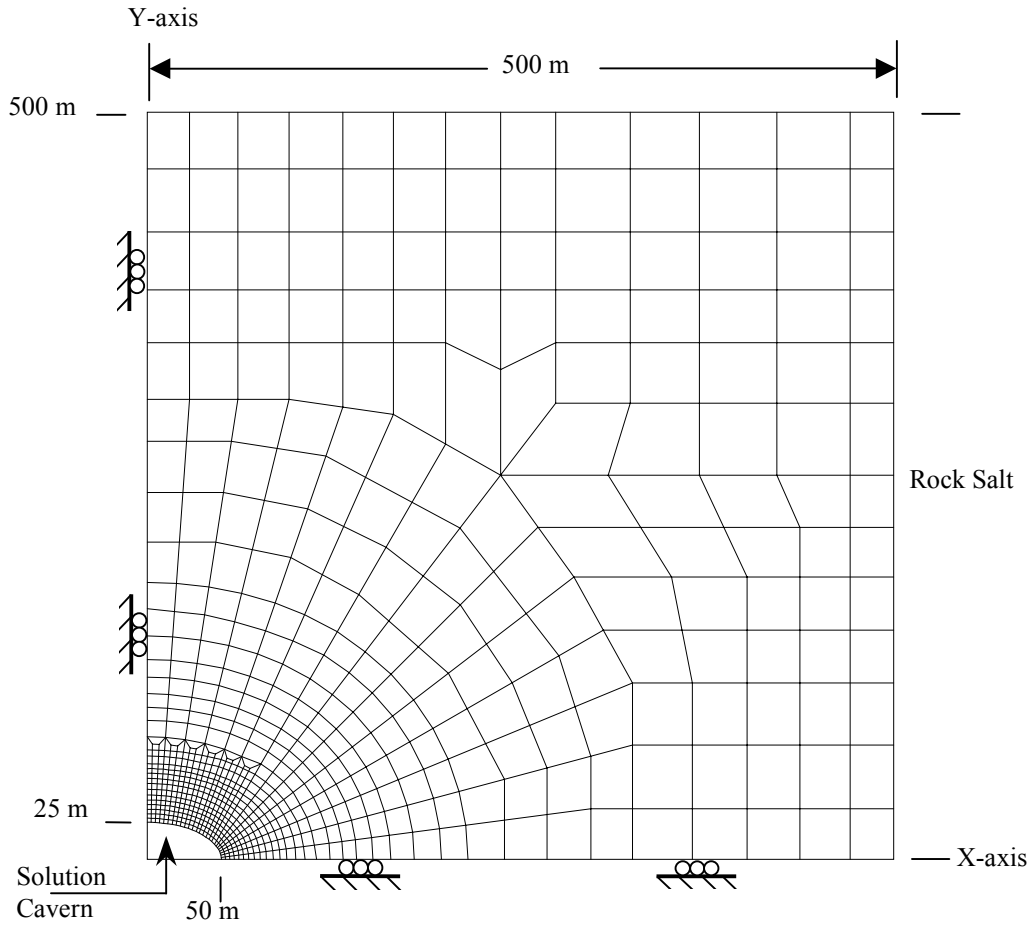

Figure 5.3 Finite element mesh for Model EL15, elliptical shape with major axis = 50 m and minor axis = 25 m.

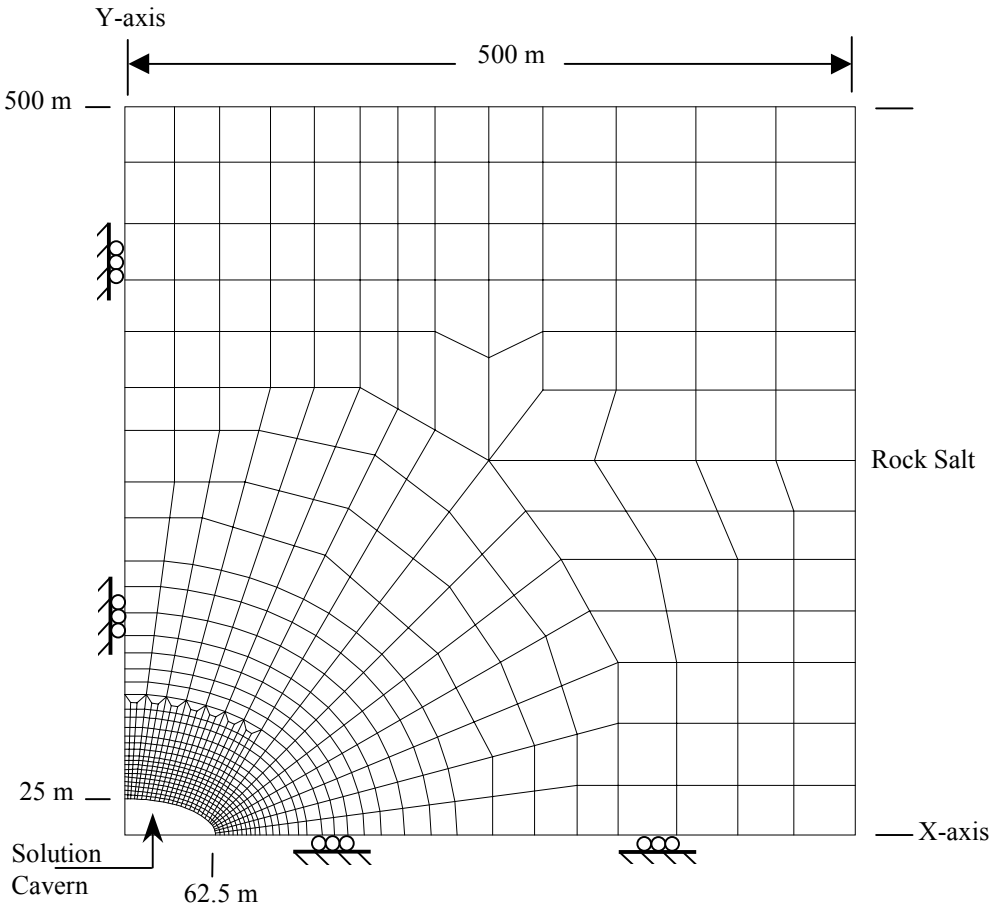

Figure 5.4 Finite element mesh for Model EL15, elliptical shape with major axis = 62.5 m and minor axis = 25 m.

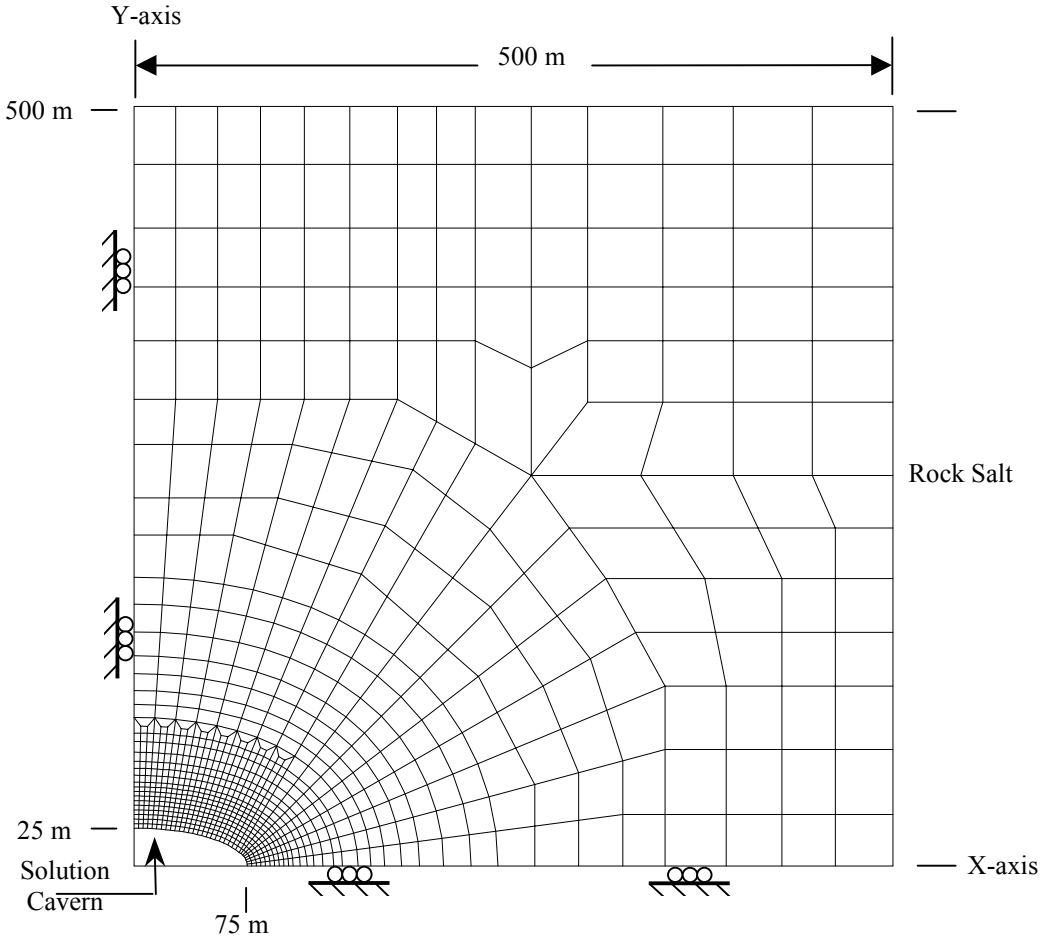

Figure 5.5 Finite element mesh for Model EL15, elliptical shape with major axis = 75 m and minor axis = 25 m.

Table 5.1 Shape and size of salt cavern in horizontal plane used in the modeling.

Model	**Shape**	**X- axis, X_c (m)**	**Y-axis, Y_c (m)**	**$Y_c : X_c$**	**Number of Elements**	**Number of Nodes**
SP10	sphere	25	25	1:1	818	875
EL15	ellipse	37.5	25	1:1.5	648	703
EL20	ellipse	50	25	1:2	717	774
EL25	ellipse	62.5	25	1:2.5	816	875
EL30	ellipse	75	25	1:3	890	951

5.3 Salt Properties for Computer Modeling

Before performing the computer analysis, physical and mechanical properties of rock salt are specified in order to use as constant values in the calculation. The GEO software is employed for this research. The GEO mechanical behavior consists of spring, dashpot and friction element and so-called GEO rheological components as illustrated in Figure 5.6. The major and significant constant values in the models are shear modulus (G_1), retarded shear modulus (G_2), elastoviscosity (V_2), plastoviscosity (V_4), ultimate bulk modulus (K_1), retard bulk modulus (K_2) and critical strain of failure (γ_c).

The coefficient of rock salt properties have been derived from calibrating of result of the rock salt testing by Wetchasat (2002) who conducts various test methods; short-term creep test, long-term creep test, uniaxial compressive strength test and cyclic loading test. Wetchasat (2002) performs the tests on rock salt from the same source with this research. The properties are tabulated in Table 5.2

5.4 Computer Modeling Results

Results of computer modeling are shown in Appendix A. The results show comparison between the cavern closure and plastic zone boundary that caused by different internal pressures, depths and shapes of cavern.

5.4.1 The Effects of Internal Pressure

The comparison of cavern closure affected by internal pressure reveals that the closure is lower for the cavern with higher internal pressure. The cavern closure at 20% of the in-situ stress is higher than the closure at 30%, 40%, 50%, 60%, 70%, 80%, and 90%.

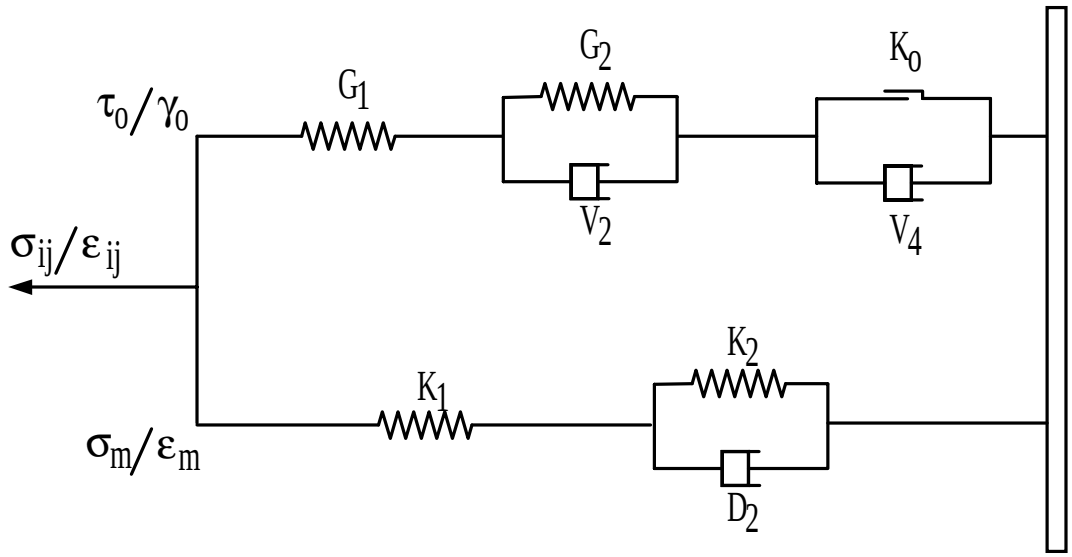

Figure 5.6 GEO rheological components (modified from Serata and Fuenkajorn, 1993)

Table 5.2 Properties of rock salt used in the computer modeling (from Wetchasat, 2002).

Properties	Symbols	Units	Ranges	Used
Shear Modulus	G_1	GPa	8.7 – 9.0	8.8
Retarded Shear Modulus ($\tau_0<K_0$)	G_2	GPa	0.2 – 2.1	1.1
Elastoviscosity ($\tau_0<K_0$)	V_2	GPa·day	0.1 – 17.0	9.1
Plastoviscosity	V_4	GPa·day	6.9 – 27.6	17.2
Ultimate Bulk Modulus	K_1	GPa	40.6 – 42.0	41.1
Retarded Bulk Modulus	K_2	GPa	0.9 – 9.8	4.9
Critical Strain of Failure	γ_c	10^{-3}	2	2
Pressure Gradient	P_{grad}	kPa/m	20.8	20.8

Figures A.1 through A.36 in Appendix A illustrate the comparison of cavern closures which do not exceed 5% of the cavern radius in each direction.

5.4.2 The Effects of Cavern Depth

From the comparison of the cavern closure in both x- and y-directions at 20 years after construction, it is found that the cavern closure increases as the depth increases. Figures A.37 to A.44 show the comparison of the cavern closure at the cavern walls for Model SP10, in x- and y-directions and at 4 different depths. Tendency of the cavern closure in x- and y-directions of the Model EL15 is the same, the closure is higher at the deeper location and lower at the shallower location. Figures A.45 to A.52 show comparison of the cavern closure of the Model EL15 in x-direction after 20 years of construction, at 4 different depths. The cavern walls in Model EL20, EL25 and EL30 show the same tendency of convergence as occurred in Model SP10 and EL15.

The comparison of plastic zone in the cavern at different depth reveals that the plastic behavior is small in the cavern at the shallow location. The plastic zone increases as the depth increases. Figure A.73 compares the plastic zones around the cavern for Model SP10 at 4 different levels.

5.4.3 The Effects of Cavern Shape

Figures A.1 to A.36 show the cavern closure occurred for various cavern shapes under the same stress condition and pressure. It is found that the cavern closure for Model SP10 (spherical shape) is smallest, and the cavern closure for Model EL30 is largest. Sequence of the cavern closure magnitude induced in each model from minimum to maximum is SP10, EL15, EL20, EL25 and EL30. The cavern closures in x- and y-directions for Model SP10 are the same. Whereas, for

elliptical shaped cavern, the closures in x-direction (major axis) is higher than those in y-direction (minor axis).

Results from this study show that the plastic zone for Model SP10 is smallest, and the plastic zone in Model EL30 is largest. The sequence of plastic zone extent around each model from the largest to the smallest is SP10, EL15, EL20, EL25 and EL30. The plastic zone for Model SP10 runs parallel to the cavern walls at every depth. Whereas for elliptical shaped cavern, the plastic zone is not parallel to the cavern walls and it is not symmetry as occurred in Model SP10. At a smaller differential internal pressure to external pressure (P_i/P_o) (between 20% - 30%) the plastic zone concentrates around the cavern walls in the major axis (x-axis), meanwhile at high P_i/P_o (ranging between 70% - 90%) the plastic zone concentrates around the minor axis (y-axis). At the lower internal pressure, the plastic zone distributes in both major and minor axis. Figures A.74 through A.81 illustrate the distribution of plastic zones for Model SP10, EL15, EL20, EL25 and EL30 under in-situ stress of 1,500 psi.

5.5 Analysis

In order to determine the suitable shape of cavern and pressure as well as the optimum mechanical stability, the analysis emphasizes on the magnitude of cavern closure and distribution of the zone where plasticity of the salt taking place around the cavern or the area where the critical strain (γ_c) exceeds 0.002 as specified by Wetchasat (2002). The study reveals that the shear stress magnitude is highest at the cavern walls, and the shear stress magnitude decreases as the distance from the cavern wall increases. Comparison between the maximum principal stresses (σ_1) and the

minimum principal stresses (σ_3) shows that the difference between the two stress levels is maximum at the cavern walls and decreases away from the wall. The difference between the maximum and minimum stresses affects the shear stress level, at high shear stress level, the plastic zone and cavern closure increase.

The magnitude of internal pressure and the depth of cavern also affect the behavior of rock salt around the cavern. The lower internal pressure induces the higher differential stress at the cavern walls and the larger cavern closure and plastic zone. The internal pressure varies with the cavern depth that the internal pressure is higher at the deeper seated cavern. Thus at deeper seated cavern, the difference between the major and minor principal stresses will be high and this will result in higher deformation and change in cavern shape and eventually causes larger cavern closure and larger distribution of plastic zone. The result confirms that the smaller cavern closure and plastic zone occur at the shallow seated cavern and under high internal pressure. The study of the cavern shaped effects reveals that the suitable shape in terms of smaller cavern closure and smaller plastic zone is the spherical shaped cavern (Model SP10).

CHAPTER VI

COMPUTER MODELING FOR CAES

6.1 Objective

The objective of computer modeling explained in this chapter is to study the behavior and mechanical stability of rock salt around the cavern for compressed air energy storage technology. The simulation results will be presented in forms of vertical and horizontal closures of cavern wall, surface subsidence, octahedral shear stress and octahedral shear strain, maximum and minimum shear stresses, maximum and minimum shear strain that affect the behavior and stability of the cavern at the period of 20 years after the construction and operation. The results from the calculation will be used to determine the optimum (minimum and maximum) pressures for CAES cavern. The non-linear finite element program, GEO (Serata and Fuenkajorn, 1991, 1992a, 1992b; Stormont and Fuenkajorn, 1994; Fuenkajorn and Serata, 1994) and the salt property parameters (from Wetchasat, 2002) are used in the computer modeling.

The study has been carried out in 3 stages: 1) to find the minimum suitable internal pressure, 2) to find the maximum suitable pressure, and 3) to study the effect of cyclic loading by the internal pressures derived from stages 1 and 2.

6.2 The Study Area

The sequences of rock salt in Thailand have been compiled by many investigators (Suwanapal, 1992; Japan International Cooperation Agency, 1981; Suwanich and Ratanajaruraks, 1982; Suwanich, et al., 1982, Yumuang, et al., 1986; Japakasetr and Suwanich, 1977). They are obtained from the borehole logging conducted as part of the potash exploration project in the northeast of Thailand. The locations of the 118 boreholes are shown in Figure 6.1 (Japakasetr, 1985). Wetchasat (2002) carried out the mechanical classification of the area from data of exploratory wells. The classification was based on thickness and depth of rock salt layers. The rock salt units were then classified into 5 corresponding areas as shown in Figure 6.2. The locations (village, district and province) are tabulated in Table 6.1. The rock salt strata existed in Thailand are relatively thin and shallow compared with the rock salt existed in the United States and Germany. Therefore, the specified areas of study are based on engineering geology that emphasizes thickness and depth of rock salt and nearby rock strata. After consideration of the thickness and depth of rock salt among 5 areas, the area of Ban Nong Pu, Borabue District, Maha Sarakham Province where the exploratory well no. K-089 located is chosen for modeling of CAES cavern. This area represents the thickest and deepest rock salt stratum.

6.3 The Properties of Rock Salt and Associated Rocks

Before starting to construct the model, the mechanical properties of rock salt and rocks in vicinity of the study area (exploratory well K-089) have been classified. Three groups of rocks had been re-classified according to their similarity in mechanical properties, including associated rocks, rock salt and sandstone/siltstone.

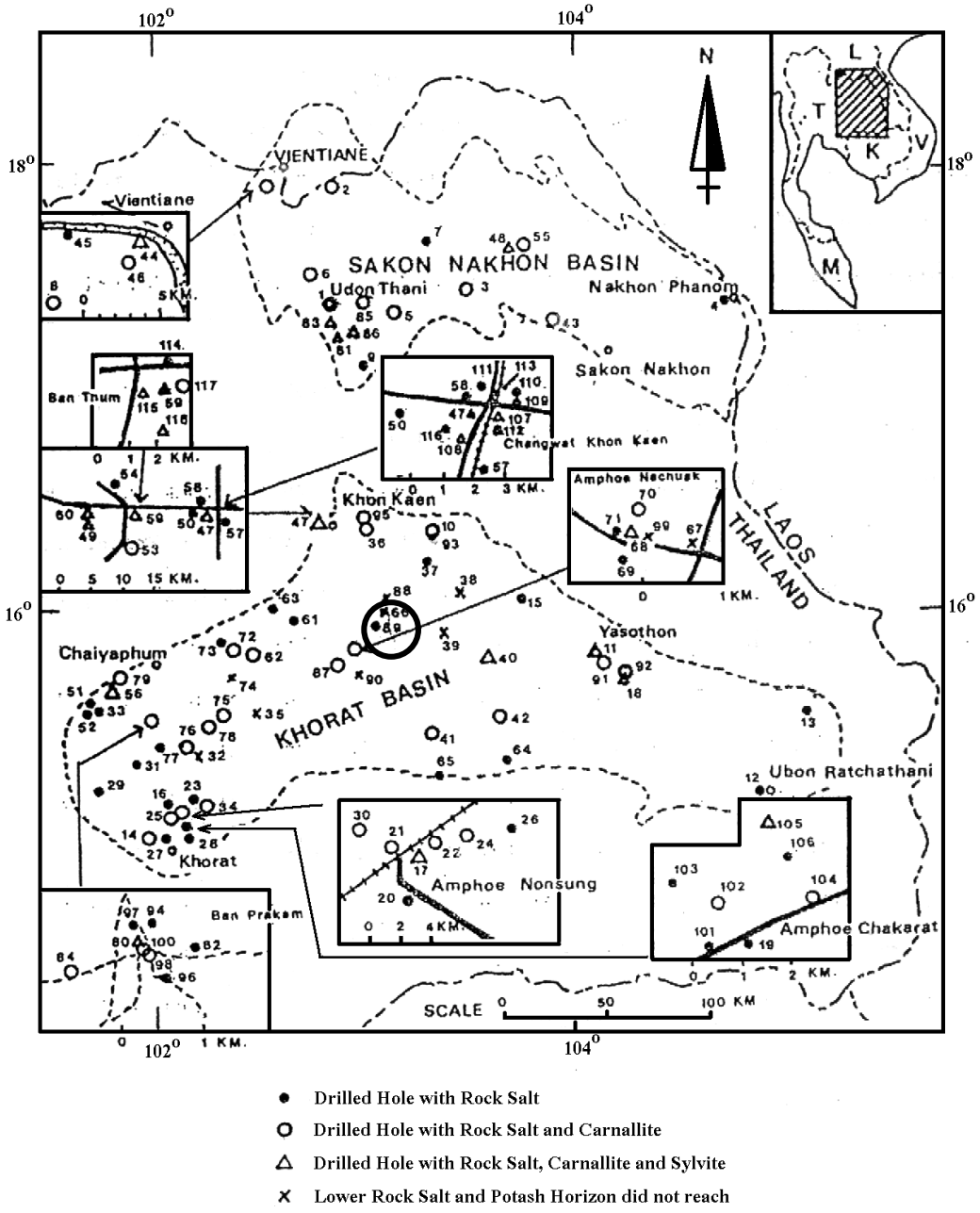

Figure 6.1 Locations of drilled holes for potash and rock salt exploration (Japakasetr, 1985). The study area is around borehole No. K-089.

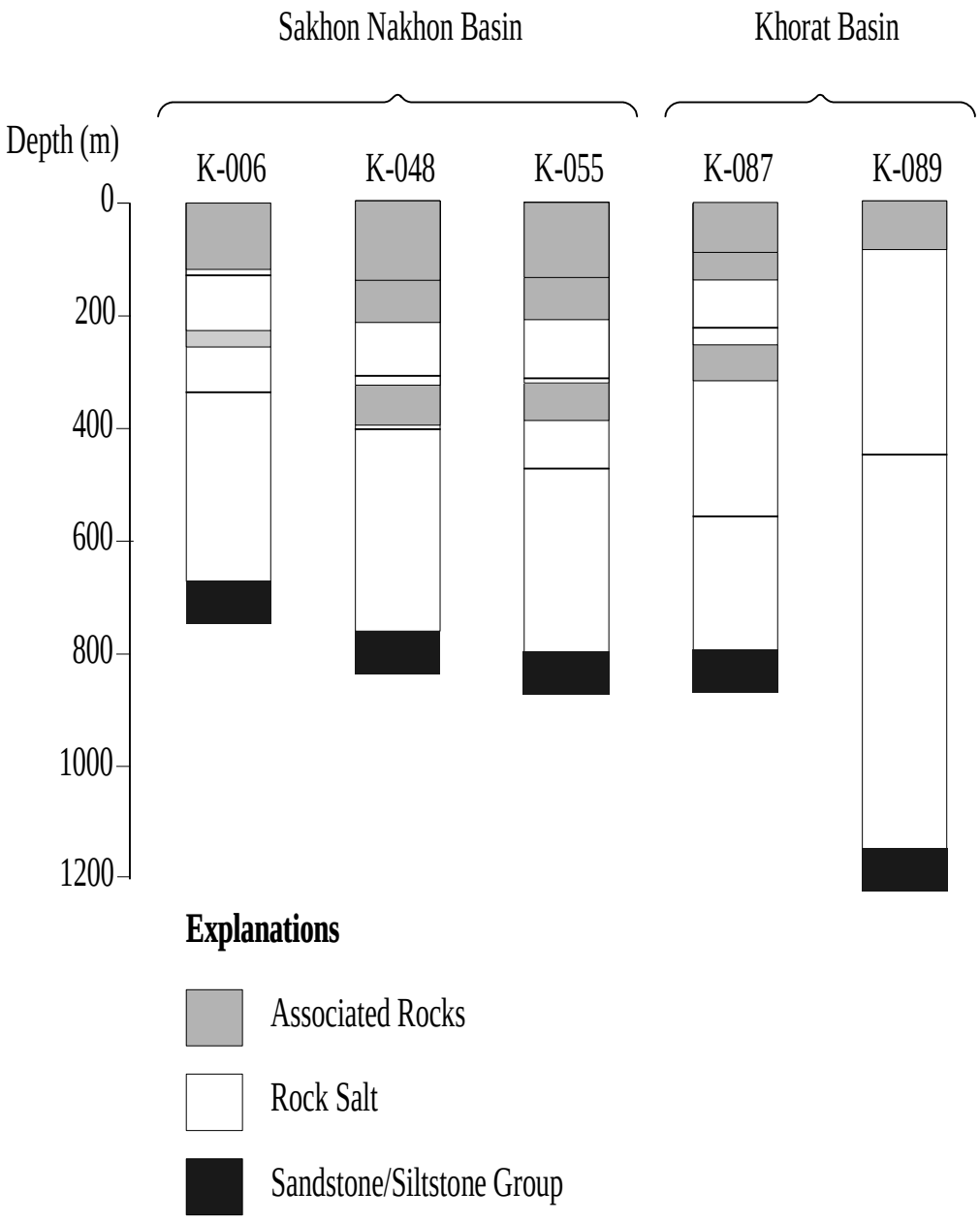

Figure 6.2 Simplified stratigraphy of salt and associated rocks in Sakon Nakhon and Khorat Basins, after reclassification into three geomechanic groups (Wetchasat, 2002).

Table 6.1 Example areas in Sakon Nakhon and Khorat Basins (Wetchasat, 2002).

Basins	Areas	Nearest Exploration
1. Sakon Nakhon	Ban Khao, Muang, Udon Thani	K-006
	Wat Nonwiake, Ban Srimuang, Wanorn Niwat, Sakon Nakhon	K-048
	Wat Umpawan, Ban Kudjig, Wanon Niwat, Sakon Nakhon	K-055
2. Khorat	Ban Po Phan, Na Chuak, Maha Sarakham	K-087
	Ban Nong Plue, Borabue, Maha Sarakham	K-089

The associated rocks include all geological formations between and above the salt formations (e.g., anhydrite, mudstone, clay, clay stone, siltstone, conglomerate, terrain sediment, alluvial deposits, etc.). The rock salt group represents the upper salt, middle salt, and lower salt beds. The sandstone/siltstone group represents all rock formations below the salt formations. The specified properties of those rocks are summarized in Table 6.2. The properties of rock salt used in the model are the same properties as explained in Chapter IV. Whereas the associated rocks properties are obtained from the database of GEO-software. The properties of these rocks do not change with time and they are rather constant, and do not directly affect the stability of the cavern. The mechanical properties selected from the database are the most conservative.

6.4 Mesh Construction

The computer model of solution cavern has been created in the 2-dimensional finite element mesh which has cross-section covering the surface to the sandstone and siltstone layer underlying the lower salt. The CAES cavern is modeled to have volume of 260,000 m^3 which is a normal size of cavern designed in other countries. Furthermore the cavern is designed for storage of air for electricity generating in the period of 20 years operation. The cylindrical cavern with half-spherical shape at the top and bottom is designed to have dimensions of 50 m-diameter and 150 m-height. The cavern roof is designed at 600 m deep from ground surface. Thus, the cavern situates at around the middle part of the rock salt layer.

The finite element mesh has its symmetrical axis at the middle part of the cavern. The study assumes that hydrostatic stresses acted on the vertical plane across

Table 6.2 Properties of rock salt and associated rocks used in the computer modeling (Wetchasat, 2002).

Properties	Symbols	Units	Associated Rocks	Rock Salt	Sandstone/ Siltstone
Shear Modulus	G_1	GPa	0.3	8.8	13.8
Retarded Shear Modulus	G_2	GPa	0.3	1.1	13.8
Elastoviscosity	V_2	GPa·day	0.3	9.1	3.4
Plastoviscosity	V_4	GPa·day	2.8	17.2	13.8
Ultimate Bulk Modulus	K_1	GPa	1.7	41.1	82.8
Retarded Bulk Modulus	K_2	GPa	1.4	4.9	82.8
Critical Strain of Failure	γ_c	10^{-3}	10	2	2
Pressure Gradient	P_{grad}	kPa/m	25	20.8	25

the cavern at the center. The finite element mesh consists of nodes and elements. The mesh size is created to be small around the cavern wall because the stress and strain gradients are high on this zone. Hence, at the area far away from the cavern wall where stress and strain gradients are lower, size of elements are bigger.

Figure 6.3 illustrates the finite element mesh created for the study in this chapter. The right and upper boundaries locate at 500-m distance from the cavern center (20 times of cavern radius). Stress acted on the right-side is a static load and there is no load acted on the upper part. The pressure acted in the internal walls is varied according to the objectives of the study. The upper and right boundaries can move freely in both x- and y-directions. The left boundary which is a symmetrical axis is freed in y-direction but is fixed in x-direction. The bottom boundary is fixed in y-direction. Elements in the cavern are not shown in the figure, so that the cavern boundary can be seen in the finite element mesh. The mesh is composed of 1,234 elements and 1,295 nodes. The smallest element at the cavern wall is 3×5 m^2 in size.

Hypothesis used for designing the cavern layout is that the cavern used for CAES has to be a single cavern and situated apart from other underground engineering structures for at least 20 times of its diameter. This is to prevent the mechanical effects from the adjacent structures. The computer analysis will prove whether the specified distance as a fore mentioned is enough or not.

6.5 In-situ Stress

The stresses in rock salt and associated rocks used in the computer modeling are assumed to be hydrostatic which depends on depth and density of the rock layers. Therefore the vertical stress and horizontal stress at any depths can be

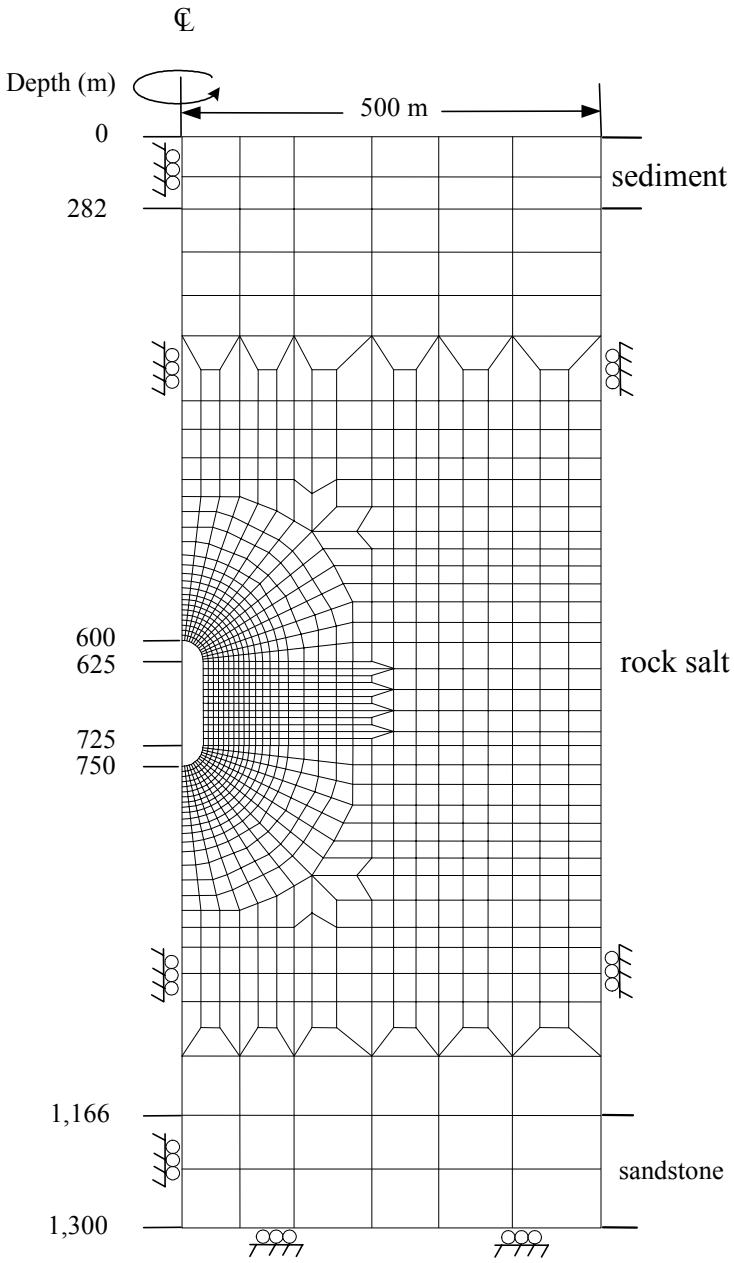

Figure 6.3 Finite element mesh for CAES model at Ban Nong Plue, Borabue District, Maha Sarakham Province. Cylindrical cavern with diameter = 50 m

calculated from the density at any depth in the model. This assumption is probably close to the actual condition because geology of the north east region is a shallow basin in between the high land. Although the in-situ stress has never been measured, the calculation by using hydrostatic pressure is conservative estimate especially for design and analysis.

The pressure gradient of rock salt in relation with depth is approximately 21 kPa/m (0.93 psi/ft). Whereas the pressure gradient of those upper and lower lying beds is approximately 25 kPa/m (1.2 psi/ft). These values have been converted to the stress acting around the cavern as data input for computer analysis. These values are multiplied by depth according to the location in the finite element mesh. The internal pressures of the cavern are varied from 20% to 90% of stress level at the cavern roof. These values will be used also to find the internal pressure at specified depth of the cavern roof.

6.6 Results from Computer Calculation

6.6.1 Minimum Internal Pressure

Results from the study of the maximum internal pressures of the cavern are shown in detail in Appendix B. Comparison of vertical closure at the axis of cavern after 20 years of construction shows that the vertical closures with the internal pressures of 10%, 20% and 30% of in-situ stress at the cavern roof are 2.5%, 2.1% and 1.5%, respectively. The rate of surface subsidence during the first 10 years after construction is higher than those of the second 10 years after construction (Figure B.1).

Comparison of the horizontal closure after 20 years of construction reveals that the horizontal closure with internal pressure of 10%, 20% and 30% of

stress at cavern roof equal 6.8%, 4.7% and 4.1% near the cavern roof, 8.7%, 5.8% and 4.3% at the middle of cavern, and 11.2%, 7.8% and 5.2% near the cavern floor, respectively (Figures B.2 to B.4). The comparison shows that the maximum horizontal closure is located at the lower part of the cavern and minimum horizontal closure is located at the upper part of cavern meanwhile the horizontal closure at the middle part of cavern will be between the upper and lower parts. The horizontal closure measured at the 3 locations tends to increase very quickly during the first year after construction then slow down and remains constant.

Comparison of surface subsidence above the cavern axis occurred during 20 years after construction shows that the surface subsidence is higher in the cavern with lower internal pressure. At the internal pressure of 30%, the surface subsidence after 20 years of construction is only 15 cm. Meanwhile, at internal pressures of 10% and 20%, the surface subsidence increases to18 and 25 cm, respectively. It is also observed that the surface subsidence occurs very quickly in the first 6 months after construction and becomes constant through 20 years after construction (Figure B.5).

Distribution of octahedral shear stress along horizontal distance of 480 m from cavern wall at the upper, middle, and lower parts of the cavern wall and at different periods of 1 day, 10 days, 100 days, 1 year, 5 years, 10 years and 20 years show the same tendency. The maximum octahedral shear stress is at the cavern wall in the first day after construction and it decreases with time (Figures B.6 to B.14). Comparison of the octahedral shear stresses occurred at 20 years for different internal pressures indicate that the octahedral shear stress is a function of the internal pressure. The octahedral shear stress is low when the internal pressure is low. In contrast, at the

distance far from the cavern wall, the octahedral shear stress is independent of the internal pressure. The octahedral shear stress is high when internal pressure is low (Figures B.15 to B.17). Distribution of the stresses around the cavern studied in 3 levels of the internal pressure shows the tendency that the stress mainly distributes at the upper and lower corners of the cavern. The magnitude of the principal stress has a tendency to decrease from the edge of the cavern into the rock salt layer (Figures B.18 to B.20).

Similarly, the distribution of octahedral shear strain around the cavern studied at 3 levels of internal pressure also shows the same tendency as the octahedral shear stress distribution. The octahedral shear strain tends of concentrate at the upper and lower corners, and decrease as the distance from the cavern increases (Figures B.21 to B.23).

Vector for magnitude and direction of the major principal stress in the rock salt layer at around the cavern decreases as internal pressure increases. The study shows that at internal pressures of 10%, 20% and 30%, the maximum stress equals 28.33 MPa (4,108 psi), 28.32 MPa (4,107 psi) and 28.27 MPa (4,100 psi), respectively. The maximum stress concentrates at the upper and lower corners of the cavern (Figures B.24 to B.26).

Vector for magnitude and direction of the major principal strain in rock salt around the cavern decreases as internal pressure increases. For the study of cavern with internal pressures of 10%, 20% and 30%, the maximum strains are 93%, 53% and 18%, respectively. The higher magnitude and direction of major principal strain distribute at the upper and lower corners of the cavern (Figures B.27 to B.39).

6.6.2 Maximum Internal Pressure

In order to determine the safe maximum internal pressure, modeling behavior of cavern with internal pressures of 80% and 90% of the stress at the cavern roof has been performed. It is found that the vertical closures at the cavern axis after 20 years of construction are 0.09% and 0.04% when internal pressures equal 80% and 90% of the in-situ stress, respectively. The vertical closure is high during the first year and eventually becomes constant (Figure B.30).

Comparison of horizontal closures at the upper, middle and lower parts of cavern at 20 years shows that at the internal pressures of 80% and 90% of the in-situ stress at the cavern roof, the vertical closure equals 0.54% and 0.37% at the upper part, 0.8% and 0.6% at the middle part, and 0.7% and 0.5% at the lower part. It can be seen that the maximum vertical closure is at the middle part. The vertical closure at the 3 locations tends to increase very quickly during the first year after construction, and after that becomes constant. The higher internal pressure, the vertical closure is lower (Figure B.31 to B.33).

The surface subsidence at 20 years after construction shows that at internal pressures of 80% and 90%, the surface subsidence equals 15 cm. The surface subsidence at 2 stress levels occurs very quickly during the first 6 months of the construction, and becomes constant through 20 years (Figure B.34).

Distribution of the octahedral shear stress along horizontal distance of 480 m from cavern wall at the upper, middle, and lower part of the cavern wall, and with different periods of 1 day, 10 days, 100 days, 1 year, 5 years, 10 years and 20 years shows similar results at low stress level. The octahedral shear stress is highest at the cavern walls, and decreases until constant at the distance far from the

cavern. In respect of time, it is found that the octahedral shear stress at the wall is high during the first day after construction, and after that it becomes lower and eventually constant (Figures B.35 to B.40). The octahedral shear stress is a function of the internal pressure. At the location far from the cavern wall, the octahedral shear stress is independent of the internal pressure. There, the octahedral shear stress is high when internal pressure is low (Figures B.41 to B.43). Distributions of the shear stresses around the cavern at internal pressures of 80% and 90% of the in-situ stress show the same tendency. Shear stress decreases as a distance from the cavern wall increases, and becomes constant at the upper and lower corners (Figures B.44 and B.45).

Distribution of the shear strains around the cavern at the internal pressures of 80% and 90% of the in-situ stress shows the same tendency as it decreases when the distance from the cavern wall increases, and concentrates at the upper and the lower corners (Figures B.46 and B.47).

Vectors for magnitude and direction of the major principal stress in rock salt layer around the cavern decrease as internal pressure increases. The study shows that at the internal pressures of 80% and 90% of in-situ stress, the maximum stresses equal 27.97 MPa (4,055 psi) and 27.95 MPa (4,054 psi), respectively. The maximum stress is at the upper and lower corners of the cavern (Figures B.48 and B.49).

Vectors for magnitude and direction of the major strain distributed around the cavern decrease as the internal pressure increases. The study of cavern with internal pressures of 80% and 90% of the in-situ stress shows that the maximum principal strain equals 0.8% and 0.4%, respectively. It concentrates at the upper and lower corners of the cavern (Figures B.51 and B.52).

6.6.3 Cyclic Loading Simulation

Suitable internal pressure changed in cycle can be achieved from the analyses to find the minimum and maximum internal pressures explained in the above two sub-headings. The suitable minimum pressure is 30% (547 psi) and the suitable maximum pressure is 90% (1,721 psi) of the in-situ stress at the cavern roof. Results from the analyses indicate that these pressure levels will result in the most stability of the cavern.

In the study, modeling of the cavern behavior in the period of 2 months during operation is performed by applying cycles of changing internal pressures to be 1 round/day (daily cycle). Pressure reduction rate for both compression and release equals 6.6 bar/hr (95.6 psi/hour). This rate is low compared with the rate accepted for the Huntorf CAES in Germany which is 15 bar/h (218 psi/hour) (Crotogino et al., 2001). The compressed air with pressure of 90% of the in-situ stress at the cavern roof will be released until the internal pressure reaches 30% in the second 12 hours. Air will be, again, compressed to store air in the cavern with constant rate until it reaches 90% at the end of 24 hours. Figure B.52 illustrates the change of internal pressure in each cycle (each day).

Result from the simulation in term of cavern closure at 2 months after construction and during operation shows that the cavern closure increases very quickly during the first 20 days, and equals 1.3% of the cavern diameter. After 20 days, it increases at a constant strain rate of 0.004% per day, and it increases up to 2%, eventually (Figure B.53).

The calculated surface subsidence above the cavern axis during 2 months after construction and operation shows that the maximum surface

subsidence about 50 cm occurs just after starting the operation and becomes constant. Finally, the absolute settlement is 16.6 cm (Figure B.54).

Vectors for the major principal stress in rock salt around the cavern reach the maximum value of 30.3 MPa (4,390 psi) and concentrate at the upper and lower corners (Figure B.55). The maximum strain in rock salt around the cavern is 90% of the in-situ stress. The vectors also concentrate at the lower and upper corners of the cavern (Figure B.56).

Shear stress around the cavern subjected to internal pressure concentrates at the upper and lower corners. It tends to decrease as the distance from the cavern increases (Figure B.57). Similarly, distribution of shear strain around the cavern concentrates at the upper and lower corners of the cavern (Figure B.58). Distribution of the octahedral shear stress along the horizontal distance of 480 m from the cavern wall at the upper, middle, and lower parts of the cavern and at the cycles of 10, 20, 30 and 40 shows that the maximum shear stress is at the vicinity of cavern walls (Figures 6.59 to B.61).

The results from the computer simulations suggest the minimum and maximum cavern pressures of 4.0 and 11.9 MPa, and the withdrawal rate of 0.66 MPa per hour. The cavern convergence or closure tends to be constant through the 20 years of operation. The surface subsidence also shows a low value of 20 cm. The results from this study imply that the CAES cavern in Maha Sarakham Formation is feasible in terms of geo-mechanical stability. Additional investigation may be however required particularly on the in-situ investigation and laboratory testing.

CHAPTER VII

CONCLUSIONS AND RECOMMENDATIONS FOR FUTURE STUDIES

7.1 Conclusions

The objective of this study is to assess the potential of rock salt in the northeast of Thailand in terms of mechanical stability by employing laboratory testing and computer modeling. The results will be used to apply for designing rock salt cavern and operating pressures for compressed air energy storage. Conservation of energy in this way will contribute in enhancing of the small power plant efficiency and also be able to produce enough energy during the peak-demand period of each day or each month.

The research has been carried out in five stages: 1) literature review, 2) sample preparation, 3) laboratory testing, 4) computer modeling and 5) result analyses.

From literature review on many references, the mechanical behavior of rock salt is complex and depends on time. This can be seen from various kinds of equations that have been developed to explain the mechanical behavior of rock salt. From the study of geological formation of rock salt in Thailand, it is found that only 2-3 areas are suitable for CAES-technology (based on thickness and depth). The rock salt specimens may have some variations in their physical properties due to the impurity. Results from testing, therefore, have some variants as reflected in standard deviation.

Laboratory testing is aimed to study the rock salt behavior under the cyclic loading and the healing of rock salt fractures. The laboratory tests consist of 3 series: 1) basic mechanical property test, 2) cyclic loading test, and 3) healing test.

The uniaxial compressive strength test determines the ultimate strength of the middle salt bed of 30.2 MPa. The specimens are failed at accumulated axial strain of 0.016 to 0.035 with an average critical shear strain of 0.0022. The Brazilian tensile strength test is performed to measure the ultimate tensile strength of the salt. The result reveals that the ultimate tensile strengths of the middle salt and lower salt are 1.9 MPa and 1.7 MPa, respectively. The point load test measures point load strength index of the middle salt and lower salt as 0.6 MPa and 0.4 MPa, respectively. Conclusion drawn from the test results is that mechanical properties of rock salt from this source are relatively high compared with other sources from foreign countries.

Results form cyclic loading tests indicate that the permanent strain increases and accumulates from each cycle until the specimen fails. The number of cycles that causes failure is a function of differential stress value (between maximum and minimum stress in each cycle or fatigue stress). Relation between the number of cycles (N) and the differential stress value (S) can be drawn as: $S = 33.61\ N^{-0.08}$.

Elastic modulus of rock salt derived from the cyclic loading test results decreases as the number of cycles increases. The elastic moduli are about 20-30 GPa. This value is the parameter for computer modeling. Strain characteristics observed from the cyclic loading test are similar to the results from the static creep test.

Healing test on rock salt fractures had been performed by taking into account of the stress state, time, impurity and fracture conditions. There are two different types of testing: 1) healing test under normal loading on specimens formed by saw-cut

fracture and formed by tension-induced fracture, and 2) healing test under confining pressure on the specimens formed by saw-cut polished surface and tension-induced fracture. Fracture healing under confining pressure has an advantage over that under uniaxial loading, in term of the maximum applied pressures. The applied axial load is limited by the compressive strength of the salt. The healing effectiveness tends to decrease as the amount of inclusion increases. However, their mathematical relationship can not be constructed due to the high variation of the results. The healing effectiveness of salt fractures depends heavily on the origin of the fractures. The hydraulic conductivity for all salt fractures decreases with increasing applied pressure and time. This implies that the fracture healing is accompanied by the fracture closure. Both processes are time-dependent.

Since all fractures tested here are well mated, the impact of fracture roughness can not be truly assessed. More testing is needed to confirm any mathematical relationship between the healing effectiveness and the inclusions. For the healing assessment method, a direct tension test could be used to minimize the impact of the stress gradient induced along the fracture plane. From the results obtained here, it can be postulated that under preferable conditions (stress state, time, temperature, purity, crystal orientation, etc.), a complete healing of salt fractures is possible.

Another work that accompanied with laboratory test is an analysis with an aid of computer modeling to study the mechanical behavior and stability of rock salt cavern with different geometry. Evaluation from the cavern closure and plastic zone distribution around the cavern can be concluded that the spherical shaped cavern is the most stable shape as the cavern closure is the lowest and having the smallest plastic zone compared with other shapes. For elliptical shaped caverns, stability

decreases when the ratio of major to minor axis increases. The plastic zone is 2-3 times of the cavern radius.

Modeling of CAES cavern in rock salt is to study the mechanical behavior and stability of the cavern during operation period. The potential area for study has been chosen by considering the thickness and depth of the rock salt. Concept of operation is to decrease and increase the internal pressures in a cyclic manner, between 90% to 30% of in-situ stress in rock salt at the cavern roof. Results from the analysis indicate that the cavern tends to be stable. The cavern convergence or closure tends to be constant through 20 years of operation. The surface subsidence also shows a low value less than 10 cm at two months. In addition, during the injection period, the fractures are closed as the pressure increased. Then the healing by chemical process are occurred. It means that the fractures around the cavern can be minimized by this healing mechanism. It, therefore, can be concluded that a possibility of applying CAES technology in rock salt in some area in the northeast of Thailand exists.

7.2 Recommendations for Future Studies

The study in this research can be counted as a preliminary guideline and process of study and design. For detailed study, more laboratory tests should be performed by emphasizing on the effects of changing in stress levels and temperature. Rock salt specimen should be obtained directly from the expected construction area so that the properties will be more reliable for analysis. Suggestions related to the testing and modeling can be summarized as follows:

1) In order to derive stress characteristics close to the actual conditions, triaxial cyclic loading test should be performed.

2) Long-term triaxial creep test should be performed for calibration of constants used in the creep rule.
3) More healing tests of fractures should be conducted by emphasizing on the effects of irregularity and impurity which may be significant factors for the healing process.
4) Equation of relation between stress, time and healing fracture should be considered in the computer program "GEO" in order to predict fracturing and healing in rock salt fracture during compressing and releasing air.
5) Rate of air compressing and releasing from rock salt cavern should be further studied because it is expected that these rates will affect the mechanical behavior and of rock salt around the cavern.
6) Rock salt specimen should come directly from the potential area, because properties of rock salt in the Northeast of Thailand may not be consistent. Therefore, results from other sources may not suitable or good enough for being a data input in the modeling.

The above suggestions for further study may be costly and time consuming. However it will be reasonable in term of economical benefit if this CAES-technology can be applied in Thailand. Furthermore, results from such study will be very useful in term of academic concern.

REFERENCES

Adler, P. M., Zazovsky, A., Baranger, Ph. Bonte, G., Laurens, J. F. and Sureau, J. F. (1996). Hydrodynamic aspects of the inhibition of a salt wall by brine initially contained in a cavity. In **Proceedings of the Third Conference on the Mechanical Behavior of Salt** (pp. 249-261). Clausthal-Zellerfeld, Germany: Trans Tech Publications.

Akai, K. and Ohnishi, Y. (1983). Strength and deformation characteristics of soft sedimentary rock under repeated and creep loading**.** In **International Congress on Rock Mechanics 5th, International Society for Rock Mechanics** (pp. 121-124). Melbourne: Australia.

Akgun, H. (1997). An assessment of borehole sealing performance in a salt environment. **Environmental Geology** 31 (1-2): 34-41.

Albers, G. (1983). MAUS–A computer code for modeling thermo-mechanical stresses in rock salt. In **Proc. Tech. Session EUR9355 EN, Computer Modeling of Stresses in Rock Salt**. Brussels.

Alheid, H. J., Knecht, M., and Luedeling, R. (1998). Investigation of the long-term development of damaged zones around underground openings in rock salt. **Int. J. Rock Mech. Min. Sci.** 35 (4/5): 589-590.

Allan, A. (1950). **Summary of published information on large-capacity compressed-air receivers for underground mines**. Washington, D.C: U.S. Dept. of the Interior, Bureau of Mines.

Allemandou, X. and Dusseault, M. B. (1993). Healing processes and transient creep of salt rock. In Anagnostopoulos, A. (eds.). **Geotechnical Engineering of Hard Soils - Soft Rocks** (Vol. 1-3, pp. 1581-1590). Rotterdam, Brookfield, USA: A. A. Balkema.

Allemandou, X. and Dusseault, M. B. (1996). Procedures for cyclic creep testing of salt rock, results and discussions. In **Proceedings of the Third Conference on the Mechanical Behavior of Salt** (pp. 207-218). Clausthal-Zellerfeld, Germany: Trans Tech Publications.

ASTM D2938-95 (1998). Standard test method for unconfined compressive strength of intact rock core specimens. In **Annual Book of ASTM Standards** (Vol. 04.08, pp. 279-281).

ASTM D3148-86 (1998). Standard test method for Elastic Moduli of intact rock core specimens in uniaxial compression. In **Annual Book of ASTM Standards**, (Vol. 04.08, pp. 306-310).

ASTM D3967-95 (1998). Standard test method for splitting tensile strength of intact rock core specimens. In **Annual Book of ASTM Standards** (Vol. 04.08, pp. 404-420).

ASTM D4341-93. (1998). Standard test method for creep of cylindrical hard rock core specimens in uniaxial compression. In **Annual Book of ASTM Standards** (Vol. 04.08, pp. 540-543.)

ASTM D4543-85. (1998). Standard practice for preparing rock core specimens and determining dimensional and shape tolerances. In **Annual Book of ASTM Standards** (Vol. 04.08, pp. 657-660).

ASTM D57312-95. (1998). Standard test method for determination of the point load strength index of rock. In **Annual Book of ASTM Standards** (Vol. 04.08, pp. 657-660).

Atterwell, P. B. and Farmer, I. W. (1973). Fatigue behavior of rock. **International Journal of Rock Mechanics and Mining Sciences** 10: 1-9.

Aubertin, M. (1996). On the physical origin and modeling of kinematics and isotropic hardening of salt. In **Proceedings of the Third Conference on the Mechanical Behavior of Salt** (pp. 1-18). Clausthal-Zellerfeld, Germany: Trans Tech Publications.

Aubertin, M., Gill, D. E. and Ladanyi, B. (1991). A unified visco-plastic model for the inelastic flow of alkali halides. **Mech. Mater.** 11: 63-82.

Aubertin, M., Gill, D. E. and Ladanyi, B. (1992a). Modeling the transient inelastic flow of rocksalt. In **the 7th Symp. On Salt** (vol. 1, pp. 93-104). Elsevier Science Pub.

Aubertin, M., Julien M. R., Servant, S. and Gill, D. E. (1999). A rate-dependent model for the ductile behavior of salt rocks. **Canadian Geotechnical Journal.** 36(4): 660-674.

Aubertin, M., Sgaoula, J. and Gill, D. E. (1992b). A damage model for rock salt: Application to tertiary creep. In **the 7th Symp. On Salt** (vol. 1, pp. 117-125). Elsevier Science Pub.

Aubertin, M., Sgaoula, J. and Gill, D. E. (1993). Constitutive modeling of rock salt: Basic considerations for semi-brittle behavior. In **Proc. of the Fourth Int. Symp. On Plasticity and It's Current Applications** (pp. 92). Baltimore.

Aubertin, M., Sgaoulla, J., Servant, S., Julien, M. R., Gill, D. E. and Ladanyi, B. (1998). An up-to-date version of SUVIC-D for modeling the behavior of salt. In **Proceedings of the Fourth Conference on the Mechanical Behavior of Salt** (pp. 205-220). Clausthal-Zellerfeld, Germany: Trans Tech Publications.

Baar, C. A. (1977). **Applied salt-rock mechanics**. Elsevier Scientific Publishing, Amsterdam.

Bailey, W. A. (1965). **The effects of salt on the consolidation behavior of saturated remolded clays**. Research report no. R65-09 (162 pp). Massachusetts Institute of Technology, Cambridge.

Barber, D. J. (1990). Regimes of plastic deformation processes and microstructure. In **An overview, Deformation Processes in Minerals, Ceramics and Rocks** (pp. 138-178). Unwin Hyman.

Bays, C. A. (1963). Use of salt solution cavities for underground storage. In **Symp. On Salt** (p. 564). Northern Ohio: Geol Soc.

Bechthold, W., Rothfuchs, T., Huertas, F., Poley, A., Ghoreychi, M., Heusermann, S. and Gens, A. (1999). Back-filling and sealing of repositories in rock salt - The BAMBUS project. In **International Conference 5th, Radioactive Waste Management Strategies and Issues** (pp. 366-369). Luxembourg: Euradwaste.

Beddoes, R. J. (1994). **Analyses of bench test area at Goderich mine**. Internal report for Sifto Canada Inc., Prepared by Golder Associate Ltd., Calgary, AB, Canada.

Berest, P. and Blum, P. A. (1993). In situ test in salt cavern. In **Proceedings of Seventh Symposium on Salt**, Kyoto, Japan, April 1992, (Vol. I, pp.353-362). Elsevier Science Publishers, Amsterdam.

Berest, P., Brouard, B. and Durup, G. (1996). Behavior of sealed solution-mined caverns. In **Proceedings of Eurock' 96**. Torino, Italy: Balkema Publishers.

Berest, P., Brouard, B. and Durup, G. (1998). Behavior of sealed solution-mined caverns. In **Proceedings of the Fourth Conference on the Mechanical Behavior of Salt** (pp. 511-524). Clausthal-Zellerfeld, Germany: Trans Tech Publications.

Bieniawski, P. W. and Bieniawski, Z. T. (1994). **Design principles and methodology applied to solution mined salt caverns.** Presented at the 1994 Spring Meeting in Houston, April 24-27, Texas.

Bieniawski, Z. T. and Hawkes, I. (1978). Suggested Methods for determining tensile strength of rock materials.. **International Journal of Rock Mechanics and Mining Sciences & Geomechanics Abstracts** (pp. 118-121). International Society for Rock Mechanics Commission on Standardization of Laboratory and Field Tests.

Bieniawski, Z. T., Franklin, J. A., Bernede, M. J., Duffaut, P., Rummel, F., Horibe, T., Broch, E., Rodrigues, E., Van Heerden, W. L., Vogler, U. W., Hansagi, I., Szlavin, J., Brady, B. T., Deere, D. U., Hawkes, I. And Milovanovic, D. (1978). Suggested Methods for determining the uniaxial compressive strength and deformability of rock materials. **International Journal of Rock Mechanics and Mining Sciences & Geomechanics Abstracts** (pp. 35-140). International Society for Rock Mechanics Commission on Standardization of Laboratory and Field Tests.

Biffle, J. H. (1984). **JAC-A two-dimensional finite element computer program for the non-linear quasistaticresponse of solids with the conjugate gradient method**. SAND81-0998, Sandia National Laboratories, Albuquerque, NM.

Billiotte, J., Guen, L. C., Deveughele, M and Brulhet, J. (1996). On laboratory measurements of porosity and permeability of salt rocks. In **Proceedings of the Third Conference on the Mechanical Behavior of Salt** (pp. 221-230). Clausthal-Zellerfeld, Germany: Trans Tech Publications.

Blanquer-Fernandez, S. (1991). **Interaction des cavities souterraines**. Project de Fin d'Etudes, EPF, LMS. French Ecole: Polytechnique.

Bodner, S. R. (2000). **Investigating on damage and healing in rock salt and their relation to phenomena observed in the 1989 Loma Prieta earthquake.** Annual meeting, 2000 Apr, Ma'alot, Israel, Israel Geological Society (p. 21).

Bonte, G. (1996). Mechanical aspects of the inhibition of a salt wall by brine initially contained in a cavity. In **Proceedings of the Third Conference on the Mechanical Behavior of Salt** (pp. 263-267). Clausthal-Zellerfeld, Germany: Trans Tech Publications.

Boontongloan, C. (2000). **Engineering properties of the evaporitic and clastic rocks of Maha Sarakham formation, Sakon Nakhon evaporite basin**. M.S. thesis, Asian Institute of Technology, Thailand.

Borns, D. J. and Stormont, J. C. (1989). Delineation of the disturbed rock zone surrounding excavation in salt. In **Proc. 30th U. S. Rock Mechanics Symp.**, Morgantown 1989 (pp. 353-360).

Brassow, C. and Thoms, R. (2000). Use of solution-mined salt caverns for disposal of hazardous and industrial waste product. In **Proceedings of the Eighth Symposia on Salt.** Elsevier: AE Amsterdam

Brighenti, G. (1979). Mechanical behavior of rocks under fatigue. In **Proceedings Fourth Congress of the International Society for Rock Mechanics**, Sep. 2-8, 1979, (Vol. 1, pp. 65-69).

Brodsky, N. S. (1990). **Crack closure and healing studies in WIPP salt using compressional wave velocity and attenuation measurements: test methods and results**. Contract Report SAND90-7076, RE/SPEC Inc, 48 p.

Brodsky, N. S. (1994). **Hydrostatic and shear consolidation tests and permeability measurements on Waste Isolation Pilot Plant crushed salt**. SAND93-7058, Sandia national laboratories, Albuquerque.

Brodsky, N. S. and Munson, D. E. (1991). The effect of brine on the creep of WIPP salt in laboratory test. In **Proceedings of the 32nd U. S. Symp. on Rock Mechanics, Rock Mech. as a Multidisciplinary Science** (pp. 703-712). A. A. Balkema, Rotterdam.

Brodsky, N. S. and Munson, D. E. (1994). The effect of brine on the creep of WIPP salt in laboratory test. In **Proceedings of the 32nd U. S. Rock Mechanics Symposium on Rock Mech. as a Multidisciplinary Science** (pp. 703-712). A. A. Balkema, Rotterdam.

Brodsky, N. S. and Munson, D. E. (1994). Thermomechanical damage recovery parameters for rock salt from WIPP, Rock Mechanics: Models and Measurements, Challenges from Industry. In **Proceedings of the 1st North American Rock Mechanics Symposium**, University of Texas at Austin, Austin, June 1994 (pp. 731-740). A. A. Balkema, Rotterdam.

Brodsky, N. S. and Pfeifle, T. W. (1992b). **Brine-permeability of consolidated crushed salt from the Waste Isolation Pilot Plant**. RSI-0408, RE/SPEC, Inc., Rapid City, USA, for Sandia National Laboratories, Albuquerque.

Brodsky, N. S., Hansen, F. D. and Pfeifle, T. W. (1998). Properties of dynamically compacted WIPP salt. In **Proceedings of the Fourth Conference on the Mechanical Behavior of Salt** (pp. 303-316). Clausthal-Zellerfeld, Germany: Trans Tech Publications.

Brodsky, N. S., Zeuch, D. H., and Holcomb, D. J. (1995). Consolidation and permeability of crushed WIPP salt in hydrostatic and triaxial compression. In **Proceeding of the 35th U. S. Symposium on Rock Mechanics**, Rono, June 1995 (pp. 497-502). A. A. Balkema, Rotterdam.

Broek, W. M. G. T. and Heilbron, H. C. (1998). Influence of salt behavior on the retrievability of radioactive waste. In **Proceedings of the Fourth Conference on the Mechanical Behavior of Salt** (pp. 561-573). Clausthal-Zellerfeld, Germany: Trans Tech Publications.

Burdine, N. T. (1963). Rock failure under dynamic loading conditions**, J. Soc. Petrol. Engrs.** 3(1): 1-8.

Callahan, G. D., Fossum, A. F. and Svalstad, D. K. (1989). **Documentation of SPECTROM-32: A finite element thermo-mechanical stress analyses program, DOE/CH10378-2**, prepared by RE/SPEC, Inc., Rapid City, SD, RSI-0269, for US Department of Energy, Chicago Operations Office, Vol.1 and 2, February.

Callahan, G. D., Loken, M. C., Hurtads, L. D. and Hansen, F. D. (1998). Evaluation of constitutive models for crushed salt. In **Proceedings of the Fourth Conference on the Mechanical Behavior of Salt** (pp. 317-330). Clausthal-Zellerfeld, Germany: Trans Tech Publications.

Cardenas, M., LeCompte, C., and Cua, G. (1999). Estimation of permeability of disturbed halite using inverse modeling. **Groundwater** 37(4): 539-545.

Carter, N. L., Horseman, S. T., Russell, J. E. and Handin, J. (1993). Rheology of rocksalt. **Structural Geology** 15(10): 1257-1272.

Chan, K. S., Bodner, S. R., and Munson, D. E. (1998a). Recovery and Healing of Damage in WIPP Salt. **International Journal of Damage Mechanics** 7(1): 143-166.

Chan, K. S., Bodner, S. R., and Munson, D. E. (2000). Application of Isochronous Healing Curves in Predicting Damage Evolution in a Salt Structure. **International Journal of Damage Mechanics** 9(2): 130-153. Technomic.

Chan, K. S., Bodner, S. R., Fossum, A. F., and Munder, D. E. (1995). Constitutive representative of damage healing in WIPP salt. In **Proceedings of the 35th U.S. Symposium, on Rock Mechanics** (pp. 485-490). A.A. Balkema, Rotterdam, Netherlands.

Chan, K. S., Bodner, S. R., Frossum, A. F., and Munson, D. E. (1996a). Inelastic flow behavior of argillaceous salt. **Int. J. Damage Mech.** 5: 292-314.

Chan, K. S., Brodsky, N. S., Frossum, A. F., Bodner, S. R., and Munson, D. E. (1994). Damage-Induced nonassociative flow in rock salt. **International Journal Plasticity** 10: 623-642.

Chan, K. S., Munson, D. E., Bodner, S. R., and Frossum, A. F. (1996b). Cleavage and creep fracture of rock salt. **Acta Mater.** 44: 3553-3565.

Chan, K. S., Munson, D. E., Fossum, A. F., and Bodner, S. R. (1998b). A Constitutive Model for Representing Coupled Creep, Fracture and Healing in Rock Salt. In **Proceeding of the Fourth Conference on the Mechanical Behavior of Salt**, The Pennsylvania State University, June 17-18, 1996 (pp. 211-234), Clausthal-Zellerfeld-Zellerfeld, Germany: Trans Tech Publications.

Change, G. C., Thompson, P. A., Allen, R. A., and Loscutoff, W. V. (1980). Underground compressed air energy storage for electric utilities. **Subsurface,** June 1980 2: 579-585.

Chen, Z., Wang, M. L. and Lu, T. (1997). Study of Tertiary Creep of Rock Salt. **Journal of Engineering Mechanics** 123 (1): 77.

Chia, J. H. and Desai, C. S. (1994). Constitutive modelling of thermoviscoplastic response of rock salt. In **Proceeding of the 8th International Conference on Computer Methods and Advances in Geomechanics**, May 1994, Morgantown, WV, Vol. 1 (pp. 555-560). A. A. Balkema, Rotterdam.

Cho, T. F. and Haimson, B. C. (1987). Effect of cyclic loading in circular openings; results of a laboratory simulation. In **Proceeding of the 28th U. S. Symposium on Rock Mechanics** (pp. 805-812). Rotterdam: AA Balkema.

Chokski, A. H. and Langdon, T. G. (1991). Characteristics of creep deformation in ceramics. **Materails Science and Technology** 7: 577-584.

Christensen, C. T., Christensen, H. F., and Foged, N. (1998). Laboratory tests of hydraulic fracturing and swell healing. In **Proceedings 1998 ISRM International Symposium, Eurock' 98**, Trondheim, July, 1998, Norway (pp. 521-526).

Cleach, J. M. L., Ghazali, A., Deveughele, H., and Brulhet, J. (1996). Experimental study of the role of humidity on the thermomechanical behavior of various halitic rocks. In **Proceedings of the Third Conference on the Mechanical Behavior of Salt** (pp. 231-236). Clausthal-Zellerfeld-Zellerfeld, Germany: Trans Tech Publications.

Cristescu, N. D. (1991). Non-associated elastic/visco-plastic constitutive equations for sand. **Int. J. Plasticity** 7: 41-64.

Cristescu, N. D. (1993a). Constitutive equation for rock salt and mining applications. In **Proceedings of the Seventh symposium on salt** (Vol. 1, pp. 105-115). Amsterdam: Elsevier Science Publishers B. V.

Cristescu, N. D. (1993b). A general constitutive equation for transient and stationary creep of rock salt. **Int. J. Rock Mech. Sci. & Geomech. Abstr.** 30 (2): 125-140.

Cristescu, N. D. (1994a). A procedure to determine nonassociated constitutive equations for geomaterials. **Int. J. Plasticity** 10: 103-131.

Cristescu, N. D. (1994b). **Viscoplasticity of geomaterials**. Visco-Plastic Behaviour of Geomaterials. Springer Verlag, Vienna. pp. 103-207.

Cristescu, N. D. (1996). Stability of large underground caverns in rock salt. In **Proceedings of the 2nd Symposium, North American Rock Mechanics** (pp. 101-108). Canada: A. A. Balkema.

Cristescu, N. D. and Hunsche, U. (1996). A comprehensive constitutive equation for rock salt determination and application. In **Proceedings of the Third Conference on the Mechanical Behavior of Salt** (pp. 191-205). Clausthal-Zellerfeld-Zellerfeld, Germany: Trans Tech Publications.

Cristescu, N. D. and Hunsche, U. (1996). A comprehensive constitutive equation for rock salt determination and application. In **Proceedings of the Third Conference on the Mechanical Behavior of Salt** (pp. 191-205). Clausthal-Zellerfeld-Zellerfeld, Germany: Trans Tech Publications.

Crotogino, F. and Quast, P. (1980). Compressed-air storage caverns at Huntorf. In **Proc. Int. Symp. Subsurface Space (Rockstore 80)**, Stockholm, Vol. 2 (pp. 593-600).

Crotogino, F., Mohmeyer, W. U., and Scharf, R. (2001). **Huntorf CAES: More then 20 years of successful operation**. Spring 2001 Meeting, Orlando, Florida, USA.

Cruden, D. M. (1974). The static fatigue of brittle rock under uniaxial compression. **Int. J. Rock. Mech. Min. Sci.** 11: 67-73.

Cuevas, C. D. L. (1998). Pore structure characterization in rock salt. **Engineering geology** 47(1-2): 17.

Cuevas, C. D. L. and Pueyo, J. J. (1995). The influence of mineralogy and texture in the water content of rock salt formations, Its implication in radioactive waste disposal. **Applied Geochemistry** 10(3): 317-327.

Dale, T. and Hurtodo, L, D. (1998). WIPP air-intake shaft disturbed-rock zone study. In **Proceedings of the Fourth Conference on the Mechanical Behavior of Salt** (pp. 525-535). Clausthal-Zellerfeld, Germany: Trans Tech Publications.

Davidson, B. C. and Dusseault, M. B. (1998). Granular halite backfill as a structural and disposal medium. In **Proceedings of the Fourth Conference on the Mechanical Behavior of Salt** (pp. 341-352). Clausthal-Zellerfeld, Germany: Trans Tech Publications.

De Menezes, J. E. Q. and Nguyen-Minh, D. (1998). Numerical modeling of leached cavern fields using mized BEM-FEM method. In **Proceedings of the Fourth Conference on the Mechanical Behavior of Salt** (pp. 417-426). Clausthal-Zellerfeld, Germany: Trans Tech Publications.

De Orellana, A. J. C. (1998). Non-Associated Pressure Solution Creep in Salt Rock Mines. In **Proceeding Fourth Conference on the Mechanical behavior of salt** (pp. 429-444): Clausthal-Zellerfeld-Zellerfeld, Germany: Trans Tech Publications.

DeLong, M. M., Nelson, C. R., and Petersen, D. L. (1989). Subsurface cavern system requirements for compressed air energy storage and associated uses. In Nilsen & Olsen (eds.). **Storage of Gases in Rock Caverns** (ISBN 90 6191 896 0, pp. 33-36). Balkema, Rotterdam.

DeVries, K. L. and Callahan, G. D. (1998). WIPP panel simulations with gas generation. In **Proceedings of the Fourth Conference on the Mechanical Behavior of Salt** (pp. 537-550). Clausthal-Zellerfeld, Germany: Trans Tech Publications.

Dies, J., Cuevas, C. D. L., and Tarrasa, F. (1999). MISCELLANEOUS - The Influence of Irradiation Temperature on the Thermoluminescence Response of Rock Salt Irradiated in the MGy Range. **Radiation Protection Dosimetry** 85 (1): 487.

DiMento, L. J. (1982). **Integrated environmental and safety assessment of selected mechanical energy storage systems**. Palo Alto, CA, Electric Power Research Institute.

Dreyer, W. (1972). **The Science of Rock Mechanics, Part 1: The strength properties of rocks**. Cleveland, OH: Trans Tech Publications.

Dreyer, W. (1991). Crude oil storage in a system of salt caverns. In **Proceedings of the First Conference on the Mechanical Behavior of Rock Salt** (pp. 71-83). Clausthal-Zellerfeld, Germany: Trans Tech Publications.

Durup, G. and Xu, J. (1996). Comparative study of certain constitutive laws used to describe the rheological deformation of salts. In **Proceedings of the Third Conference on the Mechanical Behavior of Salt** (pp. 75-84). Clausthal-Zellerfeld-Zellerfeld, Germany: Trans Tech Publications.

Dusseault, M.B. and Fordham, C.J. (1993). Time-dependent behavior of rocks. In J.A. Hunson (ed.). **Comprehensive Rock Engineering Principles, Practice and Project: Rock Testing and Site Characterization** (Vol. 3, pp. 119-149). London, Pergamon.

Eduardo, J., Menezes, Q. D. and Ngugen-Minh, D. (1996). **Numerical modeling of leached cavern fields using mixed BEM-FEM method (**pp. 417-426).

Ehgartner, B. L. and Linn, J. K. (1994). **Mechanical behavior of sealed SPR caverns**, SMRI Spring Meeting, Hannover, Germany.

Elliott, G.M. (1993). Triaxial testing for rock strength. In J.A. Hunson (ed.). **Comprehensive Rock Engineering Principles, Practice and Project: Rock Testing and Site Characterization** (Vol. 3, pp. 87-104). London, Pergamon.

EPRI. (1986). **Dynamic Operating Benefits of Energy Storage**. EPRI Report No.AP-4875, Palo Alto, CA, Electric Power Research Institute.

EPRI. (1987). **Design Guidelines for Pressure Tunnels and Shafts.** EPRI Report No.AP-5273, Palo Alto, CA, Electric Power Research Institute.

EPRI. (1990a). **Compressed Air Storage for Electric Power Generation**. EPRI Report No.GS-6784, Palo Alto, CA, Electric Power Research Institute.

EPRI. (1990b). **Compressed-air energy storage using hand-rock geology**. Palo Alto, CA, Electric Power Research Institute.

EPRI. (1990c). **Rock concern linings for compressed-air energy storage**. Palo Alto, CA, Electric Power Research Institute.

EPRI. (1992a). **Alabama Electric Cooperative (AEC) Builds First U.S. Compressed Air Energy Storage (CASE) Plant Using EPRI-Developed Low - Pressure Expander**. EPRI Report No.IN-101511, Palo Alto, CA, Electric Power Research Institute.

EPRI. (1992b). **CASE goes on-line [Video recording]**. Palo Alto, CA, Electric Power Research Institute.

EPRI. (1992c). **EPRI-Developed Acquisition System Monitors Compressed-Air Energy Storage CASE) Plant On-line Performance**. EPRI Report No.IN-101510, Palo Alto, CA, Electric Power Research Institute.

EPRI. (1993). **Application of Load Duration and Monte Carlo Techniques: EPRI Monographs on Simulation of Electric Power Production**. EPRI Report No.IE-7511, Palo Alto, CA, Electric Power Research Institute.

EPRI. (1994a). **Compressed Air Handbook**. EPRI Report No. CR-104546, Palo Alto, CA, Electric Power Research Institute.

EPRI. (1994b). **Compressive Analyses of Compressed–Air Cycles; CASE, CASE-ES, CRCAES/CRCASH-ES, and MRCAES/MRCASH-ES**. EPRI Report No.TR-103521, Palo Alto, CA, Electric Power Research Institute.

EPRI. (1994c). **Development of Turbomachinery Trains for the CASHING, NGCASH, and IGCASH Cycle Applications**. EPRI Report No.TR-103348, Palo Alto, CA, Electric Power Research Institute.

EPRI. (1994d). **Moisture Remove from Compressed Air Tech Application** Vol. 6, No. 2, 1994. EPRI Report No. TA-104079-V6P2, Palo Alto, CA, Electric Power Research Institute.

EPRI. (1994e). **Standard Compressed-Air Energy Storage Plant : Design and Cost**. Research Project No. TR-103209. Palo Alto, CA, Electric Power Research Institute.

EPRI. (1997). **Energy Storage in a Restructured Electric Utility Industry: Report on EPRI Think Tanks I and II**. EPRI Report No.TR-108894, Palo Alto, CA, Electric Power Research Institute.

EPRI. (1998). **Compressed Air Storage with Humidification : An Economic Evaluation**. EPRI Report No.TR-111691, Palo Alto, CA, Electric Power Research Institute.

EPRI. (1999). **Conceptual Engineering and Cost Estimate for 100-MW and 20MW Nominal Capacity CASH Plants**. EPRI Report No.TR-113360, Palo Alto, CA, Electric Power Research Institute.

Farmer, I. W. (1983). **Engineering behavior of rock** (2nd edition). New York: Chapman and Hall, Ltd.

Farmer, I. W. and Gilbert, M. J. (1984). Time dependent strength reduction of rock salt. In **Proceedings of the First Conference on the Mechanical Behavior of Salt** (pp. 3-18). Clausthal-Zellerfeld, Germany: Trans Tech Publications.

Fokker, P. A. (1995). **The behavior of salt and salt caverns**. Ph.D Thesis, Delft University of Technolgoy.

Fokker, P. A. (1998). The micro-mechanics of creep in rock salt. In **Proceedings of the Fourth Conference on the Mechanical Behavior of Salt** (pp. 49-61). Clausthal-Zellerfeld, Germany: Trans Tech Publications.

Fokker, P. A. and Kenter, C. J. (1994). The micro mechanical description of rock salt plasticity. In **Eurock'94** (pp. 705-713). Rotterdam: Balkema.

Fokker, P. A., Kenter, C. J., and Rogaar, H. P. (1993). The effect of fluid pressures on the mechaical stability of rock salt. In **Proceedings of the Seventh Symposium on Salt**, Kyoto, Japan, April 1992 (Vol. I, pp. 75-82). Amstterdam: Elsevier Science Publishers.

Fossan, N. E. V. and Whelply, F. V. (1985). **Nitrogen as a testing medium for proving the mechanical integrity of wells**. Presented at the Solution Mining Research Institute Meeting, October 13-16, 1985, Houston, Texas.

Fossum, A. F., Munson, D. E., Chan, K. S., and Bodner, S. R. (1998). Constitutive basis of the MDCF model for rock salt. In **Proceedings of the Fourth Conference on the Mechanical Behavior of Salt** (pp. 235-247). Clausthal-Zellerfeld, Germany: Trans Tech Publications.

Franssen, R. C. M. (1998). Mechanical anisotropy of synthetic polycrystalline rock salt. In **Proceedings of the Fourth Conference on the Mechanical Behavior of Salt** (pp. 63-75). Clausthal-Zellerfeld, Germany: Trans Tech Publications.

Franssen, R. C. M. and Spiers, C. J. (1990). Deformation of polycrystalline salt in compression and in shear at 250-350°C. **Deformation Mechanisms, Rheology and Tectonics, Geological Society Special Publication** 45: 201-213.

Frayne, M. A. (1996). Four cases study in salt rock: Determination of material parameters for numerical modeling. In **Proceedings of the Third Conference on the Mechanical Behavior of Salt** (pp. 471-482). Clausthal-Zellerfeld-Zellerfeld, Germany: Trans Tech Publications.

Frayne, M. A. (1998). The goderich salt mine: past, present & future. In **Proceedings of the Fourth Conference on the Mechanical Behavior of Salt** (pp. 445-458). Clausthal-Zellerfeld, Germany: Trans Tech Publications.

Fuenkajorn, K and Wetchasat, K. (2001). **Rock salt formations as potential nuclear waste repository**. The 6th Mining, Metallurgical, and Petroleum Engineering Conference: Resources Exploration and Utilization for Sustainable Environment (REUSE). Bangkok, Thailand.

Fuenkajorn, K. (2000). Geohydrological integrity of storage caverns in salt formation. In **Symposium on Mineral, Energy, and Water Resources of Thailand: Towards the year 2000**, October 28-29, 1999 (pp. 270-275). Bangkok, Thailand.

Fuenkajorn, K. (2002). Design guideline for salt solution mining in Thailand. **Research and Development Journal** 13(1): 1-8.

Fuenkajorn, K. and Daemen, J. J. K. (1988). **Boreholes closure in salt**. Technical Report Prepared for The U.S. Nuclear Regulatory Commission. Report No. NUREG/CR-5243 RW. University of Arizona.

Fuenkajorn, K. and Daemen, J. J. K. (1992a). Borehole Sealing. In **Compressed-Air Energy Storage Proceedings of the Second International Conference**, Electric Power Research Institute, July 7-9, San Francisco, CA (pp. 5.1-5.21).

Fuenkajorn, K. and Daemen, J. J. K. (1992b). Drilling-Induced Fractures in Borehole Walls. **Journal of Petroleum Technology** 44(2): 210-216.

Fuenkajorn, K. and Daemen, J. J. K. (1996). **Sealing of Boreholes and Underground Excavations in Rock**. London: Chapman & Hall.

Fuenkajorn, K. and Serata, S. (1992). Geohydrological integrity of CAES in rock salt. In **Proceedings of the Second International Conference on Compressed-Air Energy Storage** (pp. 4.1-4.21). San Francisco, CA: Electric Power Research Institute.

Fuenkajorn, K. and Serata, S. (1994). Dilation-induced permeability increase around caverns in rock salt. In **Proceeding of the 1st North American Rock Mechanics Symposium** (pp. 648-656). Rotterdam: A. A. Balkema.

Fuenkajorn, K. and Stormont, J. C. (1997). **Geomechanics and geohydrological issues in mine sealing**. Presentation at the SME Annual Meeting, February 24-27, 1997, Denver, Colorado.

Gartling, D.K. (1981a). **COYOTE- A finite element computer program for nonlinear heat conduction problems.** SAND77-0463. Sandia National Laboratories, Albuquerque, NM.

Gartling, D.K. (1981b). **MERLIN- A computer program to transfer data between finite element meshes**. SAND81-0463. Sandia National Laboratories, Albuquerque, NM.

Gaul, G. (1993). A case for compressed air energy storage. **Modern power system** 13(3): 19.

Gegen, P. M. (1988). **A test of two program that model compressed air energy storage (CASE)**. M.S. thesis, Wichita State University, Dept. of Electrical Engineering.

Gehle, R. M. and Thoms, R. L. (1986). **Tests of U.S. rock salt for long-term stability of CAES reservoirs**. Richland, Wash: Pacific Northwest Laboratory.

Gevantman, L. H. (1981). **Physical properties data for rock salt**. National Bureau of Standards Monograph 167 (282 pp.). Washington: U.S. Government Printing Office.

Ghoreychi, M., Raynal, M., and Roman, J. (1992). Implementing and monitoring thermo-mechanical tests in a salt formation of a French potash mine. In **Proc. 33rd U. S. Rock Mech. Symp.** (pp. 181-190). Rotterdam: A. A. Balkema.

Goodman, R. E. (1989). **Introduction to rock mechanics** (2nd ed.). Canada: John Wiley & Sons.

Goodson, J. O. (1992). **History of first U.S. compressed air energy storage (CASE) plant (110-MW-26h)**. Palo Alto, CA, Electric Power Research Institute.

Habib, P. and Berest, P. (1993). Rock mechanics for underground nuclear waste disposal in France: Developments and case studies. In **Comprehensive Rock Engineering**, **Geothermal Energy and Radioactive Waste Disposal** (Vol. 5, pp. 547-563). Great Britain: Pergamon.

Haimson, B. C. (1972). **Mechanical behavior of rock under cyclic fatigue**. Annual Technical Report to the Bureau of Mines, Contract H0210004.

Haimson, B. C. and Kim, C. M. (1972). Mechanical behavior of rock under cyclic fatigue. In **Proceedings of the Thirteenth Symposium on Rock Mechanics**, ASCE (pp.845-864).

Hamami, M. (1999). Simultaneous effect of loading rate and confining pressure on the deviator evolution in rock salt. **International Journal of Rock Mechanics and Mining Sciences** 36(6): 827-831.

Hamami, M., Tijani, S. M. and Vouille, G. (1996). A methodology for the identification of rock salt behavior using multi-step creep tests. In **Proceedings of the Third Conference on the Mechanical Behavior of Salt** (pp. 53-66). Clausthal-Zellerfeld-Zellerfeld, Germany: Trans Tech Publications.

Hampel, A., Hunsche, U., Weidinger, P. and Blum, W. (1998). Description of the creep of rock salt with the composite model – II: Steady-state creep. In **Proceedings of the Forth Conference on the Mechanical Behavior of Salt** (pp. 287-300). Montreal, Canada: Trans Tech Publications.

Hansen, F. D. Mellegard, K. D. and Senseny, P. E. (1984). Elasticity and strength of ten natural rock salts. In **Proceedings of the First Conference on the Mechanical Behavior of Salt** (pp. 71-83). Clausthal-Zellerfeld, Germany: Trans Tech Publications.

Hansen, F. D., Callahan, G. D. and van Sambeek, L. L. (1996). Reconsolidating of salt as applied to permanent seals for the Waste Isolation Pilot Plant. In **Proceedings of the Third Conference on the Mechanical Behavior of Salt** (pp. 232-336). Clausthal-Zellerfeld, Germany: Trans Tech Publications.

Hansen, F. D., Senseny, P. E., Pfeifle, T. W., and Vogt, T. J. (1987). Influence of impurities on creep of salt from the Palo Duro Basin. In **Proceedings of the 29th U.S. Symposium on Rock Mechanics,** University of Minnessota (pp. 199-206). A. A. Balkema, Rotterdam.

Hardy, H. R. (1996). Application of the Kaiser effect for the evaluation of in-situ stress in salt. In **Proceedings of the Third Conference on the Mechanical Behavior of Salt** (pp. 85-100). Clausthal-Zellerfeld, Germany: Trans Tech Publications.

Hardy, H. R. (1998). Strength and acoustic emission in salt under tensile loading. In **Proceedings of the Fourth Conference on the Mechanical Behavior of Salt** (pp. 143-162). Clausthal-Zellerfeld, Germany: Trans Tech Publications.

Hardy, H. R. and Chugh, Y. P. (1970). Failure of geological materials under low-cycle fatigue. In **Proceedings of the Sixth Canadian Symposium on Rock Mechanics** (pp. 33-47). Montreal.

Harrington, T. J., Chabannes, C. R. and Shukla, K. (1991). Rock mechanics consolidations in the WIPP room design. In **Proceedings of the First Conference on the Mechanical Behavior of Rock Salt** (pp. 681-696). Clausthal-Zellerfeld, Germany: Trans Tech Publications.

Heemann, U., Heusermann, S., Sarfeld, W., and Faust, B. (1999). Numerical modeling of the compaction behavior of crushed rock salt. In **Proceedings of the 7th International Symposium on Numerical Models in Geomechanics**, Graz, September 1999 (pp. 627-632). Netherlands.

Heusermann, S. (1996). Measurement of initial rock stress at the Asse Salt Mine. In **Proceedings of the Third Conference on the Mechanical Behavior of Salt** (pp. 101-114). Clausthal-Zellerfeld, Germany: Trans Tech Publications.

Heusermann, S., Kob, S., and Sonnke, J. (1998). Analysis of stress measurements in the TSDE at the Asse salt mine. In **Proceedings of the Fourth Conference on the Mechanical Behavior of Salt** (pp. 17-29). Clausthal-Zellerfeld, Germany: Trans Tech Publications.

Hickman, S. H. and Evans, B. (1987). Influence of geometry upon crack healing rate in calcite. **Physics Chemistry Minerals** 15: 91-102. Springer-Verlag.

Hoek, E., Kaiser, P. K. and Bawden, W. E. (1995). **Support of underground excavations in hard rock** (215 pp.). Rotherdam: A. A. Balkema.

Hofmannm, R. (1976). **STEALTH, a lagrange explicit finite-difference code for solid, structural, and themohydraulic analysis**. User's manual, EPRI NP-260, Vol. 1. Electric Power Research Institute, Palo Alto, California, August 1976, Prepared by Science Applications, Inc. San Leandro, California.

Honecker, A. and Wulf, A. (1988). The FE-system ANSALT a dedicated tool for rock and salt-mechanics. In **Proceedings second Conference on the Mechanical Behavior of Rock Salt** (pp. 4409-4520). Clausthal-Zellerfeld, Germany: Trans Tech Publications.

Hou, Z. and Lux, K. H. (1999). Some new developments in the design of pillars in salt mining. In **International Congress on Rock Mechanics 9th, International Society for Rock Mechanics** (pp. 297-300). Balkema.

Hunsche, U. (1993). Failure behaviour of rock salt around underground cavities. In **Proceedings of the Seventh Symposium on Salt** (Vol. 1, pp. 59-65). Amsterdam: Elsevier Science Publishers B. V.

Hunsche, U. and Schulze, O. (1996). Effect of humidity & confining pressure on creep of rock salt. In **Mechanical behavior of salt, Series on Soil and Rock Mechanics** (Vol. 20, pp. 237-248). Trans Tech Publications.

Hunsche, U., Mingerzahn, G., and Schulze, O. (1996). The influence of textural parameters and mineralogical composition on the creep behavior of salt. **In Proceeding of the Third Conference on the Mechanical behavior of salt** (pp. 143-151). Clausthal-Zellerfeld, Germany: Trans Tech Publications.

Hwang C. L., Wang, M. L., and Miao, S. (1993). Proposed healing and consolidation mechanism of rock salt revealed by ESEM. **Microscopy research and technique**, Vol. 25, pp.456-464.

INTERA. (1982). **VISCO Maual**, Technical Report, Houston, TX.

Ishizuka, Y. and Abe, T. (1990). Fatigue behavior of granite under cyclic loading. In Brummer (eds.). **Static and Dynamics Considerations in Rock Engineering** (ISBN 90 6191 1453 2, pp. 139-146). Rotterdam: Balkema.

Itasca (1992). **User manual for FLAC–fast Langrangian analysis of continua, version 3.0**. Itasca Consulting Group Inc., Minneapolis, MN.

Itasca (1994). **User manual for FLAC–fast Langrangian analysis of continua in 3 dimensions, version 1.0**. Itasca Consulting Group Inc., Minneapolis, MN.

Japakasetr, T. (1985). Review on rock salt and potash exploration in Northeast of Thailand. In **Conference on Geology and Mineral Resources Development of the Northeast**. Thailand: Khon Kaen University.

Japakasetr, T. (1992). Thailand's mineral potential and investment opportunity. In **National Conference on Geologic Resources of Thailand**: Potential for Future Development, November 1992 (pp. 641-652). Bangkok, Thailand: DMR.

Japakasetr, T. and Suwanich, P. (1977). **Potash and rock salt in Thailand.** (pp. A1-A252). Bangkok: Economic Geology Division, Department of Mineral Resources.

Japakasetr, T. and Workman, D. R. (1981). Evaporite deposits of Northeast of Thailand. **Circum-Pacific Conferences** (pp. 179-187). Hawaii.

Japaksetr, T. (1985). Review on rock salt and potash exploration in Northeast Thailand. In **Conference on Geology and Mineral Resources Development of the Northeast** (pp. 135-147). Thailand: Khon Kaen University.

Japan International Cooperation Agency. (1981). **Evaluation study report for ASEAN rock salt-soda ash project in the kingdom of Thailand**. Tokyo, Japan.

Jeremic, M. L. (1994). **Rock mechanics in salt mining** (530 pp.). Rotherdam: A. A. Balkema.

Jin, J. and Cristescu, N. D. (1998). An elastic/visco-plastic model for transient creep of rock salt. **International Journal of Plasticity** 14 (1-3): 85.

Jin, J., Cristescu, N. D. and Hunche, U. (1998). A new elastic/visco-plastic model for rock salt, In **Proceedings of the Fourth Conference on the Mechanical Behavior of Salt** (pp. 249-262). Clausthal-Zellerfeld, Germany: Trans Tech Publications.

Julien, M. R., Foerch, R., Aubertin, M. and Cailletaud, G. (1998). Some aspects of numerical implementation of SUVIC-D. In **Proceedings of the Fourth Conference on the Mechanical Behavior of Salt** (pp. 389-402). Clausthal-Zellerfeld, Germany: Trans Tech Publications.

Junmaha, S. (1987). Salt dome in Khorat plateau (in Thai). In **Proceeding of the Conference on Geology and Mineral Resources of Thailand, 13-14 August** (pp. 301-317). Bangkok, Thailand: Department of Mineral Resources.

Katz, D. L. and Lady, E. R. (1976). **Compressed air storage**, Ann Arbor, Michigan: Ulrich's Books.

Khan, I. A., Mahtab, M. A., and Yegulalp, T. M. (1988). Predicting strength of salt from point load tests. In **Proceeding of the Second Conference on the Mechanical Behavior of Salt** (pp. 211-222). Clausthal-Zellerfeld, Germany: Trans Tech Publications.

Kim, C. M. (1973). **Fatigue failure of rock in cyclic uniaxial compression**. Ph. D. Thesis, University of Wisconsin, Madison.

Kleczek, Z. and Flisiak, D. (1995). Geomechanical model of rock salt for stress and stability analysis of underground disposal cavern. In **International Symposium 4th on Mine Planing and Equipment Selection** (pp. 961-966). Canada: A. A. Balkema.

Knowles, M. K., Borns, D., Fredrich, J., Holcomb, D., Price, R. and Zeuch, D. (1998). Testing the disturbed zone aroud a rigid inclusion in salt. In **Proceedings of the Fourth Conference on the Mechanical Behavior of Salt** (pp. 175-188). Clausthal-Zellerfeld, Germany: Trans Tech Publications.

Koenig, J. W. J. (1994). **Preparing motor gasoline for salt cavern storage of up to 10 years**. SMRI Fall Mtg (p. 425).

Korthaus, E. (1988). Effect of backfill material on cavity closure. In **Proceedings of the Second Conference on the Mechanical Behavior of Rock Salt** (pp. 521-532). Clausthal-Zellerfeld, Germany: Trans Tech Publications.

Korthaus, E. (1996). Measurement of crushed salt consolidation under hydrostatic and deviatoric stress conditions. **In Proceedings of the Third Conference on the Mechanical Behavior of Salt** (pp. 311-322). Clausthal-Zellerfeld, Germany: Trans Tech Publications.

Korthaus, E. (1998). Consolidation and deviatoric deformation behavior of dry crushed salt at temperatures up to 150 °C. **In Proceedings of the Fourth Conference on the Mechanical Behavior of Salt** (pp. 365-378). Clausthal-Zellerfeld, Germany: Trans Tech Publications.

Krieg, R. D., Morgan, H. S. and Stone C. M. (1988). Structural analyses overview on the WIPP project. In **Proceedings second Conference on the Mechanical Behavior of Rock Salt** (pp. 533-549). Clausthal-Zellerfeld, Germany: Trans Tech Publications.

Kwon, S. and Miller, H. (1998). Using a neutral network to the deformation of underground excavations in rock salt. In **Proceedings of the Fourth Conference on the Mechanical Behavior of Salt** (pp. 405-416). Clausthal-Zellerfeld, Germany: Trans Tech Publications.

Langer, M. (1993). Geoscientific evaluation of geological and geotechnical barriers with respect to waste disposal projects. In **Proceedings of the 7th Int. IAEG Congr.** (pp. 2827-2935). Rotterdam, Balkema.

Langer, M. (1993). Use of solution-mined caverns in salt for oil and gas storage and toxic waste disposal in Germany. **Engineering Geology** 35 (3-4): 183-190.

Langer, M. (1994). Geoengineering confidence building for the design and construction of salt caverns. In **The Netherlands, EUROCK - SPE ISRM International Conference 2nd** (pp. 697-704). Balkema.

Langer, M. (1996). Underground disposal of wastes requiring special monitoring in salt rock masses. In **Proceedings of the Third Conference on the Mechanical Behavior of Salt** (pp. 583-603). Clausthal-Zellerfeld, Germany: Trans Tech Publications.

Langer, M. (1998). Engineering geological evaluation of geological barrier rocks at landfills and repositories. **Environmental Geology** 35 (1): 19-27.

Langer, M. (1999). Principles of geomechanical safety assessment for radioactive waste disposal in salt structures. **Engineering Geology**. 52 (3-4): 257-269.

Liang, J. and Lindblom, U. (1994). Critical pressure for gas storage on unline rock caverns. **International Journal of Rock Mechanics & Mining Sciences** 31 (4): 337-381.

Lindblom, U. (1990). **City energy management through underground storage**. Tunneling & Underground Space Technology (pp. 225-232).

Lu, M. and Broch, E. (1997). Study of large volume gas storage in rock salt caverns by FEM. In **International Conference, 9th, Computer Methods and Advances in Geomechanics** (Vol. 2, pp. 1489-1494). Balkema.

Lux, K. H. and Schmidt, T. (1996). Optimizing underground gas storage operations in salt caverns, with special reference to the rock mechanics and thermodynamics involved. In **Proceedings of the Third Conference on the Mechanical Behavior of Salt** (pp. 445-458). Clausthal-Zellerfeld, Germany: Trans Tech Publications.

Maleki, H. and Chaturvedi, L. (1997). Prediction of long-term closure and stability of underground workings in the waste isolation pilot plant. **International Journal of Rock Mechanics and Mining Sciences** 34 (3-4): 493.

Massier, D. (1996). Rate type constitutive equations with applications to the calculus of the stress state and of the displacement field around cavities in rock salt. In **Proceedings of the Third Conference on the Mechanical Behavior of Salt** (pp. 545-558). Clausthal-Zellerfeld, Germany: Trans Tech Publications.

Matalucci, R. V. and Hunter, T. O. (1984). Geomechanical applications for the waste isolation pilot plant (WIPP) project. In **Proceedings of the First Conference on the Mechanical Behavior of Salt**. (pp. 791-812). Clausthal-Zellerfeld, Germany: Trans Tech Publications.

Mattick, W., Stys, W. Z. and Haddenhorst, H. G. (1975). **Huntorf – the world's first 290 MW gas turbine air storage peaking plant.** Proc. Amer. Power Conf. II. Inst. Tech, Chaicago.

McKay, H. G., Steffens, R. E., and Curlin, B. W. (1989). Review of the design methodology for the Bad Creek underground powerhouse as it would apply to a hard rock cavern design for compressed air energy storage (CAES). In Nilsen & Olsen (eds.). **Storage of Gases in Rock Caverns** (ISBN 90 6191 896 0). Balkema, Rotterdam.

Mehta, B. (1991). **First U.S. compressed air energy storage plant status**. SMRI Fall Meeting.

Miao, S., Wang, M. L., and Schreyer H. L. (1995). Constitutive Models for healing of materials with application to compaction of crushed rock salt. **Journal of Engineering Mechanics** (ASCE) 10 (121): 1122-1129.

Mlakar, V., Hassani, F. P., and Momayez, M. (1993). Crack development and acoustic emission in potash rock. **Int. J. Rock Mech. and Mining Sciences** 30: 305-320.

Mogi, K. (1962). Study of elastic shocks caused by the fracture of heterogeneous materials and its relations to earthquake problem. **Bulletin of the Earthquake Research Institute**, Vol. 40, pp. 125-173.

Morfeldt, C. O. and Lindblom, U. (1975). **Unline rock caverns for compressed air storage: a ecological, technical and economic study**. Washingtiom: U. S. Energy Research and Development Administratin.

Munson, D. E. and Wawersik, W. R. (1993). Constitutive modeling of salt behavior – State of the technology. In **Proceedings of the 7th Int. Cong. Rock Mech**. (Vol. 3, pp. 1797-1810). Balkema.

Munson, D. E., Chan, K. S., and Fossum, A. F. (1999). **Fracture and healing of rock salt related to salt caverns**. Meeting paper, April 14-16, 1999. Solution Mining Research Institute, Las Vagas, 21 pp.

Nguyen-Minh, D. and Quintanilha de Menezes, E. (1996). Incompressible numerical modeling for long term convergence evaluation of underground works in salt. In **Proceedings of the Third Conference on the Mechanical Behavior of Salt** (pp. 523-531). Clausthal-Zellerfeld, Germany: Trans Tech Publications.

Nguyen-Minh, D., Braham, S. and Durup, J. G. (1996). Modelling subsidence of the tersanne underground gas storage field. In **Proceedings of the Third Conference on the Mechanical Behavior of Salt** (pp. 405-416). Clausthal-Zellerfeld, Germany: Trans Tech Publications.

Nopper, J. R. W. and Clark, J. E. (1991). **Stability analysis of a solution cavity resulting from underground injection.** Presented at Solution Mining Research Institute Meeting, October 27-29, 1991. Las Vegas, Nevada.

Olivella, S., Gens, A., Carrera, J., and Alonso, E. (1998a). Porosity variation in salt aggregates caused by dissolution/ Precipitation processes induced by temperature gradients. In **Proceedings of the Fourth Conference on the Mechanical Behavior of Salt** (pp. 379-386). Clausthal-Zellerfeld, Germany: Trans Tech Publications.

Olivella, S., Gens, A., Carrera, J., and Alonso, E. (1998b). Analysis of creep deformation of galleries backfilled with porous salt aggregates. In **Proceedings of the Fourth Conference on the Mechanical Behavior of Salt** (pp. 379-386). Clausthal-Zellerfeld, Germany: Trans Tech Publications.

Ong, V. (1994). **Evaluation of 3D VISAGE finite element program**. Report submitted to SPPA.

Ong, V., Unrau, J., Jones, J. Coode, A. and Mackintosh, D. (1998). Triaxial creep testing of saskatchewan potash samples. In **Proceedings of the Fourth Conference on the Mechanical Behavior of Salt** (pp. 469-480). Clausthal-Zellerfeld, Germany: Trans Tech Publications.

Passaris, E. K. S. (1982). Fatigue characteristics of rock salt with reference to underground storage caverns. In **Proceeding ISRM Symposium**, May 26-28, 1982 (pp. 983-989). Aachen.

Peach, C. J. (1991). **Influence of deformation on the fluid transport properties of salt rock**. Geological Ultraiectina No. 77. Nederlands.

Peach, C. J. (1996). Deformation, dilatency and permeability developed in halite/anhydrite composition. In **Proceeding of the Third Conference on the Mechanical behavior of salt** (pp. 153-166). Clausthal-Zellerfeld, Germany: Trans Tech Publications.

Peach, C. J. and Spiers, C. J. (1996). Influence of crystal plastic deformation on dilatancy and permeability development in synthetic salt rock. **Tectonophysics** 256 (1-4): 101.

Pearson, A. G. A. and Alseth, A. (1995). **Method for refuse disposal in solution-mined salt cavities.** U.S. Patent No. 5,433,553, July 18.

Pfeifle, T. W., Vogt, T. J. and Brekken, A. (1998). Correlation analyses of dome salt cahracteristics. In **Proceedings of the Fourth Conference on the Mechanical Behavior of Salt** (pp. 87-114). Clausthal-Zellerfeld, Germany: Trans Tech Publications.

Pincus, H. J. (1980). **Underground compressed air energy storage : rock mechanics and geology components**. Annual report for F Y 1980 and final report for the project, Milwaukee, Wisconsin, University of Wisconsin, Milwaukee.

Plookphol, T. (1987). **Engineering properties of the evaporite in the Khorat plateau**. M.S. thesis, Asian Institute of Technology, Thailand.

Pudewills, A. (1998). Influence of anhydrite strata on a waste disposal drift. In **Proceedings of the Fourth Conference on the Mechanical Behavior of Salt** (pp. 551-560). Clausthal-Zellerfeld, Germany: Trans Tech Publications.

Pudewills, A. and Hornberger, K. (1996). A unified visco-plastic model for rock salt. In **Proceedings of the Third Conference on the Mechanical Behavior of Salt** (pp. 45-52). Clausthal-Zellerfeld, Germany: Trans Tech Publications.

Purvis, M.R.I. and Street, P. J. (1979). Energy storage. **Energy World** 58: 6-11.

Raj, S. V. and Pharr, G. M. (1992). Effect of temperature on the formation of creep substructure in sodium chloride single crystal. **American Ceramic Society** 75 (2): 347-352.

Ratanajanurak, P. (1990). The effect of salt strata on salty of clay in eastern Thailand (in Thai). In **Proceeding of the Conference on Geology and Mineral Resources of Thailand, 16-17 August** (pp. 15-25). Bangkok, Thailand: Department of Mineral Resources.

Ratigan, J. L. (1991). **Ground subsidence at Mont Belvieu, Texas**. Presented at SMRI meeting, April 29, 1991, Atlanta, Georgia.

Ratigan, J. L. and Vogt, T. J. (1993). LPG storage at Mont Belvieu, Texas: A case history. **SPE Advanced Technologies Series** 1 (1): 204-211.

Ray, S. K., Sarkar, M., and Singh, T. N. (1999). Effect of cyclic loading and strain rate in the mechanical behavior of sandstone. **International Journal of Rock Mechanics and Mining Science** 36: 543-549.

Reeves, M. J. and Stead, D. (1991). SALTDATA: A graphical database for the physical properties of rocks associated with mining of potash and salt. In **Proceeding of the 32nd U. S. Rock Mechanics Symposium on Mechanics as a Multi-Disciplinary Science** (pp. 169-177). Oklahoma.

Renard, F. (1999). **Pressure solution and crack healing and sealing, Geology related to nuclear waste disposal**. Institute of Geology and Department of Physics. Roztez, Norway: Czech Republic. 32pp.

Rizkalla, M. (1991). **Comparison of three different geotechnical codes, using GEOROC**. Report Submitted to SPPA by Noranda Technology Centre.

Rokahr, R. and Staudtmeister, K. (1996). The assessment of the stability of a cavern field in bedded salt with the help of the new hannover dimensioning concept. In **Proceedings of the Third Conference on the Mechanical Behavior of Salt** (pp. 533-544). Clausthal-Zellerfeld, Germany: Trans Tech Publications.

Rolnik, H. (1988). High-level waste repository in rock salt: Suitable rheological forms. In **Proceedings second Conference on the Mechanical Behavior of Rock Salt** (pp. 625-643). Clausthal-Zellerfeld, Germany:Trans Tech Publications.

Rranstetter, L. J., Stone, C. M. and Krieg, R. D. (1981). **WIPP benchmark II result using SANCHO.** SAND81-0853, Sandia Nationa Laboratories, Albuquerque, New Maxico 87185, November 1981.

Saint-Leu, C. and Sirieys, P. (1971). La Fatigue des Roches. In **Proceedings of International Symposium on Rock Fracture**. Nancy.

Salter, M. G., Macfarlane, I. M., Willett, D. C., and Byrne, R. J. (1984). **Design aspects for an underground compressed air energy storage system in hard rock**. Design and Performance of Underground Excavations, (pp.37-44). Cambridge.

Salzer, K. and Scheriner, W. (1998). Long-term safety of salt mines in flat bedding. In **Proceedings of the Fourth Conference on the Mechanical Behavior of Salt** (pp. 481-494). Clausthal-Zellerfeld, Germany: Trans Tech Publications.

Sattayarak, N. (1983). Review of continental Mesozoic stratigraphy of Thailand. In **Proceeding Stratigraphic Correlation of Thailand and Malaysia** (Vol. 1, pp. 127-148). Geol. Soc., Thailand.

Sattayarak, N. (1985). Review on geology of Khorat plateau. In **Conference on Geology and Mineral Resources Development of the Northeast** (pp. 23-30). Thailand: Khon Kaen University.

Sattayarak, N. and Ponjun, T. (1990). Rock salt in Khorat plateau (in Thai). In **Proceeding of the Conference on Geology and Mineral Resources of Thailand, 16-17 August** (pp. 1-14). Bangkok, Thailand: Department of Mineral Resources.

Schneefub, J., Droste, J. (1996). Thermo-mechanical effects in back-filled drifts. In **Proceedings of the Third Conference on the Mechanical Behavior of Salt** (pp. 373-380). Clausthal-Zellerfeld, Germany: Trans Tech Publications.

Senseny, P. E. and Fussum, A. F. (1998). Testing to estimate the Munson-Dawson parameters. In **Proceedings of the Fourth Conference on the Mechanical Behavior of Salt** (pp. 263-272). Clausthal-Zellerfeld, Germany: Trans Tech Publications.

Senseny, P. E., Handin, J. W., Hansen, F. D. and Russell, J. E. (1992). Mechanical behavior of rock salt: phenomenology and micro-mechanisms. **International Journal of Rock Mechanics & Mining Sciences** 29 (4): 363-378.

Serata (1991). **GEO/REM computer program for Sifto Canada's Goderich salt mine**. Internal report prepared by Serata Geomechanics Inc., Goderich, ON, Canada.

Serata, S. and Fuenkajorn, K. (1991). **Permeability studies in relation to stress state and cavern design, Phase I**. Research Project Report, Contract 1-91, prepared for Solution Mining Research Institute by Serata Geomechanics, Inc., Richmond, CA.

Serata, S. and Fuenkajorn, K. (1992a). Formulation of a constitutive equation for salt. In **Proceedings of the Seventh International Symposium on Salt** (Vol. 1, pp. 483-488). Amsterdam: Eisevier Science.

Serata, S. and Fuenkajorn, K. (1992b). **Finite element program "GEO" for modeling brittle-ductile deterioration of aging earth structures**. SMRI Paper, presented at the Solution Mining Research Institute, Fall Meeting, October 19-22, Houston, Texas. (24 pp.).

Serata, S., Mehta, B., and Hiremath, M. (1989). Geomechanical stability analysis for CAES cavern operation. In Nilsen and Olsen (eds). **Storage of Gases in Rock Caverns** (pp. 129-135). Balkema, Rotterdam.

Shidahara, C., Kaneko, K., Nozaki, A., Oyama, T., and Nakagawa, K. (2000). Geotechnical evaluation of a conglomerate for compressed air energy storage: The influence of the sedimentary cycle and filling mineral in the rock matrix. **Engineering Geology** 56(1-2): 125-135.

Shimadzu corporation. (1995). **Instruction manual for Shimadzu universal testing machine UH-A series and computer-controlled hydraulic servo system**. Kyoto, Janpan.

Skrotzki, W. (1988). Texture influence of texture on creep of salt. In **Proceedings of the Second Conference on the Mechanical Behavior of Salt** (pp. 83-88). Clausthal-Zellerfeld, Germany: Trans Tech Publications.

Soil Testing Siam Corporation. (1995). **Instruction service manual and part-lists**. Bangkok, Thailand.

Spiers, C. J. and Carter, N. L. (1998). Microphysics of rock salt flow in nature. In **Proceedings of the Fourth Conference on the Mechanical Behavior of Salt** (pp. 115-128). Clausthal-Zellerfeld, Germany: Trans Tech Publications.

Stead, D. and Szczepanik, Z. (1991). Time dependent acoustic emission studies on potash. In **Proceedings 32nd U. S. Rock Mech. Symp.** (pp.471-479). Oklahoma.

Stead, D. and Szczepanik, Z. (1995). Acoustic Emission during uniaxial creep in potash. In **Proceedings 5th Conf. On Acoustic Emission/Microseismic Activity in Geologic Structures and Materials**, Penn State University, June 1991 Trans (pp. 97-133). Clausthal-Zellerfeld, Germany: Tech Punlications.

Stead, D., Szczepanik, Z., and Gaskin, W. (1998). Acoustic characterization of potash. In **Proceedings of the Fourth Conference on the Mechanical Behavior of Salt** (pp. 31-45). Clausthal-Zellerfeld, Germany: Trans Tech Publications.

Stone, C. M., Krieg, R. D. and Beisinger, Z.E. (1985). **SANCHO, A finite element computer program for the quasistatic, large deformation, Inelastic response of two-dimensional solid**, SAND84-2618.

Stormont, J. C. (1990). Discontinuous behavior near excavations in a bedded salt formation. **Int. Jour. Mining and Geological Eng.** 8: 35-36.

Stormont, J. C. (1991). **Gas permeability changes in rock salt during deformation**. Ph. D. Thesis, University of Arizona.

Stormont, J. C. and Daemen, J. J. K. (1991). **Laboratory study of gas permeability changes in rock salt during deformation**, SAND90-2638 (p. 40). Sandia National Laboratories, Albuquerque, NM.

Stormont, J. C. and Fuenkajorn, K. (1994). Dilation-induced permeability changes in rock salt. In **Proceedings of the 8th International Conf, Computer Methods and Advances in Geomechanics** (pp. 1296-1273). Morgantown, West Virginia.

Stormont, J. C., Daemen J. J. K. and Desai, C. S. (1992). Prediction of dilation and permeability changes in rock salt. **International Journal for Numerical & Analytical Methods in Geomechanics** 16 (8): 545-569.

Stormont, J. C., Howard, C. L., and Daemen, J. J. K. (1991a). Changes in rock salt permeability due to nearby excavation. **Rock Mechanics as a Multidisciplinary Science** (pp. 899-907). A. A. Balkema.

Stormont, J. C., Howard, C. L., and Daemen, J. J. K. (1991b). **In situ measurements of rock salt permeability change due to nearby excavation**, SAND 90-3134. Sandi National Laboratories, Albuquerque.

Supajanya, T., Vichapan, K. and Sri-israporn, S. (1992). Surface expression of shallow salt dome in northeast Thailand. In **National conference on geologic resources of Thailand: Potential for future development** (pp. 89-95). Thailand: Department of Mineral Resources.

Suwanapal, A. (1992). Potash mine: A co-operative project among ASEAN countries and private sectors. In **National Conference on Geologic Resources of Thailand: Potential for Future Development**. Bangkok, Thailand: Department of Mineral Resources.

Suwanich, P. (1978). Potash in northeastern of Thailand (in Thai). **Economic Geology Document No. 22.** Bangkok: Economic Geology, Division, Department of Mineral Resources.

Suwanich, P. and Ratanajaruraks, P. (1982). Sequences of rock salt and potash in Thailand. **Nonmetallic Minerals Bulletin No. 1**. Bangkok: Economic Geology, Division, Department of Mineral Resources.

Suwanich, P. and P. Ratanajaruraks (1986). Potash and rock salt in Thailand: Appendix A core log of K-holes. **Nonmetallic minerals bulletin no.2**. Bangkok: Economic Geology Division, Department of Mineral Resources, Thailand.

Suwanich, P., Ratanajaruraks, P. and Kunawat, P. (1982). **Core log Bamnet Narong area Chaiyaphum Province**. Bangkok: Economic Geology Division, Department of Mineral Resources.

Tabakh, M. E., Utha-aroon, C., Coshell, L. and Warren, K. (1995). Cretaceous saline deposits of the Maha Sarakham Formation in the Khorat basin, Northeastern Thailand. In **International Conference on Geology, Geotechnology and Mineral Resources of Indochina (GEO-INDO'95),** 22-25 November 1995. Khon Kaen, Thailand: Khon Kaen University.

Tharp, T. M. (1973). **Behavior of three calcite rocks under tensile cyclic loading**. M. S. Thesis, University of Wisconsin, Madison.

Thoms, R. L. and Gehle, R. (1982). Experimental study of rock salt for compressed air energy storage. In **ISRM Symposium**, 26-28 May 1982. (pp. 991-1002). Aachen.

Thoms, R. L. and Gehle, R. (1988). Survey on existing cavern in U. S. salt domes. In **Proceedings second Conference on the Mechanical Behavior of Rock Salt** (pp. 703-716). Clausthal-Zellerfeld, Germany: Trans Tech Publications.

Thoms, R. L. and Gehle, R. (1994). **Analysis of a solidified waste disposal cavern in gulf coast salt dome.** SMRI Fall Meeting (p. 637).

Thoms, R. L. and Martinez, J. D. (1978). **Preliminary long-term stability criteria for compressed air energy storage caverns in salt domes**. Prepared for Battelle Northwest Laboratories, Richland, Washington, Special Agreement B-54804-A-L, Prime Contact EY-76-C-06-1830, 84 pp. Institute for Environmental Studies, Louisiana State University, Baton Rouge, LA.

Thoms, R. L., Nathany, M., and Gehle, R. (1980). Low-frequency cyclic loading effects in rock salt. In **Proc. Int. Symp. Subsurface Space (Rockstore 80)**, Vol. 2 (pp. 755-761). Stockholm

Thorel, L. and Ghoreychi, M. (1996). Rock salt damage - Experimental results and interpretation. In **Proceedings Third Conference on the Mechanical Behavior of Salt** (pp. 175-189). Clausthal-Zellerfeld, Germany: Trans Tech Publications.

Thorel, L., Ghoreychi, M., Cosemza, Ph., and Chanchole, S. (1998). Rocksalt damage and failure under wet or dry conditions. In **Proceedings of the Fourth Conference on the Mechanical Behavior of Salt** (pp. 189-202). Clausthal-Zellerfeld, Germany: Trans Tech Publications.

Utha-aroon, C. (1993). Continental origin of the Maha Sarakham evaporites, northeastern Thailand. **Journal of Southeast Asian Earth Sciences**. 8 (1-4): 193-203.

Van Eekelen, H. A. (1988). Cavity arrays in layered salt systems. In **Proceedings second Conference on the Mechanical Behavior of Rock Salt** (pp. 473-492). Clausthal-Zellerfeld, Germany: Trans Tech Publications.

Viboonsawat, P. (1998). Vision of energy: Quality of life and development. In **Vision Thailand in science, technology, environmental, telecommunication, energy and human resources** (pp. 108-55). Bangkook: Office of the Civil Service Commission, Association of Thai Government Scholarships.

Vogler, U. W. and Kovari, K. (1978). Suggested Methods for determining the strength of rock materials in triaxial compression. **International Journal of Rock Mechanics and Mining Sciences & Geomechanics Abstracts**. 15 (2): 47-54.

Vouille, G., Bergues, J., Durup, J. G. and You, T. (1996). Study of the stability of caverns in rock salt created by solution mining proposal for a new design criterion. In **Proceedings of the Third Conference on the Mechanical Behavior of Salt** (pp. 427-444). Clausthal-Zellerfeld, Germany: Trans Tech Publications.

Wallner, M. (1984). Analysis of thermo-mechanical problems related to the storage of heat producing radioactive waste in rock salt. In **Proceedings of the First Conference on the Mechanical Behavior of Salt** (pp. 739-763). Clausthal-Zellerfeld, Germany: Trans Tech Publications.

Wallner, M. and Wulf, A. (1982). Thermomechanical calculations concerning the design of a radioactive waste repository in rock salt. In **ISRM Symposium**, 26-28 May 1982, (pp. 1003-1012). Aachen.

Wang, M. L. and Miao, S. (1995). Constitutive models for Anisotropic Healing of Crushed Rock Salt. In **5th Annual WERC Technology Conference**, April 18-20. Las Cruces, NM. 461-470.

Wanten, P. H., Spiers, C. J. and Peach, C. J. (1996). Deformation of NaCl single crystals at $0.27T_m < T < 0.44T_m$. In **Proceedings of the Third Conference on the Mechanical Behavior of Salt** (pp. 117-128). Clausthal-Zellerfeld, Germany: Trans Tech Publications.

Warren, J. (1999). **Evaporites: Their evolution and economics** (pp. 235-239). Blackwell Science.

Wassman, T. H. (1983). Cavity utilization in the Netherlands. Presented at **the Sixth International Symposium on Salt** (Vol. 2, pp. 191-201). Toronto, Canada.

Weidinger, P., Blum, W., Hampel, A. and Hunsche, U. (1998). Description of the Creep of Rock Salt with the Composite Model - I. Transient Creep. In **Proceeding Fourth Conference on the Mechanical behavior of salt** (pp. 277-286): Clausthal-Zellerfeld, Germany: Trans Tech Publications.

Wetchasat, K. (2002). Assessment of mechanical performance of rock salt formations for nuclear waste repository in northeastern Thailand. **The 3rd National Symposium on Graduate Research: Extended Abstracts**, 18-19 July 2002 (pp. 427-428). Nakhon Ratchasima, Thailand: Suranaree University of Technology.

Whittaker, B.N. and Reddish, D.J. (1993). Subsidence behavior of rock structures. In J.A. Hunson (ed.). In **Comprehensive rock engineering principles, practice and project: Excavation, support and monitoring** (Vol. 4, pp. 751-780). London, Pergamon.

Wittke, W., Pierau, B., and Schetelig, K. (1980). Planning of a compressed-air pumped-storage scheme at Vianden/Luxembourg. In **Proc. Int. Symp. Subsurface Space**, Rockstore 80 (Vol. 2, pp. 367-376). Stockholm.

Wongsawas, S. and Panjasutharos, S. (1990). Potential and method for the developing of Khorat Aquifer (in Thai). In **Proceeding of the Conference on Geology and Mineral Resources of Thailand, 16-17 August** (pp. 39-58). Bangkok, Thailand: Department of Mineral Resources.

Yang, J. (1981). **Thermophysical properties, Physical Properties for Rock Salt**. NBS Monograph 167, U. S. Government, Washington, p. 211.

You, T, Maisons, C. and Valette, M. (1994). **Experimental procedure for the closure of the brine production caverns on the saline de Vauvert site.** SMRI Fall Meeting, Hannover, Germany.

Yumuang, S. (1983). **On the origin of evaporite deposits in the Maha Sarakham formation in Bamnet Narong area, Changwat Chaiyaphum.** A thesis submitted in Partial Fulfillment of the Requirements for the Degrees of Master of Science, Department of Geology, Graduate School, Chulalongkorn University, Thailand.

Yumuang, S. (1995). **Potash ore reserve evaluation of Bamnet Narong area, Northeast of Thailand**. Department of Geology, Faculty of Science, Chulalongkorn University.

Yumuang, S., Khantaprab, C. and Taiyagupt, M. (1986). The evaporite deposits in Bamnet Narong area, Northeastern Thailand. In **Proceedings of the Five on GEOSEA** (pp. 249-267). Bulletin, Geological Society of Malaysia.

Zeigler, T. W. (1976). **Determination of rock mass permeability**. U. S. Army Ener. Waterways Expt. Station, Technical Report S-76-2.

Zhang, C., Schmidt, M. M. and Staupendahl, G. (1996). Experimental and modeling results for compaction of crushed salt. In **Proceedings of the Third Conference on the Mechanical Behavior of Salt** (pp. 391-402). Clausthal-Zellerfeld, Germany: Trans Tech Publications.

APPENDIX A

RESULTS FROM THE COMPUTER

MODELING OF HORIZONTAL MODEL

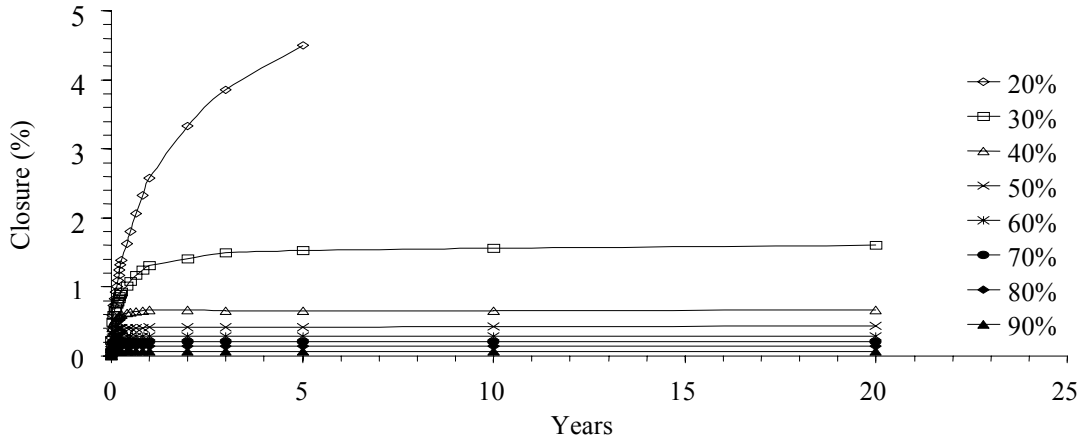

Figure A.1 Comparison of cavern wall closure in x- and y-directions of model SP10 for 20 years after construction. The internal pressure in the cavern range between 20% to 90% of the in-situ stress at the cavern roof. The in-situ stress at the cavern roof for this model is 10.34 MPa (1,500 psi).

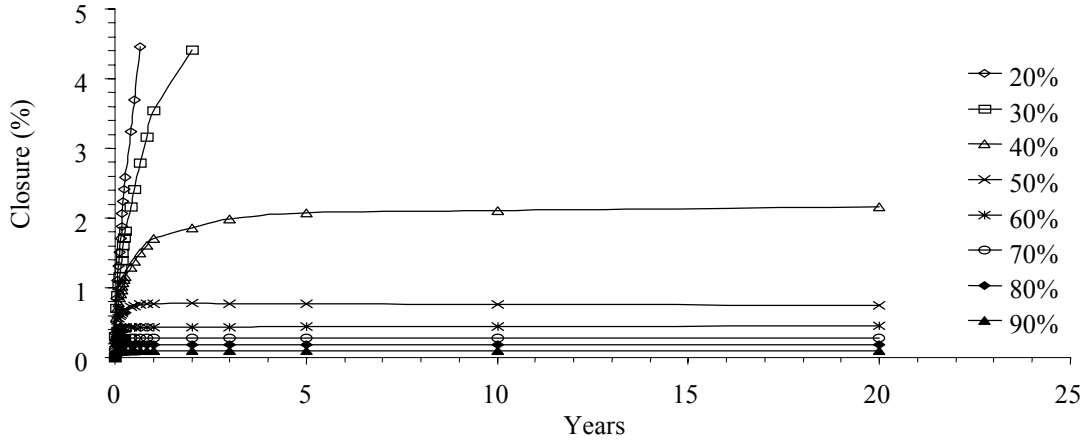

Figure A.2 Comparison of cavern wall closure in x- and y-directions of model SP10 for 20 years after construction. The internal pressure in the cavern range between 20% to 90% of the in-situ stress at the cavern roof. The in-situ stress at the cavern roof for this model is 13.79 MPa (2,000 psi).

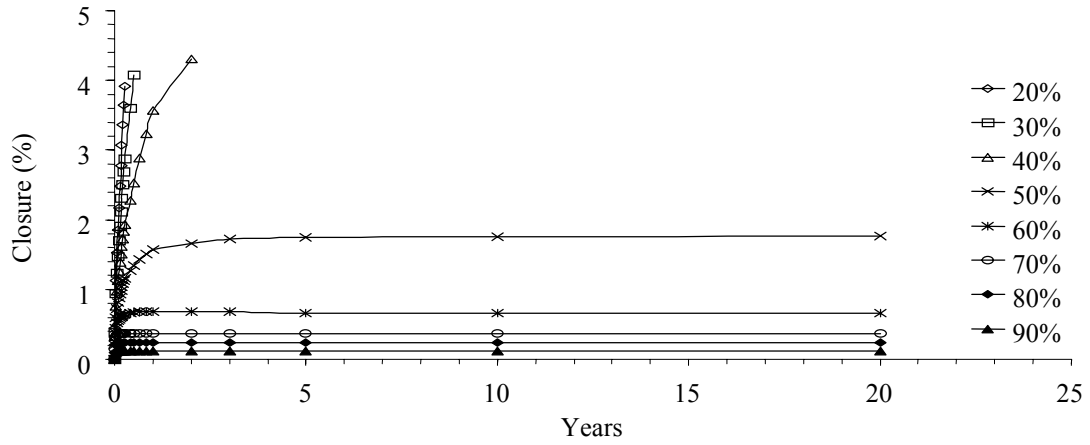

Figure A.3 Comparison of cavern wall closure in x- and y-directions of model SP10 for 20 years after construction. The internal pressure in the cavern range between 20% to 90% of the in-situ stress at the cavern roof. The in-situ stress at the cavern roof for this model is 17.24 MPa (2,500 psi).

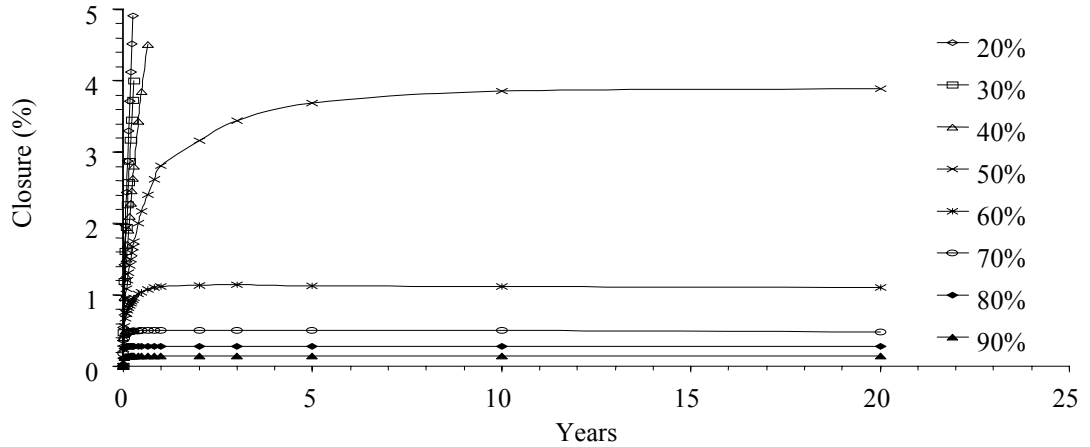

Figure A.4 Comparison of cavern wall closure in x- and y-directions of model SP10 for 20 years after construction. The internal pressure in the cavern range between 20% to 90% of the in-situ stress at the cavern roof. The in-situ stress at the cavern roof for this model is 20.69 MPa (3,000 psi).

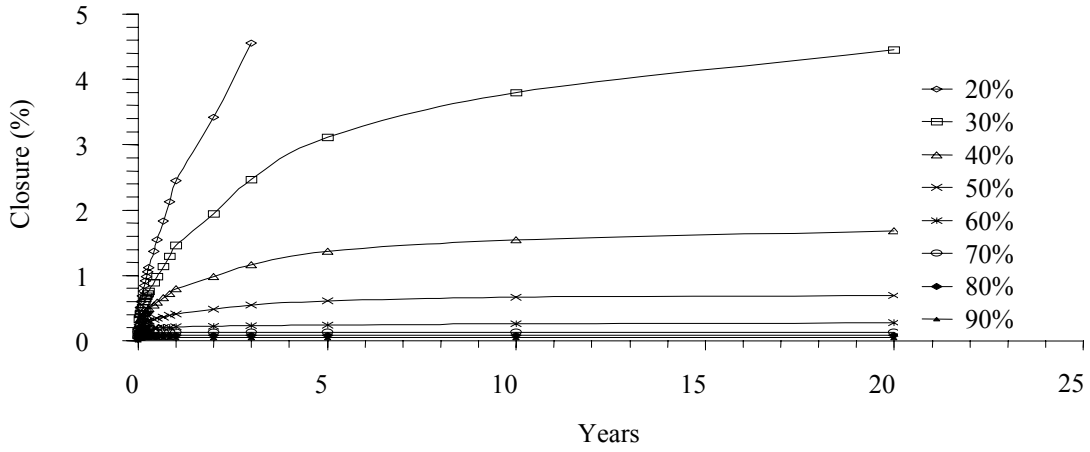

Figure A.5 Comparison of cavern wall closure in x-direction of model EL15 for 20 years after construction. The internal pressure in the cavern range between 20% to 90% of the in-situ stress at the cavern roof. The in-situ stress at the cavern roof for this model is 10.34 MPa (1,500 psi).

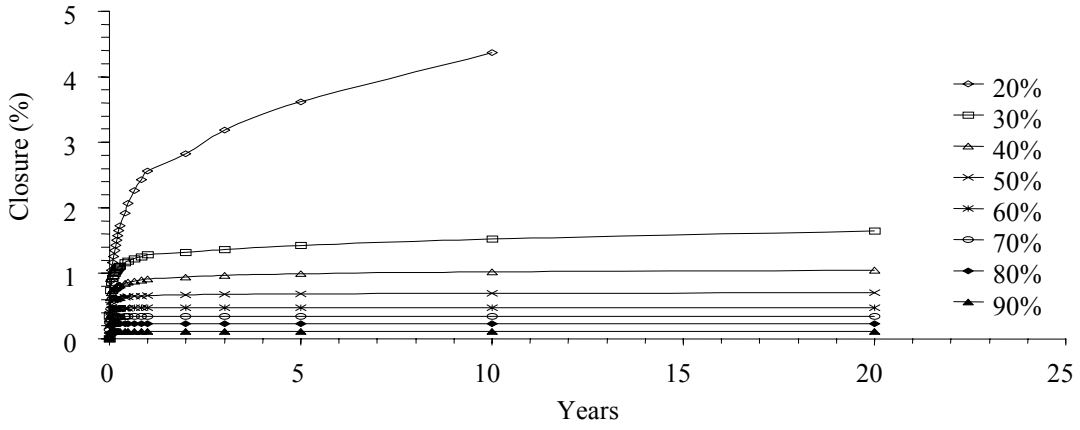

Figure A.6 Comparison of cavern wall closure in y-direction of model EL15 for 20 years after construction. The internal pressure in the cavern range between 20% to 90% of the in-situ stress at the cavern roof. The in-situ stress at the cavern roof for this model is 10.34 MPa (1,500 psi).

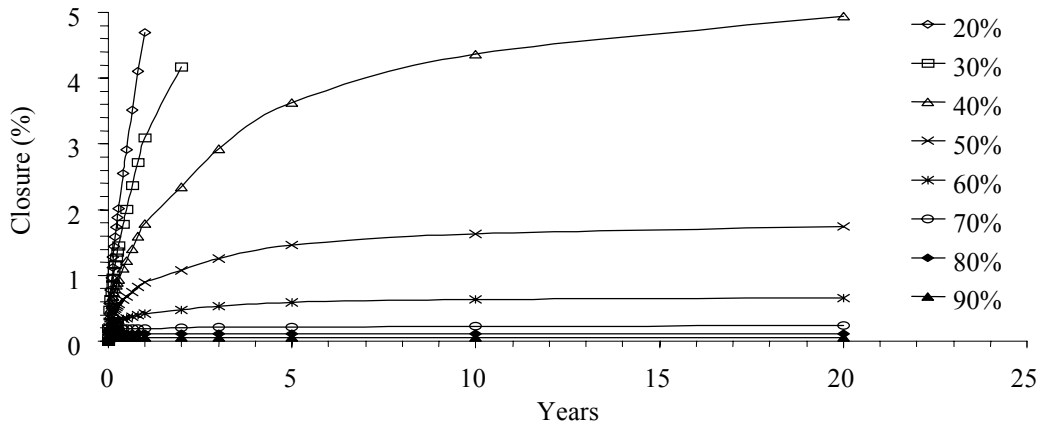

Figure A.7 Comparison of cavern wall closure in x-direction of model EL15 for 20 years after construction. The internal pressure in the cavern range between 20% to 90% of the in-situ stress at the cavern roof. The in-situ stress at the cavern roof for this model is 13.79 MPa (2,000 psi).

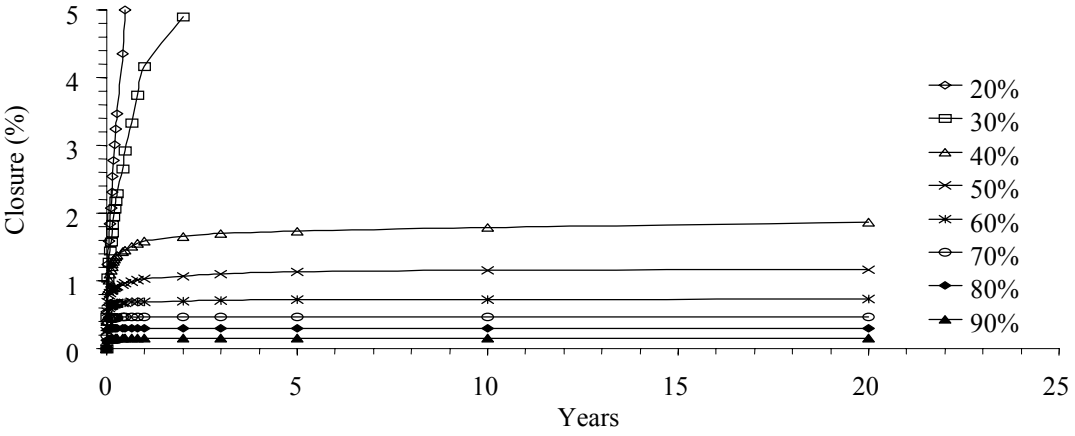

Figure A.8 Comparison of cavern wall closure in y-direction of model EL15 for 20 years after construction. The internal pressure in the cavern range between 20% to 90% of the in-situ stress at the cavern roof. The in-situ stress at the cavern roof for this model is 13.79 MPa (2,000 psi).

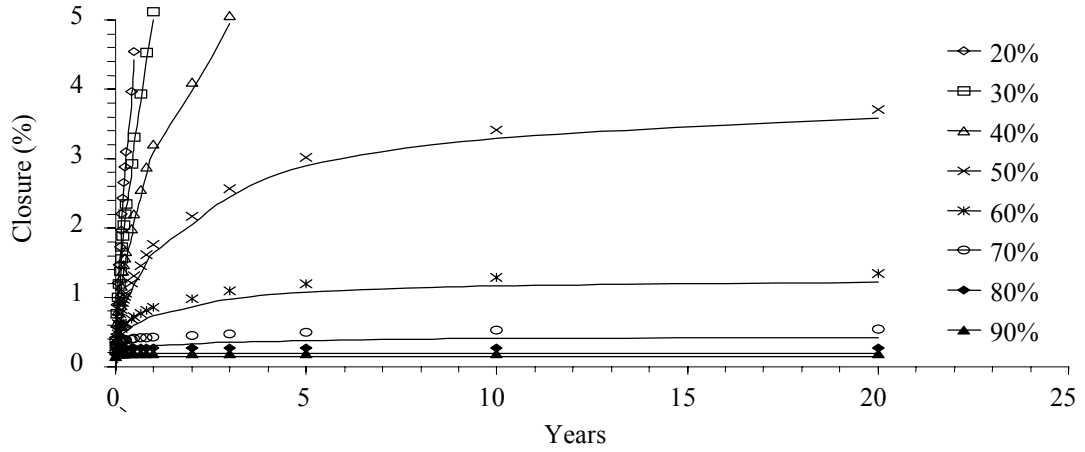

Figure A.9 Comparison of cavern wall closure in x-direction of model EL15 for 20 years after construction. The internal pressure in the cavern range between 20% to 90% of the in-situ stress at the cavern roof. The in-situ stress at the cavern roof for this model is 17.24 MPa (2,500 psi).

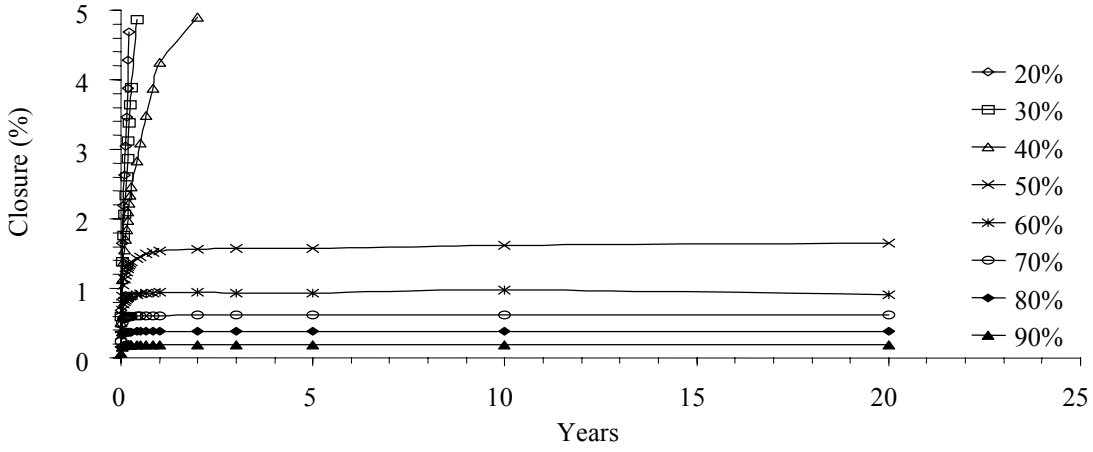

Figure A.10 Comparison of cavern wall closure in y-direction of model EL15 for 20 years after construction. The internal pressure in the cavern range between 20% to 90% of the in-situ stress at the cavern roof. The in-situ stress at the cavern roof for this model is 17.24 MPa (2,500 psi).

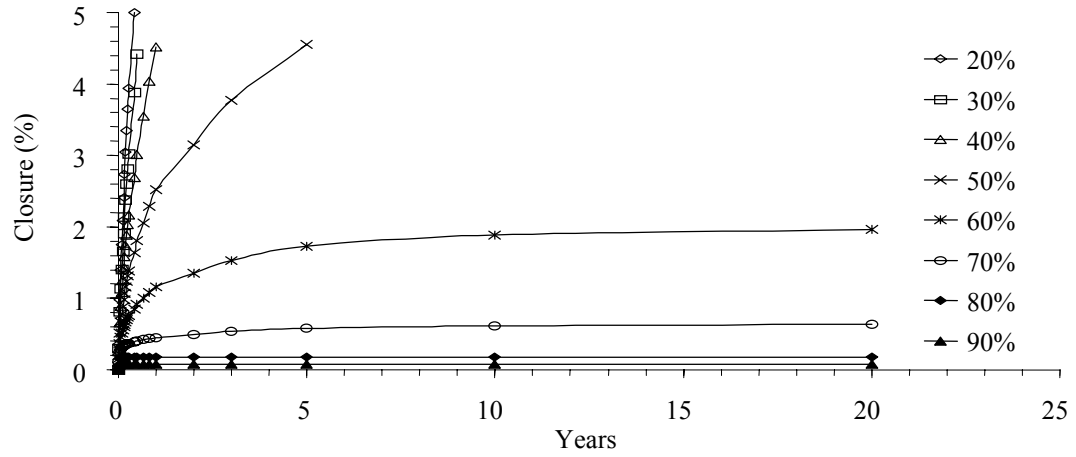

Figure A.11 Comparison of cavern wall closure in x-direction of model EL15 for 20 years after construction. The internal pressure in the cavern range between 20% to 90% of the in-situ stress at the cavern roof. The in-situ stress at the cavern roof for this model is 20.69 MPa (3,000 psi).

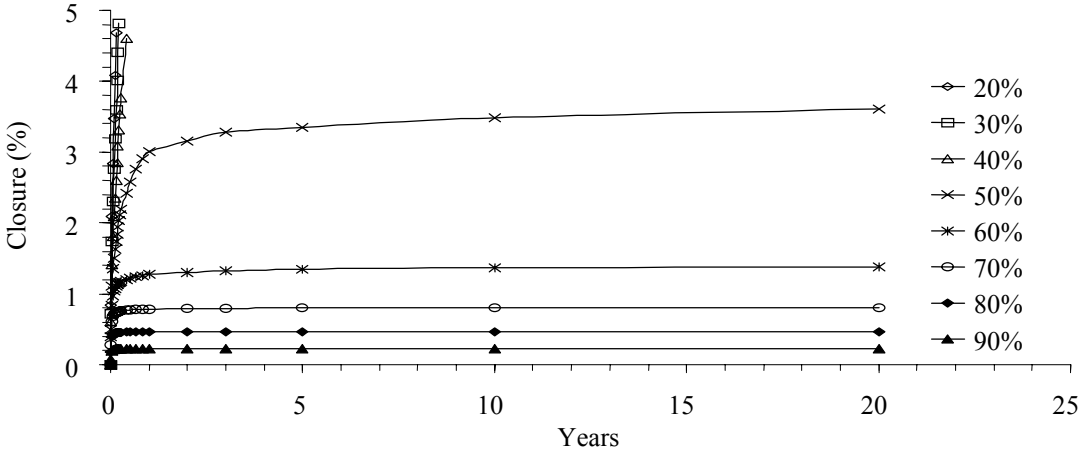

Figure A.12 Comparison of cavern wall closure in y-direction of model EL15 for 20 years after construction. The internal pressure in the cavern range between 20% to 90% of the in-situ stress at the cavern roof. The in-situ stress at the cavern roof for this model is 20.69 MPa (3,000 psi).

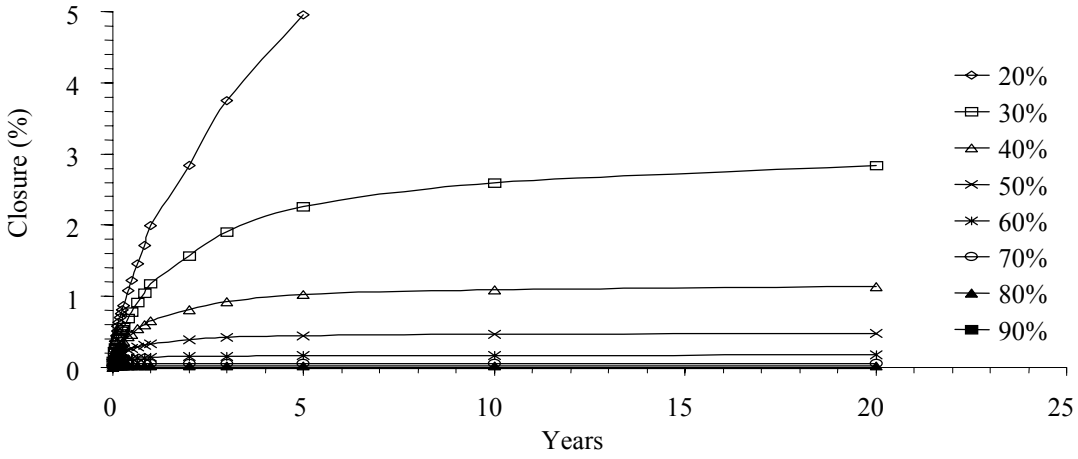

Figure A.13 Comparison of cavern wall closure in x-direction of model EL20 for 20 years after construction. The internal pressure in the cavern range between 20% to 90% of the in-situ stress at the cavern roof. The in-situ stress at the cavern roof for this model is 10.34 MPa (1,500 psi).

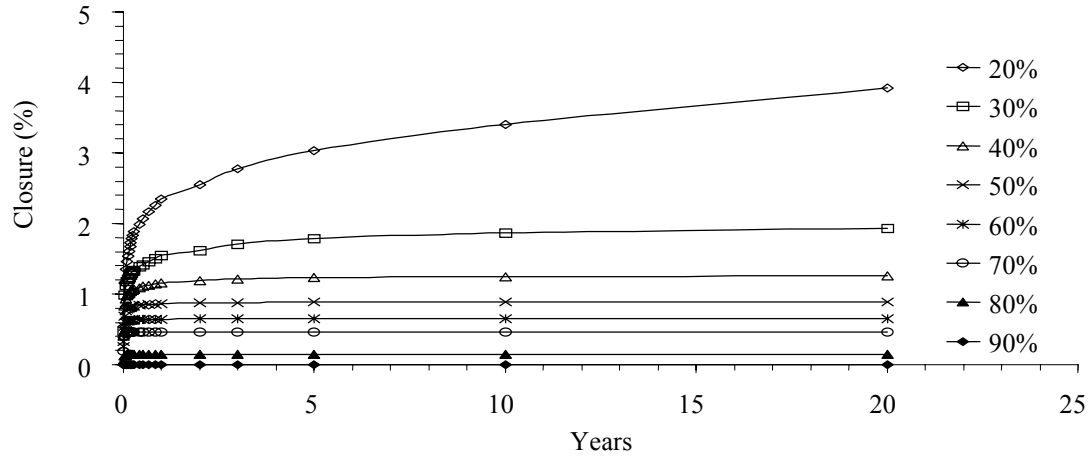

Figure A.14 Comparison of cavern wall closure in y-direction of model EL20 for 20 years after construction. The internal pressure in the cavern range between 20% to 90% of the in-situ stress at the cavern roof. The in-situ stress at the cavern roof for this model is 10.34 MPa (1,500 psi).

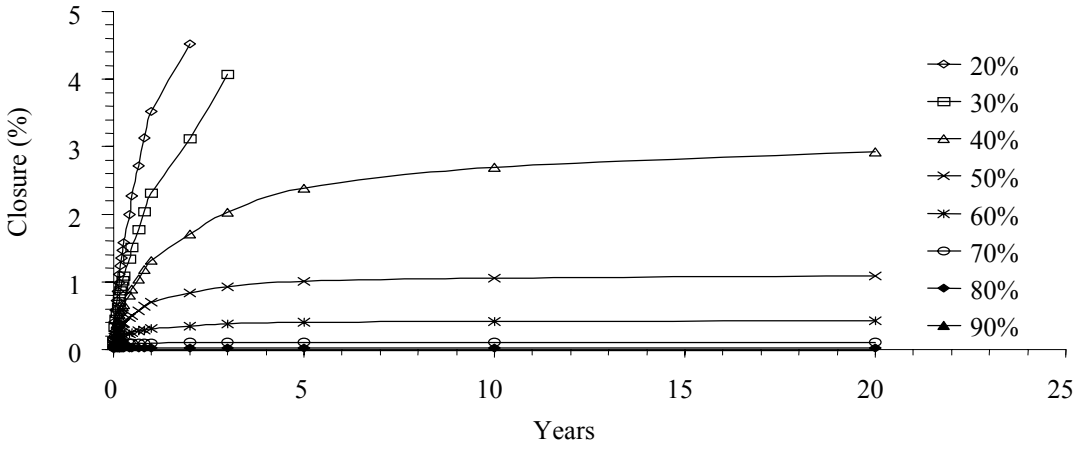

Figure A.15 Comparison of cavern wall closure in x-direction of model EL20 for 20 years after construction. The internal pressure in the cavern range between 20% to 90% of the in-situ stress at the cavern roof. The in-situ stress at the cavern roof for this model is 13.79 MPa (2,000 psi).

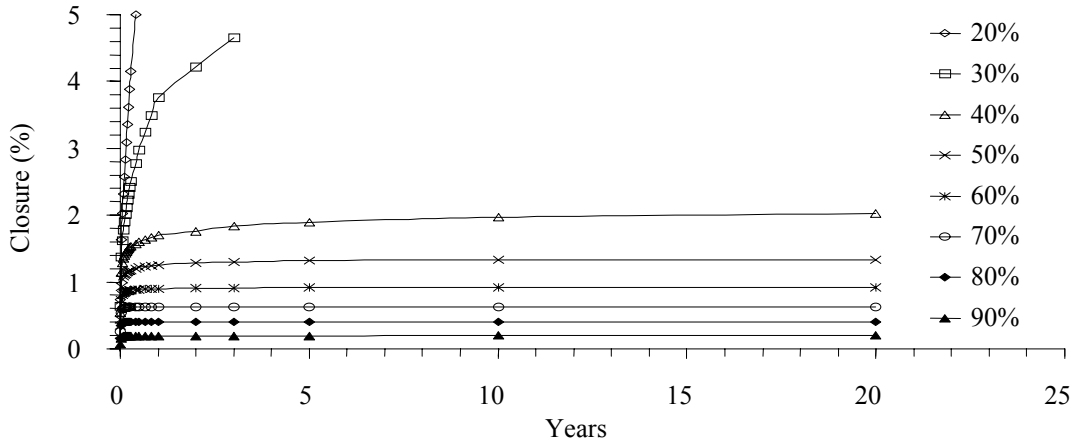

Figure A.16 Comparison of cavern wall closure in y-direction of model EL20 for 20 years after construction. The internal pressure in the cavern range between 20% to 90% of the in-situ stress at the cavern roof. The in-situ stress at the cavern roof for this model is 13.79 MPa (2,000 psi).

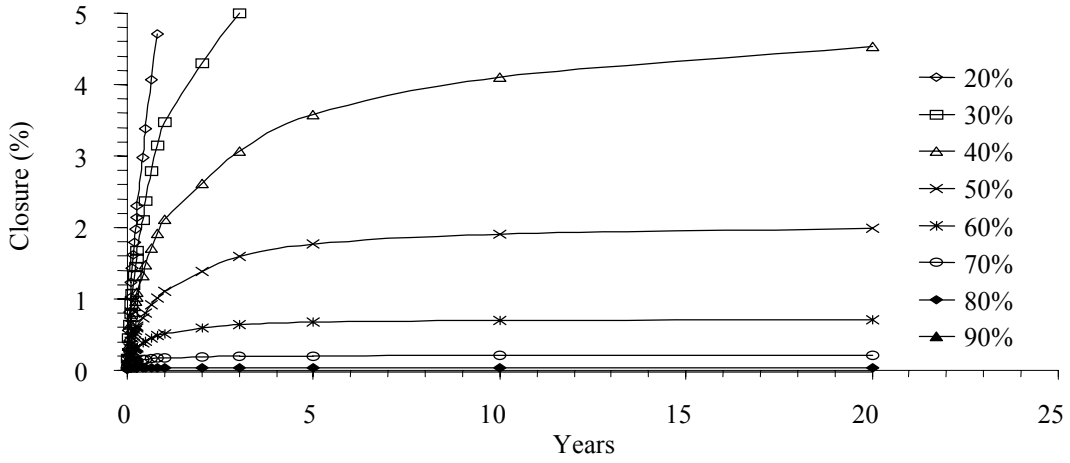

Figure A.17 Comparison of cavern wall closure in x-direction of model EL20 for 20 years after construction. The internal pressure in the cavern range between 20% to 90% of the in-situ stress at the cavern roof. The in-situ stress at the cavern roof for this model is 17.24 MPa (2,500 psi).

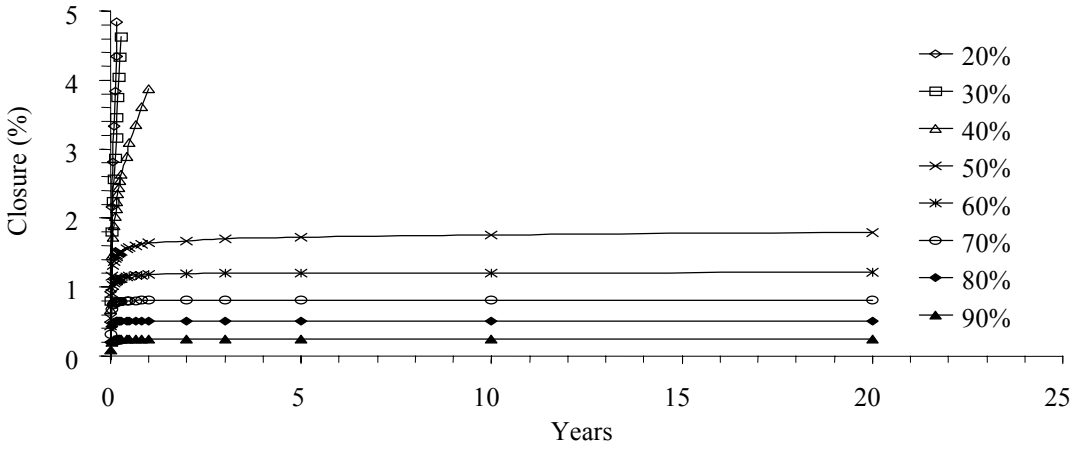

Figure A.18 Comparison of cavern wall closure in y-direction of model EL20 for 20 years after construction. The internal pressure in the cavern range between 20% to 90% of the in-situ stress at the cavern roof. The in-situ stress at the cavern roof for this model is 17.24 MPa (2,500 psi).

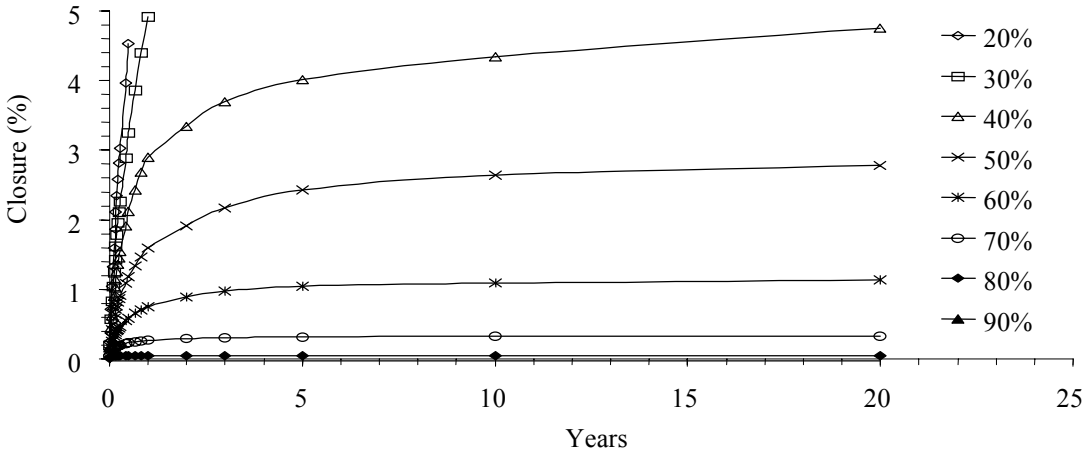

Figure A.19 Comparison of cavern wall closure in x-direction of model EL20 for 20 years after construction. The internal pressure in the cavern range between 20% to 90% of the in-situ stress at the cavern roof. The in-situ stress at the cavern roof for this model is 20.69 MPa (3,000 psi).

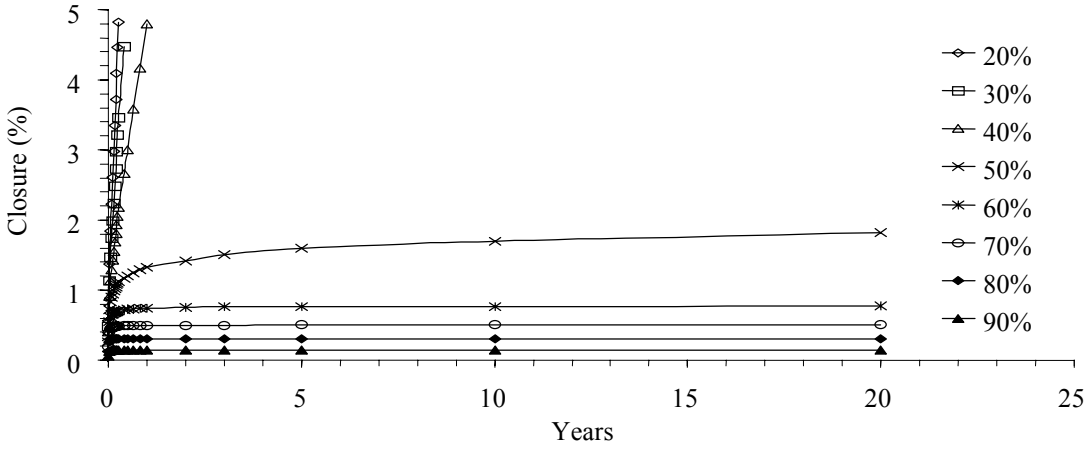

Figure A.20 Comparison of cavern wall closure in y-direction of model EL20 for 20 years after construction. The internal pressure in the cavern range between 20% to 90% of the in-situ stress at the cavern roof. The in-situ stress at the cavern roof for this model is 20.69 MPa (3,000 psi).

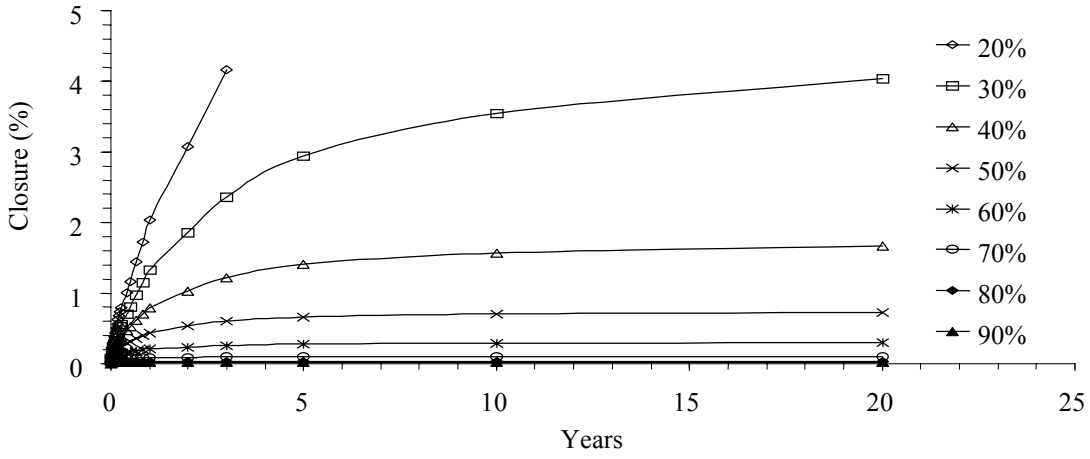

Figure A.21 Comparison of cavern wall closure in x-direction of model EL25 for 20 years after construction. The internal pressure in the cavern range between 20% to 90% of the in-situ stress at the cavern roof. The in-situ stress at the cavern roof for this model is 10.34 MPa (1,500 psi).

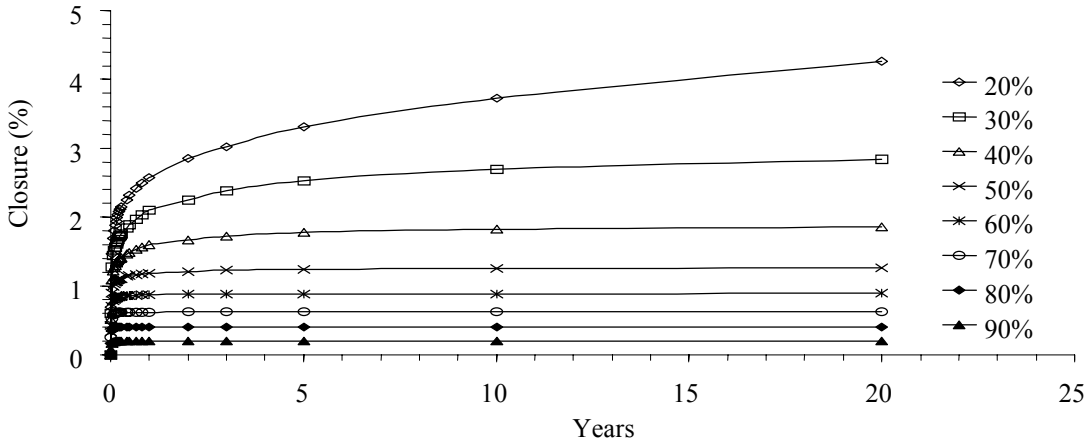

Figure A.22 Comparison of cavern wall closure in y-direction of model EL25 for 20 years after construction. The internal pressure in the cavern range between 20% to 90% of the in-situ stress at the cavern roof. The in-situ stress at the cavern roof for this model is 10.34 MPa (1,500 psi).

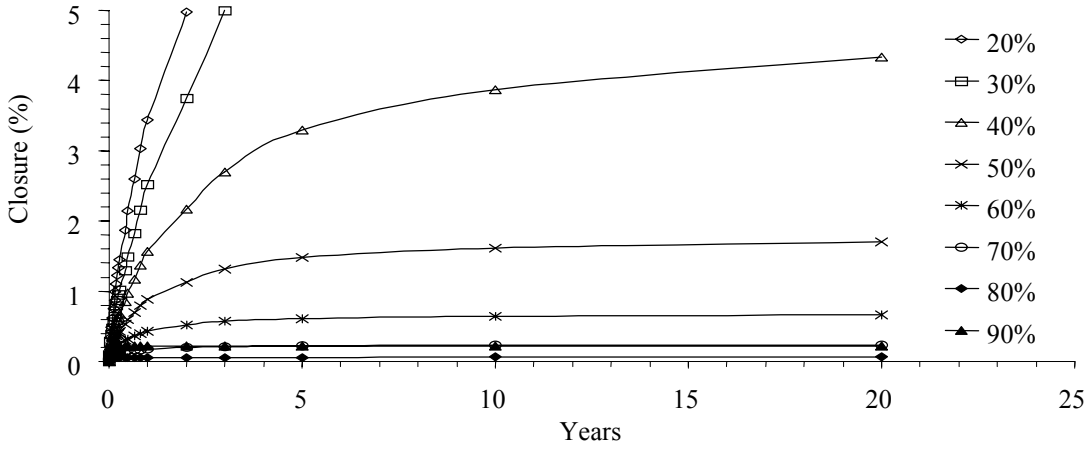

Figure A.23 Comparison of cavern wall closure in x-direction of model EL25 for 20 years after construction. The internal pressure in the cavern range between 20% to 90% of the in-situ stress at the cavern roof. The in-situ stress at the cavern roof for this model is 13.79 MPa (2,000 psi).

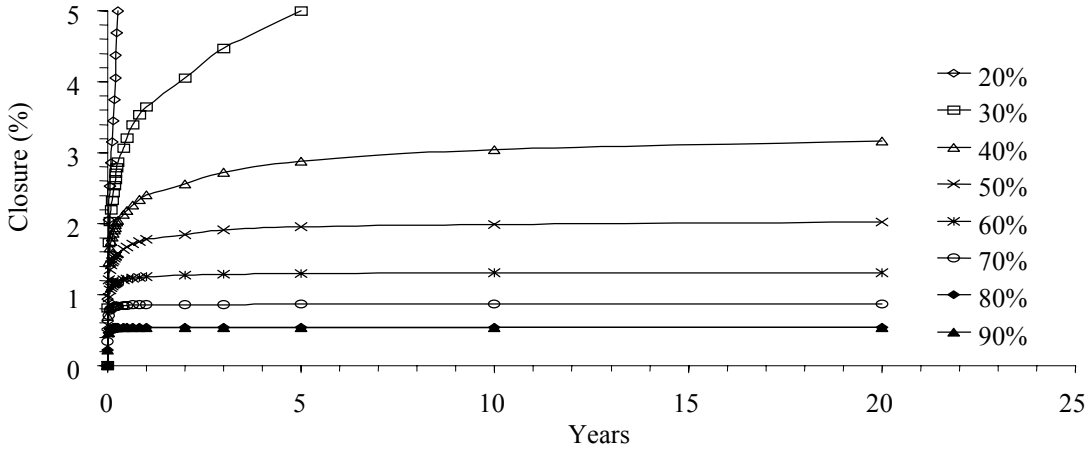

Figure A.24 Comparison of cavern wall closure in y-direction of model EL25 for 20 years after construction. The internal pressure in the cavern range between 20% to 90% of the in-situ stress at the cavern roof. The in-situ stress at the cavern roof for this model is 13.79 MPa (2,000 psi).

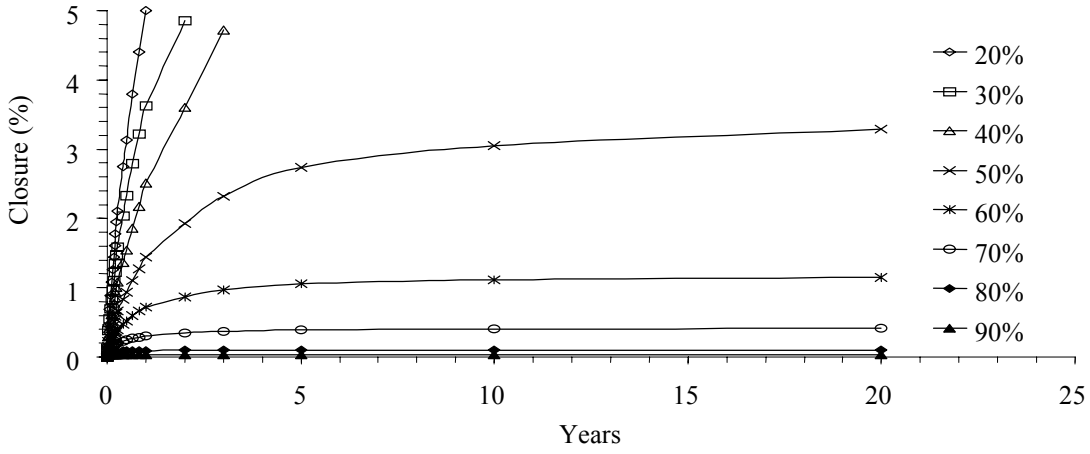

Figure A.25 Comparison of cavern wall closure in x-direction of model EL25 for 20 years after construction. The internal pressure in the cavern range between 20% to 90% of the in-situ stress at the cavern roof. The in-situ stress at the cavern roof for this model is 17.24 MPa (2,500 psi).

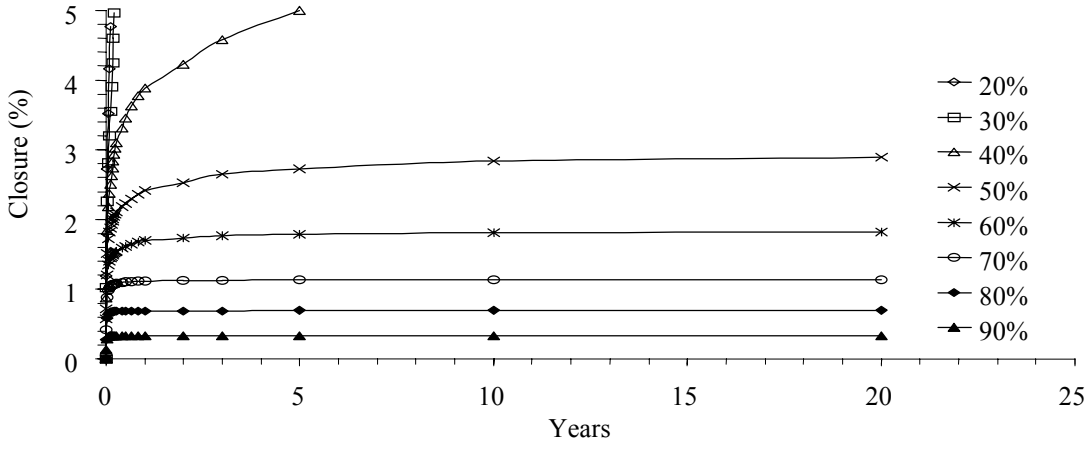

Figure A.26 Comparison of cavern wall closure in y-direction of model EL25 for 20 years after construction. The internal pressure in the cavern range between 20% to 90% of the in-situ stress at the cavern roof. The in-situ stress at the cavern roof for this model is 17.24 MPa (2,500 psi).

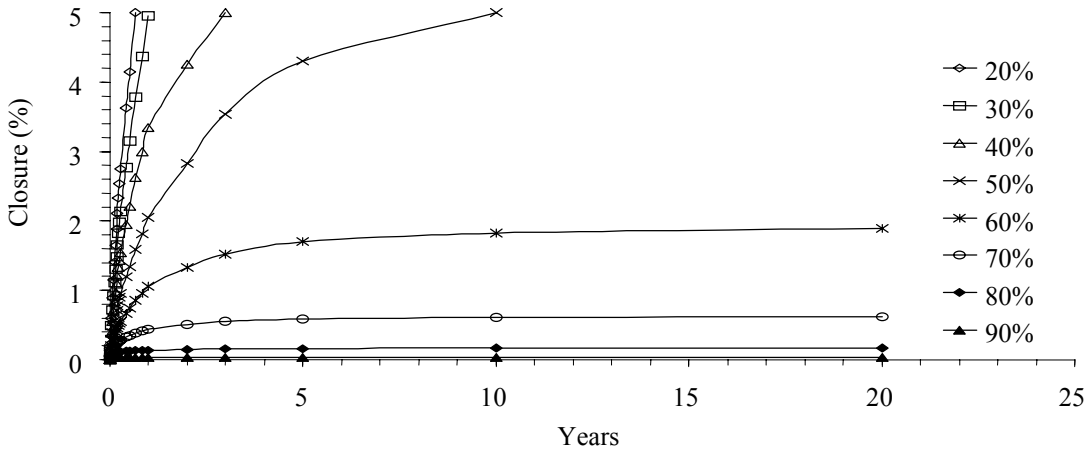

Figure A.27 Comparison of cavern wall closure in x-direction of model EL25 for 20 years after construction. The internal pressure in the cavern range between 20% to 90% of the in-situ stress at the cavern roof. The in-situ stress at the cavern roof for this model is 20.69 MPa (3,000 psi).

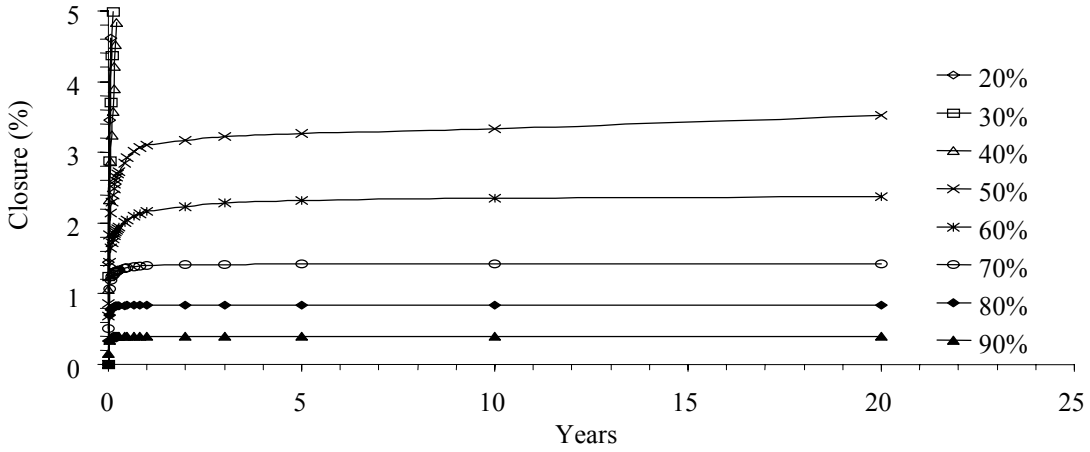

Figure A.28 Comparison of cavern wall closure in y-direction of model EL25 for 20 years after construction. The internal pressure in the cavern range between 20% to 90% of the in-situ stress at the cavern roof. The in-situ stress at the cavern roof for this model is 20.69 MPa (3,000 psi).

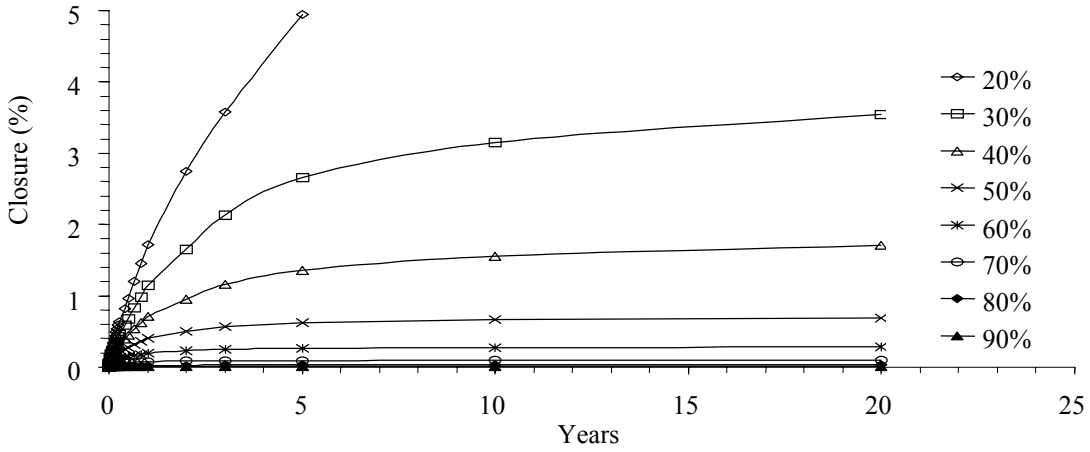

Figure A.29 Comparison of cavern wall closure in x-direction of model EL30 for 20 years after construction. The internal pressure in the cavern range between 20% to 90% of the in-situ stress at the cavern roof. The in-situ stress at the cavern roof for this model is 10.34 MPa (1,500 psi).

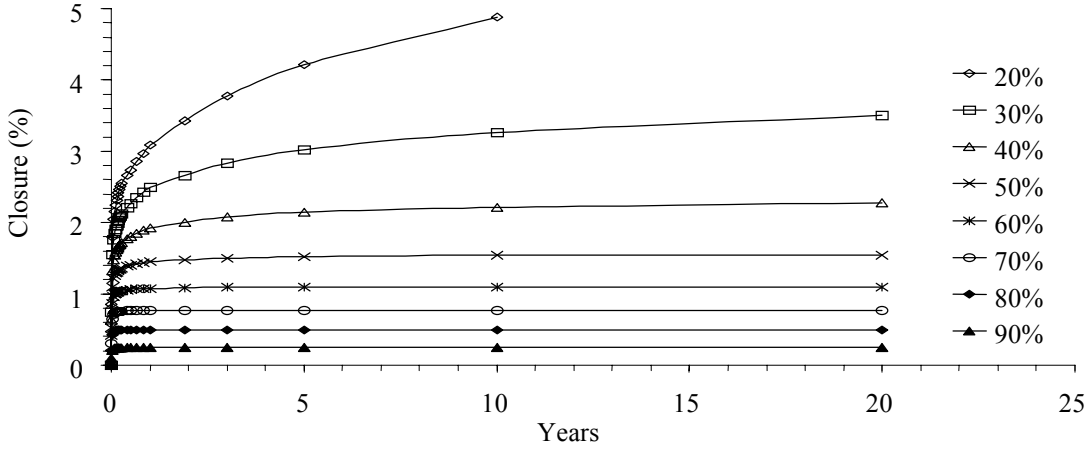

Figure A.30 Comparison of cavern wall closure in y-direction of model EL30 for 20 years after construction. The internal pressure in the cavern range between 20% to 90% of the in-situ stress at the cavern roof. The in-situ stress at the cavern roof for this model is 10.34 MPa (1,500 psi).

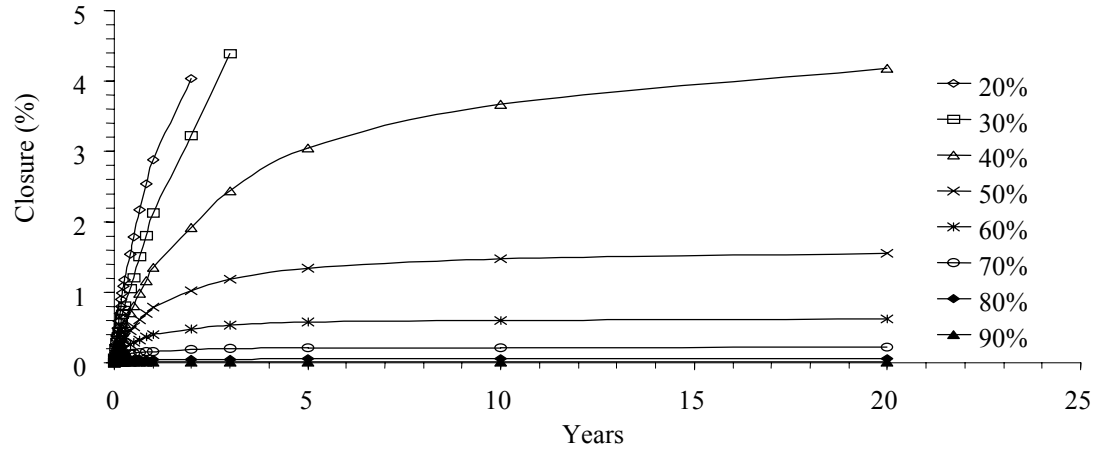

Figure A.31 Comparison of cavern wall closure in x-direction of model EL30 for 20 years after construction. The internal pressure in the cavern range between 20% to 90% of the in-situ stress at the cavern roof. The in-situ stress at the cavern roof for this model is 13.79 MPa (2,000 psi).

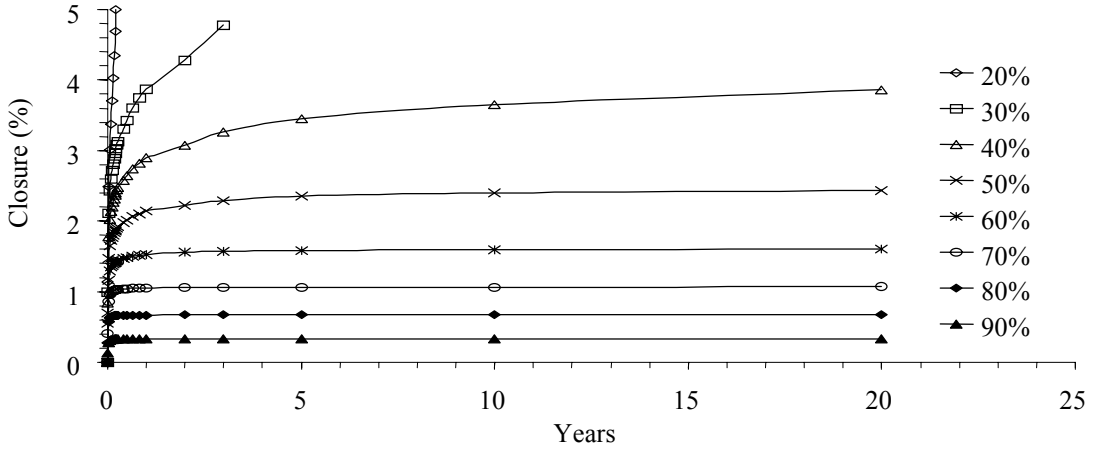

Figure A.32 Comparison of cavern wall closure in y-direction of model EL30 for 20 years after construction. The internal pressure in the cavern range between 20% to 90% of the in-situ stress at the cavern roof. The in-situ stress at the cavern roof for this model is 13.79 MPa (2,000 psi).

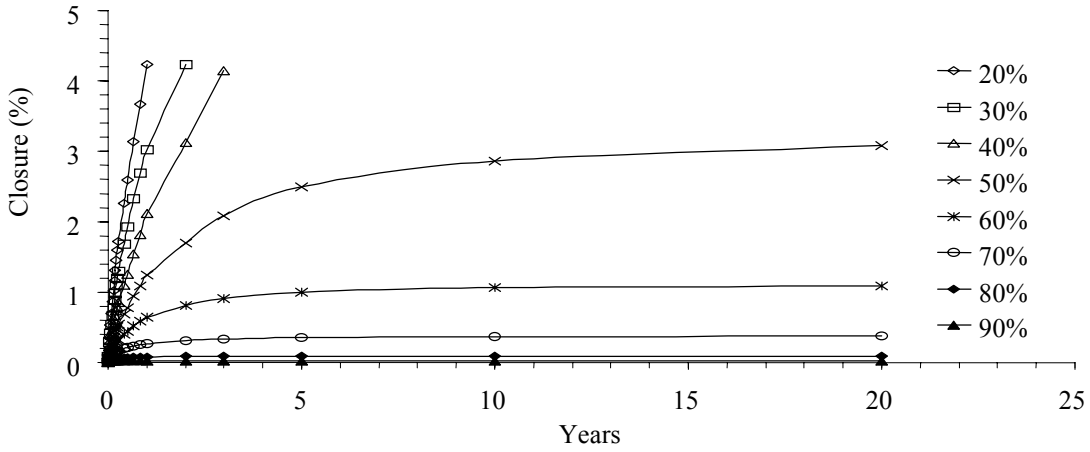

Figure A.33 Comparison of cavern wall closure in x-direction of model EL30 for 20 years after construction. The internal pressure in the cavern range between 20% to 90% of the in-situ stress at the cavern roof. The in-situ stress at the cavern roof for this model is 17.24 MPa (2,500 psi).

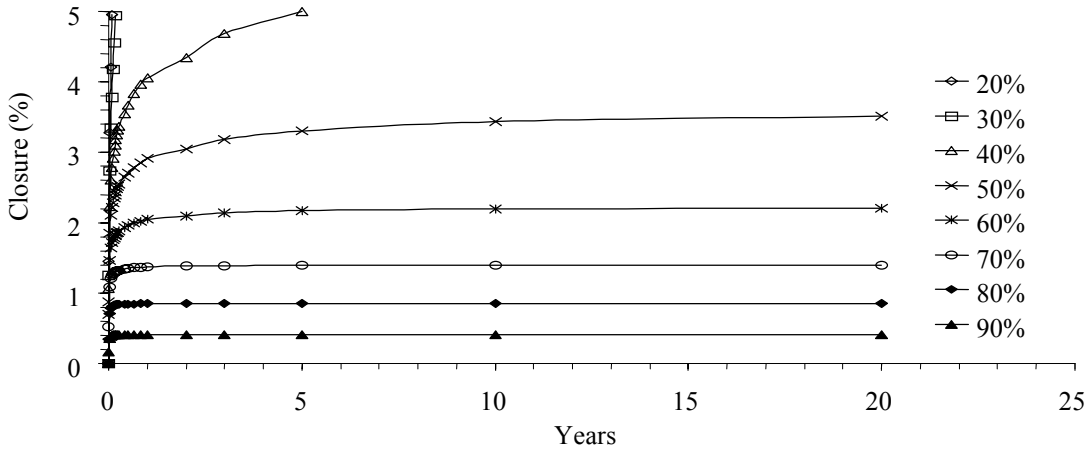

Figure A.34 Comparison of cavern wall closure in y-direction of model EL30 for 20 years after construction. The internal pressure in the cavern range between 20% to 90% of the in-situ stress at the cavern roof. The in-situ stress at the cavern roof for this model is 17.24 MPa (2,500 psi).

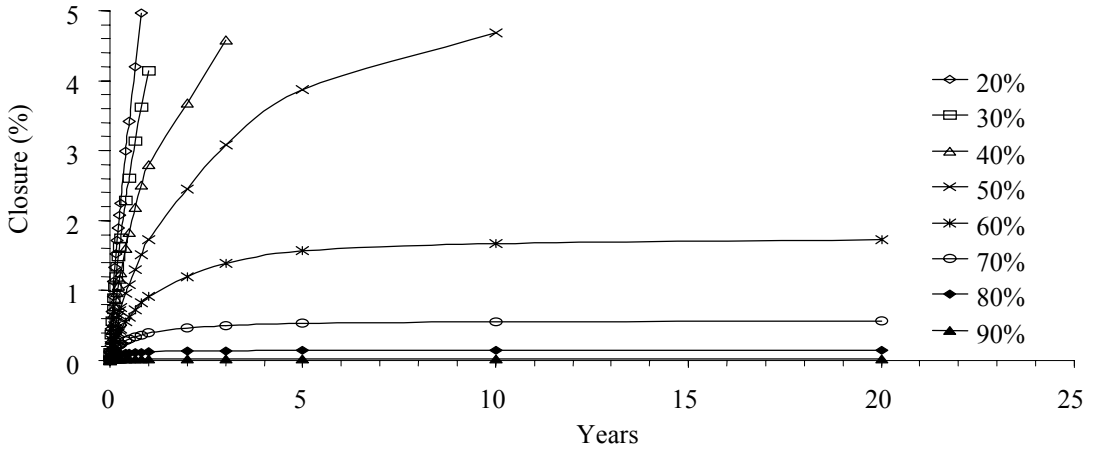

Figure A.35 Comparison of cavern wall closure in x-direction of model EL30 for 20 years after construction. The internal pressure in the cavern range between 20% to 90% of the in-situ stress at the cavern roof. The in-situ stress at the cavern roof for this model is 20.69 MPa (3,000 psi).

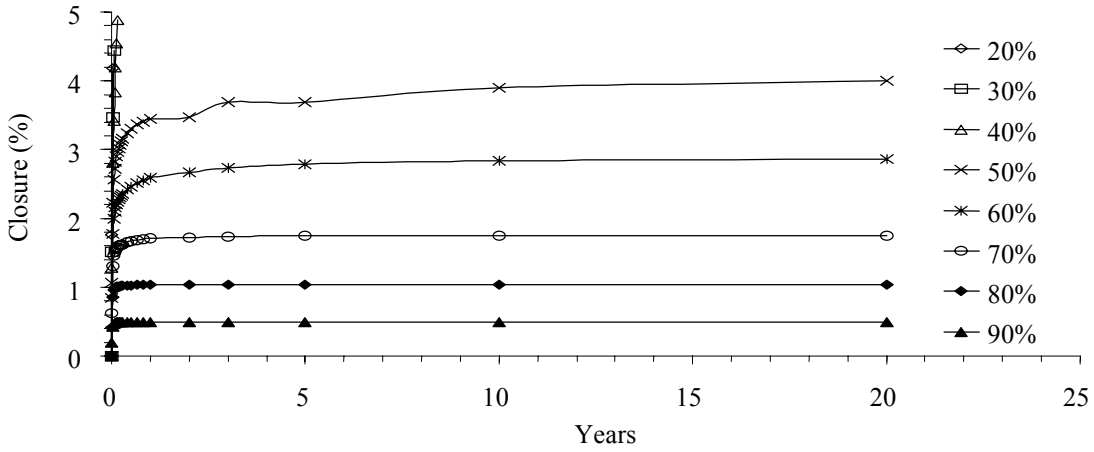

Figure A.36 Comparison of cavern wall closure in x-direction of model EL30 for 20 years after construction. The internal pressure in the cavern range between 20% to 90% of the in-situ stress at the cavern roof. The in-situ stress at the cavern roof for this model is 20.69 MPa (3,000 psi).

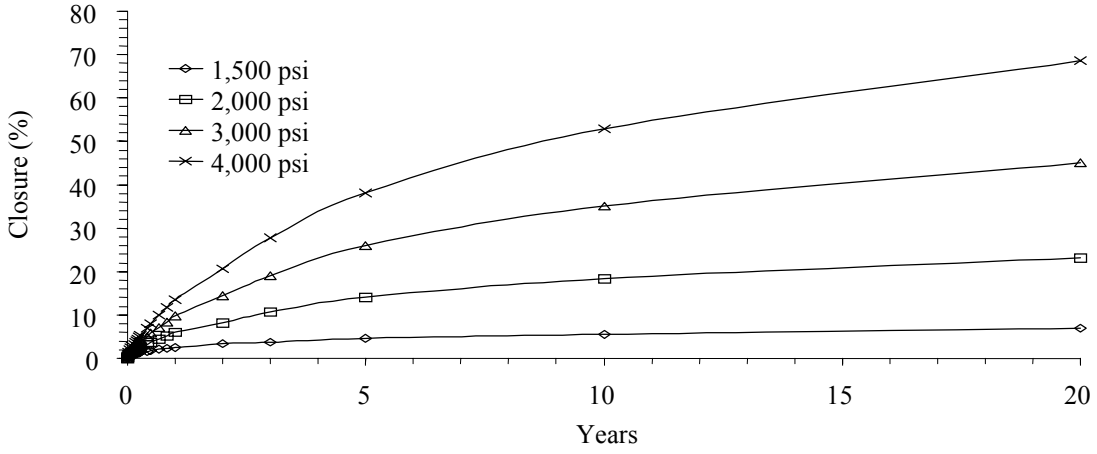

Figure A.37 Comparison of cavern wall closure in x- and y-directions of model SP10 for 20 years after construction. The internal pressure in the cavern is 20% of the in-situ stress (external pressure). The in-situ stresses for this model are 1,500, 2,000, 2,500 and 3,000 psi.

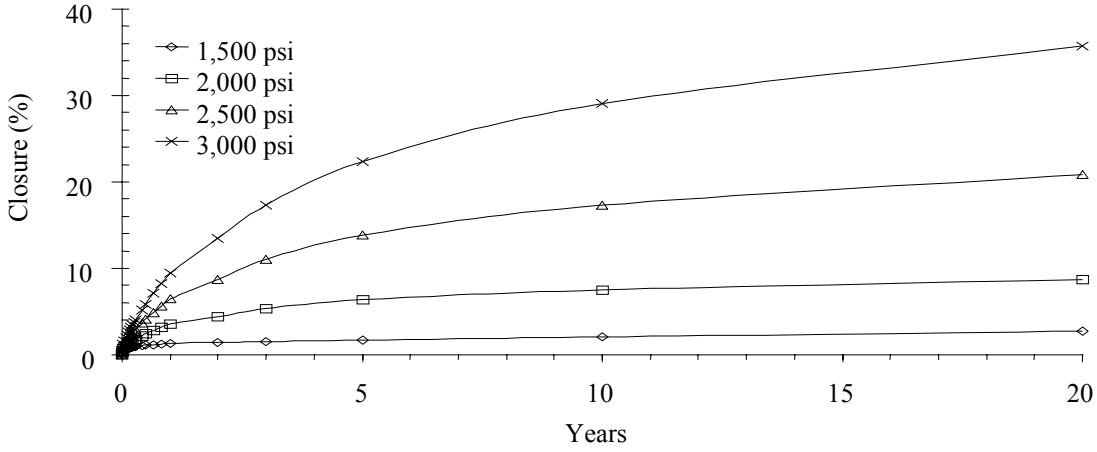

Figure A.38 Comparison of cavern wall closure in x- and y-directions of model SP10 for 20 years after construction. The internal pressure in the cavern is 30% of the in-situ stress (external pressure). The in-situ stresses for this model are 1,500, 2,000, 2,500 and 3,000 psi.

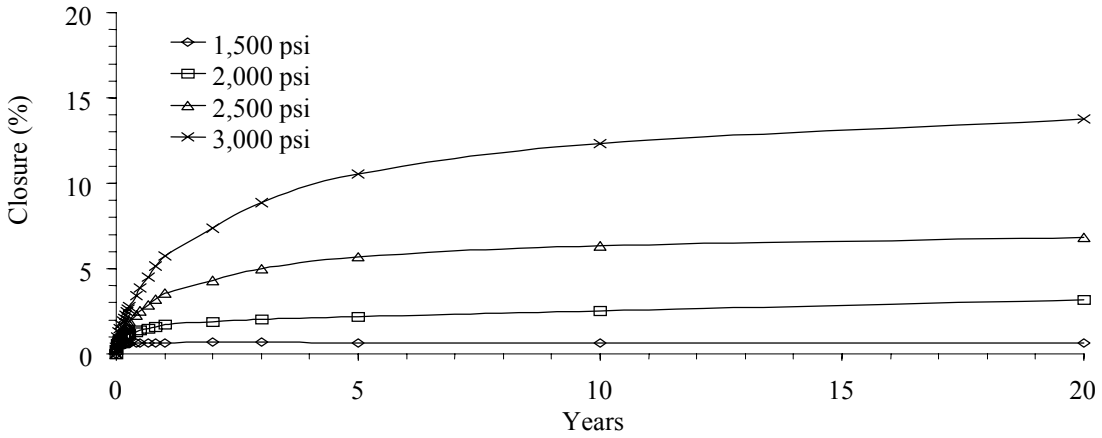

Figure A.39 Comparison of cavern wall closure in x- and y-directions of model SP10 for 20 years after construction. The internal pressure in the cavern is 40% of the in-situ stress (external pressure). The in-situ stresses for this model are 1,500, 2,000, 2,500 and 3,000 psi.

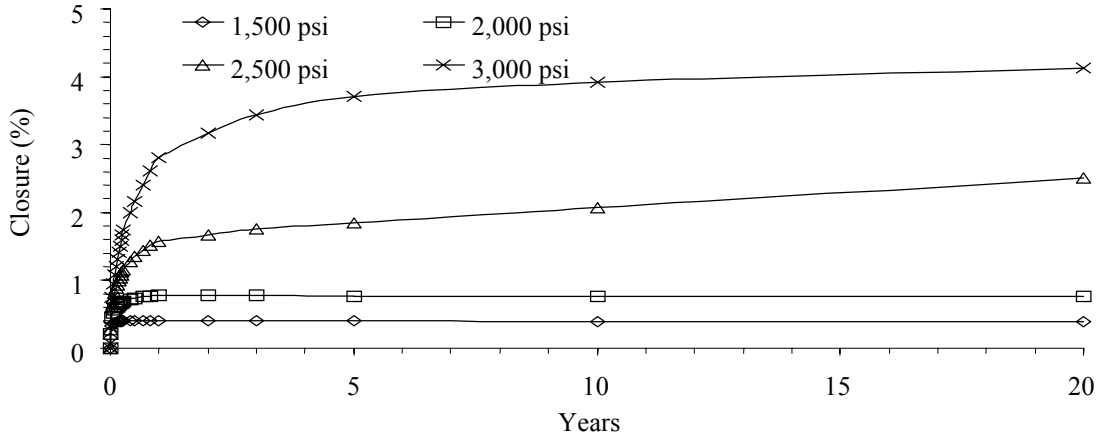

Figure A.40 Comparison of cavern wall closure in x- and y-directions of model SP10 for 20 years after construction. The internal pressure in the cavern is 50% of the in-situ stress (external pressure). The in-situ stresses for this model are 1,500, 2,500, 2,500, and 3,000 psi.

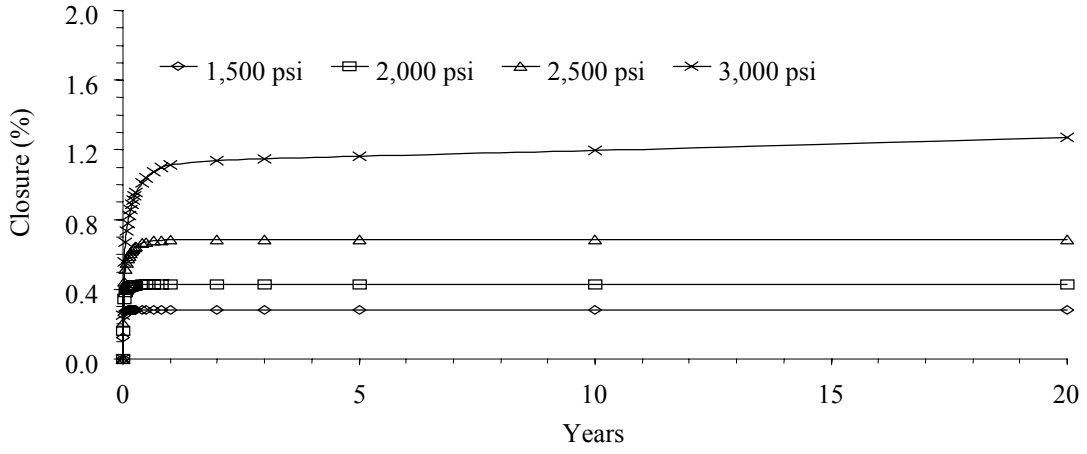

Figure A.41 Comparison of cavern wall closure in x- and y-directions of model SP10 for 20 years after construction. The internal pressure in the cavern is 60% of the in-situ stress (external pressure). The in-situ stresses for this model are 1,500, 2,000, 2,500 and 3,000 psi.

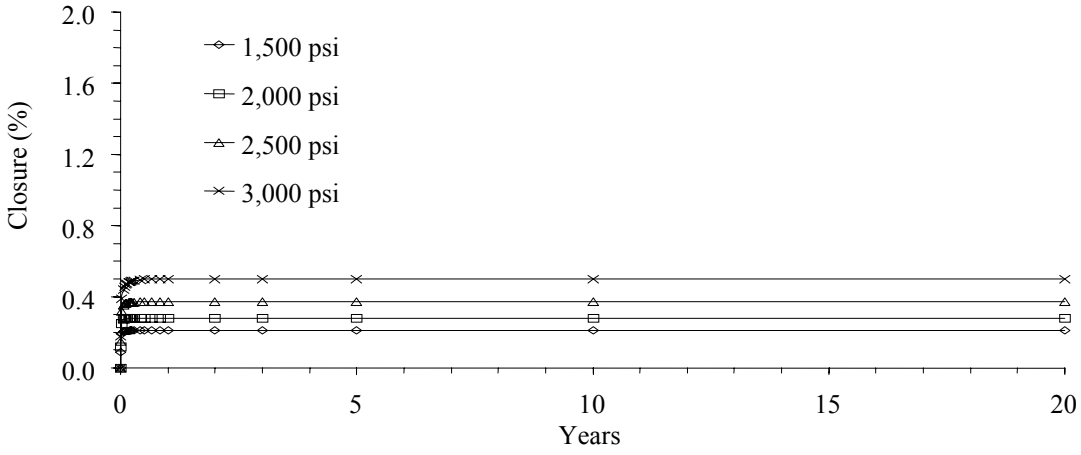

Figure A.42 Comparison of cavern wall closure in x- and y-directions of model SP10 for 20 years after construction. The internal pressure in the cavern is 70% of the in-situ stress (external pressure). The in-situ stresses for this model are 1,500, 2,000, 2,500 and 3,000 psi.

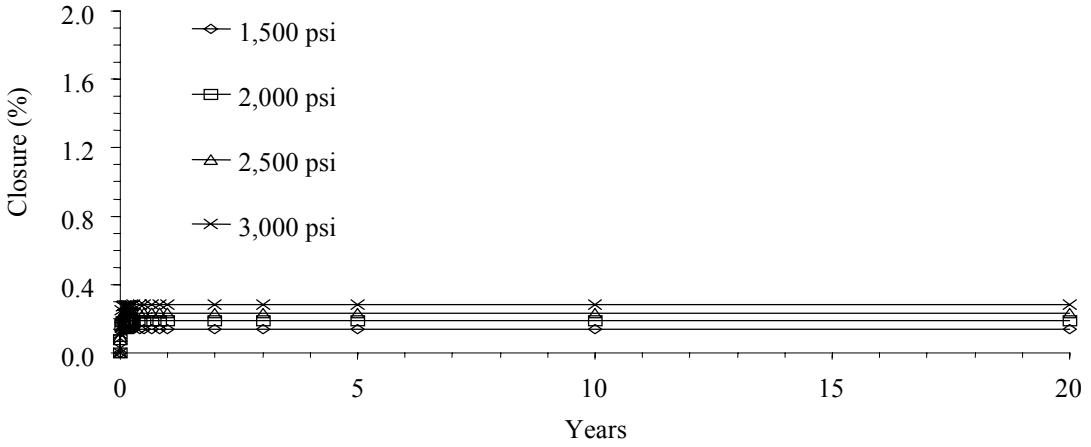

Figure A.43 Comparison of cavern wall closure in x- and y-directions of model SP10 for 20 years after construction. The internal pressure in the cavern is 80% of the in-situ stress (external pressure). The in-situ stresses for this model are 1,500, 2,000, 2,500 and 3,000 psi.

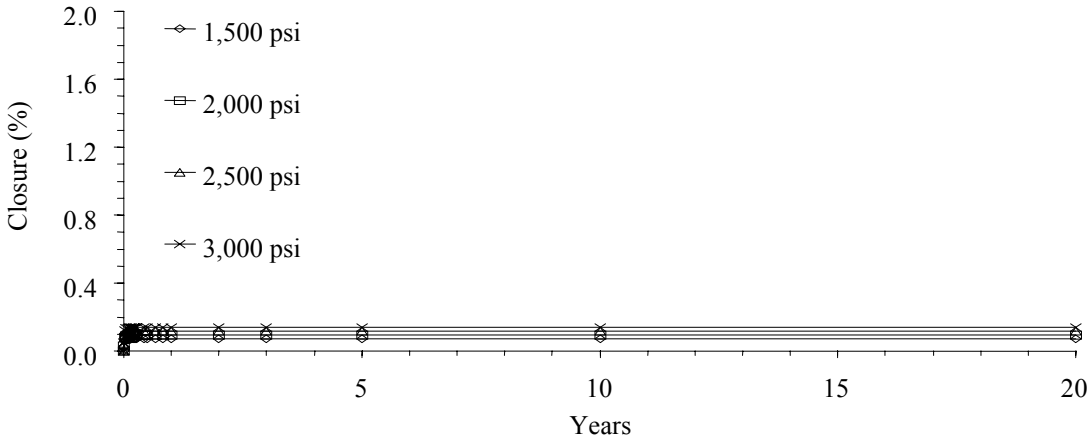

Figure A.44 Comparison of cavern wall closure in x- and y-directions of model SP10 for 20 years after construction. The internal pressure in the cavern is 90% of the in-situ stress (external pressure). The in-situ stresses for this model are 1,500, 2,000, 2,500 and 3,000 psi.

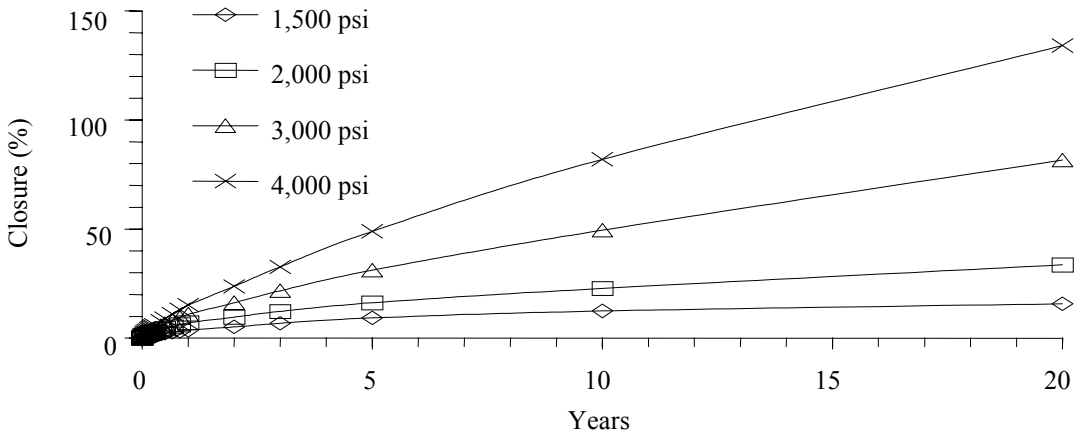

Figure A.45 Comparison of cavern wall closure in x-directions of model EL15 for 20 years after construction. The internal pressure in the cavern is 20% of the in-situ stress (external pressure). The in-situ stresses for this model are 1,500, 2,000, 2,500 and 3,000 psi.

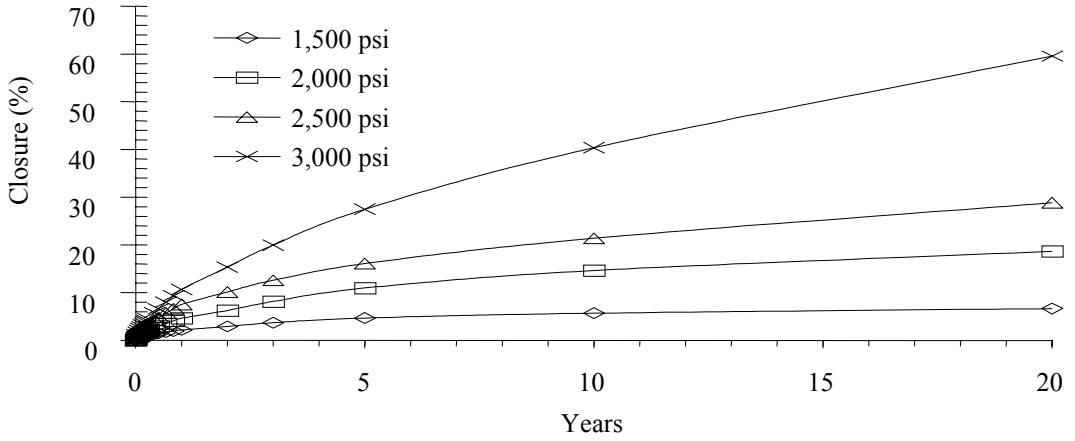

Figure A.46 Comparison of cavern wall closure in x-directions of model EL15 for 20 years after construction. The internal pressure in the cavern is 30% of the in-situ stress (external pressure). The in-situ stresses for this model are 1,500, 2,000, 2,500 and 3,000 psi.

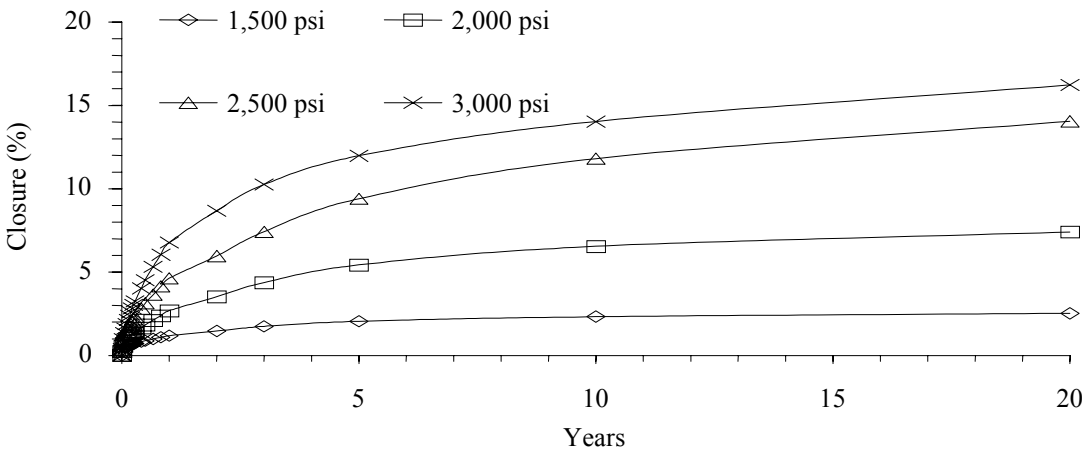

Figure A.47 Comparison of cavern wall closure in x-directions of model EL15 for 20 years after construction. The internal pressure in the cavern is 40% of the in-situ stress (external pressure). The in-situ stresses for this model are 1,500, 2,000, 2,500 and 3,000 psi.

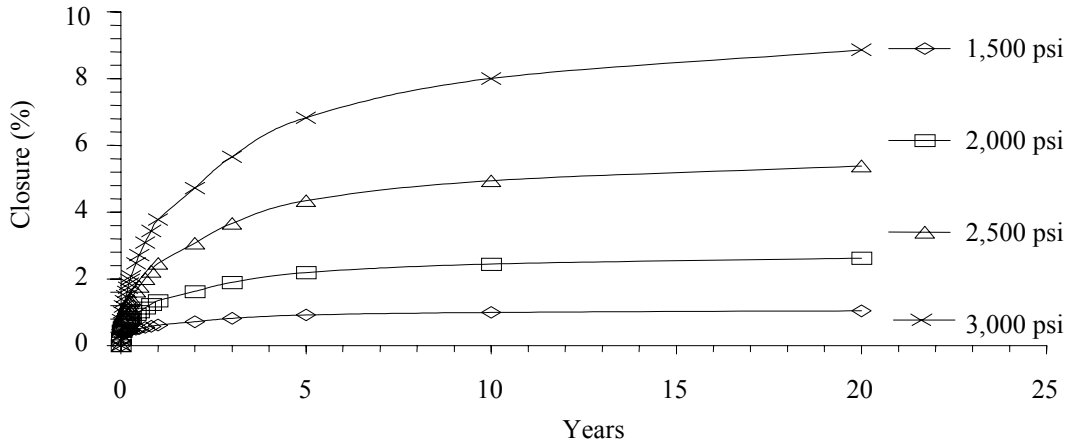

Figure A.48 Comparison of cavern wall closure in x-directions of model EL15 for 20 years after construction. The internal pressure in the cavern is 50% of the in-situ stress (external pressure). The in-situ stresses for this model are 1,500, 2,000, 2,500 and 3,000 psi.

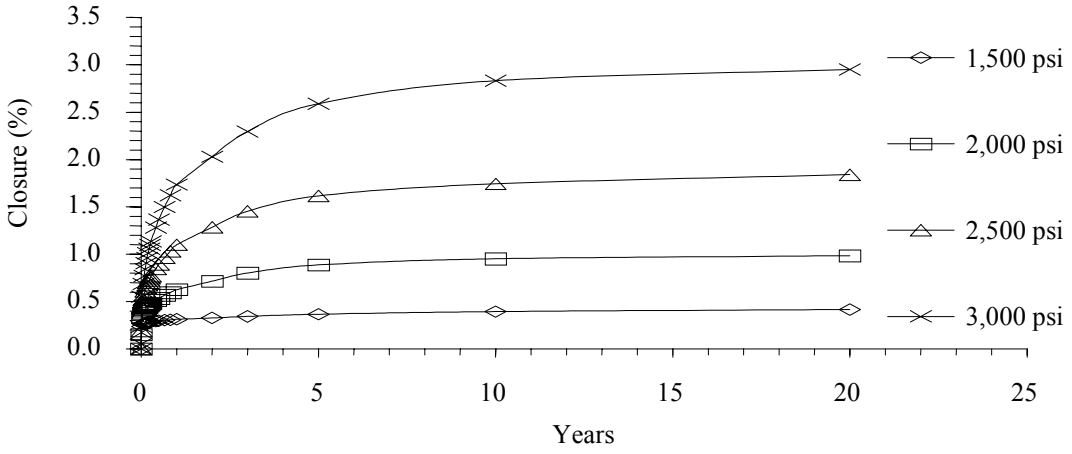

Figure A.49 Comparison of cavern wall closure in x-directions of model EL15 for 20 years after construction. The internal pressure in the cavern is 60% of the in-situ stress (external pressure). The in-situ stresses for this model are 1,500, 2,000, 2,500 and 3,000 psi.

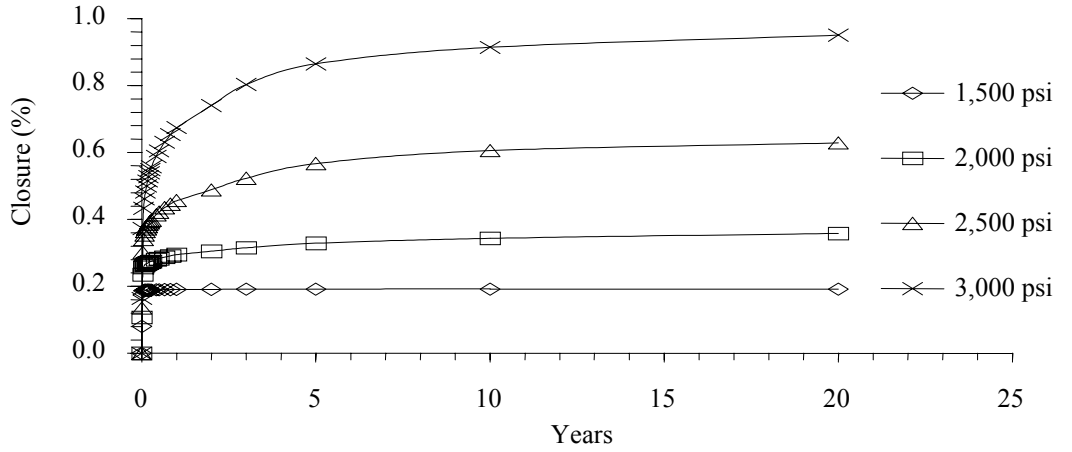

Figure A.50 Comparison of cavern wall closure in x-directions of model EL15 for 20 years after construction. The internal pressure in the cavern is 70% of the in-situ stress (external pressure). The in-situ stresses for this model are 1,500, 2,000, 2,500 and 3,000 psi.

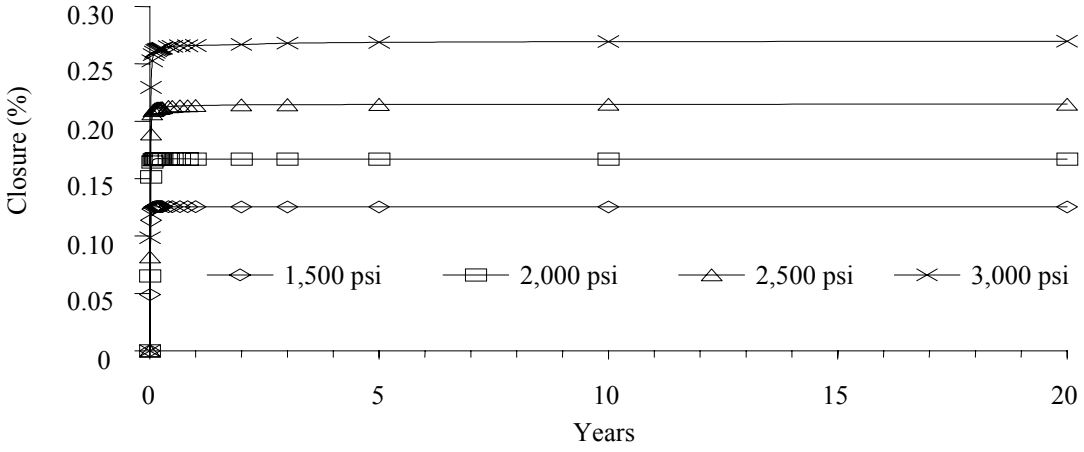

Figure A.51 Comparison of cavern wall closure in x-directions of model EL15 for 20 years after construction. The internal pressure in the cavern is 80% of the in-situ stress (external pressure). The in-situ stresses for this model are 1,500, 2,000, 2,500 and 3,000 psi.

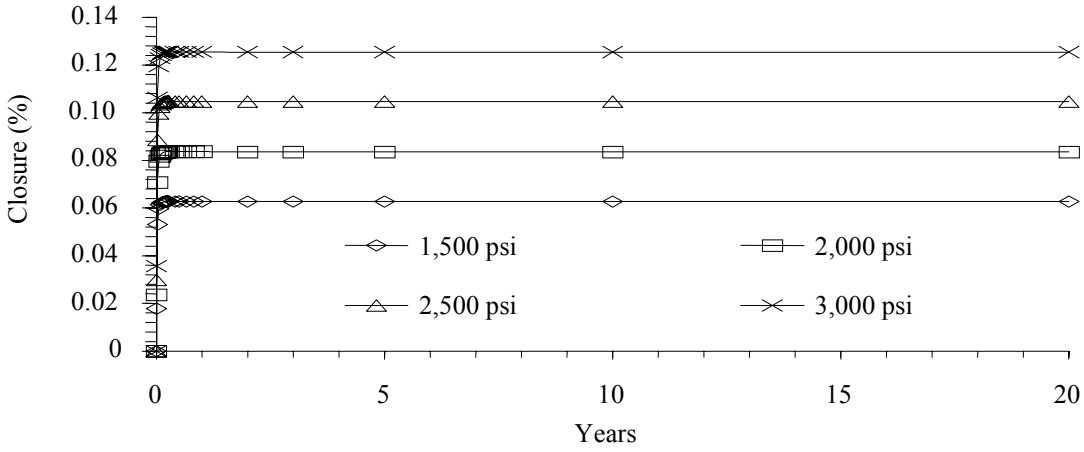

Figure A.52 Comparison of cavern wall closure in x-directions of model EL15 for 20 years after construction. The internal pressure in the cavern is 90% of the in-situ stress (external pressure). The in-situ stresses for this model are 1,500, 2,000, 2,500 and 3,000 psi.

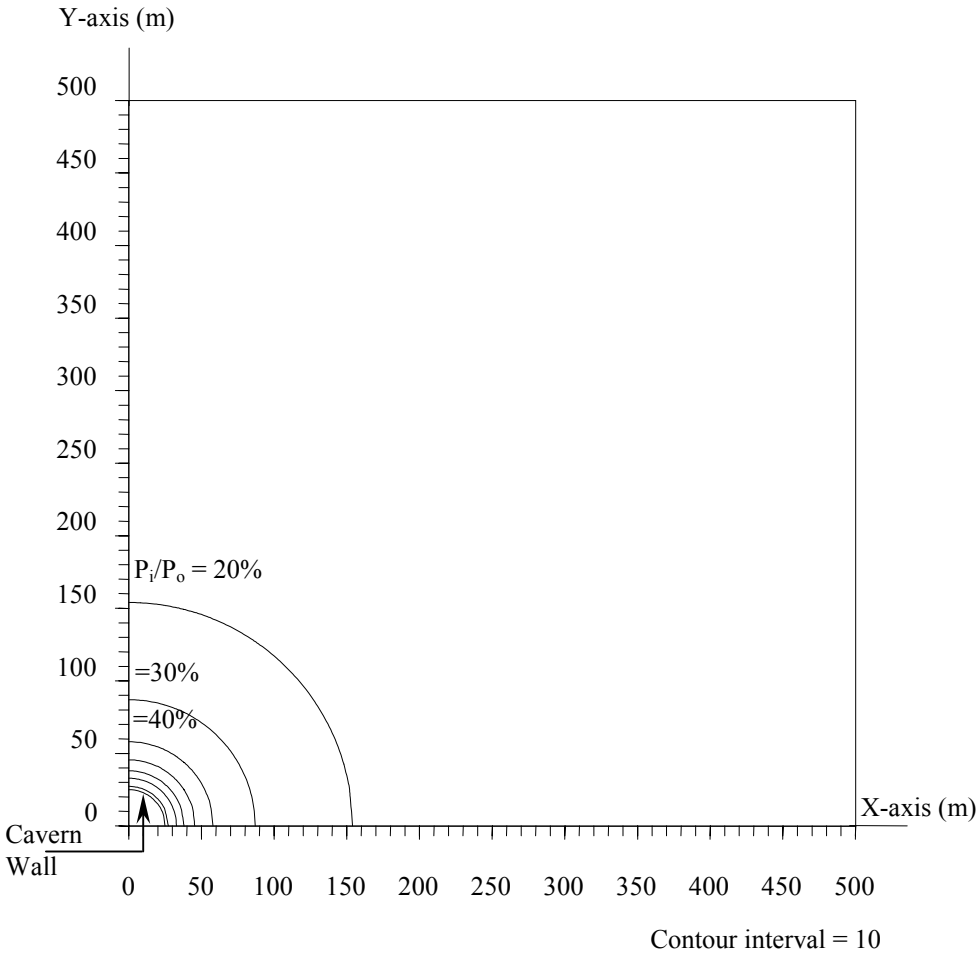

Figure A.53 Distributions of plastic zone boundary around the cavern (Model SP10) for the internal pressure ranging between 20% to 90% of in-situ stress (external pressure). The in-situ stress for this model is 10.34 MPa (1,500 psi).

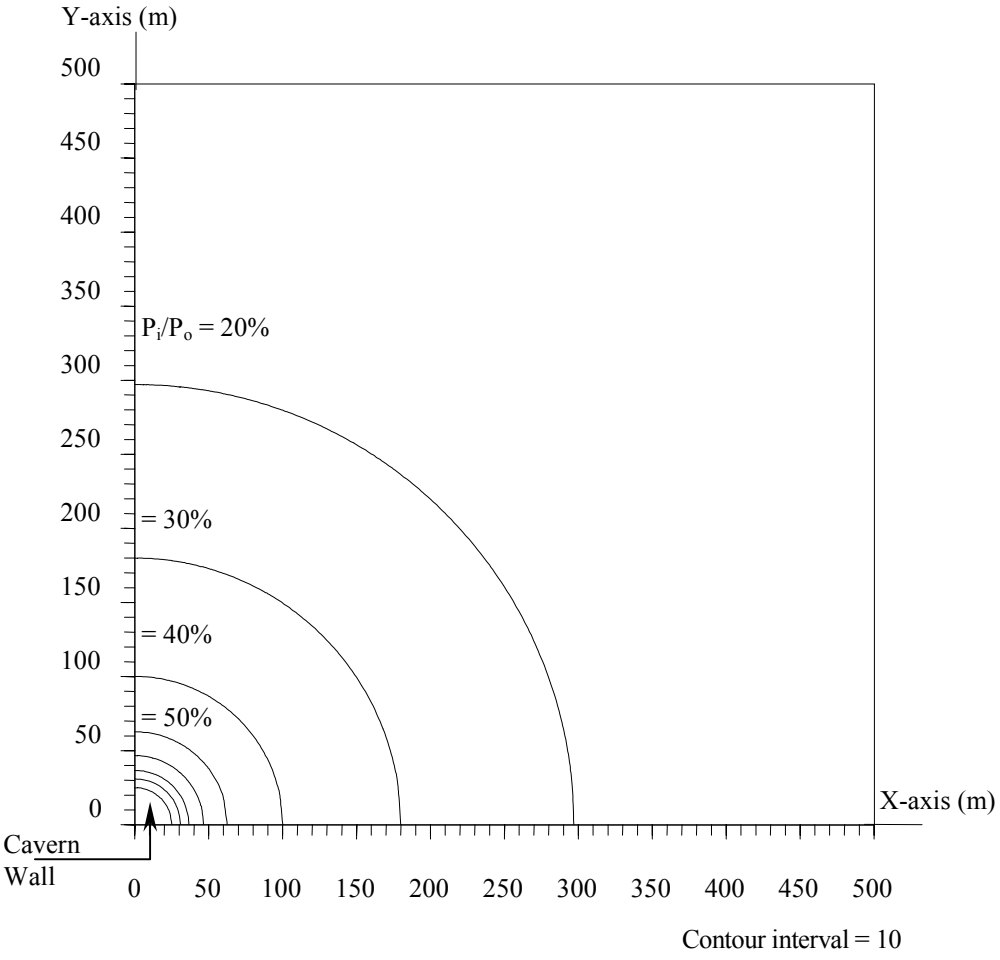

Figure A.54 Distributions of plastic zone boundary around the cavern (Model SP10) for the internal pressure ranging between 20% to 90% of in-situ stress (external pressure). The in-situ stress for this model is 13.79 MPa (2,000 psi).

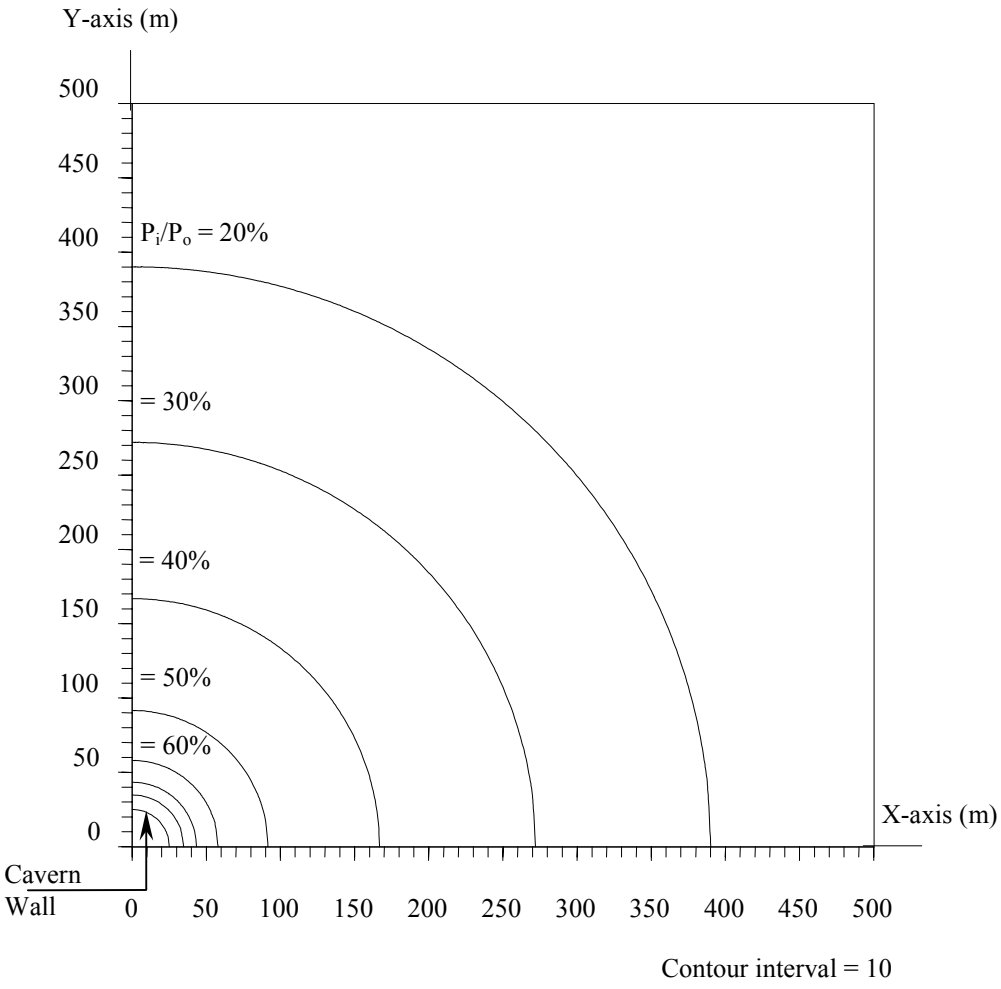

Figure A.55 Distributions of plastic zone boundary around the cavern (Model SP10) for the internal pressure ranging between 20% to 90% of in-situ stress (external pressure). The in-situ stress for this model is 17.24 MPa (2,500 psi).

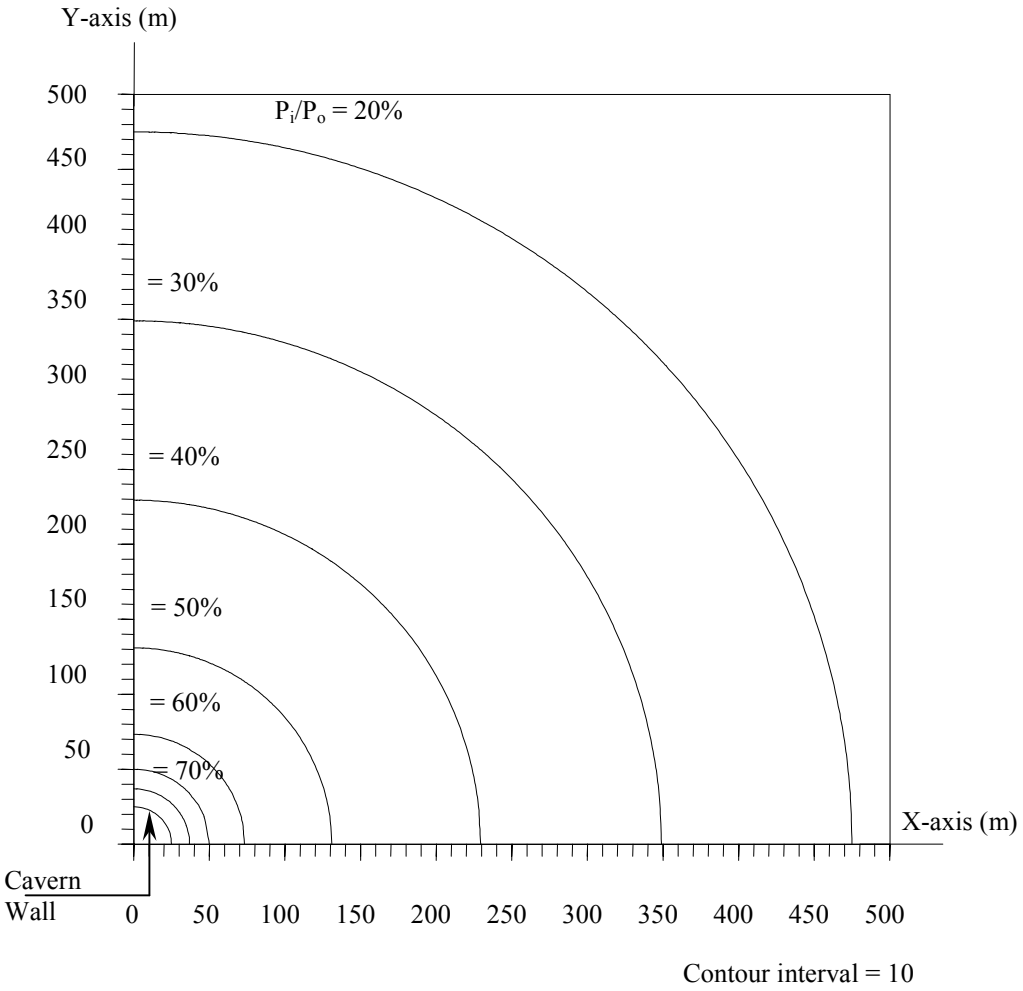

Figure A.56 Distributions of plastic zone boundary around the cavern (Model SP10) for the internal pressure ranging between 20% to 90% of in-situ stress (external pressure). The in-situ stress for this model is 20.69 MPa (3,000 psi).

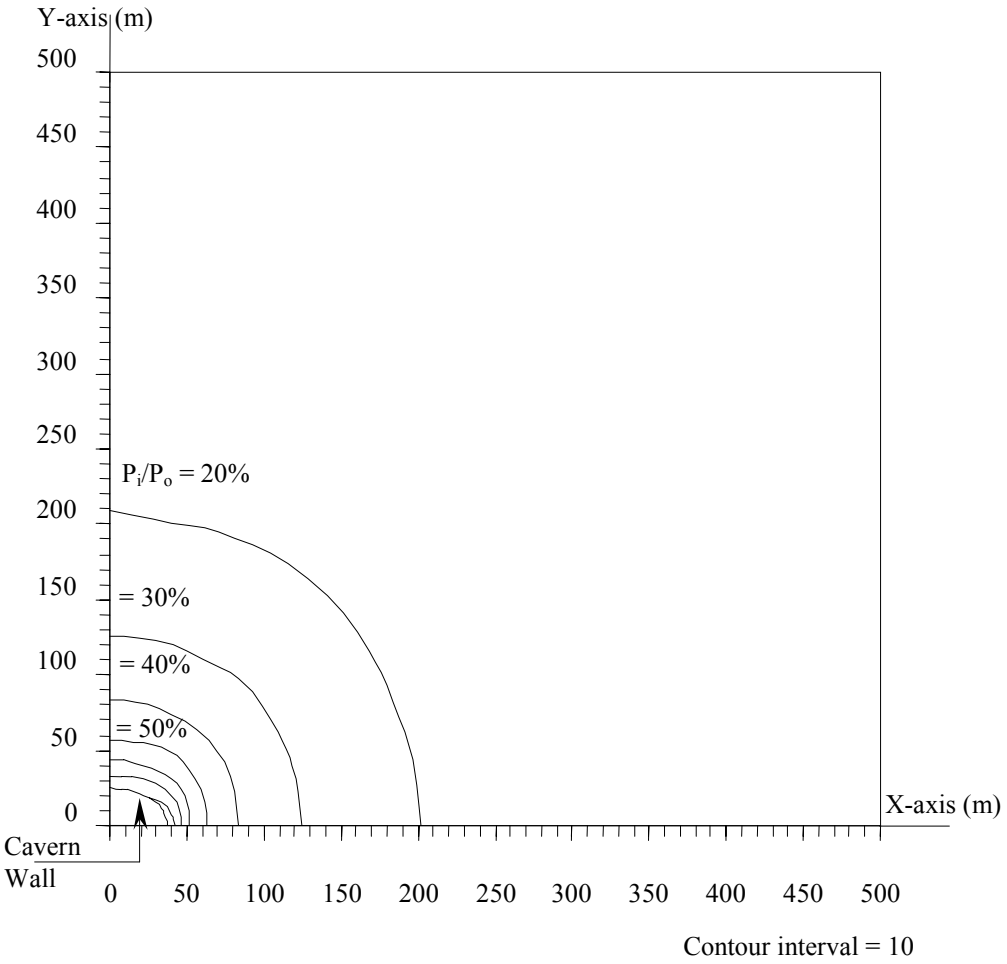

Figure A.57 Distributions of plastic zone boundary around the cavern (Model EL15) for the internal pressure ranging between 20% to 90% of in-situ stress (external pressure). The in-situ stress for this model is 10.34 MPa (1,500 psi).

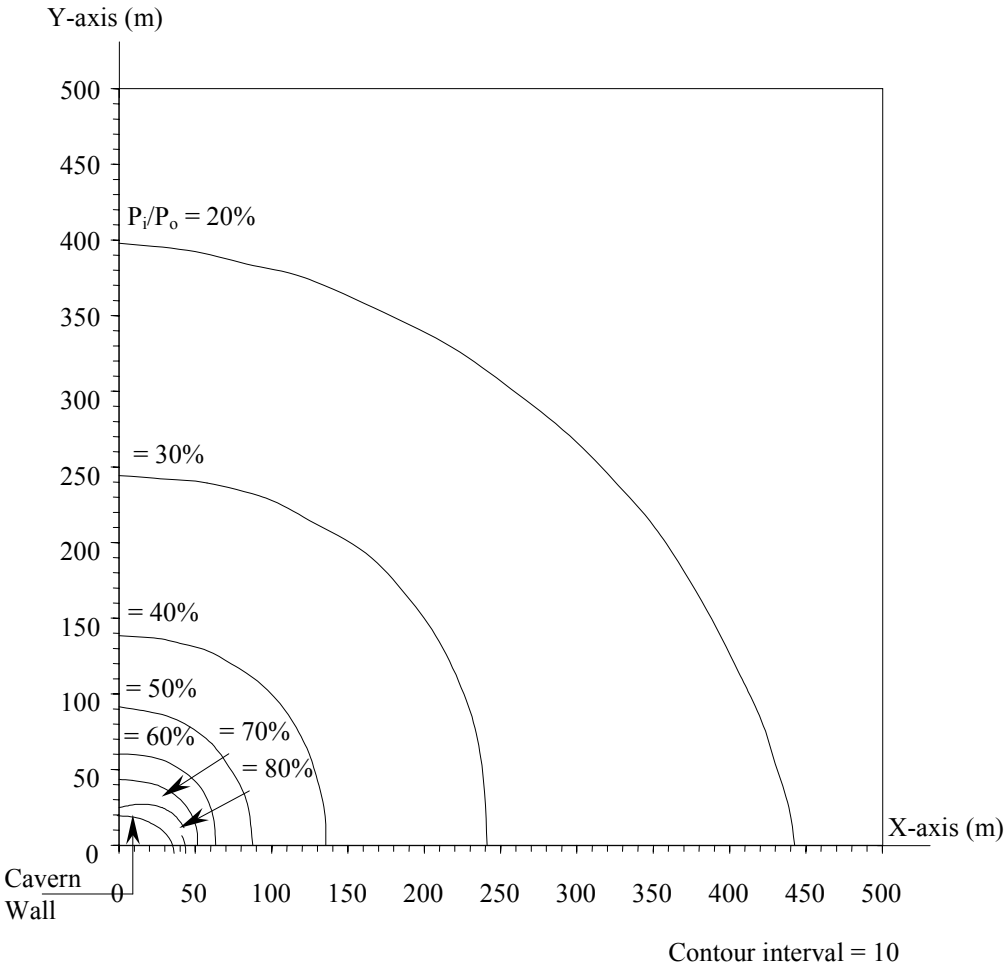

Figure A.58 Distributions of plastic zone boundary around the cavern (Model EL15) for the internal pressure ranging between 20% to 90% of in-situ stress (external pressure). The in-situ stress for this model is 13.79 MPa (2,000 psi).

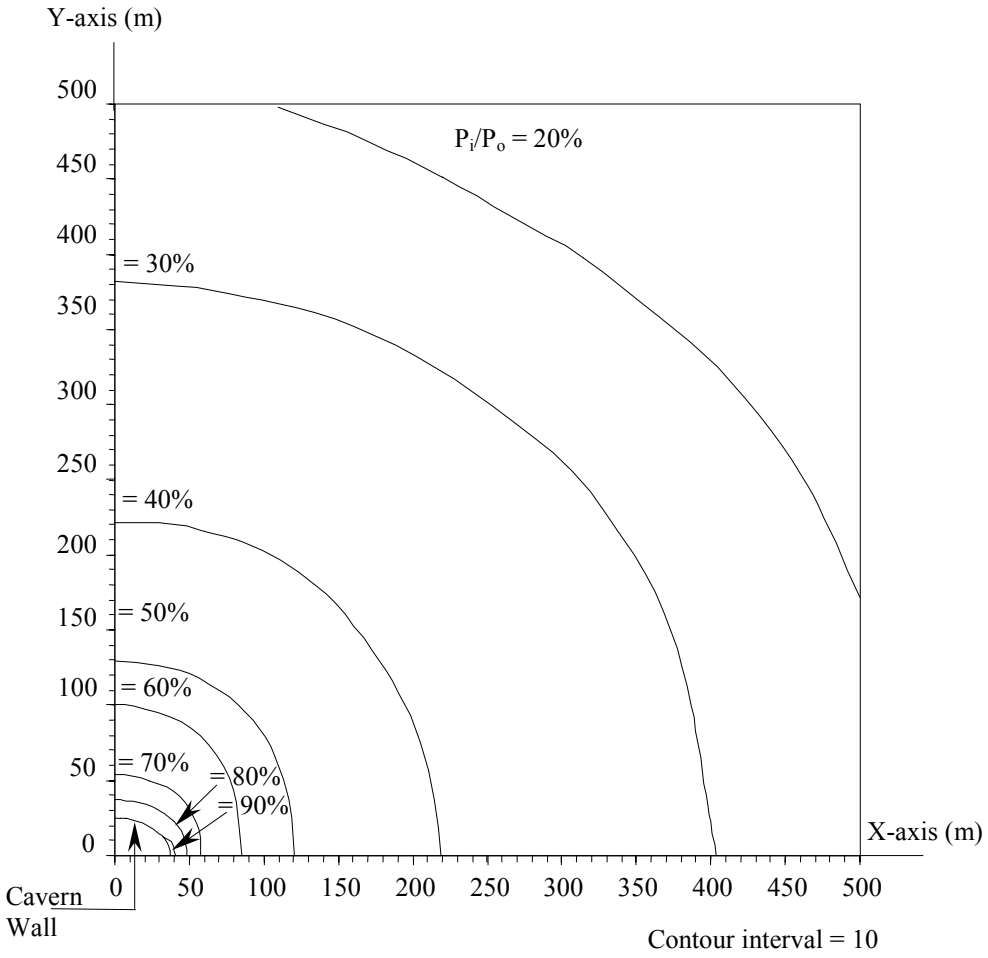

Figure A.59 Distributions of plastic zone boundary around the cavern (Model EL15) for the internal pressure ranging between 20% to 90% of in-situ stress (external pressure). The in-situ stress for this model is 17.24 MPa (2,500 psi).

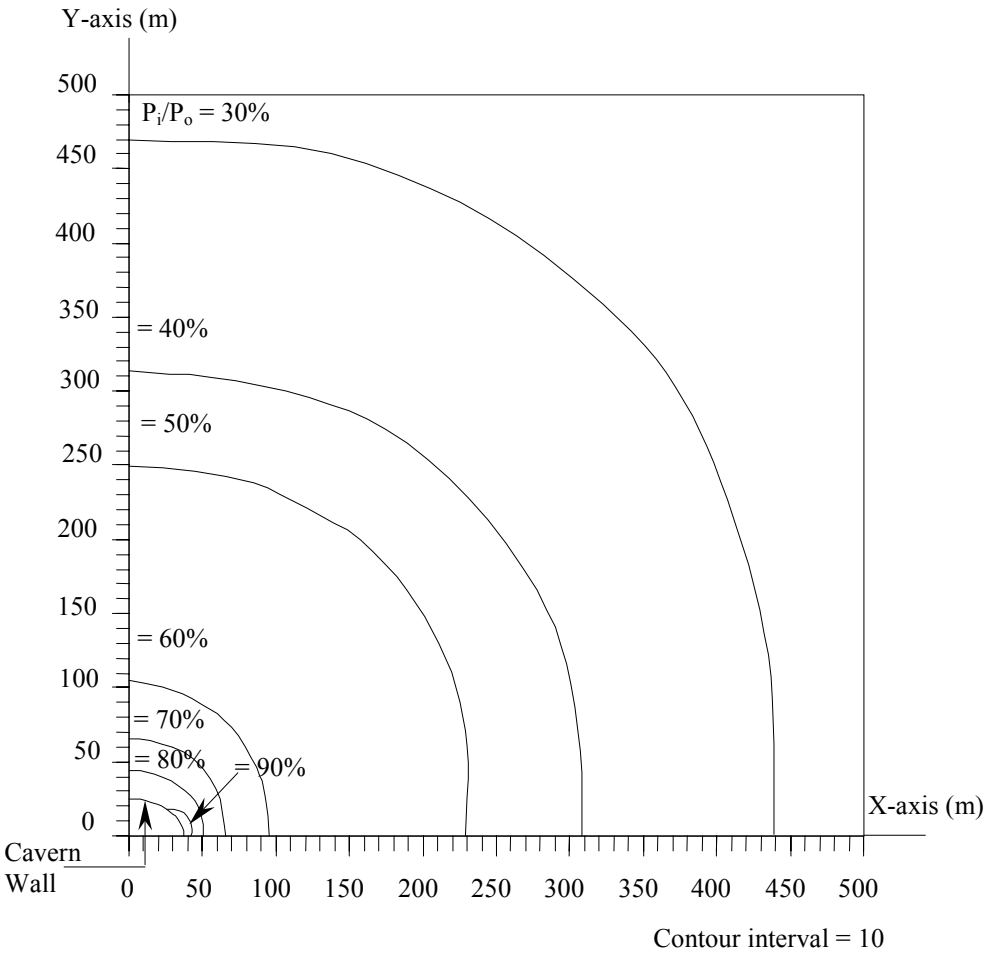

Figure A.60 Distributions of plastic zone boundary around the cavern (Model EL15) for the internal pressure ranging between 20% to 90% of in-situ stress (external pressure). The in-situ stress for this model is 20.69 MPa (3,000 psi).

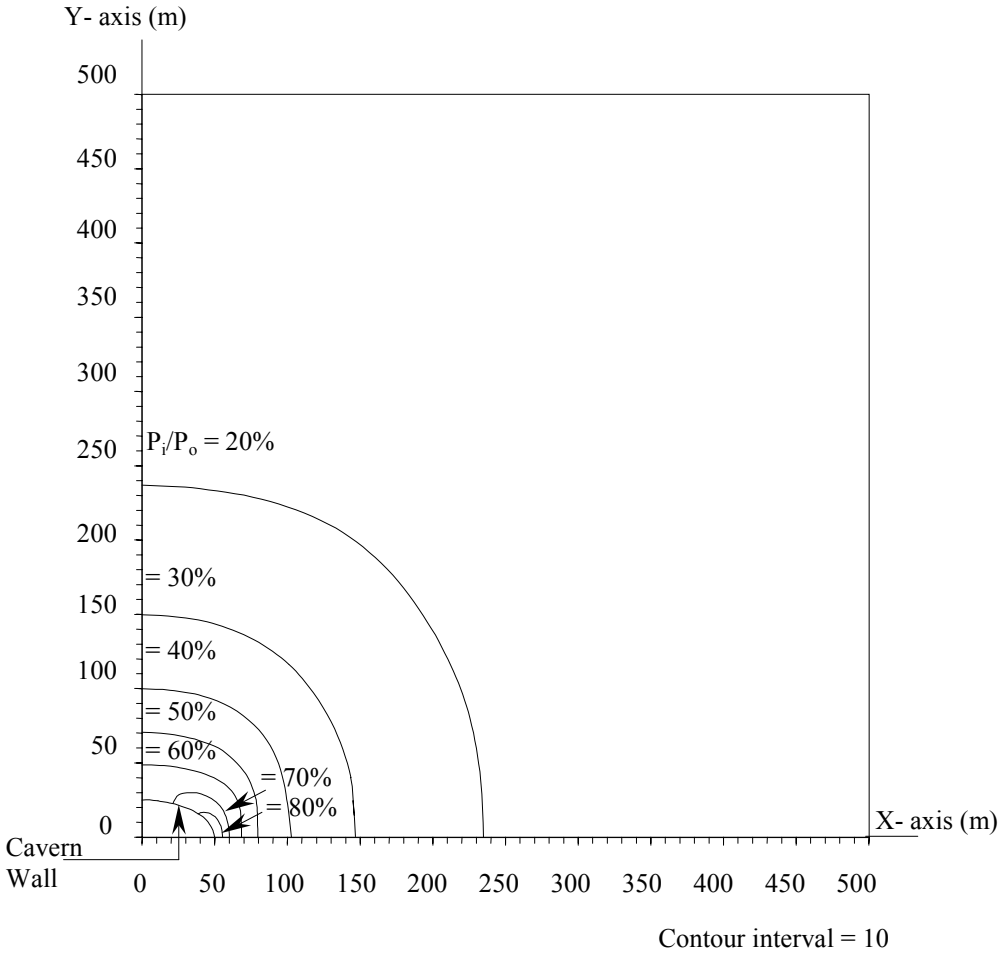

Figure A.61 Distributions of plastic zone boundary around the cavern (Model EL20) for the internal pressure ranging between 20% to 90% of in-situ stress (external pressure). The in-situ stress for this model is 10.34 MPa (1,500 psi).

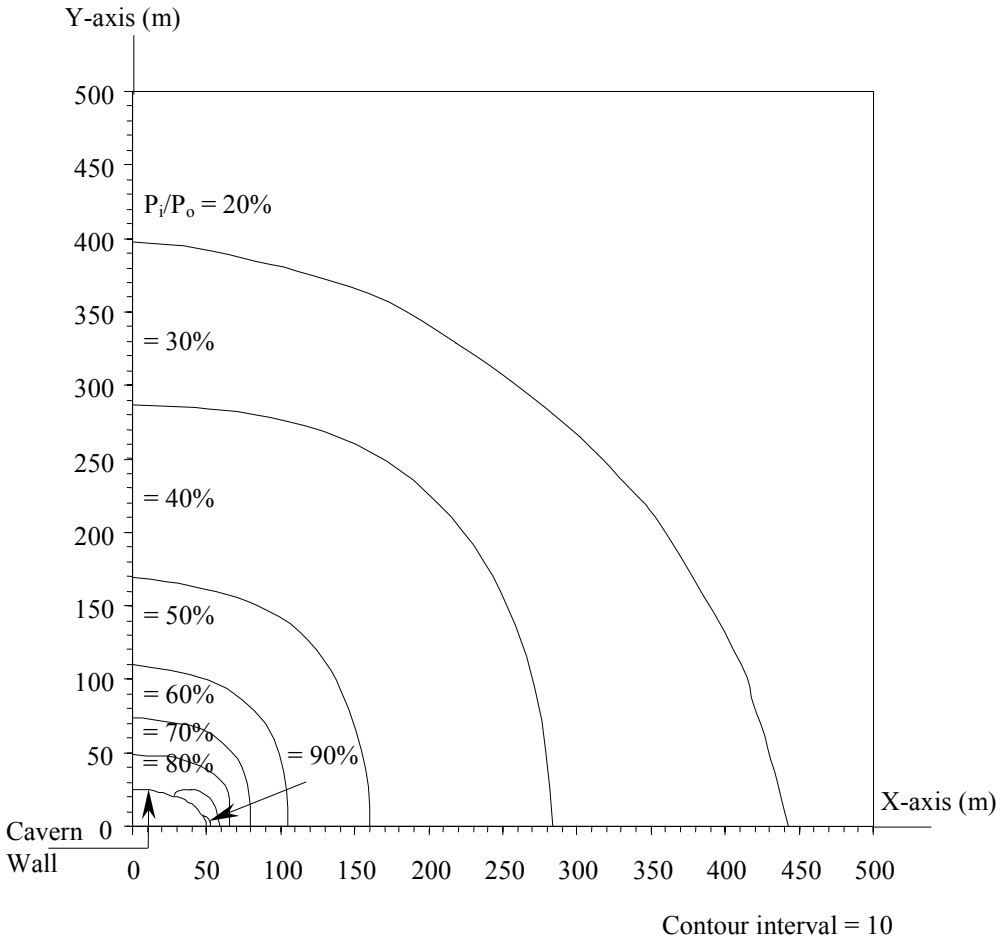

Figure A.62 Distributions of plastic zone boundary around the cavern (Model EL20) for the internal pressure ranging between 20% to 90% of in-situ stress (external pressure). The in-situ stress for this model is 13.79 MPa (2,000 psi).

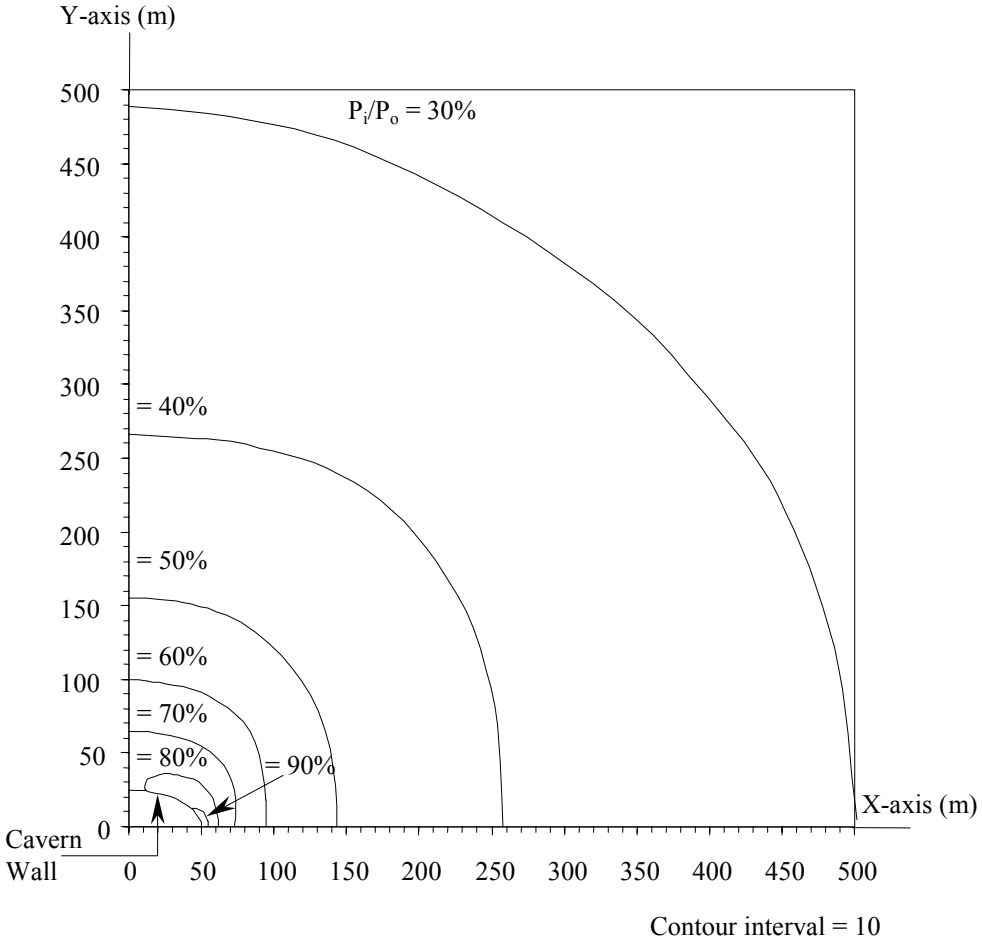

Figure A.63 Distributions of plastic zone boundary around the cavern (Model EL20) for the internal pressure ranging between 30% to 90% of in-situ stress (external pressure). The in-situ stress for this model is 17.24 MPa (2,500 psi).

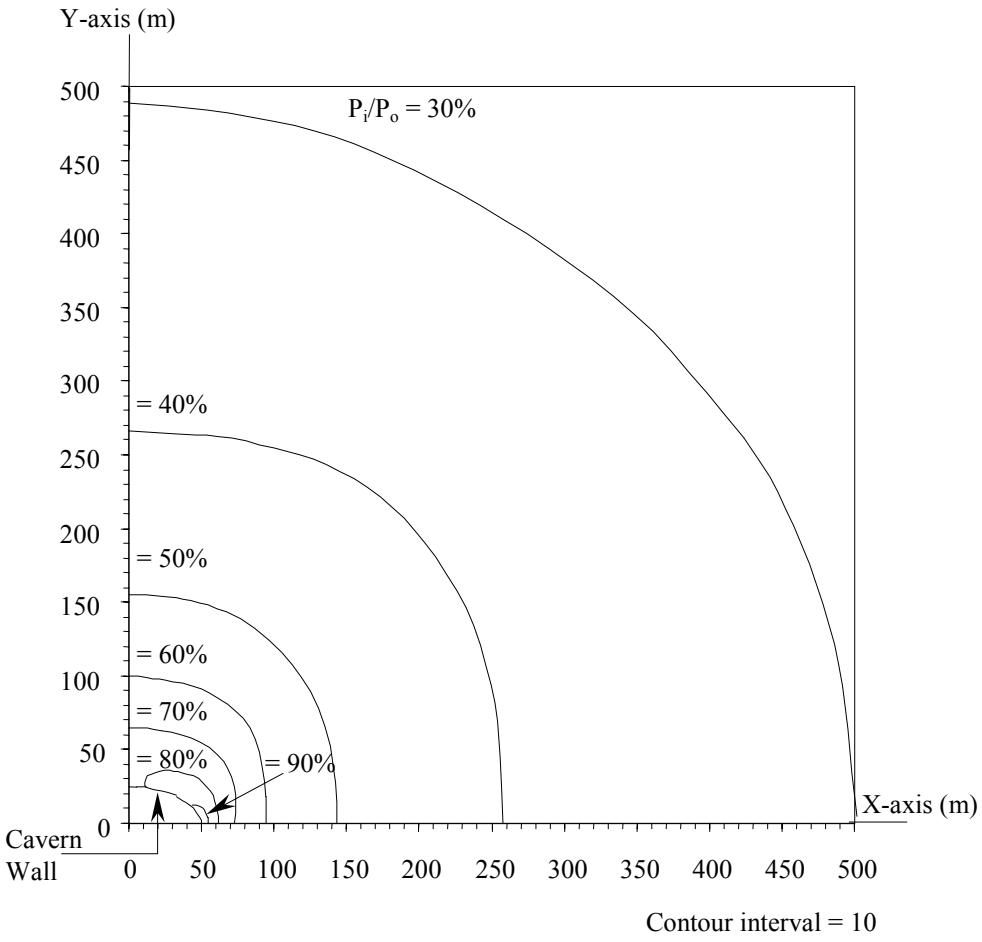

Figure A.64 Distributions of plastic zone boundary around the cavern (Model EL20) for the internal pressure ranging between 40% to 90% of in-situ stress (external pressure). The in-situ stress for this model is 20.69 MPa (3,000 psi).

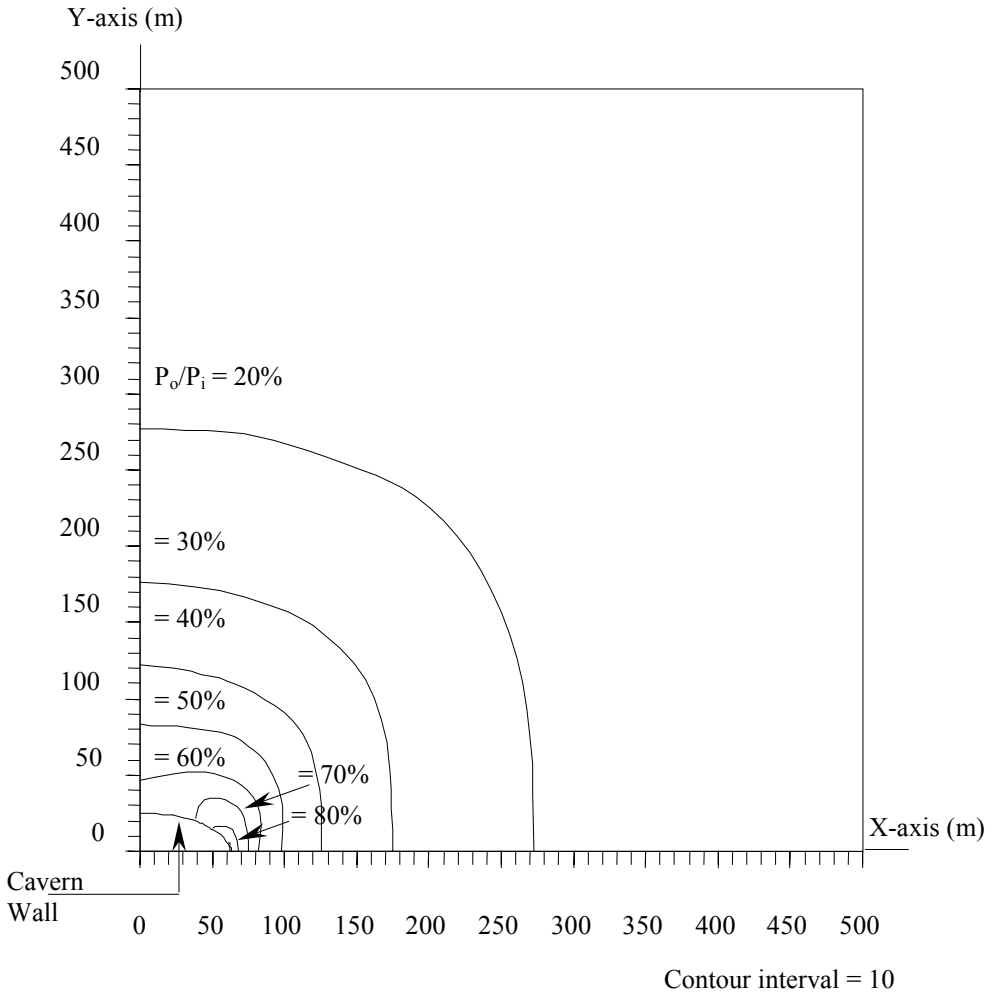

Figure A.65 Distributions of plastic zone boundary around the cavern (Model EL25) for the internal pressure ranging between 40% to 90% of in-situ stress (external pressure). The in-situ stress for this model is 10.34 MPa (1,500 psi).

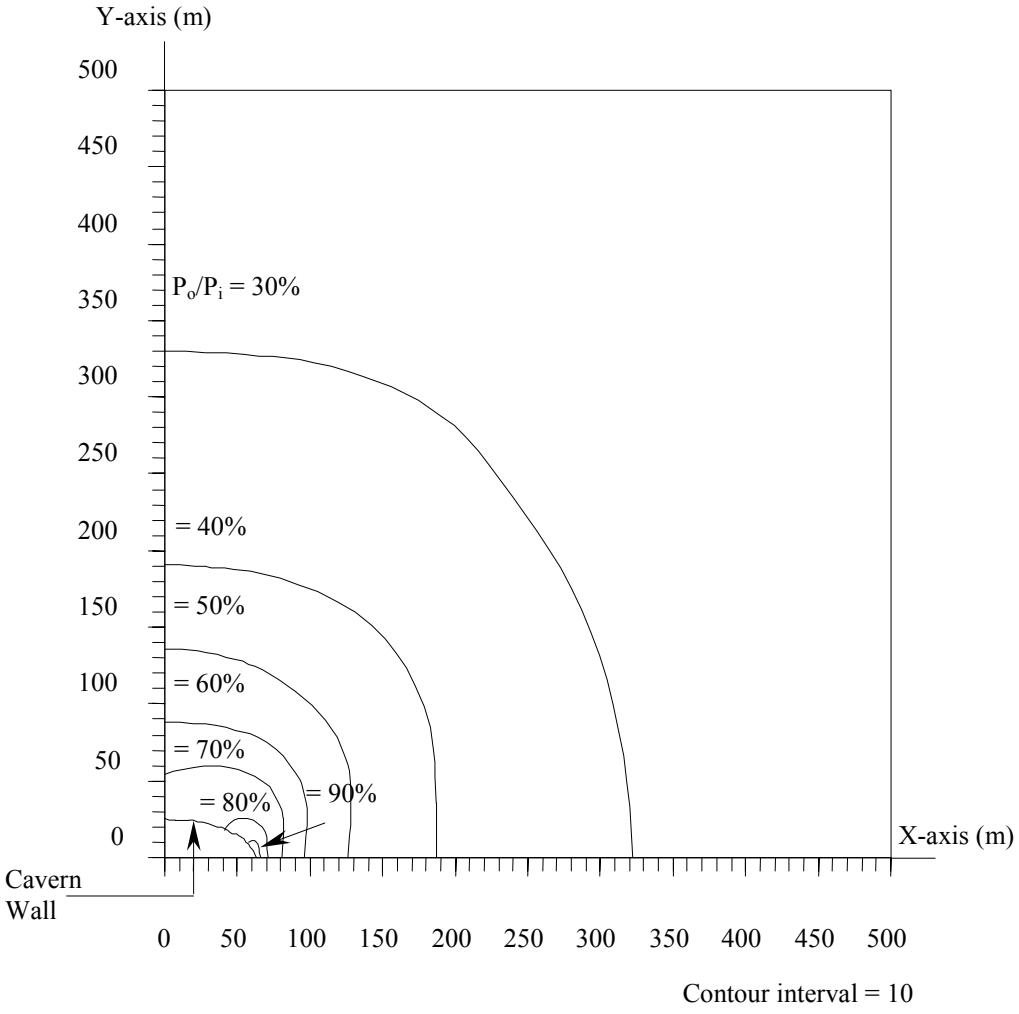

Figure A.66 Distributions of plastic zone boundary around the cavern (Model EL25) for the internal pressure ranging between 40% to 90% of in-situ stress (external pressure). The in-situ stress for this model is 13.79 MPa (2,000 psi).

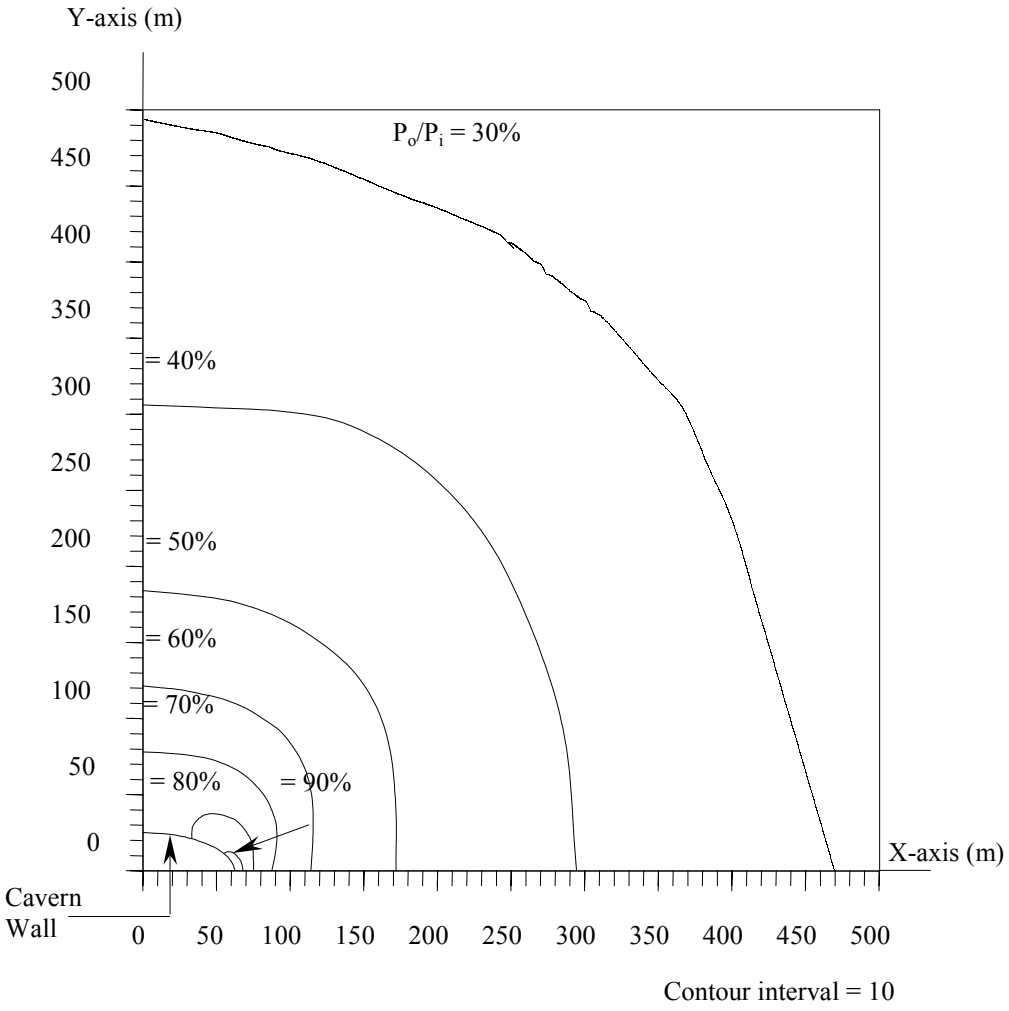

Figure A.67 Distributions of plastic zone boundary around the cavern (Model EL25) for the internal pressure ranging between 30% to 90% of in-situ stress (external pressure). The in-situ stress for this model is 17.24 MPa (2,500 psi).

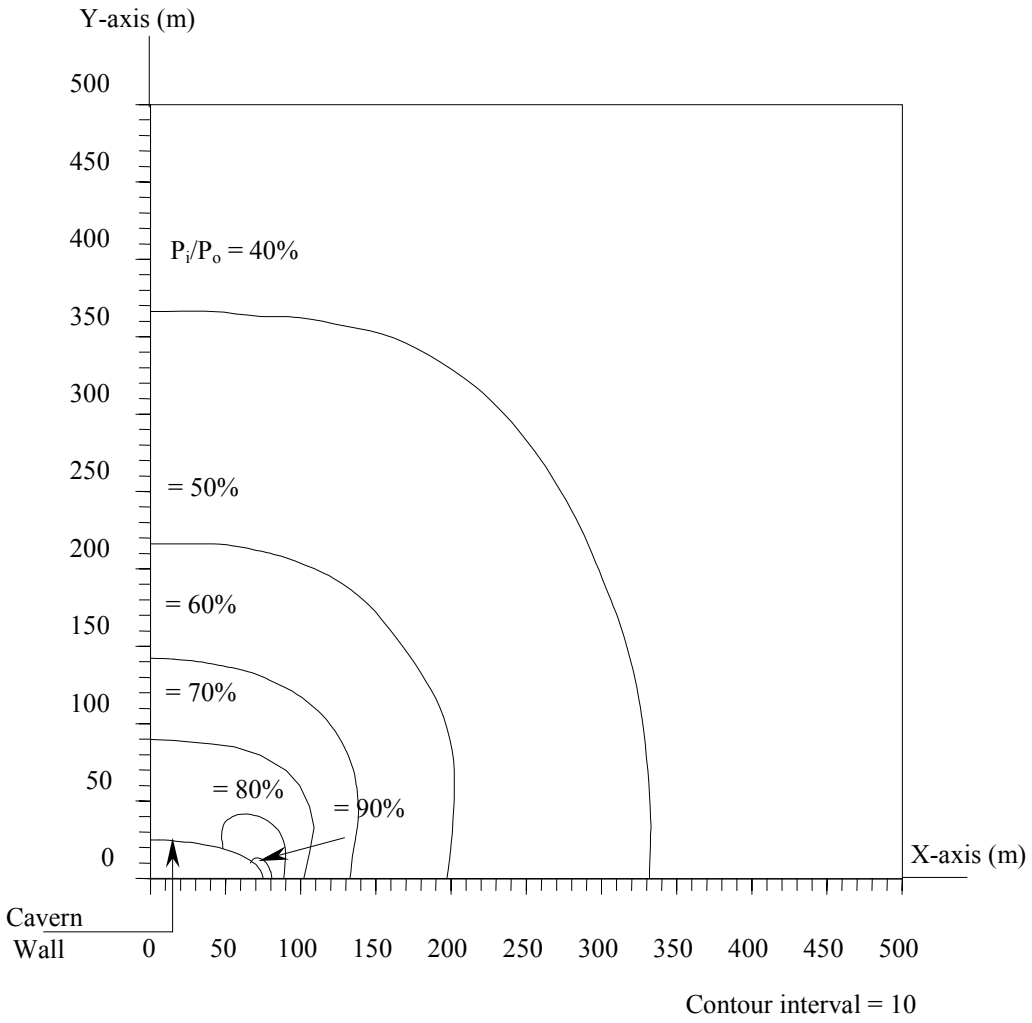

Figure A.68 Distributions of plastic zone boundary around the cavern (Model EL25) for the internal pressure ranging between 30% to 90% of in-situ stress (external pressure). The in-situ stress for this model is 20.69 MPa (3,000 psi).

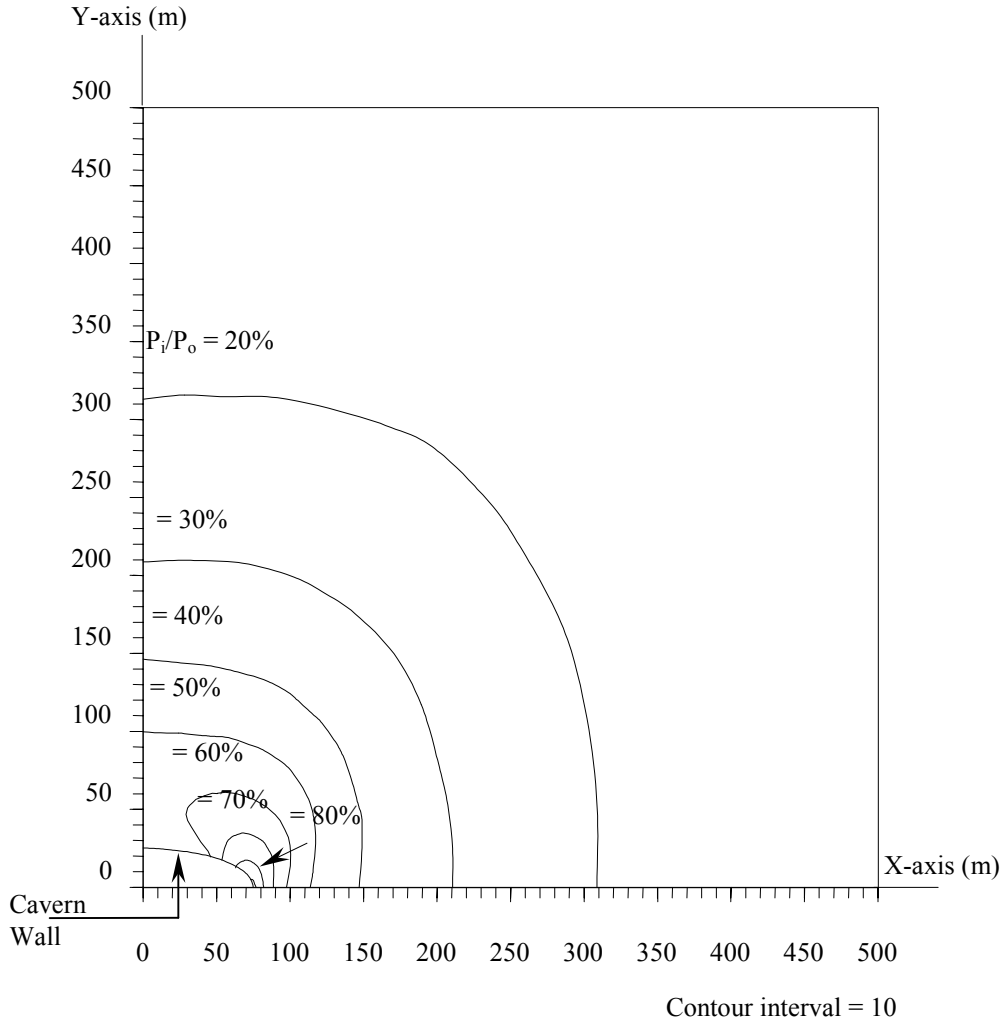

Figure A.69 Distributions of plastic zone boundary around the cavern (Model EL30) for the internal pressure ranging between 30% to 90% of in-situ stress (external pressure). The in-situ stress for this model is 10.34 MPa (1,500 psi).

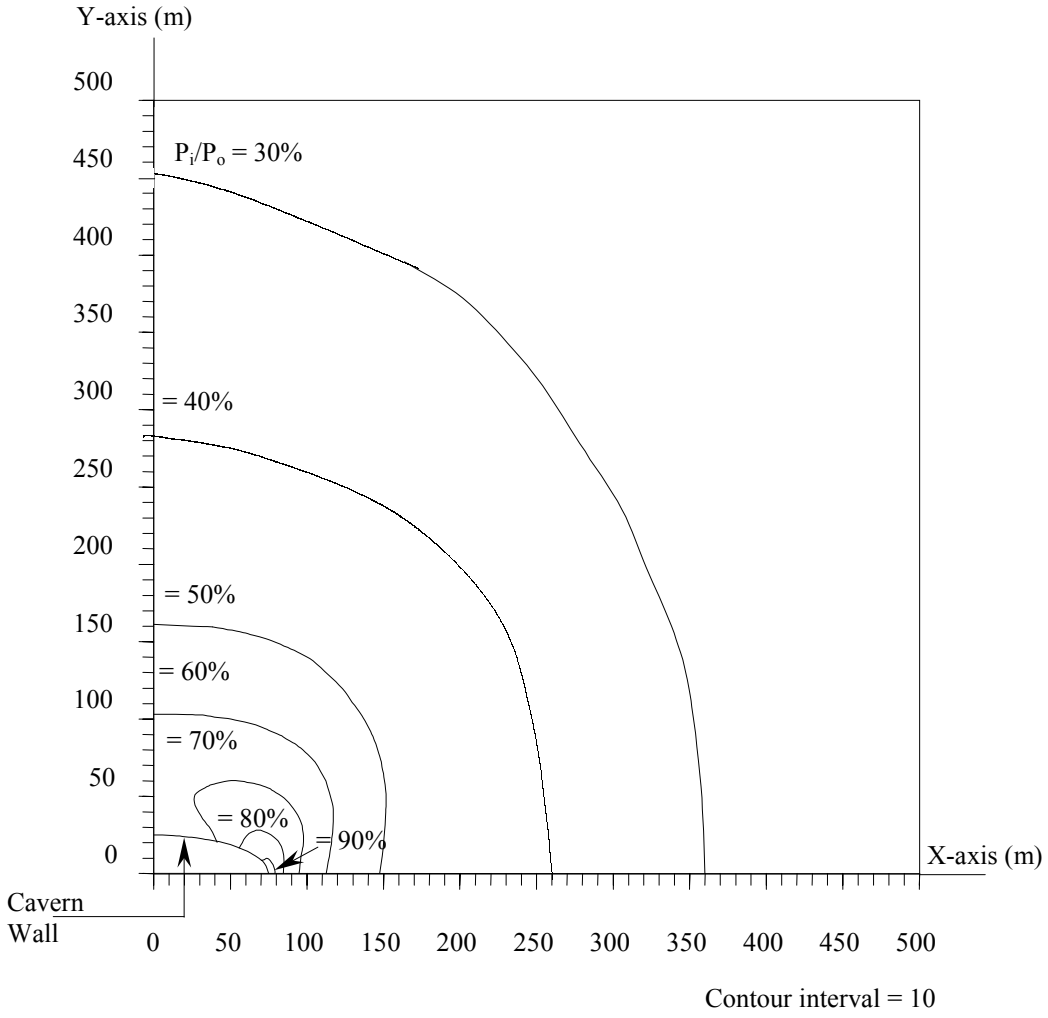

Figure A.70 Distributions of plastic zone boundary around the cavern (Model EL30) for the internal pressure ranging between 30% to 90% of in-situ stress (external pressure). The in-situ stress for this model is 13.79 MPa (2,000 psi).

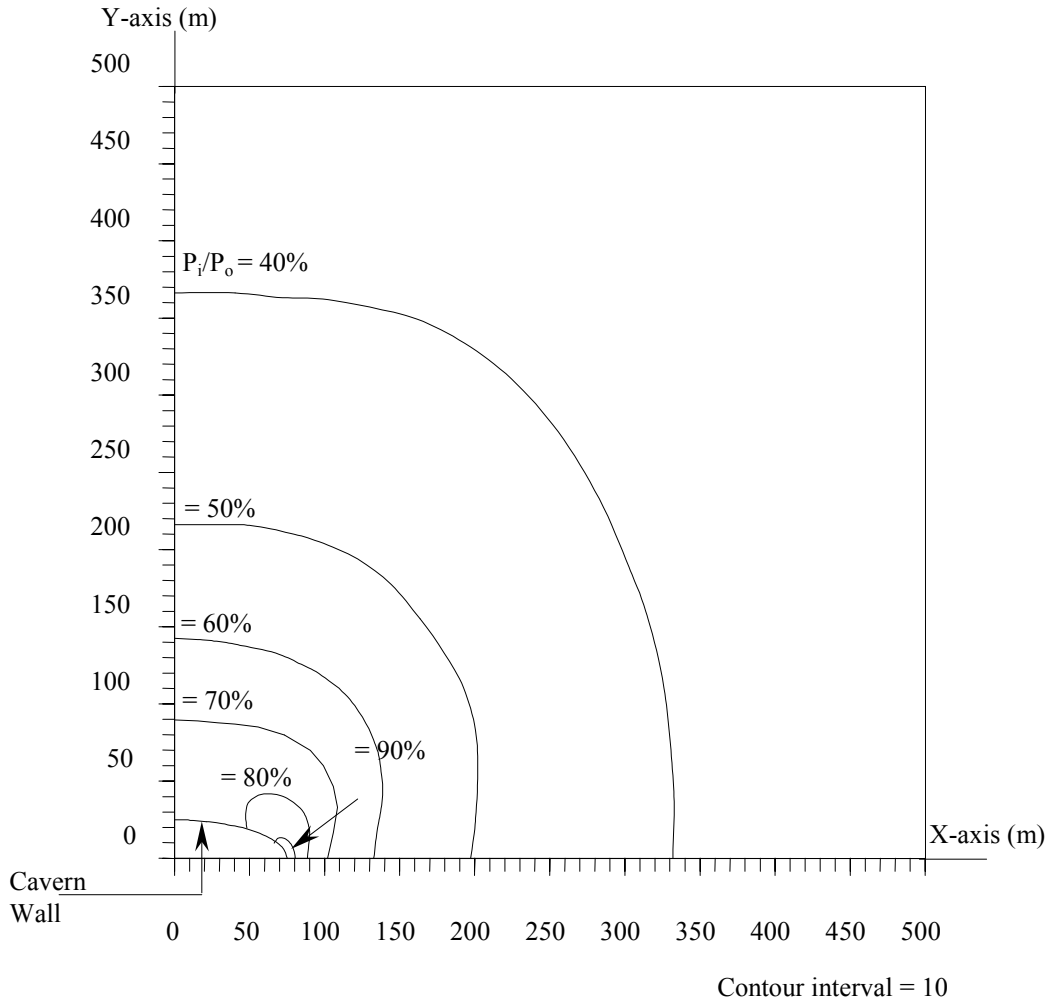

Figure A.71 Distributions of plastic zone boundary around the cavern (Model EL30) for the internal pressure ranging between 30% to 90% of in-situ stress (external pressure). The in-situ stress for this model is 17.24 MPa (2,500 psi).

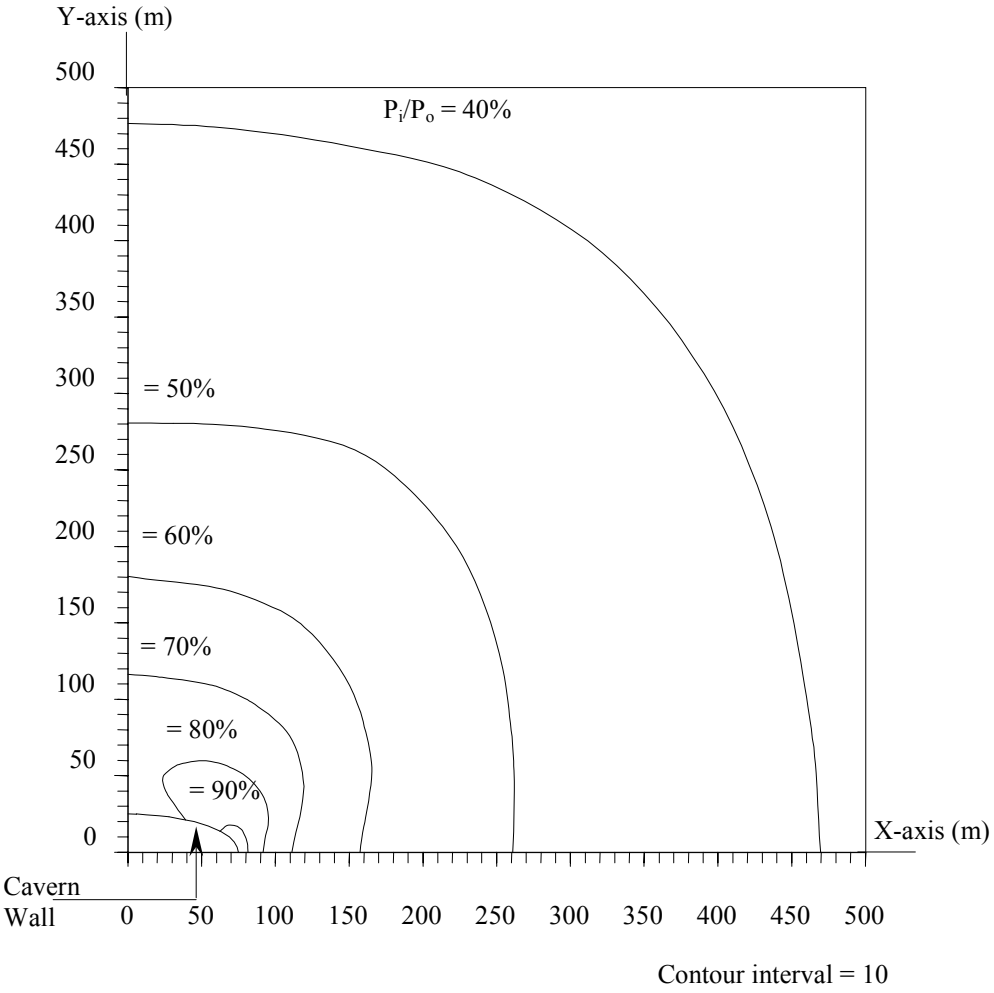

Figure A.72 Distributions of plastic zone boundary around the cavern (Model EL30) for the internal pressure ranging between 30% to 90% of in-situ stress (external pressure). The in-situ stress for this model is 20.69 MPa (3,000 psi).

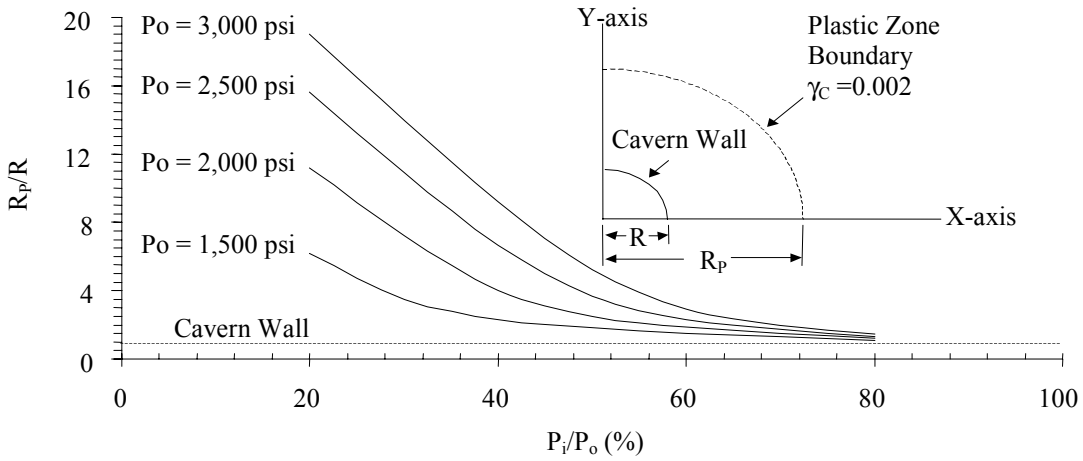

Figure A.73 Distribution of plastic zone boundary around the cavern (Model SP10) in x- and y-direction for four depths level which represent by the in-situ stress of 1500, 2000, 2500, and 3000 psi.

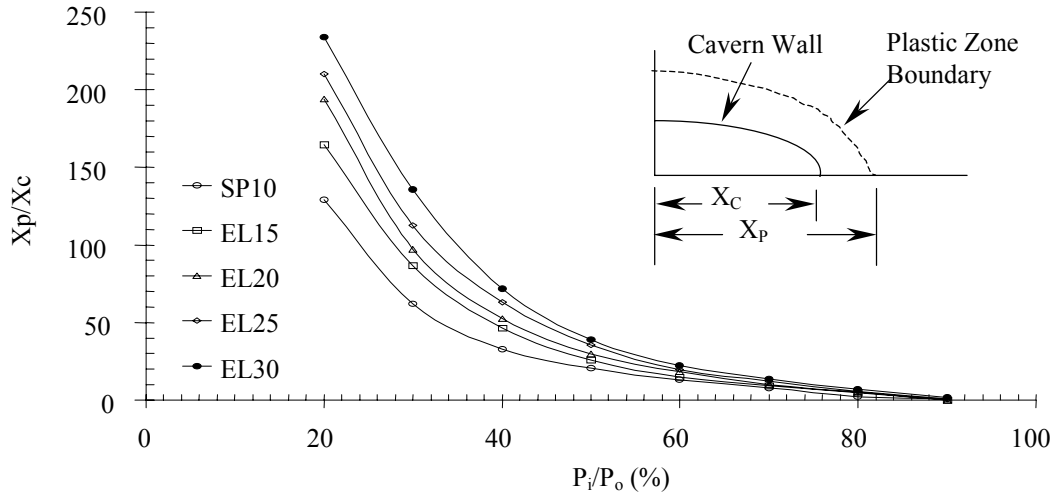

Figure A.74 Distribution of plastic zone boundary around the cavern (Model SP10, EL15, EL20, EL25, and EL30) in x-direction for the in-situ stress equal 10.34 MPa (1,500 psi). The internal pressure in the cavern range between 20% to 90% of the in-situ stress.

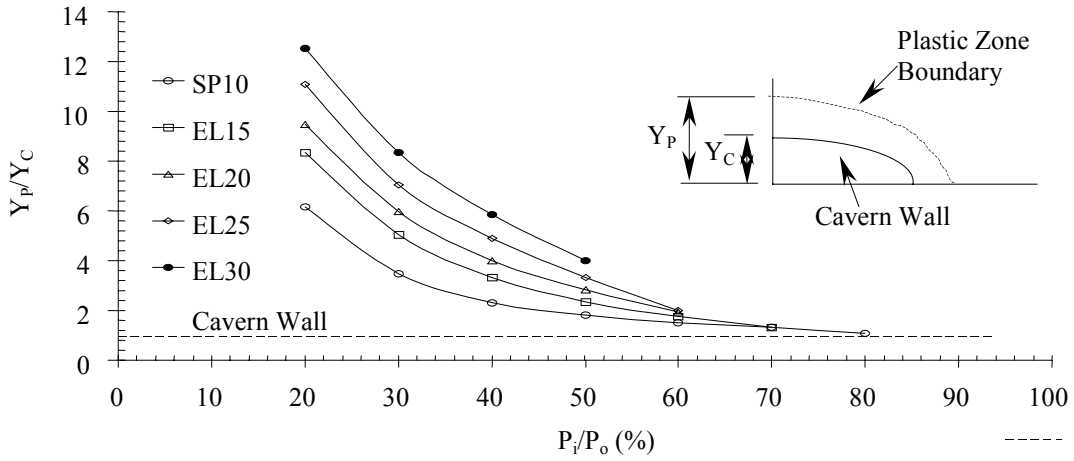

Figure A.75 Distribution of plastic zone boundary around the cavern (Model SP10, EL15, EL20, EL25, and EL30) in y-direction for the in-situ stress equal 10.34 MPa (1,500 psi). The internal pressure in the cavern range between 20% to 90% of the in-situ stress.

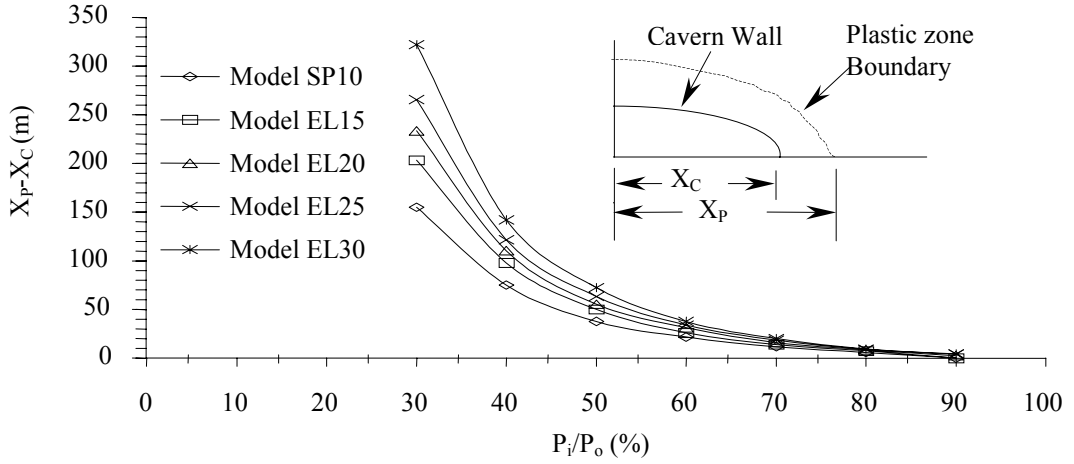

Figure A.76 Distribution of plastic zone boundary around the cavern (Model SP10, EL15, EL20, EL25, and EL30) in x-direction for the in-situ stress equal 13.79 MPa (2,000 psi). The internal pressure in the cavern range between 20% to 90% of the in-situ stress.

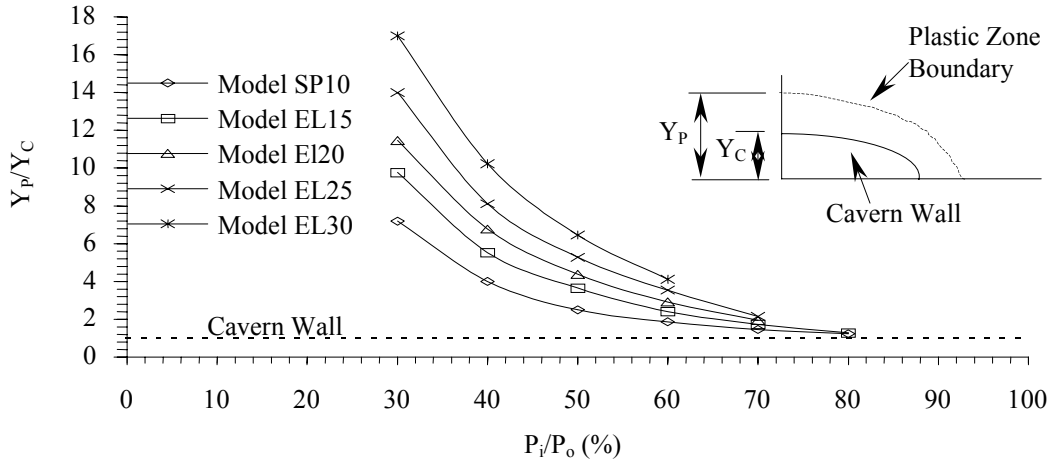

Figure A.77 Distribution of plastic zone boundary around the cavern (Model SP10, EL15, EL20, EL25, and EL30) in y-direction for the in-situ stress equal 13.79 MPa (2,000 psi). The internal pressure in the cavern range between 20% to 90% of the in-situ stress.

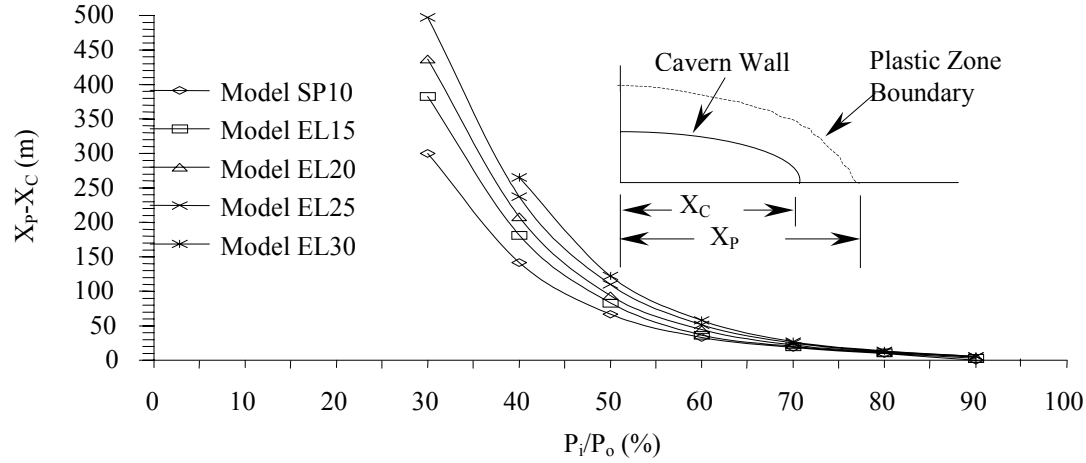

Figure A.78 Distribution of plastic zone boundary around the cavern (Model SP10, EL15, EL20, EL25, and EL30) in x-direction for the in-situ stress equal 17.24 MPa (2,500 psi). The internal pressure in the cavern range between 20% to 90% of the in-situ stress.

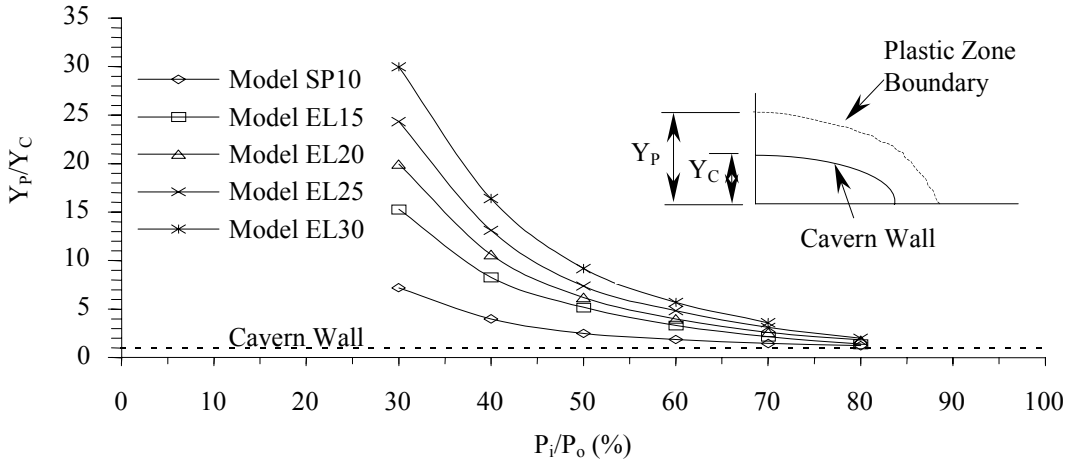

Figure A.79 Distribution of plastic zone boundary around the cavern (Model SP10, EL15, EL20, EL25, and EL30) in y-direction for the in-situ stress equal 17.24 MPa (2,500 psi). The internal pressure in the cavern range between 20% to 90% of the in-situ stress.

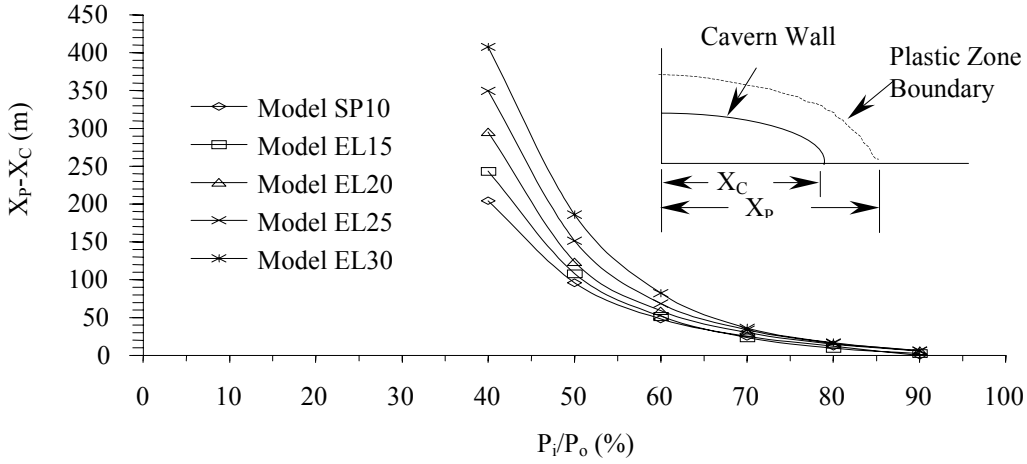

Figure A.80 Distribution of plastic zone boundary around the cavern (Model SP10, EL15, EL20, EL25, and EL30) in x-direction for the in-situ stress equal 20.69 MPa (3,000 psi). The internal pressure in the cavern range between 20% to 90% of the in-situ stress.

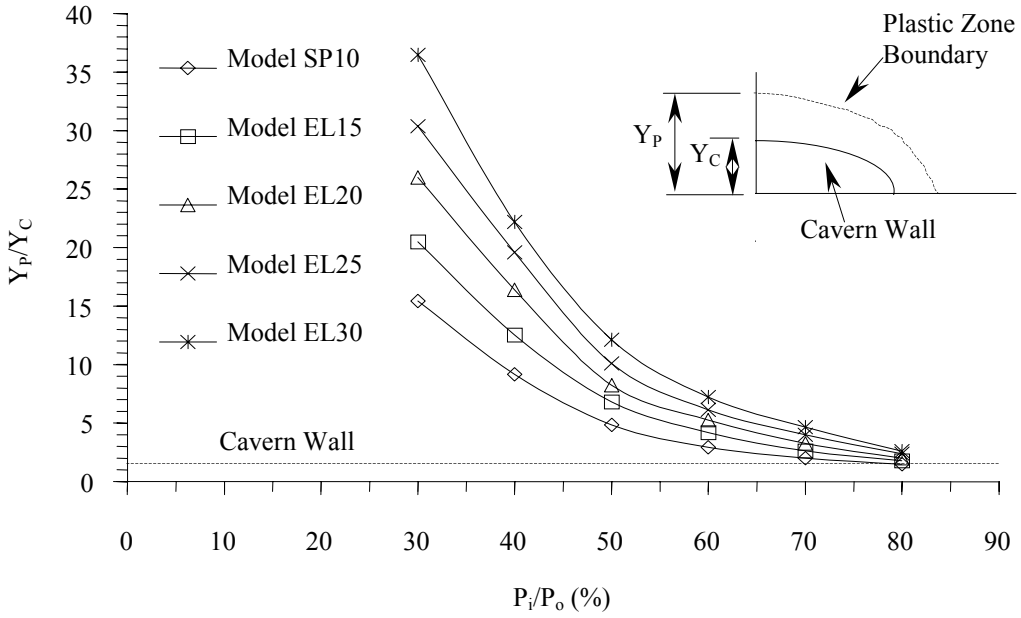

Figure A.81 Distribution of plastic zone boundary around the cavern (Model SP10, EL15, EL20, EL25, and EL30) in y-direction for the in-situ stress equal 20.69 MPa (3,000 psi). The internal pressure in the cavern range between 20% to 90% of the in-situ stress.

APPENDIX B

RESULTS FROM THE COMPUTER SIMULATION

OF COMPRESSED AIR ENERGY STORAGE

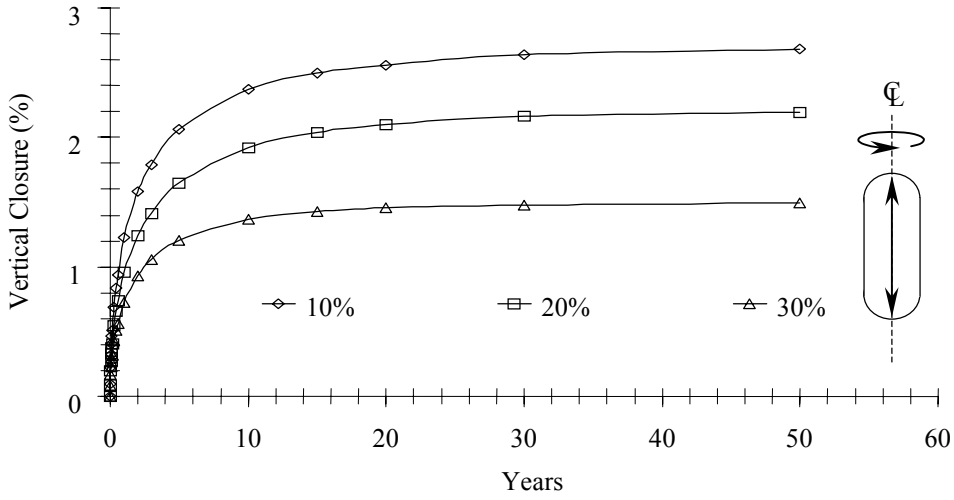

Figure B.1 Vertical closure at the centerline of cavern for the internal pressures equal 10%, 20% and 30% of the in-situ stress in salt at the cavern roof. The in-situ stress in salt at the cavern roof for this model is 13.2 MPa.

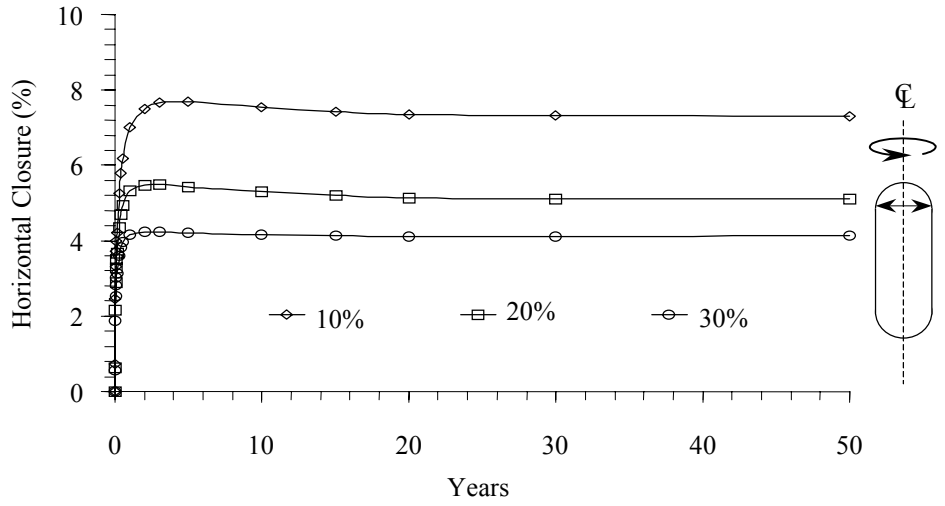

Figure B.2 Horizontal closure near the top of cavern for the internal pressures equal 10%, 20% and 30% of the in-situ stress in salt at the cavern roof. The in-situ stress in salt at the cavern roof for this model is 13.2 MPa.

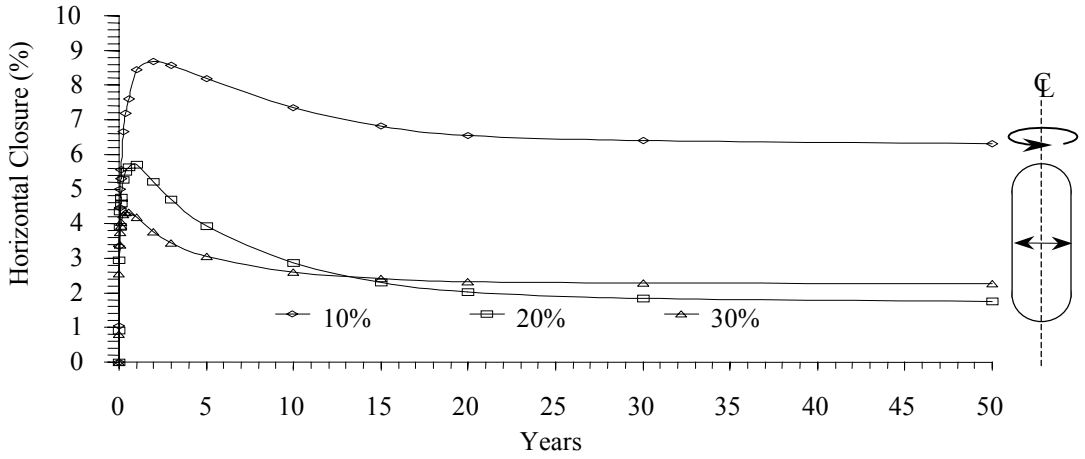

Figure B.3 Horizontal closure at the middle of cavern for the internal pressures equal 10%, 20% and 30% of the in-situ stress in salt at the cavern roof. The in-situ stress in salt at the cavern roof for this model is 13.2 MPa.

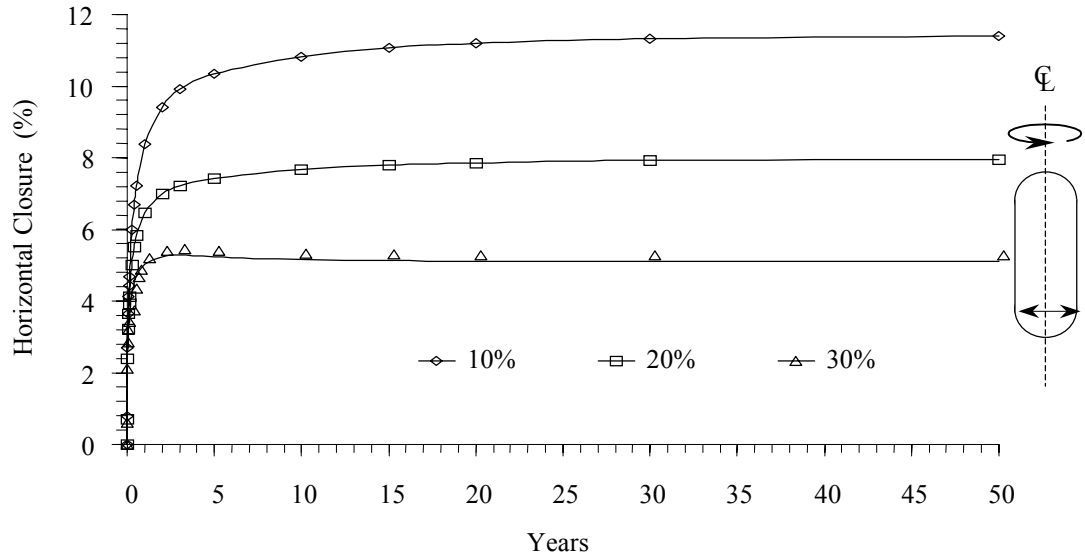

Figure B.4 Horizontal closure near the bottom of cavern for the internal pressures equal 10%, 20% and 30% of the in-situ stress in salt at the cavern roof. The in-situ stress in salt at the cavern roof for this model is 13.2 MPa.

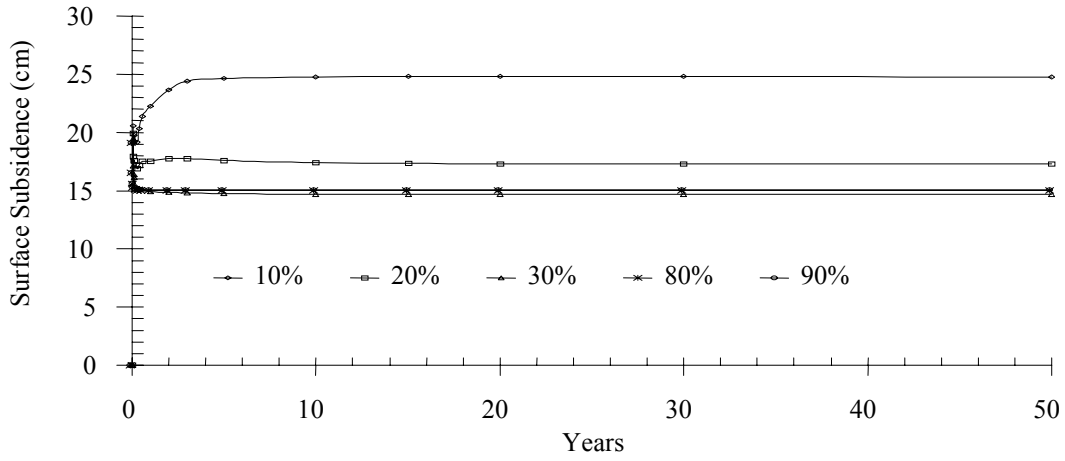

Figure B.5 Surface subsidence at the centerline of cavern for 20 year after construction. The results are compared for the internal pressure of 10%, 20% and 30% of in-situ stress in rock salt at the cavern roof. The in-situ stress in rock salt at the cavern roof for this model is 13.2 MPa (1,912 psi).

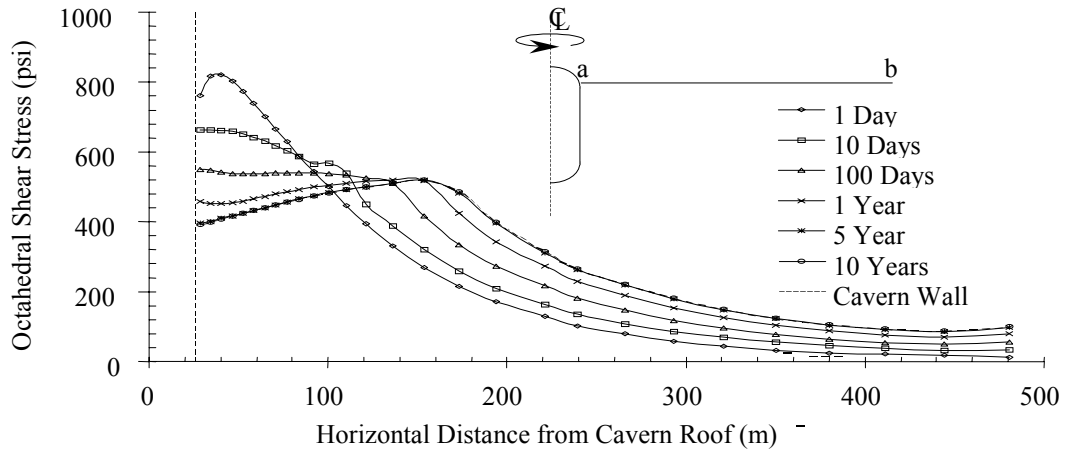

Figure B.6 Distributions of octahedral shear stresses near the top of cavern along horizontal distance from cavern wall (Line a-b). The internal pressure in the cavern is 10% of the in-situ stress in salt at the cavern roof. The in-situ stress in salt at the cavern roof for this model is 13.2 MPa (1,912 psi).

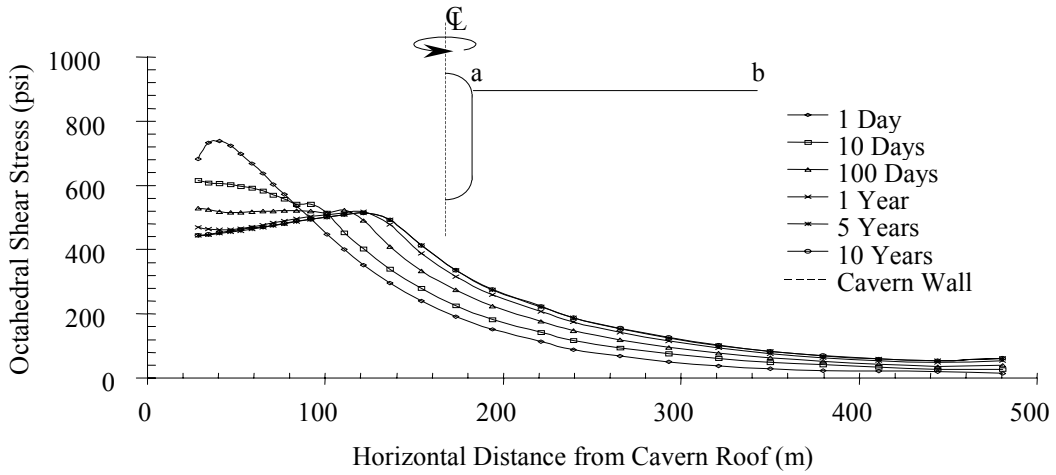

Figure B.7 Distributions of octahedral shear stresses near the top of cavern along horizontal distance from cavern wall (Line a-b). The internal pressure in the cavern is 20% of the in-situ stress in rock salt at the cavern roof. The stress in rock salt at the cavern roof for this model is 13.2 MPa (1,912 psi).

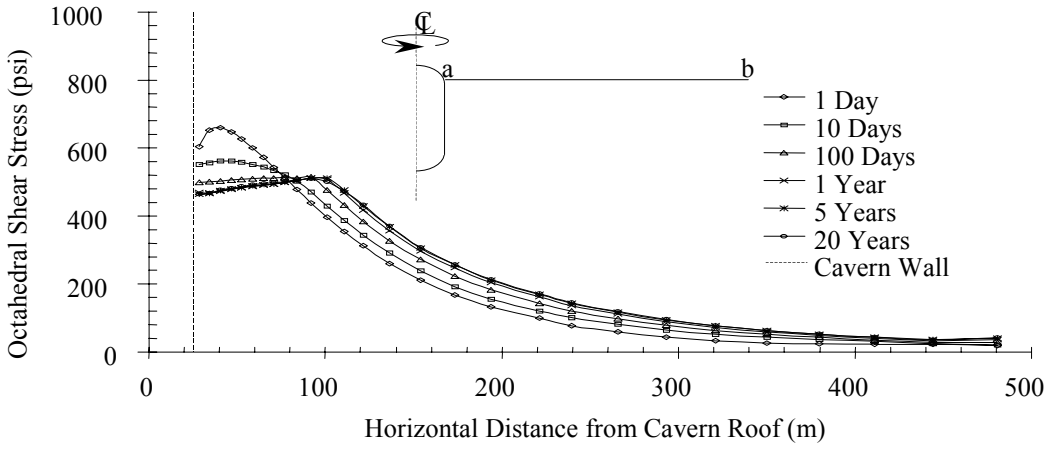

Figure B.8 Distributions of octahedral shear stresses near the top of cavern along horizontal distance from cavern wall (Line a-b). The internal pressure in the cavern is 30% of the in-situ stress in rock salt at the cavern roof. The stress in rock salt at the cavern roof for this model is 13.2 MPa (1,912 psi).

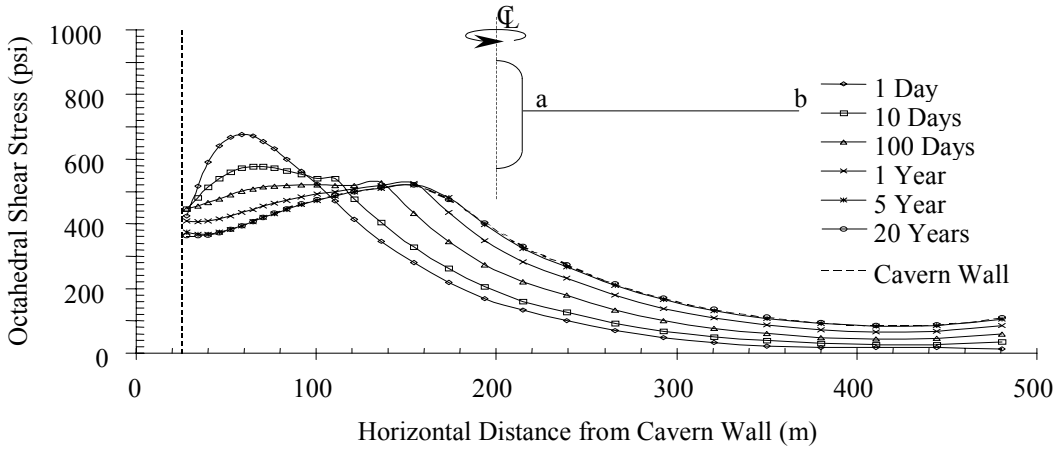

Figure B.9 Distributions of octahedral shear stresses at the middle of cavern along horizontal distance from cavern wall (Line a-b). The internal pressure in the cavern is 10% of the in-situ stress in rock salt at the cavern roof. The stress in rock salt at the cavern roof for this model is 13.2 MPa (1,912 psi).

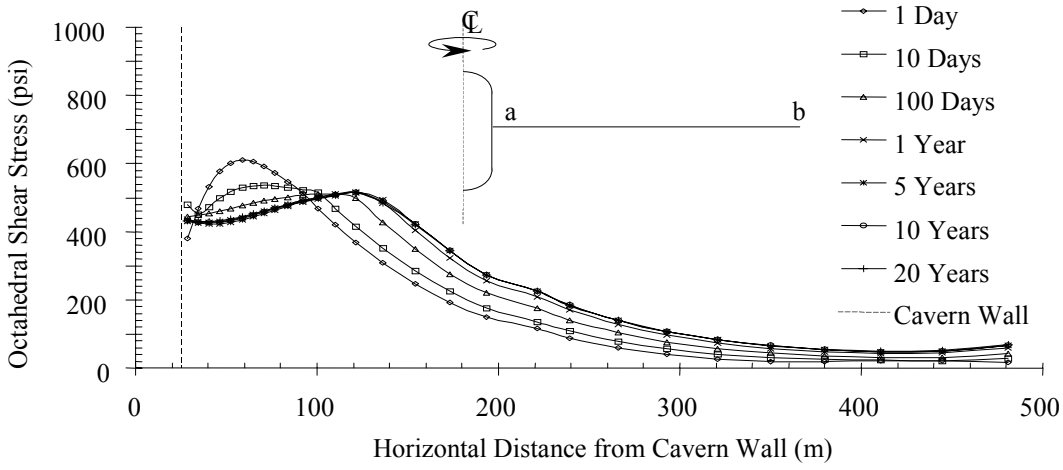

Figure B.10 Distributions of octahedral shear stresses at the middle of cavern along horizontal distance from cavern wall (Line a-b). The internal pressure in the cavern is 20% of the in-situ stress in rock salt at the cavern roof. The stress in rock salt at the cavern roof for this model is 13.2 MPa (1,912 psi).

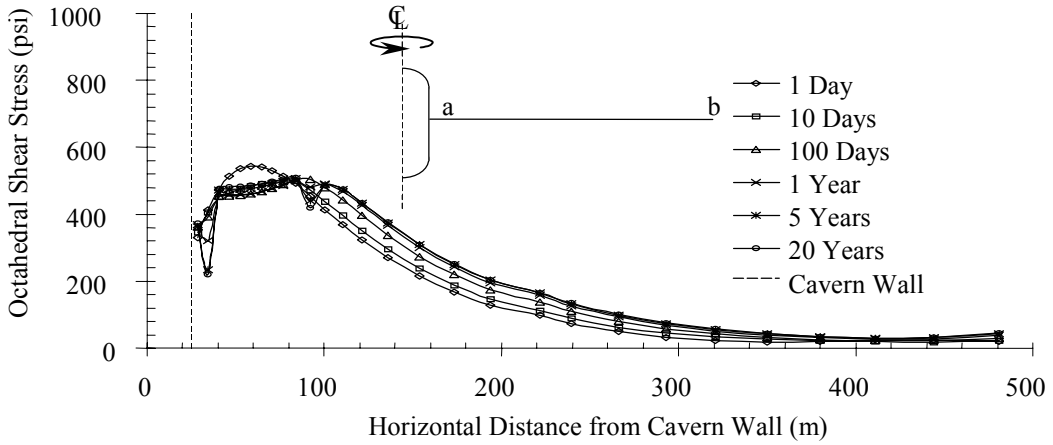

Figure B.11 Distributions of octahedral shear stresses at the middle of cavern along horizontal distance from cavern wall (Line a-b). The internal pressure in the cavern is 30% of the in-situ stress in rock salt at the cavern roof. The stress in rock salt at the cavern roof for this model is 13.2 MPa (1,912 psi).

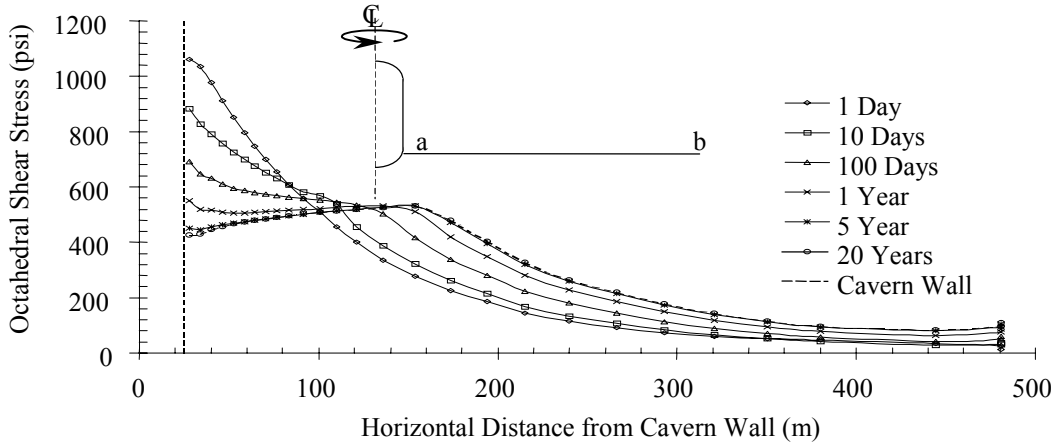

Figure B.12 Distributions of octahedral shear stresses near the bottom of cavern along horizontal distance from cavern wall (Line a-b). The internal pressure in the cavern is 10% of the in-situ stress in rock salt at the cavern roof. The stress in rock salt at the cavern roof for this model is 13.2 MPa (1,912 psi).

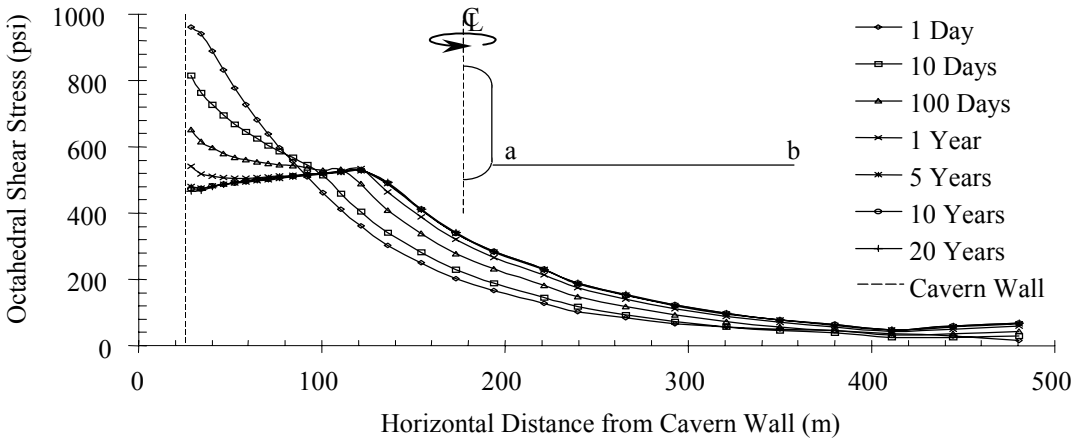

Figure B.13 Distributions of octahedral shear stresses near the bottom of cavern along horizontal distance from cavern wall (Line a-b). The internal pressure in the cavern is 20% of the in-situ stress in rock salt at the cavern roof. The stress in rock salt at the cavern roof for this model is 13.2 MPa (1,912 psi).

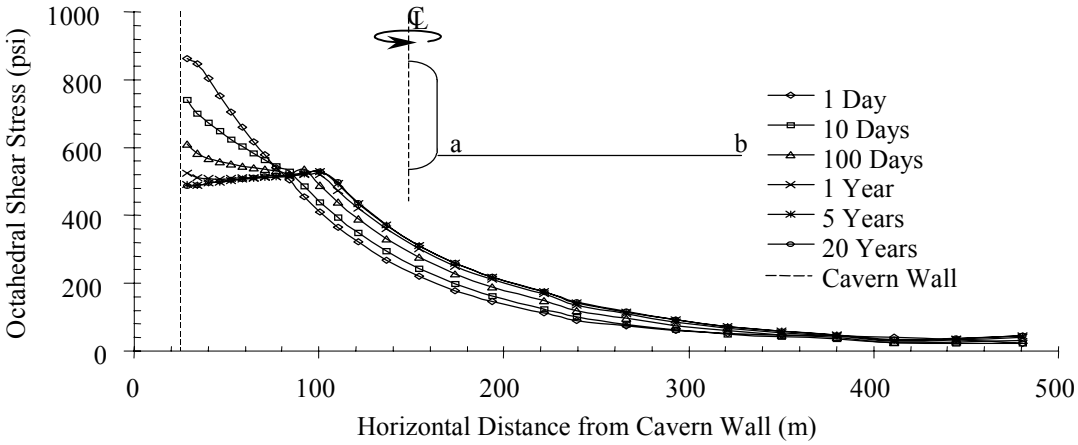

Figure B.14 Distributions of octahedral shear stresses near the bottom of cavern along horizontal distance from cavern wall (Line a-b). The internal pressure in the cavern is 30% of the in-situ stress in rock salt at the cavern roof. The stress in rock salt at the cavern roof for this model is 13.2 MPa (1,912 psi).

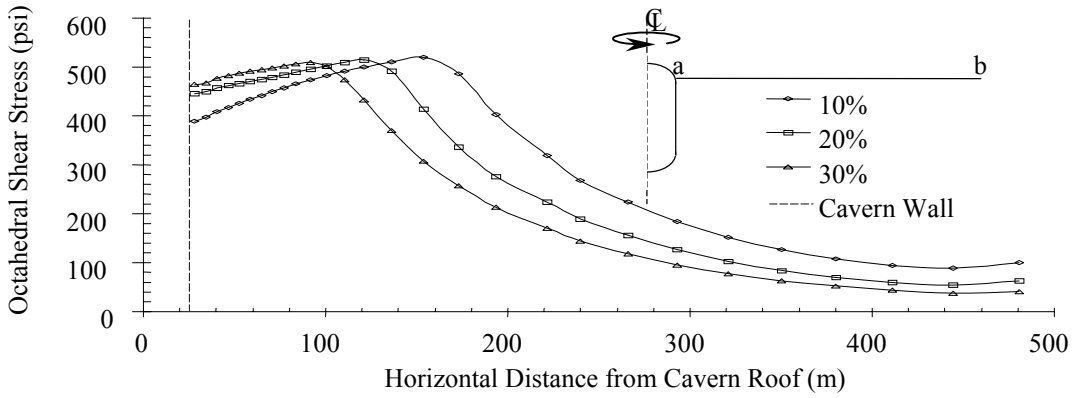

Figure B.15 Distributions of octahedral shear stresses near the top of cavern along horizontal distance from cavern wall (Line a-b) for 20 year after construction. The internal pressures in the cavern are 10%, 20% and 30% of the in-situ stress in rock salt at the cavern roof. The stress in rock salt at the cavern roof for this model is 13.2 MPa (1,912 psi).

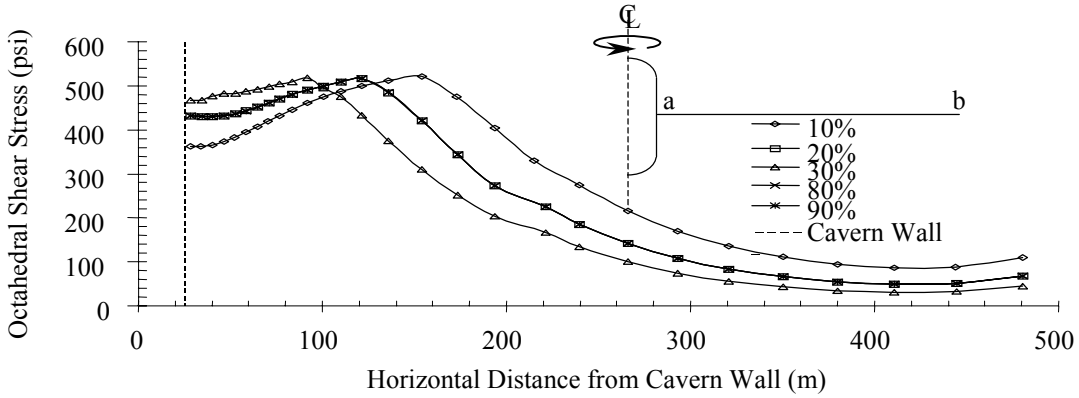

Figure B.16 Distributions of octahedral shear stresses at the middle of cavern along horizontal distance from cavern wall (Line a-b) for 20 year after construction. The internal pressures in the cavern are 10%, 20% and 30% of the in-situ stress in rock salt at the cavern roof. The stress in rock salt at the cavern roof for this model is 13.2 MPa (1,912 psi).

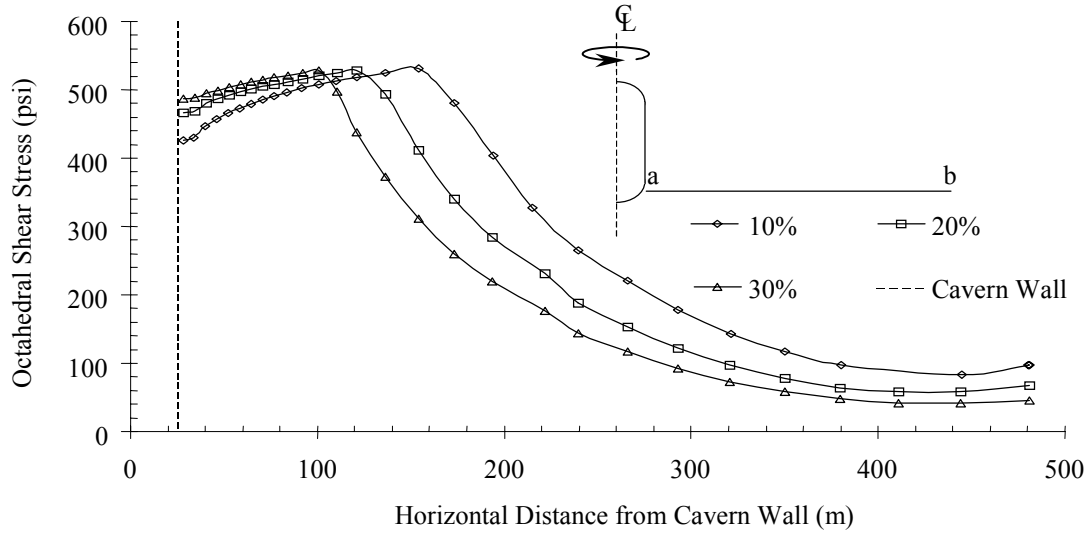

Figure B.17 Distributions of octahedral shear stress near the bottom of cavern along horizontal distance from cavern wall (Line a-b) for 20 year after construction. The internal pressures in the cavern are 10%, 20% and 30% of the stress in rock salt at the cavern roof. The stress in rock salt at the cavern roof for this model is 13.2 MPa (1,912 psi).

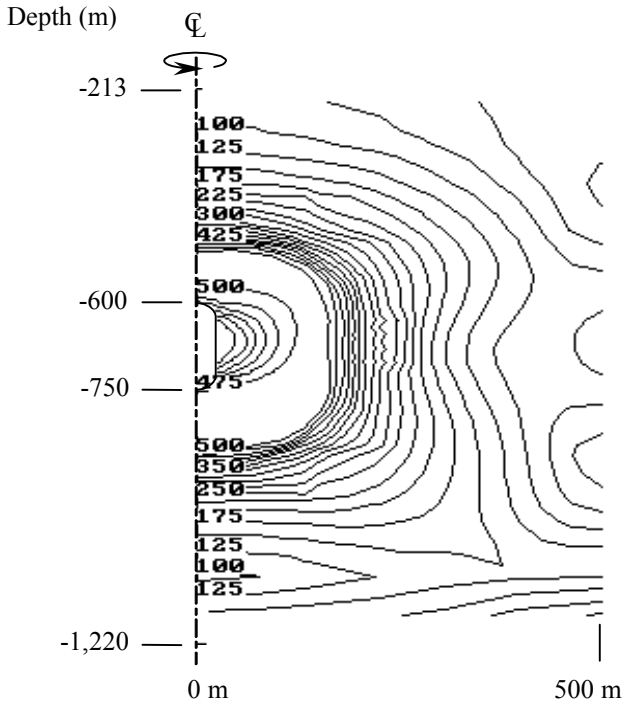

Figure B.18 Contour of octahedral shear stress around the cavern at 20 years after construction. The internal pressure is constant at 10% of the in-situ stress in salt at cavern roof. The maximum octahedral shear stress is equal 3.62 MPa (525 psi).

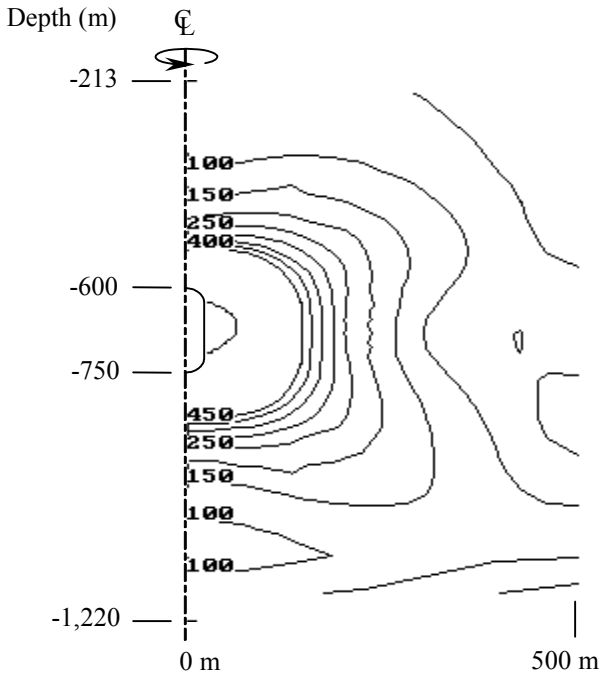

Figure B.19 Contour of octahedral shear stresses around the cavern at 20 years after construction. The internal pressure is constant at 20% of the in-situ stress at cavern roof. The maximum octahedral shear stress is equal 3.45 MPa (500 psi).

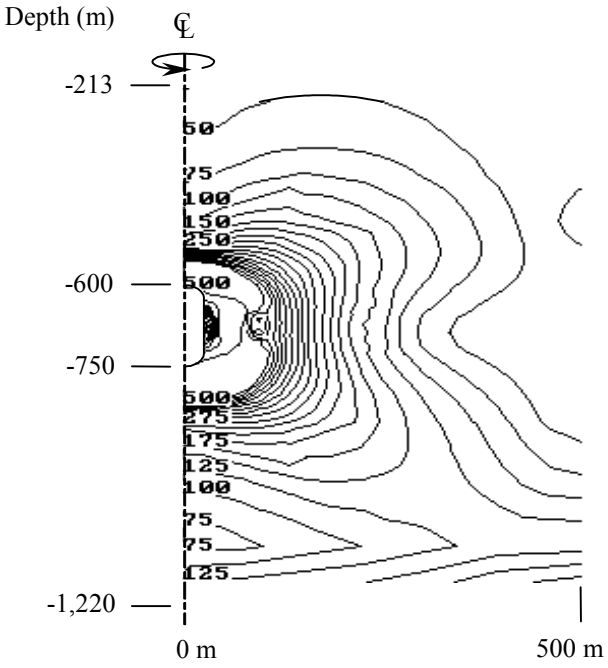

Figure B.20 Contour of octahedral shear stresses around the cavern at 20 years after construction. The internal pressure is constant at 30% of the in-situ stress at cavern roof. The maximum octahedral shear stress is equal 3.62 MPa (525 psi).

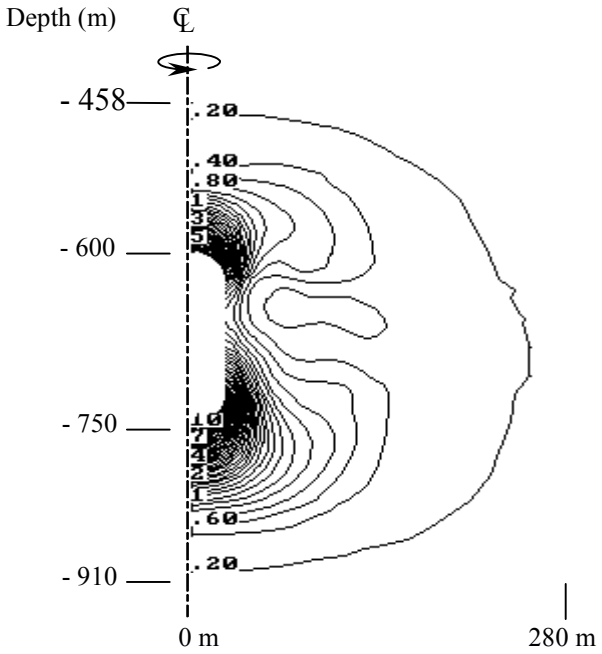

Figure B.21 Contour of octahedral shear strain around the cavern at 20 years after construction. The internal pressure is constant at 10% of the in-situ stress at cavern roof. The maximum octahedral shear strain is equal to 10.4%.

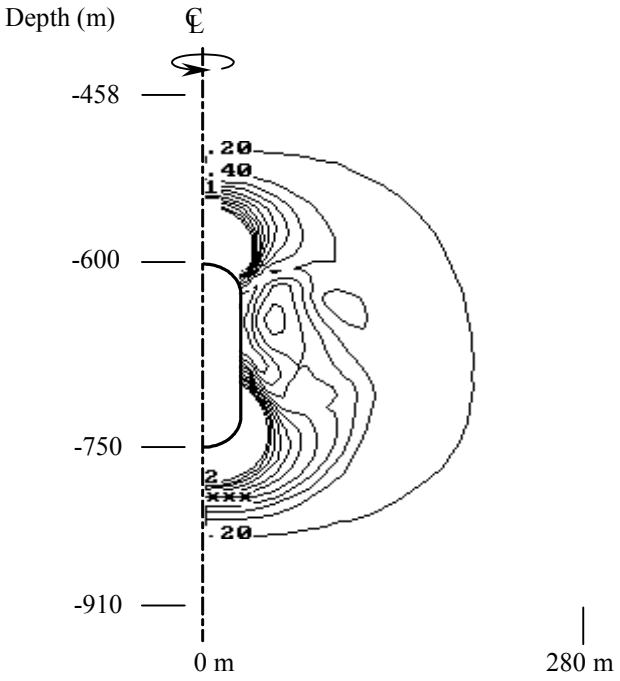

Figure B.22 Contour of octahedral shear strain around the cavern at 20 years after construction. The internal pressure is constant at 20% of the in-situ stress at cavern roof. The maximum octahedral shear strain is equal to 9.6%.

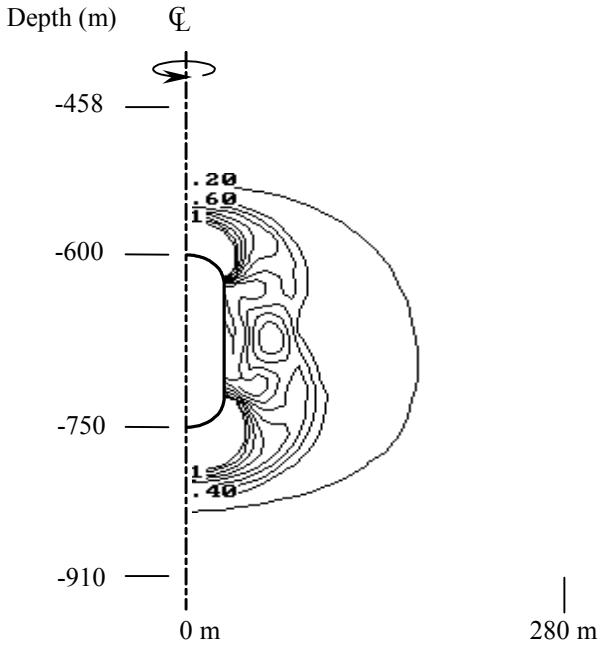

Figure B.23 Contour of octahedral shear strain around the cavern at 20 years after construction. The internal pressure is constant at 30% of the in-situ stress at cavern roof. The maximum octahedral shear strain is equal to 7.6%.

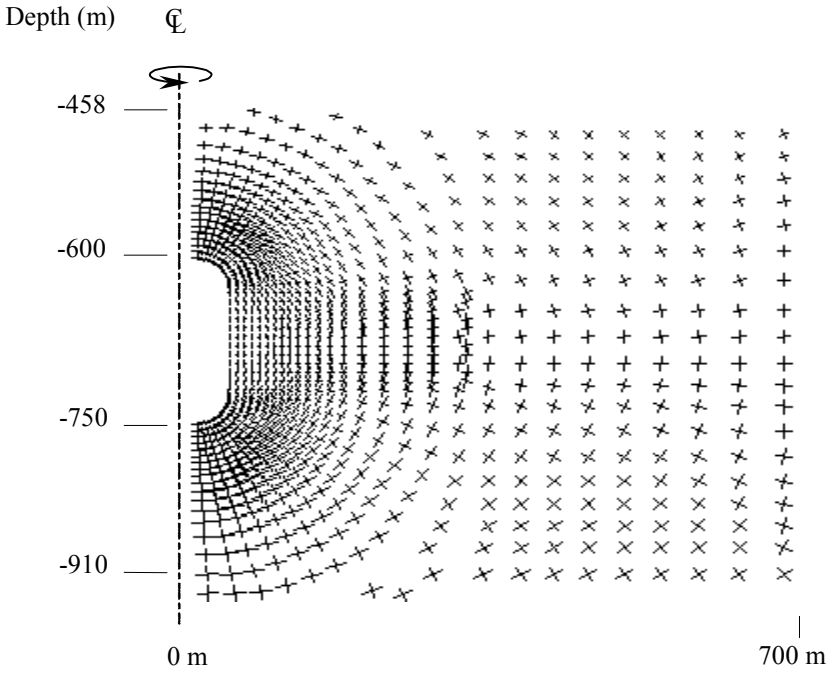

Figure B.24 Principal stresses vectors around the cavern at 20 years after construction. The internal pressure is constant at 10% of the in-situ stress at cavern roof. The maximum stress is equal to 4,108 psi (Vector Scale 20,000 psi/inch).

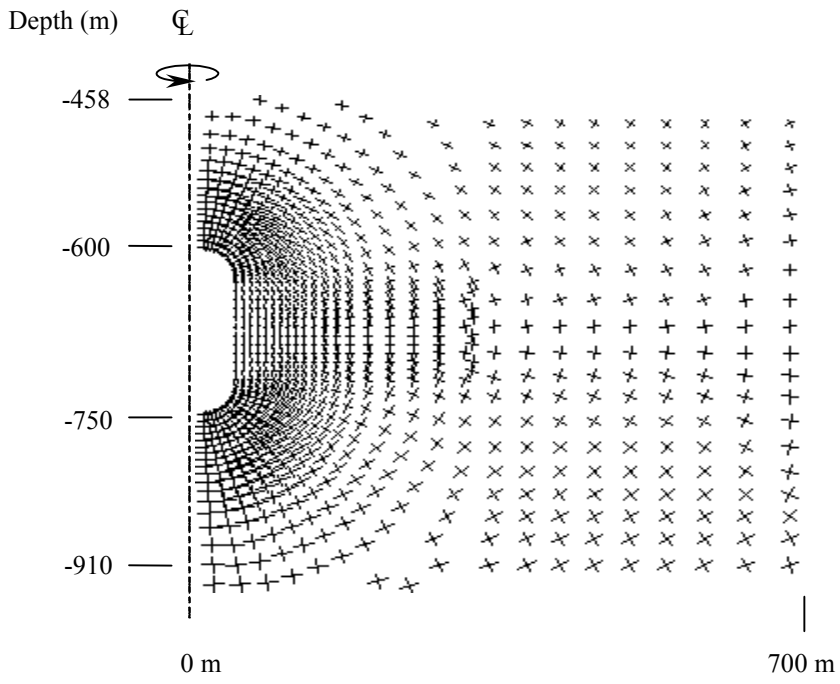

Figure B.25 Principal stresses vectors around the cavern at 20 years after construction. The internal pressure is constant at 20% of the stress at cavern roof. The maximum stress is equal to 4,107 psi (Vector Scale 20,000 psi/inch).

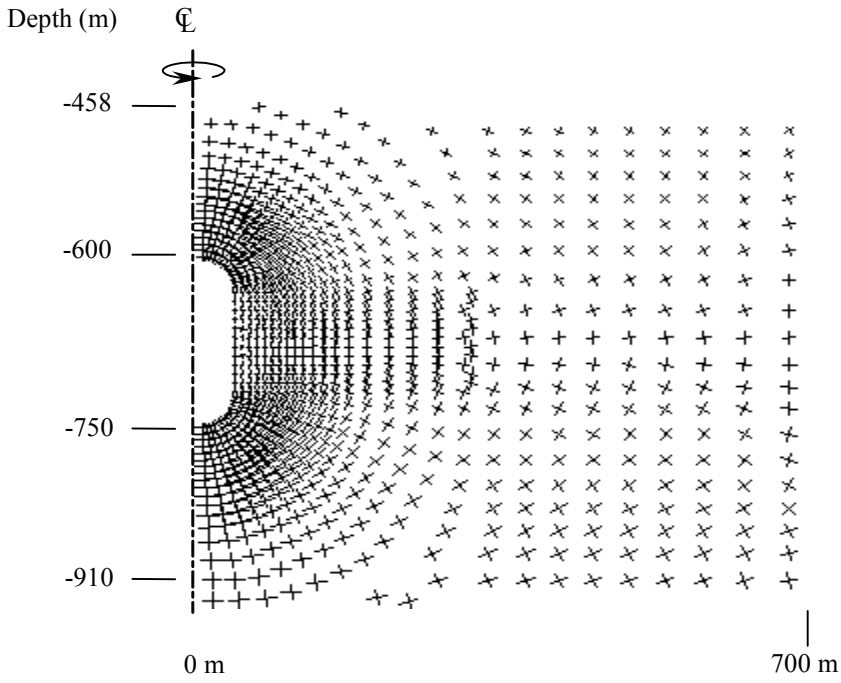

Figure B.26 Principal stresses vectors around the cavern at 20 years after construction. The internal pressure is constant at 30% of the stress at cavern roof. The maximum stress is equal to 4,100 psi (Vector Scale 20,000 psi/inch).

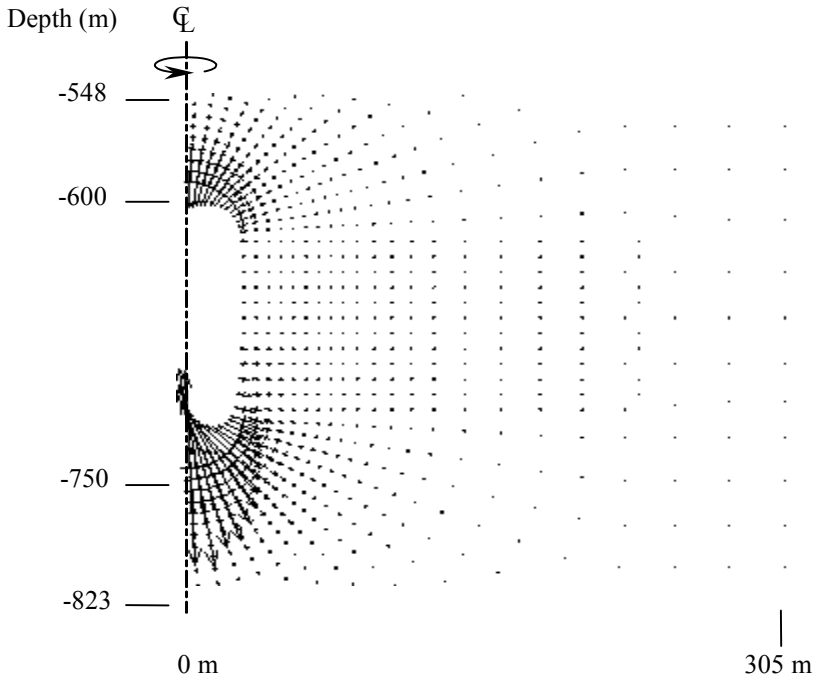

Figure B.27 Principal strain vectors around the cavern at 20 years after construction. The internal pressure is constant at 10% of the in-situ stress at cavern roof. The maximum strain is equal to 93% (Vector Scale 50% /inch).

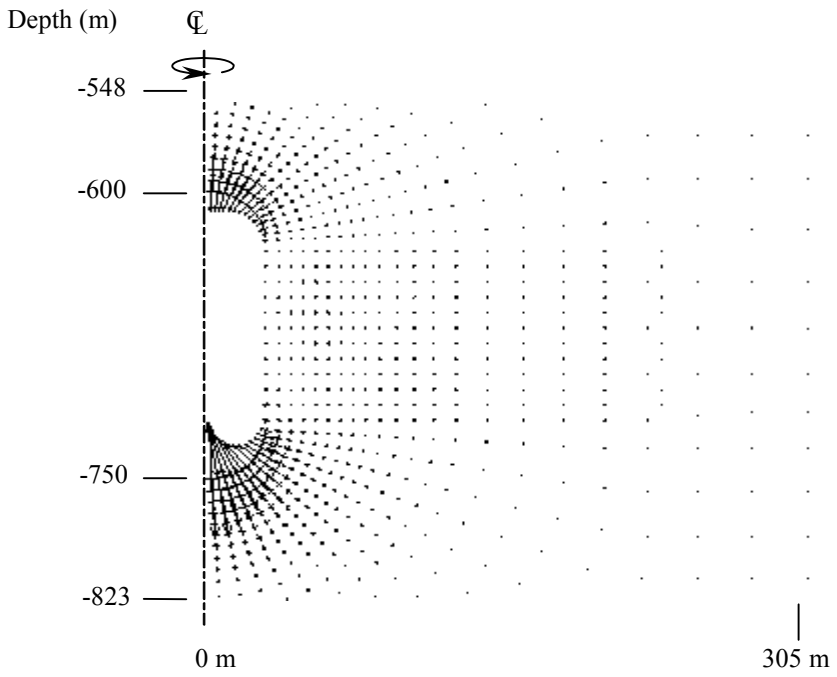

Figure B.28 Principal strain vectors around the cavern at 20 years after construction. The internal pressure is constant at 20% of the in-situ stress at cavern roof. The maximum strain is equal to 53% (Vector Scale 50% /inch).

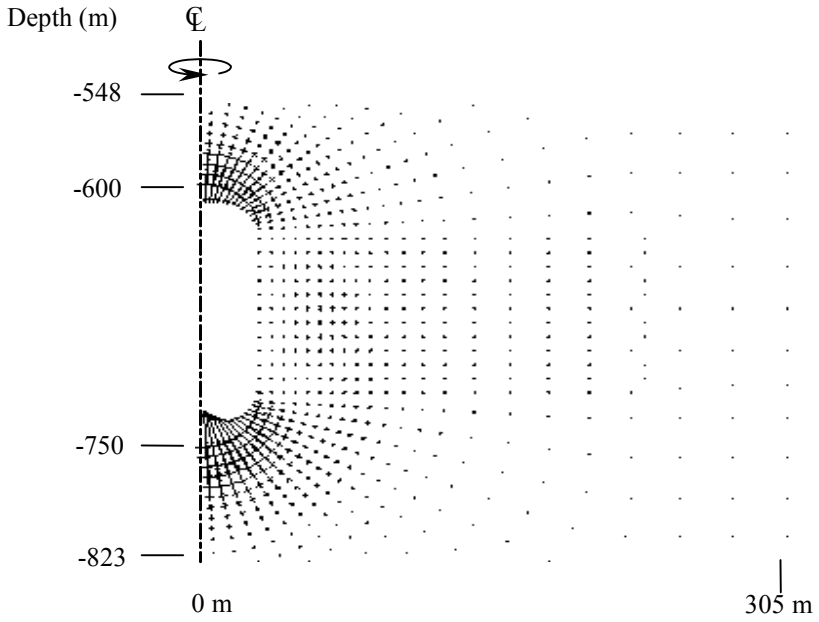

Figure B.29 Principal strain vectors around the cavern at 20 years after construction. The internal pressure is constant at 30% of the in-situ stress at cavern roof. The maximum strain is equal to 18% (Vector Scale 25% /inch).

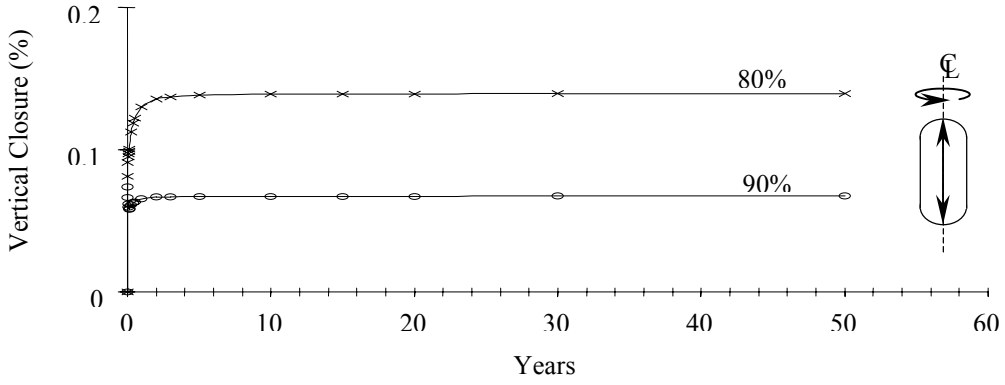

Figure B.30 Vertical closure at the centerline of cavern at the internal pressure equal 80% and 90% of the in-situ stress at the cavern roof. The stress in salt for this model is 13.2 MPa (1912 psi).

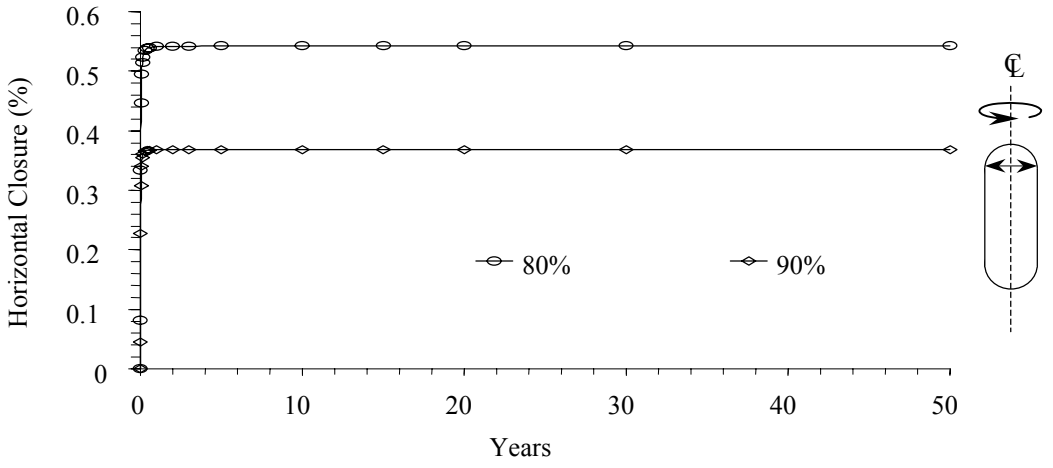

Figure B.31 Horizontal closure near the top of cavern at the internal pressure equal 80% and 90% of the stress at the cavern roof. The stress in salt for this model is 13.2 MPa (1,912 psi).

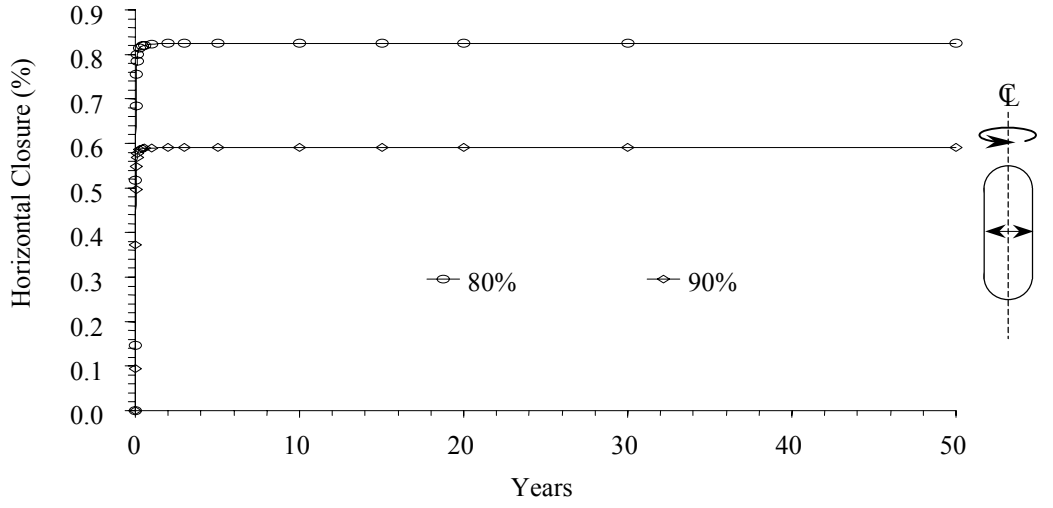

Figure B.32 Horizontal closure at the middle of cavern at the internal pressure equal 80% and 90% of the in-situ stress at the cavern roof. The stress in salt for this model is 13.2 MPa (1,912 psi).

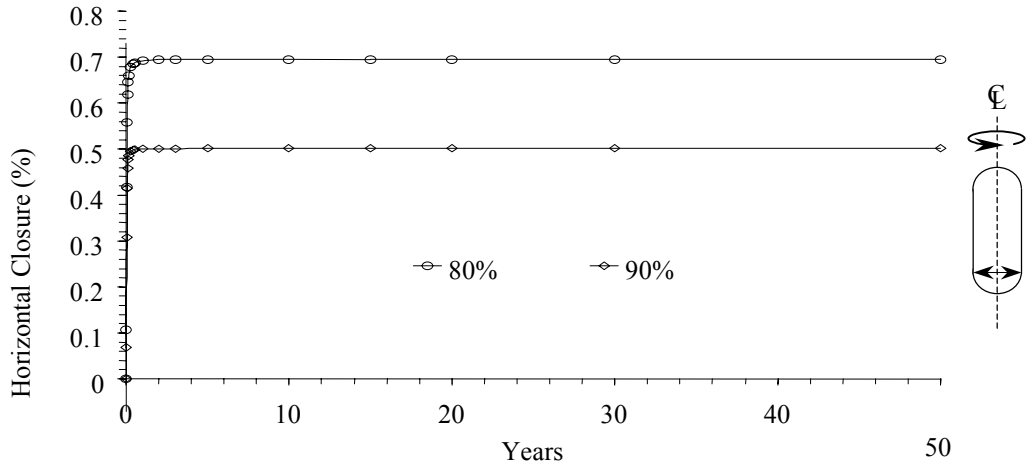

Figure B.33 Horizontal closure near the bottom of cavern at the internal pressure equal 80% and 90% of the in-situ stress at the cavern roof. The stress in salt for this model is 13.2 MPa (1,912 psi).

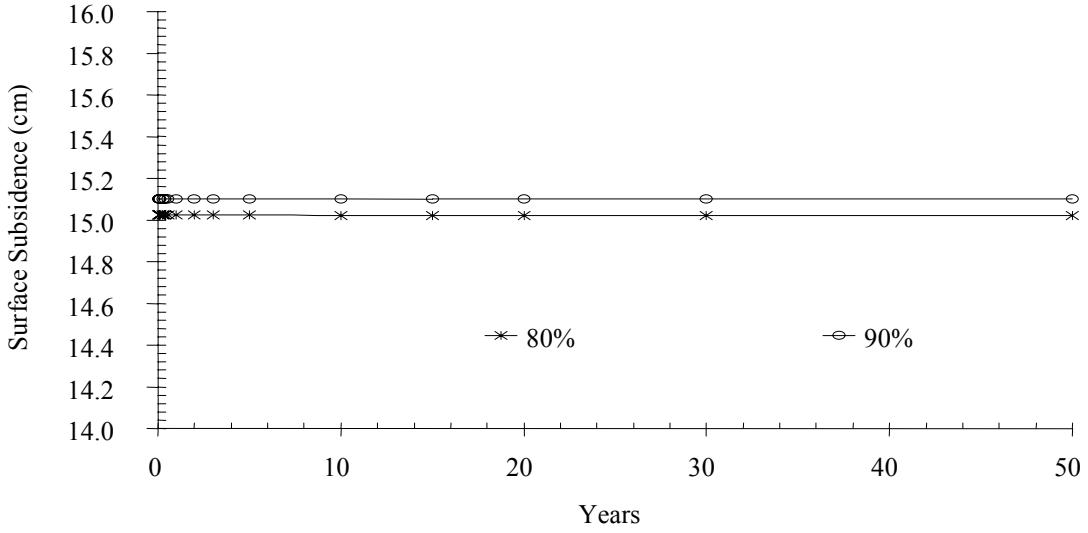

Figure B.34 Surface subsidence at the centerline of cavern for 20 year after construction. The results are compared for the internal pressure of 80% and 90% of stress at the cavern roof. The stress in rock salt at the cavern roof for this model is 13.2 MPa (1,912 psi).

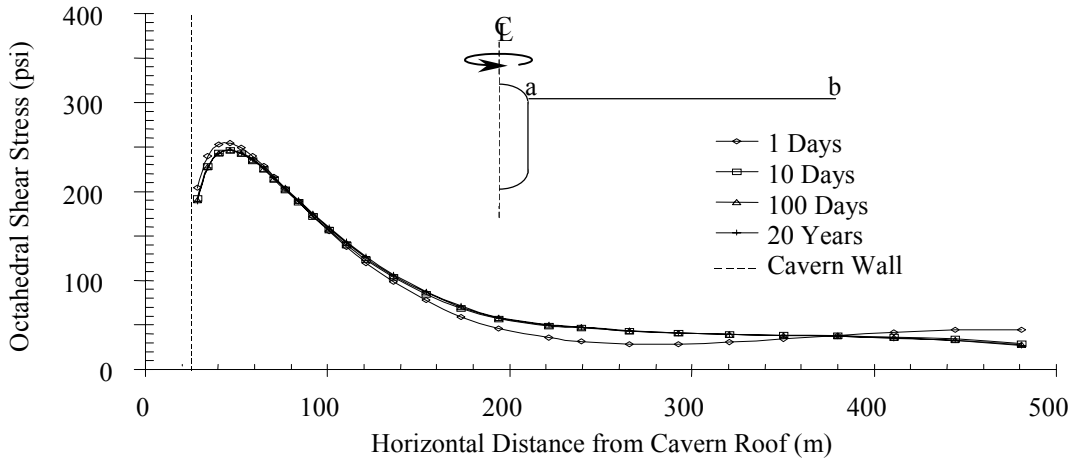

Figure B.35 Distributions of octahedral shear stress near the top of cavern along horizontal distance from cavern wall (Line a-b). The internal pressure in the cavern is 80% of the stress at the cavern roof. The stress in rock salt at the cavern roof for this model is 13.2 MPa (1,912 psi).

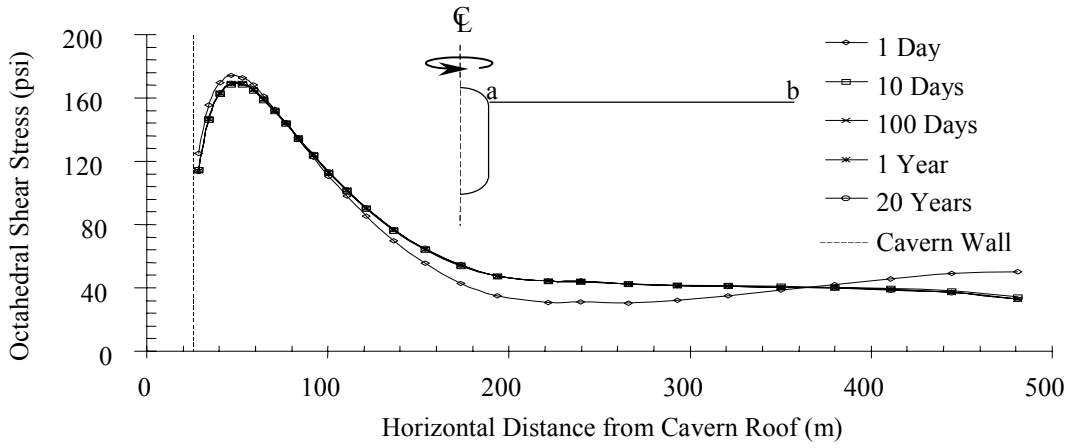

Figure B.36 Distributions of octahedral shear stress near the top of cavern along horizontal distance from cavern wall (Line a-b). The internal pressure in the cavern is 90% of the in-situ stress at the cavern roof. The stress in rock salt at the cavern roof for this model is 13.2 MPa (1,912 psi).

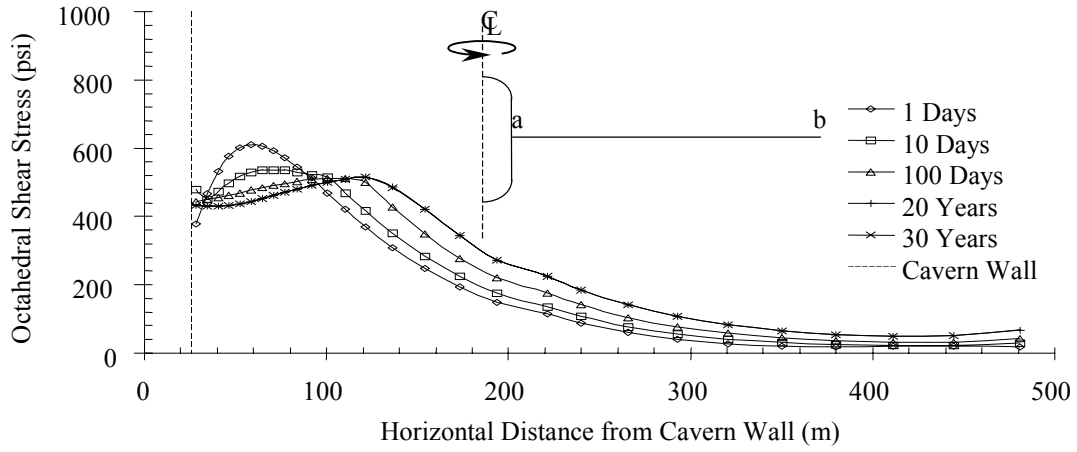

Figure B.37 Distributions of octahedral shear stresses at the middle of cavern along horizontal distance from cavern wall (Line a-b). The internal pressure in the cavern is 80% of the in-situ stress at the cavern roof. The stress in rock salt at the cavern roof for this model is 13.2 MPa (1,912 psi).

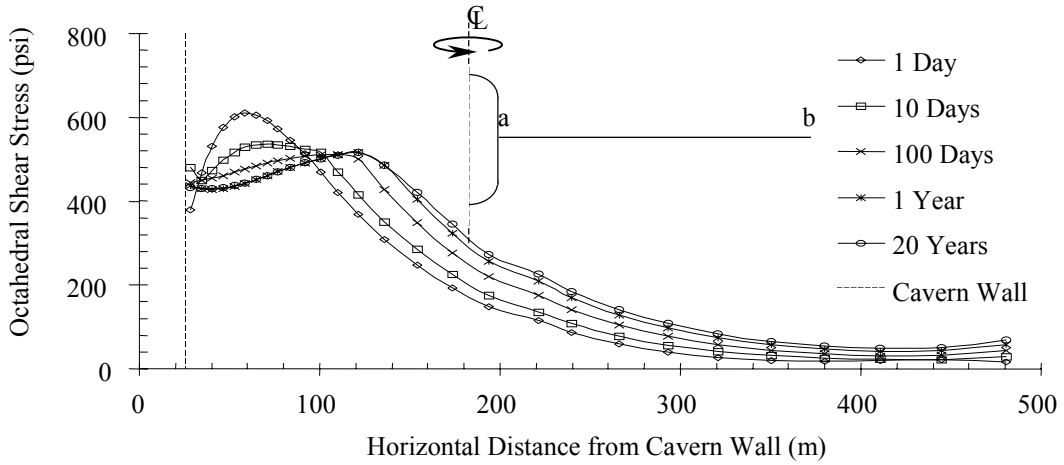

Figure B.38 Distributions of octahedral shear stress at the middle of cavern along horizontal distance from cavern wall (Line a-b). The internal pressure in the cavern is 90% of the in-situ stress at the cavern roof. The stress in rock salt at the cavern roof for this model is 13.2 MPa (1,912 psi).

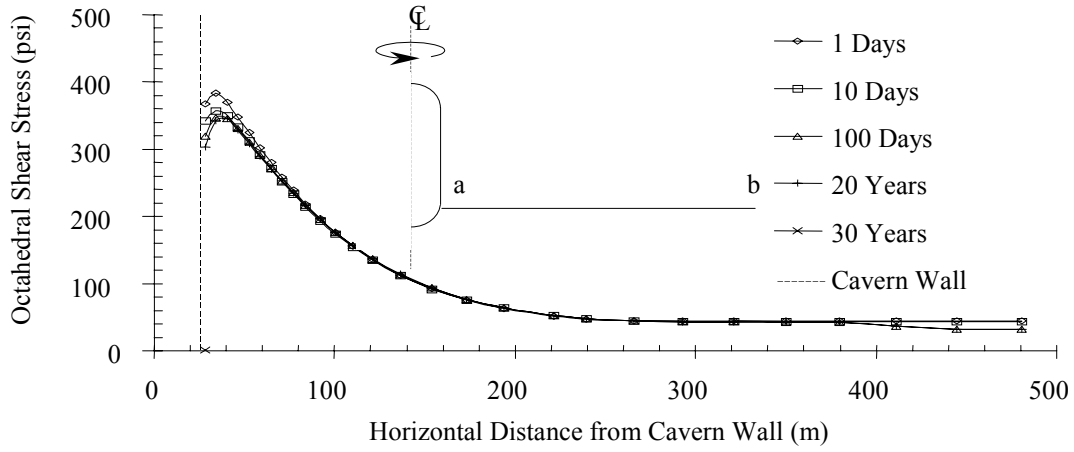

Figure B.39 Distributions of octahedral shear stresses near the bottom of cavern along horizontal distance from cavern wall (Line a-b). The internal pressure in the cavern is 80% of the in-situ stress at the cavern roof. The stress in rock salt at the cavern roof for this model is 13.2 MPa (1,912 psi).

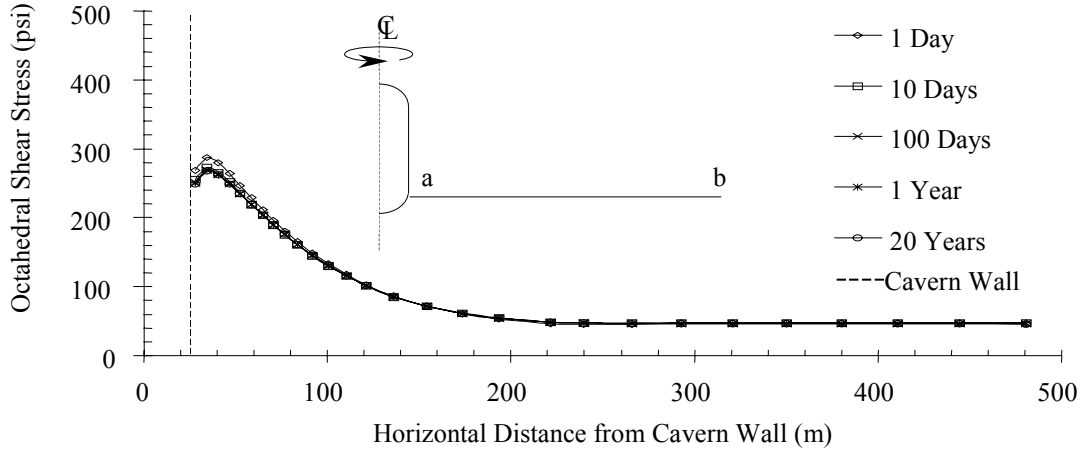

Figure B.40 Distributions of octahedral shear stress near the bottom of cavern along horizontal distance from cavern wall (Line a-b). The internal pressure in the cavern is 90% of the in-situ stress at the cavern roof. The stress in rock salt at the cavern roof for this model is 13.2 MPa (1,912 psi).

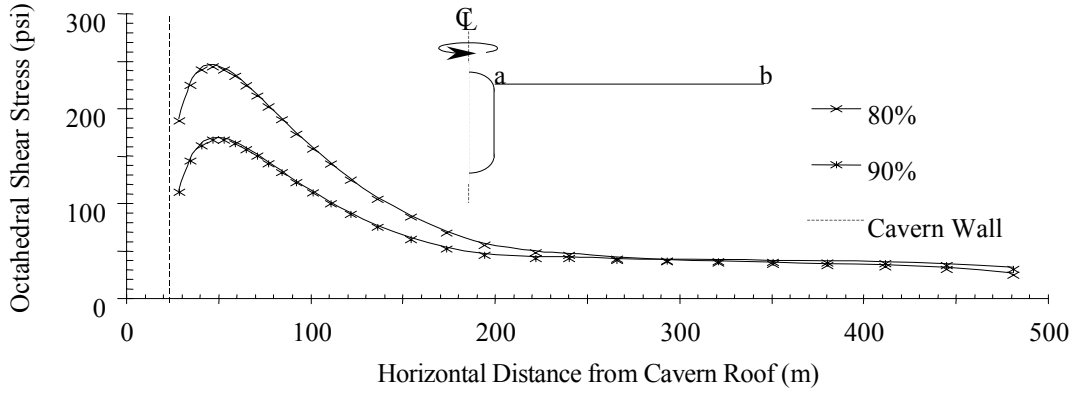

Figure B.41 Distributions of octahedral shear stresses near the top of cavern along horizontal distance from cavern wall (Line a-b) for 20 year after construction. The internal pressures in the cavern are 80% and 90% of the in-situ stress at the cavern roof. The stress in rock salt at the cavern roof for this model is 13.2 MPa (1,912 psi).

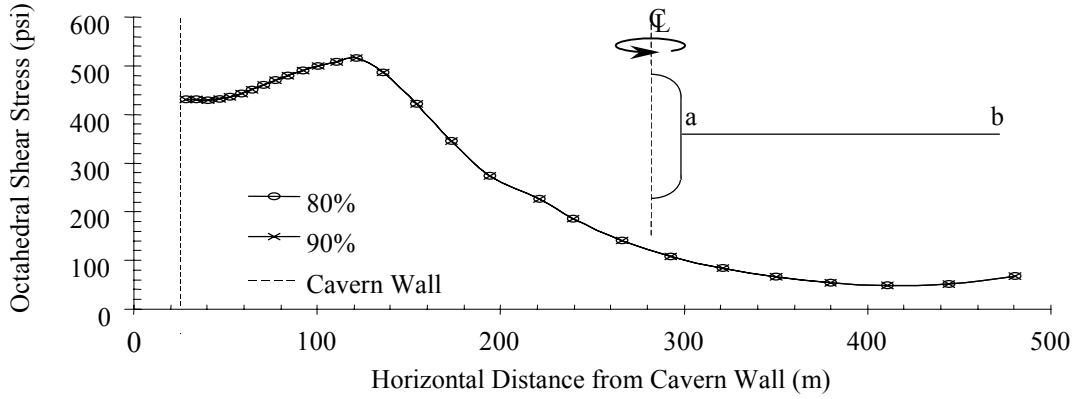

Figure B.42 Distributions of octahedral shear stresses at the middle of cavern along horizontal distance from cavern wall (Line a-b) for 20 year after construction. The internal pressures in the cavern are 80% and 90% of the in-situ stress at the cavern roof. The stress in rock salt at the cavern roof for this model is 13.2 MPa (1,912 psi).

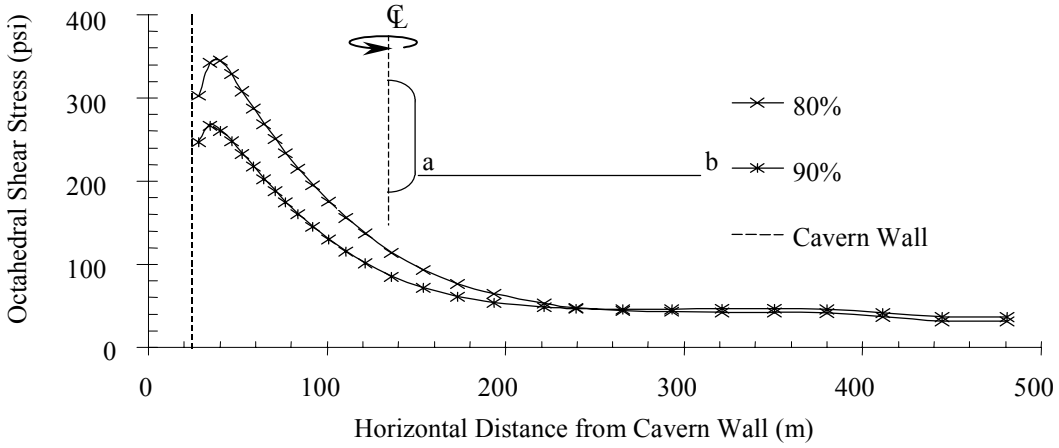

Figure B.43 Distributions of octahedral shear stresses near the bottom of cavern along horizontal distance from cavern wall (Line a-b) for 20 year after construction. The internal pressures in the cavern are 80% and 90% of the in-situ stress at the cavern roof. The stress in rock salt at the cavern roof for this model is 13.2 MPa (1,912 psi).

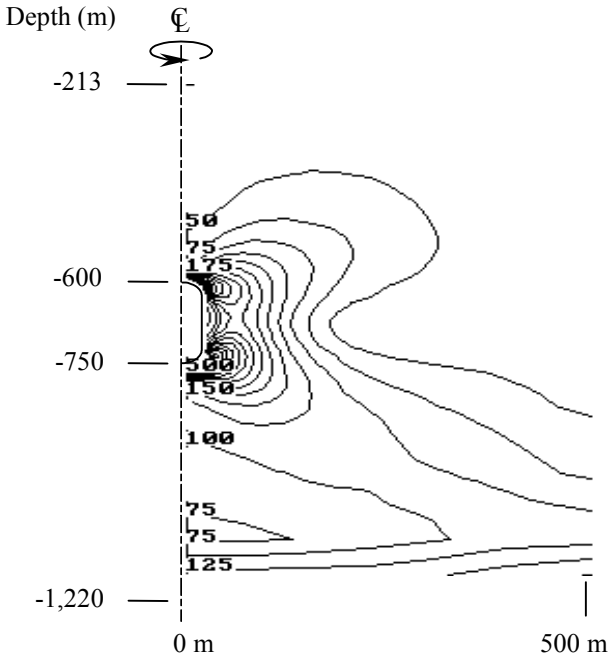

Figure B.44 Contour of octahedral shear stresses around the cavern at 20 years after construction. The internal pressure is constant at 80% of the in-situ stress at cavern roof. The maximum octahedral shear stress is equal 3.62 MPa (525 psi).

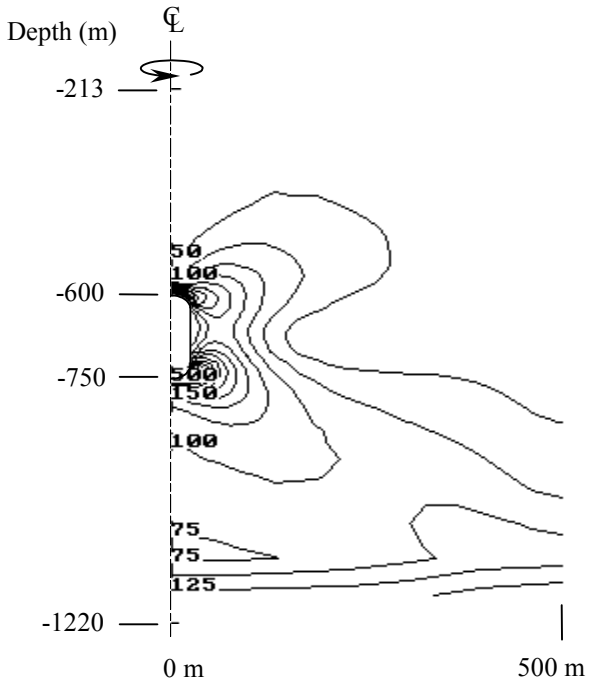

Figure B.45 Contour of octahedral shear stress around the cavern at 20 years after construction. The internal pressure is constant at 90% of the in-situ stress at cavern roof. The maximum octahedral shear stress is equal3.62 MPa (525 psi).

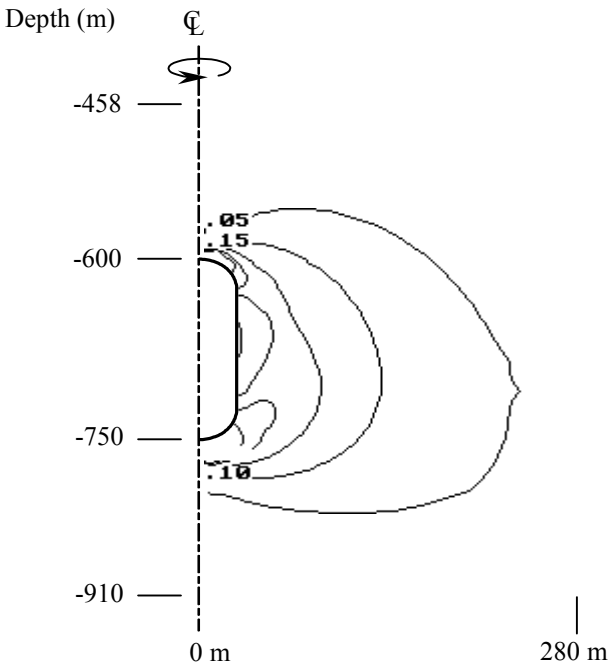

Figure B.46 Contour of octahedral shear strain around the cavern at 20 years after construction. The internal pressure is constant at 80% of the in-situ stress at cavern roof. The maximum octahedral shear strain is equal 1.1%.

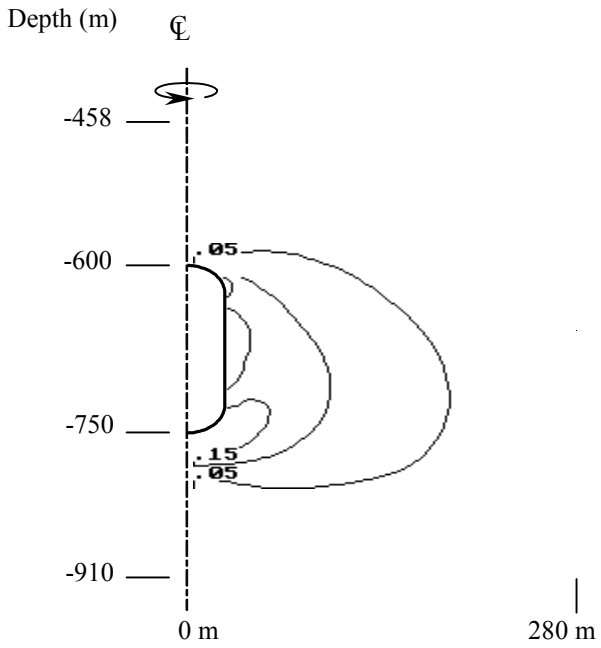

Figure B.47 Contour of octahedral shear strain around the cavern at 20 years after construction. The internal pressure is constant at 90% of the in-situ stress in rock salt at cavern roof. The maximum octahedral shear strain is equal 0.6%.

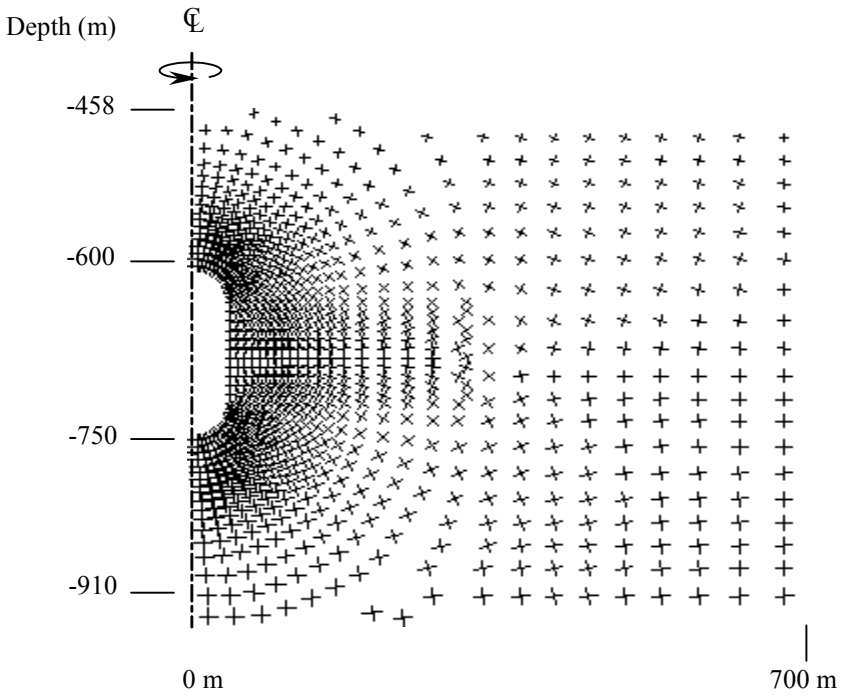

Figure B.48 Principal stress vectors around the cavern at 20 years after construction. The internal pressure is constant at 80% of the in-situ stress at cavern roof. The maximum stress is equal to 27.97 MPa (4,055 psi), (Vector Scale 20,000 psi/inch).

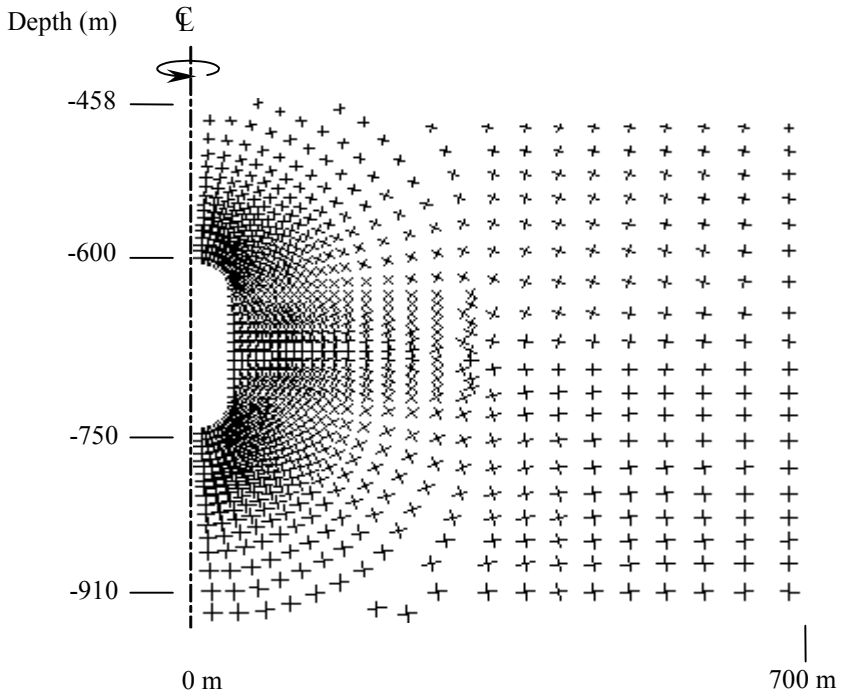

Figure B.49 Principal stress vectors around the cavern at 20 years after construction. The internal pressure is constant at 90% of the stress in rock salt at cavern roof. The maximum stress is equal to 4,054 psi (Vector Scale 20,000 psi/inch).

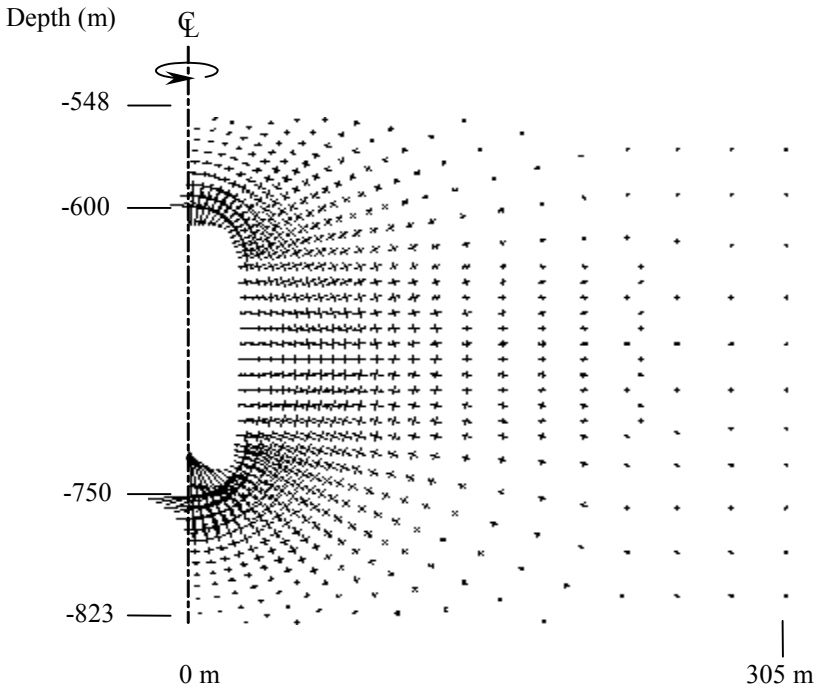

Figure B.50 Principal strain vectors around the cavern at 20 years after construction. The internal pressure is constant at 80% of the in-situ stress at cavern roof. The maximum strain is equal to 0.8% (Vector Scale 1% /inch).

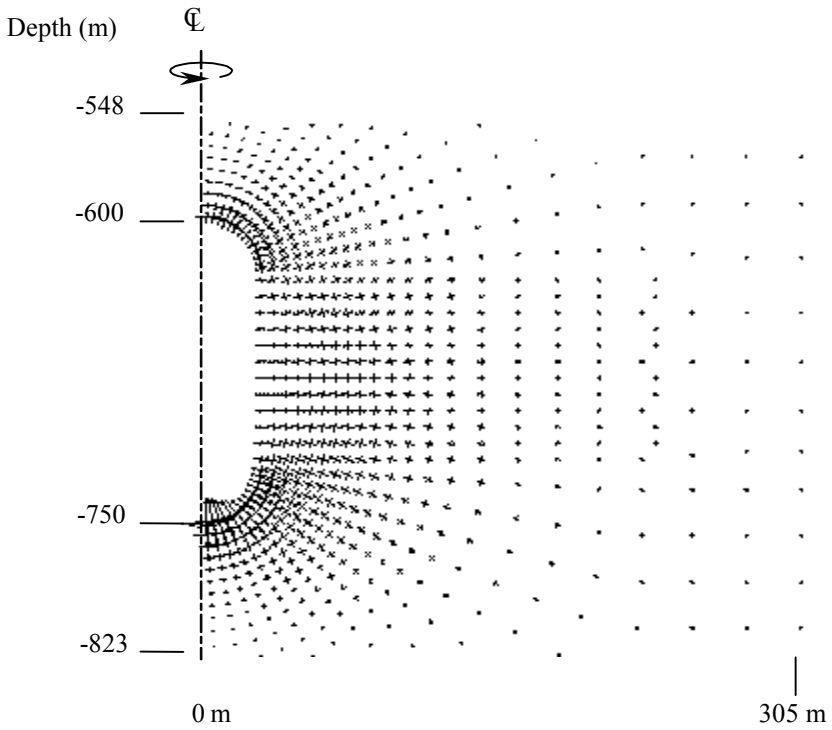

Figure B.51 Principal strain vectors around the cavern at 20 years after construction. The internal pressure is constant at 90% of the in-situ stress at cavern roof. The maximum strain is equal to 0.4% (Vector Scale 1% /inch).

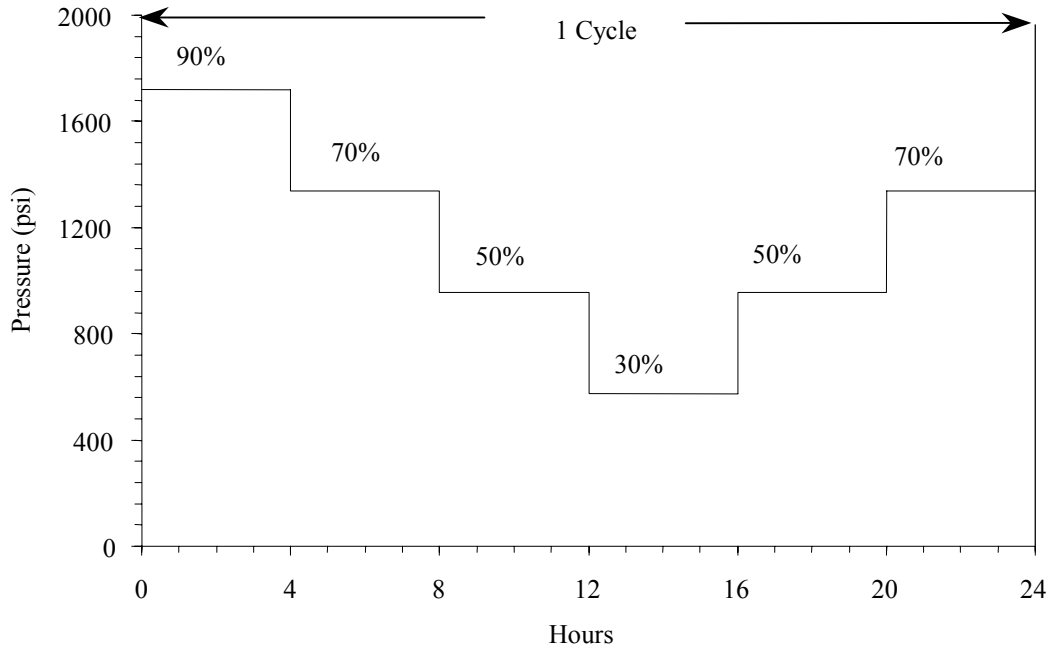

Figure B.52 The pressure change for daily cycle in the cavern. The maximum and minimum pressures are 90% and 30% of the in-situ stress at the cavern roof, respectively.

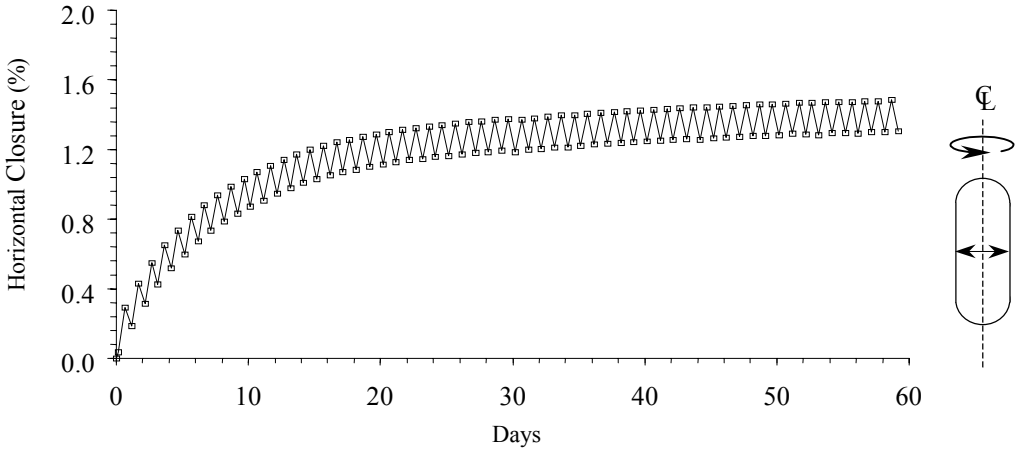

Figure B.53 Horizontal closure at the middle of cavern under cyclic pressurizing. The maximum and minimum pressures are 30% and 90% of the in-situ stress at cavern roof, respectively. The stress in rock salt at the cavern roof is 13.2 MPa (1,912 psi).

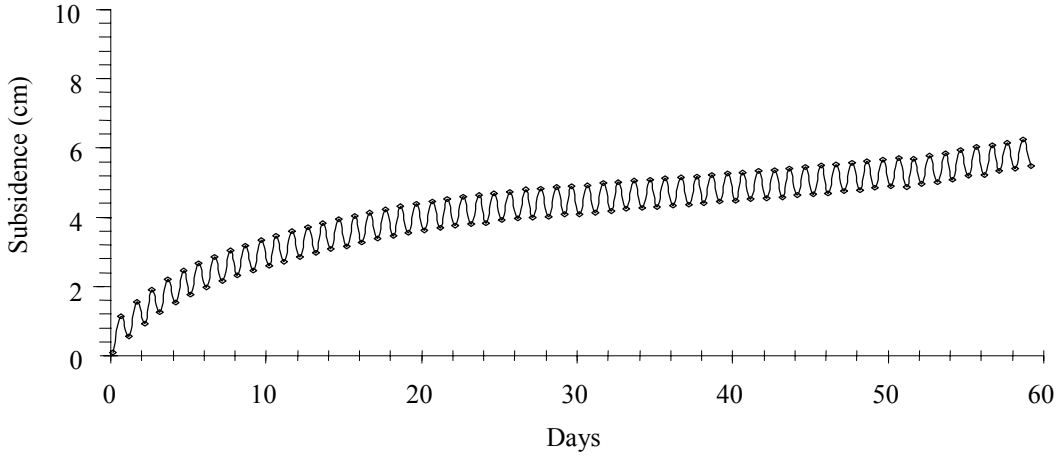

Figure B.54 Surface subsidence at the centerline of cavern under cyclic pressurizing. The maximum and minimum pressures are 30% and 90% of the in-situ stress at cavern roof, respectively. The stress in rock salt at the cavern roof is 13.2 MPa (1,912 psi).

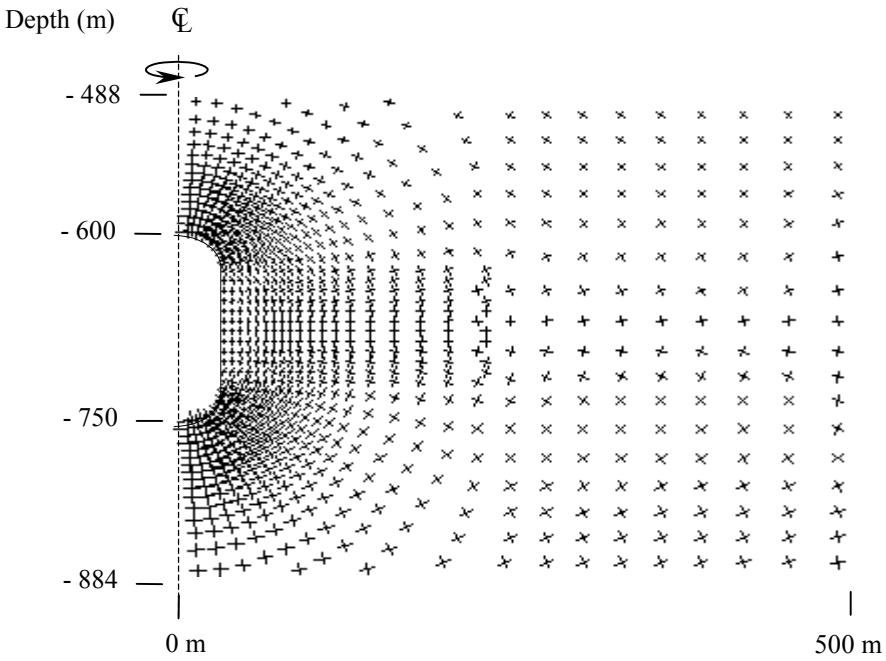

Figure B.55 Principal stress vectors around the cavern after 40 cycles of pressurizing. The maximum and minimum pressures are 30% and 90% of the in-situ stress at cavern roof, respectively. The stress in rock salt at the cavern roof is 13.2 MPa (1,912 psi). The maximum stress is 4,391 psi (Vector Scale 25,000 psi/inch).

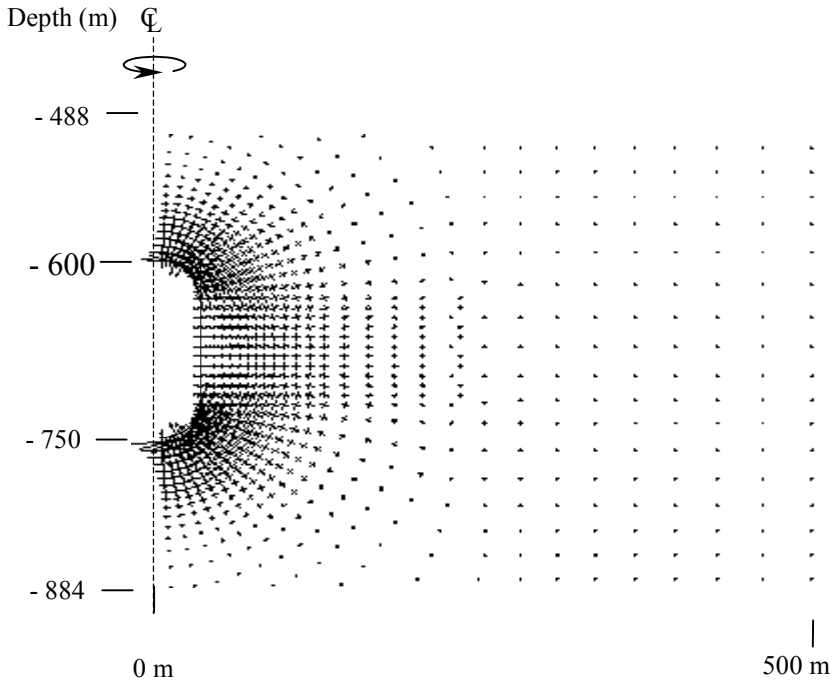

Figure B.56 Principal strain vectors around the cavern after 40 cycles of pressurizing. The maximum and minimum pressures are 30% and 90% of the stress in rock salt at cavern roof, respectively. The stress in rock salt at the cavern roof is 13.2 MPa (1,912 psi). The maximum strain is 65% (Vector Scale 2%/inch).

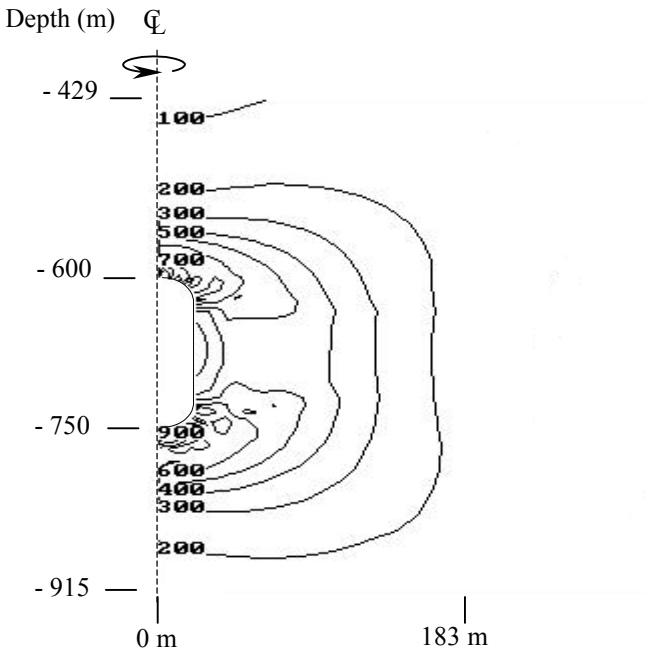

Figure B.57 Contour of octahedral shear stress around the cavern after 40 cycles of pressurizing. The maximum and minimum pressures are 30% and 90% of the in-situ stress at cavern roof, respectively. The stress in rock salt at the cavern roof is 13.2 MPa (1,912 psi). The maximum stress is 6.90 MPa (1,000 psi), (Contour interval =100).

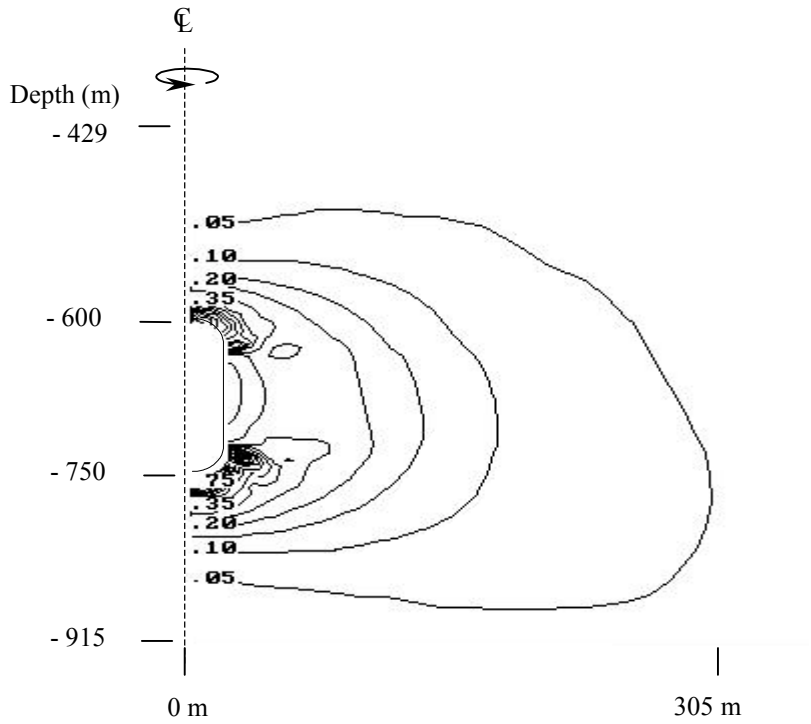

Figure B.58 Contour of octahedral shear strain around the cavern after 40 cycles of pressurizing. The maximum and minimum pressures are 30% and 90% of the stress in rock salt at cavern roof, respectively. The stress in rock salt at the cavern roof is 13.2 MPa (1,912 psi). The maximum strain is 90% (Contour interval =0.05).

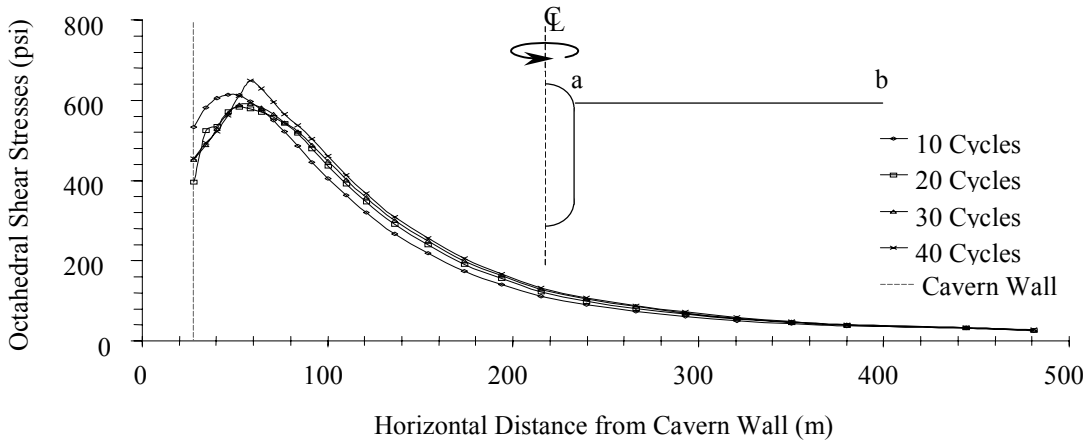

Figure B.59 Distributions of octahedral shear stresses near the top of cavern along horizontal distance from cavern wall (Line a-b) after 10, 20, 30, and 40 cycles of pressurizing.

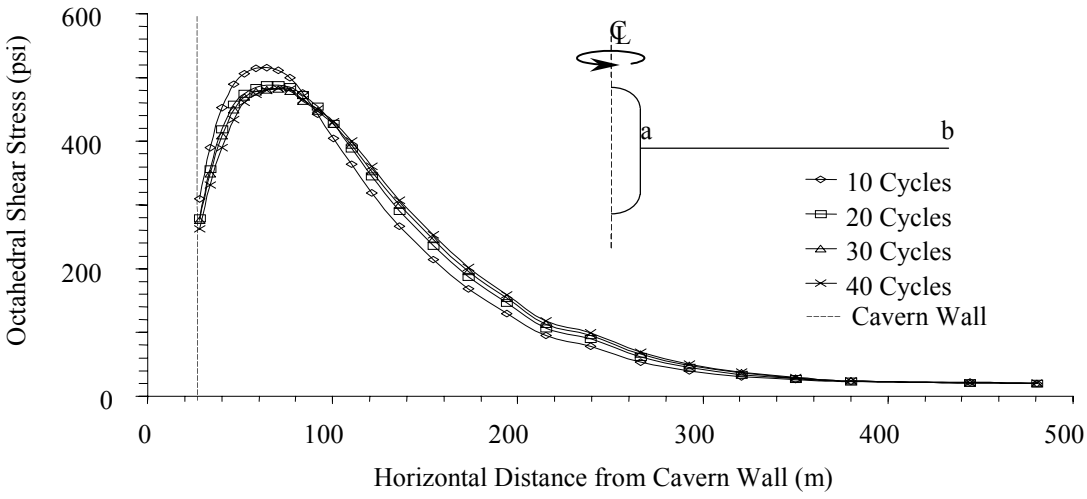

Figure B.60 Distributions of octahedral shear stress at the middle of cavern along horizontal distance from cavern wall (Line a-b) after 10, 20, 30, and 40 cycles of pressurizing.

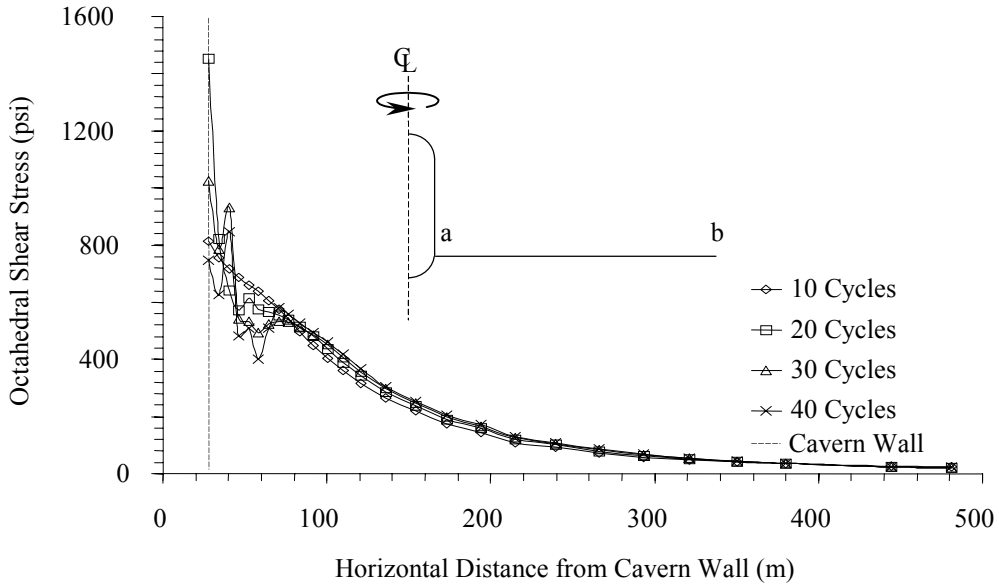

Figure B.61 Distributions of octahedral shear stress near the bottom of cavern along horizontal distance from cavern wall (Line a-b) after 10, 20, 30, and 40 cycles of pressurizing.

BIOGRAPHY

Mr. Decho Phueakphum was born on the 7th of June 1977 in Surat Thani province. He earned his Bachelor's Degree in Civil Engineering from Suranaree University of Technology (SUT) in 1999. After graduation, he continued with his Master's degree in the School of Geotechnology, Institute of Engineering, SUT with the major in Geological Engineering. Between 2000-2003, he was a research assistant at SUT. His expertises are in the areas of soil and rock mechanics, hydrology and foundation engineering.